

Mud Diapirs and Folds in the South Caspian Basin:

Geometry and Syn-Sedimentary Evolution of Structures with Petroleum Interest

Editor: Universidad de Granada. Tesis Doctorales
Autora: Idaira Santos Betancor
ISBN: 978-84-9125-359-4
URI: <http://hdl.handle.net/10481/42148>

PH. D. THESIS



University of Granada
Department of Geodynamics

**Mud diapirs and folds in the South Caspian
Basin: geometry and syn-sedimentary evolution
of structures with petroleum interest**

IDAIRA SANTOS BETANCOR

University of Granada 2015

TESIS DOCTORAL

Programa de doctorado Ciencias de la Tierra
UNIVERSIDAD DE GRANADA



Mud diapirs and folds in the South Caspian Basin: geometry and syn-sedimentary evolution of structures with petroleum interest

Diapiros de barro y pliegues en el Mar Caspio meridional: análisis geométrico y evolución sin-sedimentaria de estructuras con interés petrolero

Memoria de Tesis Doctoral presentada por la Licenciada en Geología Doña Idaira Santos Betancor para optar al Grado de Doctor por la Universidad de Granada.

Granada, 29 de septiembre de 2015

Dirigida por:

JUAN IGNACIO SOTO HERMOSO

VºBº del Director

Fdo. Juan Ignacio Soto Hermoso

Fdo. La doctoranda

La doctoranda Doña Idaira Santos Betancor y el director de la tesis doctoral Don Juan Ignacio Soto Hermoso garantizamos, al firmar esta tesis doctoral, que el trabajo ha sido realizado por la doctoranda bajo la dirección del director y hasta donde nuestro conocimiento alcanza, en la realización del trabajo, se han respetado los derechos de otros autores a ser citados, cuando se han utilizado sus resultados o publicaciones.

Granada, 29 de septiembre de 2015

Director de la tesis

Doctoranda

Fdo. Juan Ignacio Soto Hermoso

Fdo. Idaira Santos Betancor

A mi familia y a todos los que han hecho posible este logro.

ACKNOWLEDGEMENTS

First of all, I would like to express my deepest gratitude to my supervisor Professor Juan Ignacio Soto Hermoso, who guided me and gave me his unconditional support throughout this research adventure. I would like to extend my thanks to my co-supervisor Dr. Lidia Lonergan for her reception at Imperial College, who was resourceful and very helpful.

I have to thank Dr. Ismael Sánchez Borrego, from the Departamento de Estadística e Investigación Operativa in the Universidad de Granada, who contributed to the statistical part of this thesis. I cannot forget Pablo, who patiently helped me with great part of the drawing work.

I want to show gratitude to my workmates, the “geological” pre- and post-doctorates, for accompanying me in this important achievement: in special, Enric and Edu, for sharing every moment, Fran and our sweet coffees, Yasmina for their important advices, Julia, Juan Antonio, Mohammed, Aratz, Irene and our tupperes, Juanpe, Lourdes, Ángel and his empathy, Carlos, Manuel, Rafa,... My most sincere thanks go to old workmates: Lucía and Rocío, now also close friends, and Pedro; they all helped me in many challenging and hard situations and made me feel better in the most difficult moments. I really appreciate the help of Marina, Fabiola and, above all, Raquel that made my days a bit easier and that at one time to another gave me energy. Mayte, Miguel, Chiara, “Oce” and Eva, thank you for our laughing moments.

I give my loving acknowledgment to my dad and my mum, and also to Edu, who was very patient, being my compass when I felt lost, always there. Many thanks to my family-in-law, especially important in the final countdown. Finally, last but not least, I cannot forget the inspiring people that taught me about scientific world, and made me to feel more confident and strong.

This research was administered by the Andalusian Institute of Earth Sciences (IACT), under the auspices of the High Council of Scientific Research (CSIC) in Spain. This study would not be possible without the data survey from REPSOL and specially, help from Dr. Tomás Zapata and Carlos Macellari. I am grateful to Seismic Micro Technology for providing the Kingdom Suite software, recently acquired by IHS, through a research agreement. I also say thanks to IHS for supplying regional maps and to Schlumberger for his authorization to use Petrel. Special thanks to the Departamento de Geodinámica that hosted me and provided me technical facilities. I

want to express my acknowledgment on the RNM 376 group, which provided me economic support.

AGRADECIMIENTOS

En primer lugar he de dar las gracias a mi supervisor, Juan Ignacio; él me ha permitido alcanzar este hito y sobre todo, ha sido un buen maestro en mi formación profesional y personal, que espero y deseo que sean útiles en la etapa que se avecina. También quiero expresar mi gratitud a mi supervisora Lidia Lonergan, durante mi estancia en el Imperial College, que me enseñó a sacar el máximo partido a mi trabajo.

Mi enorme agradecimiento a Ismael, del Departamento de Estadística e Investigación Operativa de la UGR, por su colaboración. No me puedo olvidar de agradecer a Pablo, que me ayudó en gran parte de las ilustraciones, aunque a veces nos costara hacernos entender.

Muchísimas gracias a todos los becarios que me han acompañado en esta andadura y con los que el camino se ha hecho más fácil; por una parte, a los “geológicos”: especialmente, Enric y Edu, por compartir cada momento, Fran y nuestros cafés, Yasmina y sus importantísimos consejos, Julia, Juan Antonio, Mohammed, Aratz, Irene y nuestros tupperes, Juanpe, Lourdes, Ángel y su empatía, Carlos, Manuel, Rafa,... y por otro lado, a Lucía y Rocío, ahora también amigas, y Pedro, que me ayudaron a no venirme abajo en los momentos más difíciles. Marina, Fabiola y, sobre todo, Raquel, también me ayudaron con su fiel compañía en el transcurso del camino. Mayte, Miguel, y Chiara, “Oce” y Eva, gracias por más de unas risas.

Y ante todo, quiero agradecer profundamente a mis padres y a mi novio Edu, que han sido mi apoyo fundamental y siempre han estado ahí, en las duras, y ahora también en las maduras, y aguantándome sin dudar ni preguntar. Y por supuesto, también agradecer a mi familia política, que me sustentaron con especial fuerza en la cuenta atrás. Por último, pero no por ello menos merecedor, a todos aquellos que, aunque quizá no se acuerden de mi existencia, me han hecho más conocedora del mundo científico, de mí misma y gracias a los cuales he aprendido a ser más fuerte.

Esta tesis ha sido financiada por el Instituto Andaluz de Ciencias de la Tierra (IACT), auspiciado por el Consejo Superior de Investigaciones Científicas (CSIC). El estudio no habría sido posible sin los datos proporcionados por REPSOL, y especiales gracias a Tomás Zapata y Carlos Macellari. Agradecer el apoyo informático de IHS que nos concedió la licencia de Kingdom Suite, así como mapas regionales, a través de acuerdos académicos. Schlumberger nos ha autorizado el uso

de Petrel. Mi más sincero agradecimiento al departamento de Geodinámica al que “usurpé” las instalaciones. Esta investigación se ha desarrollado parcialmente bajo el apoyo del Grupo de Investigación RNM 376 de la Junta de Andalucía.

INDEX

LIST OF FIGURES	ix
LIST OF TABLES	xv
ABSTRACT	xvii
RESUMEN	xx
1. INTRODUCTION.....	1
<i>Objectives of this thesis</i>	<i>3</i>
2. THE SOUTH CASPIAN BASIN	5
2.1. Situation.....	5
2.2. Present-day Tectonics.....	7
2.3. Deep Structure	12
2.4. Structure and Tectonic Evolution.....	14
2.5. Mud Diapirs and Volcanoes	19
2.6. Sedimentary Sequence.....	21
2.7. The Petroleum System.....	27
3. SEISMIC DATASET AND INTERPRETATION PROCEDURES.....	33
3.1. Basics of the Seismic Reflection	33
3.1.1. Marine Acquisition	37
3.1.2. Signal Processing.....	38
3.2. The Kurdashi Seismic Dataset.....	39
3.3. Seismic Interpretation.....	41
3.3.1. Softwares	42
3.3.2. Seismic Interpretation Workflow	43
3.3.3. Seismic Attributes	45
3.3.4. Mud-diapir Signal.....	46
3.3.5. Reconstruction of Mud Diapirs	49
4. WELL DATA AND SEISMIC UNITS.....	53
4.1. The Araz Deniz Well.....	53
4.2. Borehole Stratigraphy.....	55
4.3. Seismic Units.....	59

4.3.1. Chrono-Stratigraphy	59
4.3.2. Seismic Units	61
4.3.3. Mass-Transport Complexes	65
5. 3D GEOMETRY	75
5.1. Vertical Seismic Sections	75
5.1.1. IL 540	76
5.1.2. IL 1140	78
5.1.3. IL 1640	80
5.1.4. IL 2000	82
5.1.5. Western Line.....	83
5.1.6. Central Line	85
5.1.7. Eastern Line.....	87
5.2. Horizontal Slices.....	88
5.2.1. Depth Slice at 4 km	89
5.2.2. Depth Slice at 2 km	90
5.3. Structural Maps.....	92
5.3.1. PS-bottom	94
5.3.2. Pereryva-Old.....	95
5.3.3. Sabunchi	96
5.3.4. Sk 6	96
5.3.5. PS-top	97
5.3.6. Akchagyl.....	98
5.3.7. Apsheron.....	98
5.3.8. Seafloor.....	99
5.4. The KAD Structure.....	99
5.4.1. 3D Fold and Faults Geometries	99
5.4.2. Mud-diapirs	104
6. DEFORMATION ESTIMATE.....	107
6.1. Detachment Folds	107
6.1.1. Pre- and Syn-growth Sequences	109
6.1.2. Shortening Estimate.....	110
6.1.3. Fold Elements in the KAD Anticline	113
6.2. Nonparametric Estimation	116
6.3. Shortening Results	120
6.3.1. IL 540	120
6.3.2. ILS 720, 1140, and 1640	129
7. DEFORMATION HISTORY AND FOLD EVOLUTION	137
7.1. Basin Sedimentary Evolution	137
7.1.1. Isopach Maps	137
7.1.2. Sedimentary Sequence: Rates and Burial	140
7.1.2. Subsidence and Basin Tilting	143
7.2. Folding Style.....	144
7.2.1. Fold Geometry	144
7.2.2. Folding Type and Mechanism	147
7.2.3. Mechanisms of Folding	147
7.3. Anticline Growth	148
7.3.1. Growth Sequences	148
7.3.3. Mass-instabilities Processes	151

7.4. Structural Evolution.....	154
7.4.1. Diapirism Episodes.....	154
7.4.2. Faulting Style.....	157
7.4.3. KAD Deformation History	159
7.5. Implications for the Petroleum System	164
8. CONCLUSIONS	167
CONCLUSIONES.....	171
9. REFERENCES.....	175

LIST OF FIGURES

Figure 2.1: Geographic map of the Caspian Sea minibasins: North, Middle and South Caspian basins, respectively abbreviated as NCB, CCB and SCB	5
Figure 2.2: Topographic-bathymetric map of the Caspian Sea	6
Figure 2.3: Base Pliocene structural map merged with the present-day topography in the Caspian Sea.....	7
Figure 2.4: Plate tectonic map combined with GPS measurements in the Arabia-Eurasia collision zone.....	8
Figure 2.5: Schematic tectonic map and GPS measurements in the SCB region.....	9
Figure 2.6: Map of earthquake activity in the CCB and SCB regions	10
Figure 2.7: Map of focal mechanisms in the CCB and SCB domains	11
Figure 2.8: Moho depth map below the CCB and SCB areas	12
Figure 2.9: a) Map of the Bouguer anomaly in the CCB and SCB sectors. b) Crustal section derived by gravimetric modelling.....	13
Figure 2.10: Contour map of the sedimentary infill of the SCB	14
Figure 2.11: Tectonic map of the SCB	15
Figure 2.12: NW-SE geological profile from the Kura basin to Turkmenistan	16
Figure 2.13: SW-NE crustal section from the Alborz Mountains to the Apsheron Ridge.....	17
Figure 2.14: Deep seismic transect from offshore Azerbaijan to the Apsheron Ridge.....	17
Figure 2.15: Cenozoic evolution of the paleogeography in the Caspian Sea region.....	18
Figure 2.16: a) Seismic image of a buried mud volcano in the Caspian. b) Satellite image of a mud volcano in onshore Azerbaijan	20
Figure 2.17: Paleogeographic reconstruction of the deltaic systems in the Caspian Sea from the Pliocene to the Quaternary	22
Figure 2.18: Summary column of the stratigraphy of the Caspian Sea.....	23
Figure 2.19: Stratigraphic table of the western SCB.....	24
Figure 2.20: Paleogeographic maps of the Caspian Sea (a) before and (b) after the deposit of the PS	25
Figure 2.21: Stratigraphic architecture of (a) the western and (b) the eastern SCB, respectively.....	26
Figure 2.22: Production and exploration map of oil and gas in the Caspian Sea in 2013	28
Figure 2.23: Comparative panel of petroleum system in the western and eastern SCB.....	29

Figure 2.24: Schematic chart of the petroleum system in the SCB since the Oligocene.....	29
Figure 2.25: Data of (a) oil production from 2000 to 2012 and (b) gas production from 2000 to 2011 in the Caspian Sea region	30
Figure 3.1: Explicative diagram of the Snell’s Law	33
Figure 3.2: Scheme of the construction of a seismic trace during reflection campaigns from rock physical properties	34
Figure 3.3: Diagram of marine seismic configuration towed by a vessel	35
Figure 3.4: a) Scheme that explains how to obtain the geometry of the CDP and CMP in a seismic reflection survey. b) Seismic traces from the CDP converted to the final CMP	36
Figure 3.5: Seismic image of the same polygonal faulted interval on a (a) 2D and (b) 3D profiles	36
Figure 3.6: Cartoons to compare interpretation of the same area conducted by (a) 2D vs. (b) a 3D seismic dataset	37
Figure 3.7: Basics scheme for marine seismic acquisition.....	37
Figure 3.8: Imaged results of the same seismic section processed with different stacking methods	39
Figure 3.9: Studied seismic survey that includes the AD-1X well.....	40
Figure 3.10: 3D Pre-SDM velocity section in the studied area.....	41
Figure 3.11: A comparison between conventional time-processed and Pre-SDM for a 3D vertical section.....	41
Figure 3.12: Scheme of signal feature tracking.....	44
Figure 3.13: Comparison between (a) seismic reflection data and (b) coherence display in a time slice	45
Figure 3.14: a) Time slice section that highlights fluvial channels. b) Discontinuity display of the slice shown in (a).	46
Figure 3.15: Seismic image of (a) a salt diapir and (b) a Christmas-tree mud structure	47
Figure 3.16: a) Seismic buried mud volcano in offshore Azerbaijan. b) Pipe observed in seismic in the Eastern Mediterranean formed due to evaporate dissolution.....	49
Figure 3.17: 2D example of delineation of a mud diapir picked in Kingdom Suite	50
Figure 3.18: Screenshots from Landmark during diapir interpretation through (a) seed techniques and (b) Geobody tools	50
Figure 3.19: Screenshots to illustrate (a) the dip-structure cube attribute and (b) the dip-magnitude attributes	51
Figure 4.1: Surveyed area in the Kurdashi Permit showing the seismic IL 1940 that is crosscut by the AD-1X well.....	53
Figure 4.2: Scheme of a deviated well that includes different well measures. Depth measurements along deviated wells are referred as measured depths (MD).....	54
Figure 4.3: Borehole seismic image and stratigraphy in the AD-1X well in IL 1940 accompanied by GR and ATR logs, lithology and shows of oil and gas for each formation	57
Figure 4.4: (a) Non-interpreted and (b) interpreted seismic IL 1940	61
Figure 4.5: Seismic interpreted profile where it is observed numerous clinofolds dominant in the NW of the studied area	65
Figure 4.6: Cartoon of the morphology of the western SCB seafloor.....	66
Figure 4.7: Seafloor structural map	67

Figure 4.8: Seismic profile IL 870 taken through the largest example of Type A MTC.....	68
Figure 4.9: RMS map to highlight the largest slide of Type A	69
Figure 4.10: a) Seismic profile section of the IL 956 where is observed a western MTC of Type B in the Apsheron Unit. b) Depth section at 1 km depth illustrates the MTC seen in (a) and another example of Type B distinguished in the Gelasian Unit	70
Figure 4.11: Dip map of the Present-day seafloor. Notice the abundance of “cookie bites” along the actual topography that correspond to numerous MTCs of Type C	71
Figure 4.12: Seismic section of depth slices of (a) 500 m and (b) 750 m that show the evolution of the studied MTC of Type C.....	72
Figure 5.1: Base map showing the main seismic lines interpreted in this thesis.....	76
Figure 5.2: (a) Non-interpreted and (b) interpreted seismic IL 540	77
Figure 5.3: (a) Non-interpreted and (b) interpreted seismic IL 1140	79
Figure 5.4: (a) Non-interpreted and (b) interpreted seismic IL 1640	81
Figure 5.5: (a) Non-interpreted and (b) interpreted seismic IL 2000	83
Figure 5.6: (a) Non-interpreted and (b) interpreted seismic of the Western Line.....	84
Figure 5.7: (a) Non-interpreted and (b) interpreted seismic of the Central Line.....	86
Figure 5.8: (a) Non-interpreted and (b) interpreted seismic of the Eastern Line	87
Figure 5.9: (a) Non-interpreted and (b) interpreted seismic of the depth slice of the KAD area at 4 km depth	89
Figure 5.10: (a) Non-interpreted and (b) interpreted seismic of the depth slice of the KAD area at 2 km depth	91
Figure 5.11: Contour maps for the (a) PS-bottom, (b) Pereryva Old, (c) Sabunchi, (d) Surakhany 6 (Sk 6), (e) PS-top, (f) Akchagyl, (g) Apsheron and (h) seafloor surfaces	92
Figure 5.12: 3D panel of the PS-bottom structural map intersected by vertical ILs	100
Figure 5.13: Seismic cube combined with 3D NKG structural map and 2D displays	101
Figure 5.14: Seismic cube combined with 3D Sabunchi structural map and 2D displays	102
Figure 5.15: Seismic cube combined with 3D PS-top structural map and 2D displays	103
Figure 5.16: 3D panel of the PS-top structural map intersected by vertical ILs	104
Figure 5.17: (a) Non-interpreted and (b) interpreted chair-cut seismic cube to show mud diapirism in the KAD anticline in the Southern Culmination.....	105
Figure 6.1: Seismic survey used for this study containing seismic lines used for statistical approaches	108
Figure 6.2: Three-dimensional kinematic models of (a) a detachment anticline and (b) a fault-bend fold.....	109
Figure 6.3: Kinematic models of detachment folds with a high ratio of sedimentation with respect to fold uplift	110
Figure 6.4: Two modelled examples of detachment folds where (a) fold limb rotation and (b) hinge migration occurs	110
Figure 6.5: Geometrical estimations of shortening in a simple detachment fold.....	111
Figure 6.6: Plot to show the approximated calculus of shortening and detachment depth in a detachment anticline.	112
Figure 6.7: Schematic view of the IL 540 to illustrate some fold parameters measured in this thesis.....	113

Figure 6.8: Diagram of fold elements for a single horizon used for nonparametric estimations of planimetric shortening (S_A), considering (a) a continuous folded surface, (b) a surface pierced by mud, and (c) a faulted horizon	115
Figure 6.9: Schematic illustrations of seismic lines and measured parameters in lines (a) 720, (b) 1140 and (c) 1640	117
Figure 6.10: Examples of the effect that different values of the bandwidth parameter have on the estimation of depth data for the (a) Pereryva-Old (b) and the seafloor surfaces taken from the anticline in selected IL 540	119
Figure 6.11: Areas calculus of the seafloor (sf), the top and bottom of the Productive Series (PS-t and PS-b, respectively) and the Pereryva-Old after nonparametric fitting procedures in the IL 540	120
Figure 6.12: Graph of the A_i - H_i relationship for each horizon and results of planimetric shortening (S_A) according to different fits for the studied sequences	123
Figure 6.13: Comparative diagrams for both planimetric (S_A) and curvilinear (S_C) shortening measured in the IL 540 against time (Ma).....	125
Figure 6.14: Graph that shows the dip of the Present-day regional level measured along the different surfaces in the IL 540, as a function of age (Ma)	125
Figure 6.15: Representation of the flanks dip in the IL 540 and its evolution in time	126
Figure 6.16: Comparative graph of S_C values against time measured in the lines 540, 720, 1140 and 1640	130
Figure 6.17: A_i - H_i relationship for each horizon in the ILs 540, 720, 1140 and 1640	131
Figure 6.18: Comparative diagram for the S_A magnitudes against time in the selected fold sections: ILs 540, 720, 1140 and 1640.....	132
Figure 6.19: Graph of dip variation of the regional level in the key lines.....	133
Figure 6.20: Evolution of flanks dips along the KAD fold in time across the selected profiles	134
Figure 7.1: Schematic picture that explains the TST methodology to measure units thickness	138
Figure 7.2: TST maps of the packages (a) PS-bottom to Surakhany 12 (Sk 12), (b) Surakhany 9 (Sk 9) to PS-top and (c) Post-PS	139
Figure 7.3: Sedimentation rates measured in the Kurdashi Permit in the (a) Lower PS, (b) Surakhany, (c), Akchagyl, and (d) Apsheron units	141
Figure 7.4: Chair-cut seismic volume including the 3D display of the (a) Sabunchi top and (b) the PS-top.....	145
Figure 7.5: Interpreted seismic sections of Figures 5.2 to 5.5 from (a) to (d).....	146
Figure 7.6: Interpreted seismic sections flattened with respect to the PS-top surface from (a) to (c).....	149
Figure 7.7: Plot that compares shortening magnitudes above detachment (S_C and S_A) and also illustrates sedimentation rates of the studied sequences in the IL 540	150
Figure 7.8: Variance maps at (a) 1.65 km depth and (b) 1.0 km depth. MTCs of types A, B and C are highlighted.....	152
Figure 7.9: Wedge-tip geometries for a mobilized body of Type B delineated (a) in a seismic rendered volume, (b) in a 2D section and (c) in a schematic cartoon ...	154
Figure 7.10: Map of the western SCB to illustrate anticline culminations and Quaternary mud volcanoes	155
Figure 7.11: Seismic sections (a) vertically and (b) horizontally disposed in the KAD survey that describe mud diapirs facies	156

Figure 7.12: Seismic cube in the Southern Culmination that includes horizon interpretation, fault structures and MTCs occurrence 158

Figure 7.13: 3D schematic panels to show the evolution of the KAD anticline from the deposition of the Maykop Unit to Present 161

Figure 7.14: Evolution of the petroleum system in the KAD anticline 165

LIST OF TABLES

Table 2.1: Oil and gas proved and probable reserves in 2012 in the Caspian Sea region.....	31
Table 3.1: Summary table of the most common geological influences on acoustic impedance.....	35
Table 3.2: Diagram of the workflow followed in this thesis from the data loading, interpretation and visualization	42
Table 3.3: Chart to explain the characteristics of the seismic signal of mud diapirs	48
Table 4.1: Summary chart of the most common types of logs, accompanied by the main measured property and objectives	54
Table 4.2: Summary table of the wireline logging operations realized along the AD-1X well	55
Table 4.3: Depth estimations in meters of the geological formations tops penetrated by the AD-IX well, according to cuttings and data logs.....	56
Table 4.4: Ages of geological units	60
Table 6.1: List of magnitudes of fold elements	116
Table 6.2: Bandwidth parameter selection for the seafloor (sf) and the PS-bottom (PS-b) surfaces in the IL 540	119
Table 6.3: Magnitudes values for the IL 540 fold section.....	121
Table 6.4: Effect of the bandwidth parameter on the curvilinear shortening (S_C) of nonparametric (\widehat{m}_{np}) and parametric (\widehat{m}_{par}) estimators measured in the IL 540	122
Table 6.5: Comparison between S_C and handwriting results in the IL 540.....	122
Table 6.6: S_A (planimetric shortening) and S_C magnitudes of selected lines 540, 720, 1140 and 1640. The depth to the detachment surface (Z_{det}) is also included	129
Table 6.7: Summary table of sedimentation and shortening rates obtained for the studied sections: ILs 540, 720, 1140 and 1640.....	135

ABSTRACT

The South Caspian Sea is flooded by a presumable oceanic crust and it was generated during the Arabia-Eurasia collision in Mesozoic times. Plate convergence has triggered deformation and subsidence forming a hydrocarbon-rich province with active oil and gas production. From the Late Miocene to Present, the western margin of the basin has been strongly controlled by uplift and deformation of the Caucasus Mountains, which has promoted flexure of the crust, fast subsidence and an enormous rate of sedimentation towards the Kura deltaic system.

Depocenters in the basin reach up to 20 km depth, which represents one of the major sedimentary accumulations in the World. The Productive Series (PS; Late Miocene-Late Pliocene, 5.9 to ~3.4-3.1 Ma) were deposited as a 6 km-thick marine-to-deltaic sequence, overlaid by the here referred as the Post- Productive Series sequence (Post-PS; Late Pliocene to Present, <3.4-3.1).

Mud accumulations are widespread in the South Caspian Basin (SCB) shaping innumerable shale diapirs and mud volcanoes. Diapir geometry depicts well-delineated bodies usually connected with depleted feeder channels. The regional source rock for mud structures is the Maykop Formation (Late Eocene to Early Miocene, ~36-16.5 Ma). This shale-rich unit is also the major source rock for hydrocarbons in the area. Hydrocarbons are majorly stored in the PS reservoirs and are trapped by a Late Pliocene regional unconformity that represents a stratigraphic seal in the top of the PS (~3.4-3.1 Ma).

This thesis has studied the Kirgan-Araz Deniz anticline (abbreviated as KAD) within the Kurdashi structure, which involves the folded PS and the Post-PS packages. Our work is based on the interpretation of over 700 km² of seismic data from a post-stack 3D seismic dataset migrated in depth, which has been correlated with drill and logging information from the Araz Deniz IX exploration well. This valuable information has been provided by REPSOL. The fold is a NW-SE anticline located in the western margin of the SCB, in offshore Azerbaijan, to the South of the Kura River mouth. Our research is focused on the reconstruction of the three-dimensional geometry of the structure, and the shape of the overpressured-mud bodies that pierce the anticline. Deformation and sedimentation rates are also estimated to reconstruct the accurate growth history of this anticline.

Fold profile evolves along strike from symmetrical, gentle anticlines with a box-like shape that can host double-vergent reverse faults, to a marked asymmetrical structure pierced by mud. The axial trace shows a sigmoidal structure with two culmination domains and predominant eastward vergence. Noticeable differences are registered in fold flanks that are consistent with a detachment fold; the eastern limb leads the deformation as the forelimb, whereas the western flank is dragged as the backlimb. The decoupling layer is presumably single and low-dipping, rooted within the Maykop Formation, estimated at >9 km depth out of seismic image. Dissymmetrical flanks depth and thickness are also explained by a progressive eastwards tilting of the anticline to the inner SCB. Folding-type in the KAD structure differs from classical detachment types since progressive tilting, simultaneous sedimentation, and differential subsidence between fold flanks is registered.

The overall geometry of the PS reflects low-dipping sequences (<10° towards the SE) that correspond to different delta systems prograding basinwards. In detail, the study of the uppermost PS shows a subtle thinning due to simultaneous deposit and folding of the Surakhany Unit (Early Pliocene-Late Pliocene, 3.7 to ~3.4-3.1 Ma). According to accentuated syn-sedimentary wedges in the Post-PS package, a new folding stage took place with major relevance in the Akchagyl Unit (Late Pliocene-Early Pleistocene, ~3.4-3.1 to ~1.7-1.6 Ma), and extends to the Present-day seafloor surface. Marked shapes of the latter evidences folding intensity surpassed sedimentation rates in the last 3.1 my, whereas the incipient KAD fold was buried by high sediment loading in the Surakhany period. Our results suggest a propagation of the deformation along fold strike, with noticeable variations in timing and with maximum shortening rates detected in both culminated domains.

Mud diapirism pierces the KAD fold along both culminations. Teardrop forms are constrained within the PS and partially the Post-PS rocks, and terminate downwards with sub-vertical welds at depth. We assume the second folding event is the main responsible for mud intrusion after the PS (PS-top), and stopped in the Apsheron times (Early Pleistocene to Late Pleistocene, ~1.7-1.6 Ma to ~0.8-0.7 Ma). Mud ejecta and logs state that overpressured shales are squeezed from the Maykop Unit.

Numerous faults document fracturing history, with a variable regime and position. Fold crest is crosscut by curved and normal structures with a N-S trend, whereas reverse and mostly planar faults control the fold core parallel to the fold axis (NW-SE). Core faulting reflects a complex history of deformation with strike- and dip-slip motions through time as reactivated faults. Fractures in both flanks are characterized by two systems of large and planar structures with perpendicular orientations and opposite regimes; two pairs of NW-SE-directed and reverse structures accompany the kink-like fold, and NE-SW structures act conjugately and develop grabens. Structural levels are separated by a neutral surface positioned in the Sabunchi (Early Pliocene, 4.0 Ma to 3.7 Ma) to Surakhany units (Early Pliocene-Late Pliocene, 3.7 Ma to 3.1 Ma), due to buckling mechanisms. Deformation pattern, sigmoidal axial trace and asymmetric limbs may be a result of the strong variations in the displacement of underlying structures and eventually changes in the kinematics of the associated faults.

Active tectonics and delta progradation in the Post-PS period were accompanied by numerous slope instability processes. Mobilized sediments embedded within the Akchagyl Unit correspond to large slides, which changed to small slided deposits in

the Apsheron times. The Gelasian Formation (<0.8-0.7 Ma) registers numerous debris flows, especially along the eastern domain of the KAD fold. We state mass-transport deposits in the last 3.1 my are majorly controlled by folding but also reinforced by the migration of the Kura shelf-edge margin. A detailed understanding of mass-wasting processes and products, and their stratigraphical occurrence, are vital because they can play a significant role in hydrocarbon exploration, in as much as they can constitute unconventional types of traps and potential geohazards.

The analysed KAD fold is a non-economically profitable anticline due to low hydrocarbons storage. We propose several factors acted conjointly to trigger low oil and gas generation and later escape out of the structure since the Surakhany folding (<3.7 Ma).

RESUMEN

La Cuenca Sur del Mar Caspio (SCB) es una depresión de corteza oceánica originada durante la colisión de los Alpes e Himalaya en el Mesozoico. Dicha convergencia ha generado una gran deformación y subsidencia, formando una provincia rica en hidrocarburos con producción activa de gas y petróleo. Desde el Mioceno Superior, la parte más occidental se ha visto afectada por el plegamiento de las Montañas del Cáucaso, que ha provocado una intensa flexura de la corteza, rápida subsidencia, así como una gran tasa de sedimentación en el sistema del Río Kura.

Los depocentros de la cuenca contienen hasta 20 km de espesor de rocas, una de las mayores acumulaciones sedimentarias del mundo. Las Series Productivas (PS; Mioceno Superior-Plioceno Superior, 5.9 a ~3.4-3.1 Ma) representan unos ~6 km de una secuencia fluvio-deltaica, y yacen bajo las aquí citadas unidades Post-Series Productivas (Post-PS; Plioceno Superior a Presente, <3.4-3.1 Ma).

En el SCB existen acumulaciones de barro distribuidas por toda la cuenca las cuales dibujan geometrías variables, tales como diapiros y volcanes de lodo. Los cuerpos diapíricos se definen usualmente conectados con antiguos canales de alimentación en profundidad ya agotados. La roca madre de los diapiros y volcanes de barro se encuentra en la Formación Maykop (Eoceno Superior-Mioceno Inferior, ~36 Ma a 16.5 Ma). Esta unidad es también la roca madre de hidrocarburos del área. Petróleo y gas se encuentran principalmente en los reservorios de las PS, atrapados bajo una disconformidad regional del Plioceno Superior que representa un sello estratigráfico a techo de la secuencia (~3.4-3.1 Ma).

Esta tesis estudia el anticlinal Kirgan-Araz Deniz (abreviado como KAD), en la estructura Kurdashi, representado por las unidades PS y Post-PS. Nuestro trabajo se ha basado en el análisis de unos 700 km² de datos sísmicos que proceden de un cubo “post-stack” en 3D, migrado en profundidad, conjuntamente con datos de sondeo del pozo Araz Deniz IX. Esta valiosa información ha sido suministrada por REPSOL. El pliegue tiene dirección NO-SE, y está localizado en el margen occidental del SCB en aguas de Azerbaiyán, al Sur de la desembocadura del Río Kura. La investigación se centra en la reconstrucción de la geometría tridimensional del pliegue, y de los diapiros de lodo que lo nuclean. Las tasas de deformación y de sedimentación también han sido estimadas para reconstruir la historia de crecimiento de la estructura de forma precisa.

El perfil del pliegue varía a lo largo de la dirección del mismo, desde estructuras suaves con geometría en caja y que albergan fallas inversas con doble vergencia, a

pliegues asimétricos comúnmente nucleados por diapiros de barro. La traza axial muestra una estructura sigmoidal compuesta por dos culminaciones y una vergencia predominantemente hacia el Este. Diferencias notables se registran en los flancos consistentes con un plegamiento de tipo “detachment”; el flanco oriental es el flanco líder o “forelimb”, mientras que el occidental es arrastrado como “backlimb”. La superficie de despegue es presumiblemente simple y de bajo buzamiento, enraizada en la Unidad Maykop, a una profundidad estimada que supera los 9 km y que queda fuera de los límites del volumen sísmico. Las características de disimetría y diferencia de espesores entre ambos flancos también se pueden explicar por un progresivo basculamiento del anticlinal en dirección al interior de la cuenca. La estructura KAD difiere de los pliegues de despegue clásicos debido al progresivo basculamiento, simultánea sedimentación, y subsidencia diferencial registrada entre flancos.

La geometría de las unidades PS muestra secuencias de bajo buzamiento (<10° hacia el SE) que corresponden con diferentes sistemas deltaicos que progradan hacia la cuenca. En detalle, el estudio de las capas estratigráficas más altas de las PS, la Unidad Surakhany (Plioceno Inferior-Plioceno Superior, 3.7 Ma a ~3.4-3.1 Ma), muestra un adelgazamiento débil debido al depósito y plegamiento simultáneos. La acentuada geometría en cuña del paquete Post-PS evidencia una nueva etapa de plegamiento, que tuvo lugar con mayor relevancia en la Unidad Akchagyl (Plioceno Superior-Pleistoceno Inferior, ~3.4-3.1 a ~1.7-1.6 Ma), y que se extiende hasta el fondo marino actual. Esta forma marcada de los sedimentos más recientes evidencian que la intensidad del plegamiento superó las tasas de sedimentación en los últimos 3.1 ma, mientras que el plegamiento incipiente del KAD quedó enmascarado por el enterramiento de una gran carga sedimentaria en el período Surakhany. Nuestros resultados sugieren la propagación de la deformación a lo largo de la dirección del pliegue, con variaciones notables en el tiempo, y con mayores tasas de acortamiento detectadas en los dominios de culminación del pliegue.

El diapirismo de lodo perfora ambas culminaciones del pliegue. Las formas “teardrop” están constreñidas en las secuencias PS y parcialmente en las Post-PS, y terminan en forma de “welds” subverticales en profundidad. El segundo evento de plegamiento es el principal responsable de la intrusión de barro después del techo de las PS (PS-top), y se detiene durante el depósito de la Unidad Apsheron (Pleistoceno Inferior- Pleistoceno Superior, ~1.7-1.6 Ma a ~0.8-0.7 Ma). Muestras de lodo tomadas en superficie y a través de testigos confirman que las arcillas sobrepresurizadas proceden de la Unidad Maykop.

Numerosas fallas documentan la historia de fracturación, con un régimen y posición variables a lo largo del pliegue. La cresta del pliegue está intensamente afectada por fallas normales con geometría curva y dirección N-S, mientras que las estructuras inversas son principalmente planas y se disponen en el núcleo del pliegue de forma paralela al eje (NO-SE). La deformación de régimen inverso en profundidad refleja una historia de deformación compleja en el tiempo, con componentes de salto en dirección así como de salto en buzamiento reactivadas. Los flancos de la estructura KAD están fracturados por dos sistemas de fallas largas y planas que muestran orientaciones perpendiculares y regímenes opuestos; dos pares de fallas inversas siguen una dirección NO-SE y acompaña la estructura tipo “kink”, y un sistema de fallas normales NE-SO actúan conjuntamente y desarrollan grabens. Los niveles estructurales están separados por una superficie neutra posicionada entre las unidades Sabunchi (Plioceno Inferior, 4.0 Ma a 3.7 Ma) y Surakhany (Plioceno

Inferior-Plioceno Superior, 3.7 Ma a 3.1 Ma), debido a mecanismos de tipo “buckling”. El patrón de la deformación, la traza sigmoidal del pliegue y los flancos asimétricos pueden ser resultado de fuertes cambios en el desplazamiento de estructuras en profundidad que eventualmente pueden variar su cinemática.

La tectónica activa y la progradación deltaica en el período Post-PS estuvo acompañado por numerosos procesos de inestabilidad de talud que desarrollaron variados complejos deposicionales en masa (MTCs). Los sedimentos movilizados constreñidos en la Unidad Akchagyl se originaron debido a grandes deslizamientos, que adquirieron menor tamaño durante la época Apsheron. La Formación Gelasian (<0.8-0.7 Ma) registra numerosos flujos de derrubios, especialmente observados en los dominios orientales del KAD. En esta tesis se asume la ocurrencia de estos MTCs en los últimos 3.1 my controlados por el plegamiento y el avance de la plataforma marina hacia el Este. Una interpretación detallada de estos procesos y sus depósitos, así como la localización estratigráfica, es vital puesto que pueden jugar un papel primordial en la exploración petrolera, pues pueden suponer trampas no convencionales de hidrocarburos y riesgo potencial durante los procesos exploratorios.

El pliegue analizado no es económicamente rentable pues posee una baja acumulación de hidrocarburos. En este trabajo se propone la combinación de varios factores para explicar tal escasez, producidos por la actuación conjunta bajos niveles petróleo y gas y su posterior escape debido al plegamiento estructural desde el Surakhany (<3.7 Ma).

1. INTRODUCTION

Most of shale-cored anticlines are located in compressive settings, as folds-and-thrusts belts, and also in distal areas of passive margins, where a ductile and overpressured shale-rich unit occurs at shallow crustal levels (*e.g.*, Rowan *et al.*, 2004; Morley *et al.*, 2011). In this setting, shortening promotes mud diapirism and the development of a bedding-parallel fault within the shale layer, called as décollement or detachment surface. Displacement is transferred into folding in the decoupled overlying sediments according to a buckling mechanism (Dahlstrom, 1969; Hudleston, 1973) above the tip line of a flat fault, where a sharp decrease in faulting rate occurs (*e.g.*, Poblet and McClay, 1996; Shaw *et al.*, 2005).

In many regions, detachment folds are associated with hydrocarbon traps and develop varied geometries depending on the deformation kinematics. Different kinematic models have been proposed to explain this fold type; *e.g.*, hinge migration (Suppe, 1983), limb rotation (De Sitter, 1956), and a combination of both (Dahlstrom, 1990). These models reproduce similar final fold geometries through different evolution and amplification histories. Detachment folds shape is asymmetric and independent of the fault shape, in contrast to other fault-related folds, like fault-bend folds (Rich, 1934) and fault-propagation folds (Dahlstrom, 1970). Simple geometrical models of detachment folds assume that no thickness variations or shear within layers occur in the competent multilayer unit (*e.g.*, Mitra and Namson, 1989; Poblet, 2004). Complexity increases if it is considered in three dimensions (*e.g.*, Jamison, 1987; Mitra and Namson, 1989; Epard and Groshong, 1993a; Poblet and McClay, 1996). Study techniques used to unravel folding kinematics are based on the geometry of the pre- and syn-folding strata, *i.e.*, the sediments deposited before and during shortening, respectively. The exploration of the various geometries developed in the syn-growth sequence can provide crucial information to reconstruct deformation kinematics and timing (Medwedeff, 1989; Poblet and McClay, 1996; Poblet *et al.*, 2004). Different geometrical methods are also available to calculate shortening rates and to estimate the depth of the detachment level using the pre-growth unit of this fold type (*e.g.*, Chamberlin, 1910; Epard and Groshong, 1993b; Mitra, 2003).

This thesis studies a shale-cored anticline in the western margin of the South Caspian Basin (SCB). This is a super-deep shallow marine basin containing around 20 km of Jurassic-to-Present sediments (Abrams and Narimanov, 1997; Mangino and Priestley, 1998; Brunet *et al.*, 2003; Smith-Rouch, 2006; Forte *et al.*, 2015). The thickness of the Late Miocene-Quaternary section in particular, is higher than 10 km and was deposited in a very rapidly subsiding basin that contains a thick section of undercompacted mud-rich sediments (*e.g.*, Berberian, 1983; Devlin *et al.*, 1999; Brunet *et al.*, 2003; Hudson *et al.*, 2008). High subsidence rates in the SCB are explained by the presumable oceanic nature of

a thick crust that was generated in the Late Mesozoic (*e.g.*, Allen *et al.*, 2003). Since that time, the SCB was affected by a complex tectonic history with several episodes of rifting and compression (*e.g.*, Zonenshain and Le Pichon, 1986; Guest *et al.*, 2007). The Caucasus compression occurred during the Pliocene-to-Present and conditioned the deformation style in the basin. In the western margin of the SCB, this deformation generated NW-to-NNW detachment folds cored by mud, which appear as linear physiographic features on the Caspian seafloor (*e.g.*, Brunet *et al.*, 2003; Davies and Stewart, 2005).

Fold structures in the SCB are interpreted to be buckle folds overlying a regional, mud-rich (ductile) detachment zone. Mud diapirs commonly pierced these folds promoting the occurrence of active mud-volcanoes throughout the basin and in the onshore region (*e.g.*, Allen *et al.*, 2003; Brunet *et al.*, 2003; Stewart and Davies, 2006). Fold of this type has also collected the interest of the oil and gas industry, because the folded sequences commonly store hydrocarbons (*e.g.*, Bagirov *et al.*, 1997; Devlin *et al.*, 1999; Brunet *et al.*, 2003). In fact, the SCB is part of the Great Caspian hydrocarbon province, which is a major producing region with a total proven oil and gas reserves ranging from 15 to 31 million bbl and 230 to 360 Tcf, respectively (Belopolsky and Talwani, 1999; EIA, 2013).

The main purpose of this thesis is to carry out the seismic interpretation of the Kirgan-Araz Deniz (KAD) anticline. This fold was generated during the Pliocene-to-Recent times and deforms both, the reservoir unit of the Productive Series (PS; Late Miocene to Late Pliocene) and the youngest sediments up to the seafloor surface (here referred as the Post-PS units; Late Pliocene to Present). We evaluate the complex internal structure of a NNW-SSE anticline, which is settled in the western margin of the SCB, to the South of the Kura River mouth, in offshore Azerbaijan. Our analysis is conducted in the Kurdashi Permit through the 3D interpretation of a seismic cube migrated in depth. The stratigraphic information provided by a well situated in the studied area (the AD-IX well), has been used to tie the seismic interpretation. The cube comprises $\sim 653 \text{ km}^2$ and has been provided by REPSOL for this Ph.D. thesis.

This study examines the geometry of the KAD fold and piercing diapirs to reconstruct the deformation history. We have estimated fold growth by means of robust statistical methods from the analysis of the attitude of the sedimentary layers and fault structures. A detailed discussion on the role played by mud diapirism during the anticline growth is also presented. We have also reconstructed in the western SCB the stratigraphic architecture since Late Pliocene through the analysis of numerous mass-wasting deposits. Results will shed light on the interplay between sedimentary processes together with fold uplift, and the role of structural control on the position of the seafloor break. Recent folded structures of this type have been widely documented in the basin, although a detailed reconstruction of their 3D geometry and evolution, and an estimate of the associated rates of deformation and sedimentation, are far to be well established (*e.g.*, Devlin *et al.*, 1999; Brunet *et al.*, 2003). In addition, we believe that the studied case deviates from the classical detachment fold-type. The main differences consist on the lateral and vertical mobilization of overpressured mud shaping complex diapir-like structures, and the progressive tilting of the basin floor during deformation and sedimentation.

Objectives of this thesis

The objectives of this thesis are:

- (1) To reconstruct the three-dimensional geometry of the KAD anticline, identifying the pre- and syn-growth sequences and detailing their internal configuration,
- (2) To characterize the folding history and the deformation episodes of this structure, studying the relationships between deformation and sedimentation,
- (3) To analyse the different fault structures and establish how they relate to folding processes,
- (4) To estimate the shortening magnitude associated to the KAD anticline, calculating for example the depth to the detachment level and the rate of deformation (shortening), sedimentation, and basin tilting, and how these variables change spatially,
- (5) To reconstruct the mud-mobilization structures in 3D, examining the relationships with the fold and with the associated deformations, and inferring the possible triggering mechanisms for mud diapirism,
- (6) To identify the occurrence of syn-sedimentary instability processes during fold growth, characterizing the different types of mobilized, unconsolidated sediments during the last 3.1 my,
- (7) To discuss the role played by overpressured mud during deformation, subsidence, and rapid sedimentation in this margin of the South Caspian Basin, and finally
- (8) To evaluate the incidence of these processes in the petroleum system of the basin, to approach the structural control on the hydrocarbons migration pathways in the KAD fold, a structure with petroleum interest in South Caspian Basin.

Part of the results of this Ph.D. thesis has been recently published in *Marine and Petroleum Geology* in a paper entitled “3D geometry of a shale-cored anticline in the western South Caspian Basin” (2015, doi: 10.1016/j.marpetgeo.2015.06.012). Additionally, the method used in this thesis to evaluate the deformation history of the KAD fold is under review in *Mathematical Geosciences* (ms. MATG-D-15-00050R1). This investigation has been also presented during the last years in different international conferences (*e.g.*, American Association of Petroleum Geologists, European Association of Geoscientists and Engineers, and International Association for Mathematical Geosciences).

2. THE SOUTH CASPIAN BASIN

2.1. Situation

The Caspian Sea is a large enclosed sea located to the east of the Black Sea in western Asia that covers over 371,000 km² (Fig. 2.1). The Caspian Sea is classically divided into three different minibasins: the North Caspian Basin (NCB), Central Caspian Basin (CCB) and South Caspian Basin (SCB). Others authors also include the lowland Precaspian region in the northernmost area (e.g., Zonenshain and Le Pichon, 1986; Knapp *et al.*, 2004; Brunet, 2007). Caspian Sea level is 26.5 m below the global sea level and bathymetry reaches maximum depths of about 1000 m in SCB. Much of the basin currently has a water depth around 500 m, whereas the media in the overall sea is 170 m.



Figure 2.1: Geographic area of the western Asia region, from the Black Sea in the West and the Caspian Sea in the East, showing the different Caspian Sea minibasins. Source: EIA (2013).

The SCB is a deep intra-continental depression politically controlled by Azerbaijan, Iran and Turkmenistan, from West to East, respectively. Numerous active mountain ranges surround the SCB: the Caucasus and the Talesh in the West, the Alborz in the South and the Koppeh Dagh in the East (*Fig. 2.2*). The Apsheron Ridge comprises a series of folds that leads the topographic connexion with the CCB.

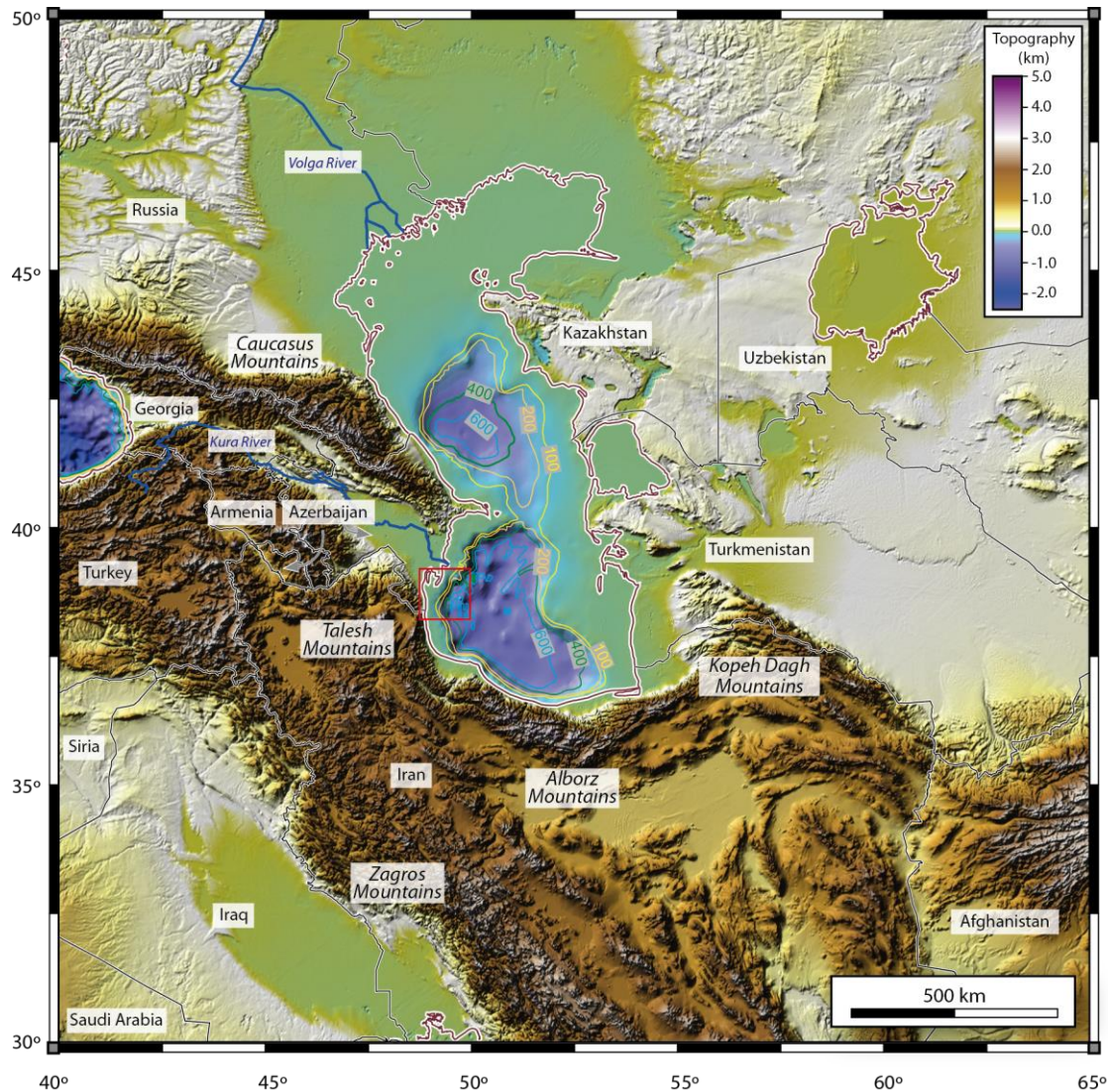


Figure 2.2: Topographic-bathymetric map of the Caspian Sea area using the global elevation database etopo1-usgs and bathymetry is taken from GEBCO 2008. Topography is measured in meters and contour lines range from 100 to 600 m below the sea level. The study area is enclosed within a red square.

Numerous rivers discharge in the Caspian Sea: the Volga, Ural, Terek and Kura rivers. The Kura River enters with the primary inflows in the SCB through Azerbaijan and empties at the Neftchala river mouth, over 115 km South of Baku system (*Fig. 2.2*). The Volga River discharges in the NCB but large submarine channels reach the SCB. Historical records state that the Amu Darya River also flowed into the eastern SCB as a major contributing fluvial system (*Fig. 2.3*).

The study area is located in offshore Azerbaijan (*Fig. 2.2*). The Kurdashi Permit is sited over 140 km South of Baku and 25 km South of the Kura River mouth. Water depth ranges between 30 and 770 m.

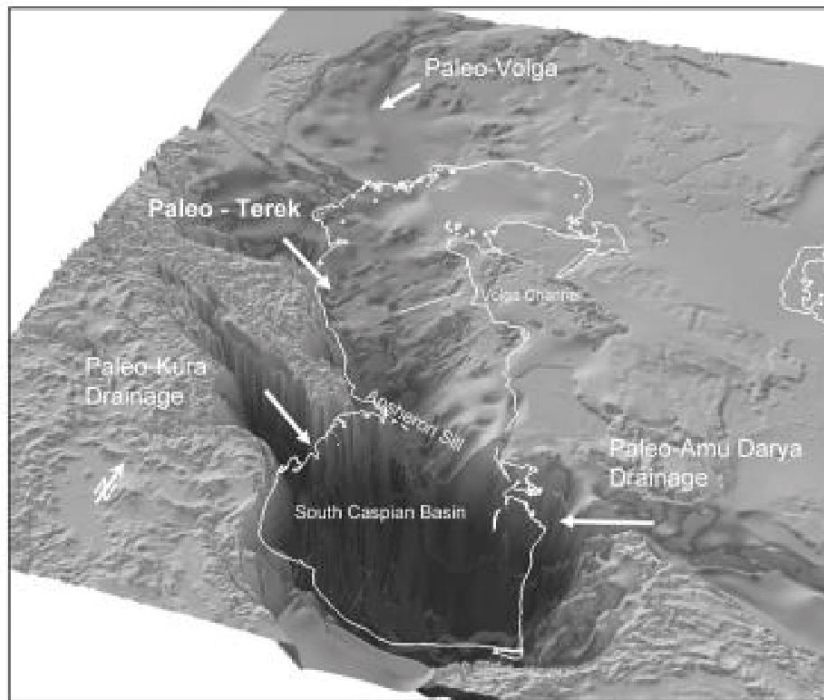


Figure 2.3: 3D-perspective view of the base Pliocene structural map merged with the present-day topography and Tertiary drainage taken from Baganz *et al.* (2012).

2.2. Present-day Tectonics

The Caspian Sea is currently dominated by the collision between the Arabia and Eurasia plates. Within the Eurasian Plate, the NCB and the CCB host the stable Russian platform, whereas the Alpine-Himalayan orogenic belt controls currently the tectonics of the SCB.

The Arabia-Eurasia collision started in the Early Miocene (23-16 Ma), promoting the counterclockwise rotation of a vast area, including the Anatolian, Arabian and the Iranian plates. The Arabian Plate moves rapidly northward (N8°E) at rates in the range of 20-30 $\text{mm}\cdot\text{yr}^{-1}$ relative to the slow-moving Eurasia ($\sim 5 \text{ mm}\cdot\text{yr}^{-1}$) (Fig. 2.4) (*e.g.*, DeMets *et al.*, 1990; Reilinger *et al.*, 2006).

The large area of interaction is differently affected by the convergence and kinematics evidence variations in slip rates, total strain and deformation timing from western Turkey to eastern Iran (*e.g.*, Allen *et al.*, 2004). Numerous microcontinents and rigid blocks have been accreted around the South of the Caspian Sea (as it is illustrated in Figure 2.5), whereas the Central and North Caspian basins remain unfractured within the Eurasia Plate. Small microplates are: South Caspian Block, Lut Plate, Central Iran Block and NW Iran Block, Caucasus Plate and Alborz Block (Vernant *et al.*, 2004; Engdahl *et al.*, 2006). These rigid microplates remain relatively immobile whereas intracontinental deformation concentrates in several surrounding mountain belts. Contrasting convergence rates are also observed between the East and West of the SCB, which are accommodated along numerous right- and left-lateral fault systems, partitioned onto separate thrust and strike-slip thrust components and not purely by strike slip.

GPS measurements indicate a significant northward motion of the SCB relative to Eurasia ($\sim 8\text{-}10 \text{ mm}\cdot\text{yr}^{-1}$), in congruence with the convergence of the Iran Plate over the SCB ($\sim 13\text{-}17 \text{ mm}\cdot\text{yr}^{-1}$) (Jackson *et al.*, 2002; Hollingsworth *et al.*, 2008). The motion of

the SCB is a response of higher rates in the plates convergence registered in the West, absorbed by the separated fold belts of the Caucasus, Talesh and Alborz systems.

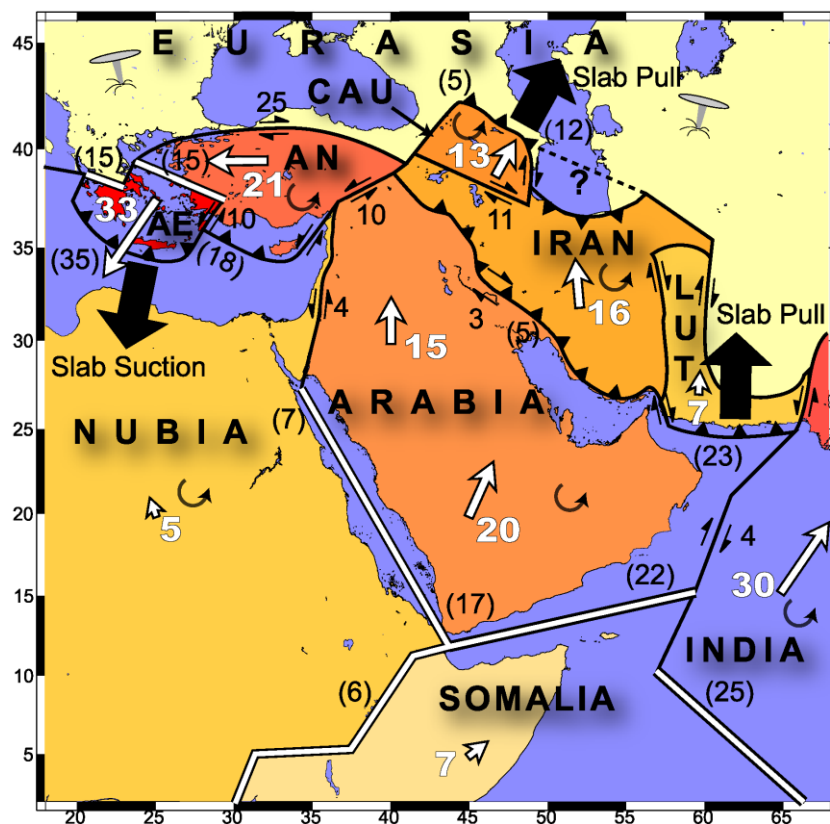


Figure 2.4: Plate tectonic map of the Arabia-Eurasia collision zone combined with GPS measured velocities for plate movements. Double lines are extensional plate boundaries. White arrows and corresponding numbers show plate velocities in $\text{mm}\cdot\text{yr}^{-1}$ relative to Eurasia. Dark numbers are GPS-derived strike slip rates ($\text{mm}\cdot\text{yr}^{-1}$) on block-bounding faults (numbers in parentheses are dip-slip rates). Dark, heavy arrows show hypothesized forces associated with active subduction acting on the plate/block system. Abbreviations: Aegean Plate (AE), Anatolia Plate, (AN), and Caucasus Plate (CAU). Taken from Reilinger *et al.* (2006).

According to Lyberis and Manby (1999), the Arabia-Eurasia convergence is relatively small in the eastern SCB, at the Kopeh Dagh range ($\sim 15 \text{ mm}\cdot\text{yr}^{-1}$), and is accommodated through several dextral, strike-slip faults (Vernant *et al.*, 2004). Slip vectors of shortening coincide with the overall N-S compression in the Alborz Mountains where $8 \pm 2 \text{ mm}\cdot\text{yr}^{-1}$ are accommodated by means of several strike-slip faults. Simultaneously in the same longitude, the southwards Zagros fold range registers a plate-convergence rate of $6.5 \pm 2 \text{ mm}\cdot\text{yr}^{-1}$. NE-directed convergence in the eastern Caucasus Mountains follows the counterclockwise rotation of the Arabia-Eurasia collision. The Anatolian Plate escapes westwards due to the NW-SE partitioning of the deformation between eastern Turkey and NW Iran, with rates between 8 and $17 \text{ mm}\cdot\text{yr}^{-1}$ (Jackson *et al.*, 2002; Talebian and Jackson, 2002; Reilinger *et al.*, 2006). The differential northward motion of the Arabia and the Iran plates is resolved in the northern Zagros as south-directed thrusting with a reduced right-lateral strike-slip faulting, which has a local rate of about $3 \pm 2 \text{ mm}\cdot\text{yr}^{-1}$ (Reilinger *et al.*, 2006).

The present collision zone is well defined by its highly active seismic margins whereas regions like the SCB stand out as an aseismic domain (Fig. 2.6). Jackson and MacKenzie

(1984) stated that large areas of central Anatolia, central Iran, Lut and the SCB behave as rigid blocks with feeble seismicity. The relatively aseismic microplates face against the surrounding belts in which the intense earthquake activity is distributed over 200-300 km width.

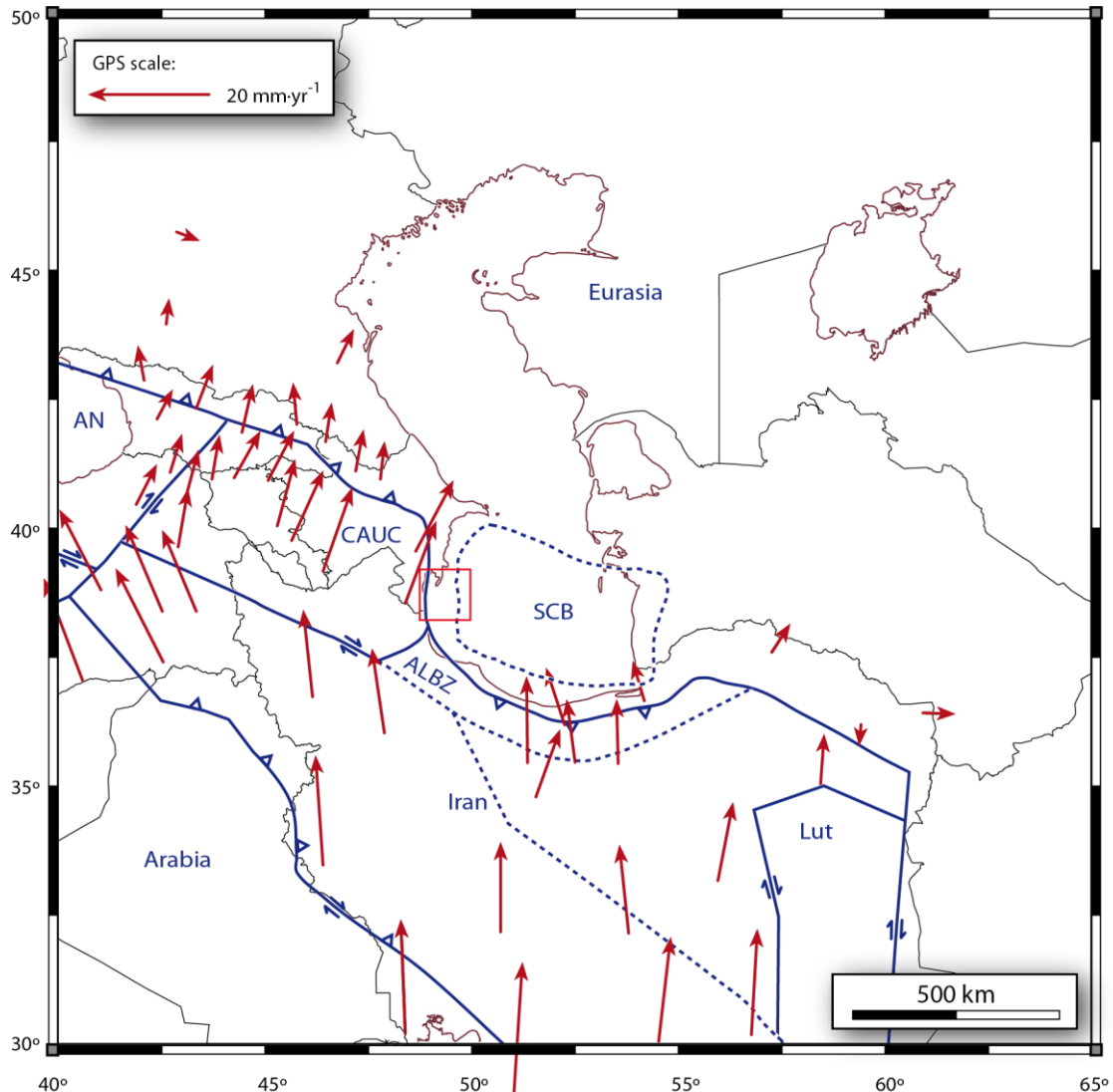


Figure 2.5: Schematic map of the Caspian area that includes tectonic blocks and detailed GPS-derived estimations for plate velocities (Reilinger *et al.*, 2006). Blue-broken line marks the presumable oceanic crust of the SCB, described by Berberian (1983). The study area is delimited by a red square. Abbreviations: Alborz block (ALBZ), Anatolian Plate (AN), Caucasus Plate (CAUC), and SCB block (SCB).

The Caspian Sea is characterized by moderate intraplate seismicity totally different from the neighbouring Caucasus, Talesh, Alborz and Kopeh Dagh folds belts. Seismic activity is also important in the Apsheron Ridge, the threshold that links the Greater Caucasus and the Kopeh Dagh and separates the CCB and the SCB. Along the coastline of the SCB magnitudes of earthquakes exceed 7. According to Guliev and Panahi (2004) aseismogenic areas coincide with zones of thick and young plastic sediments as in those with mud volcanism.

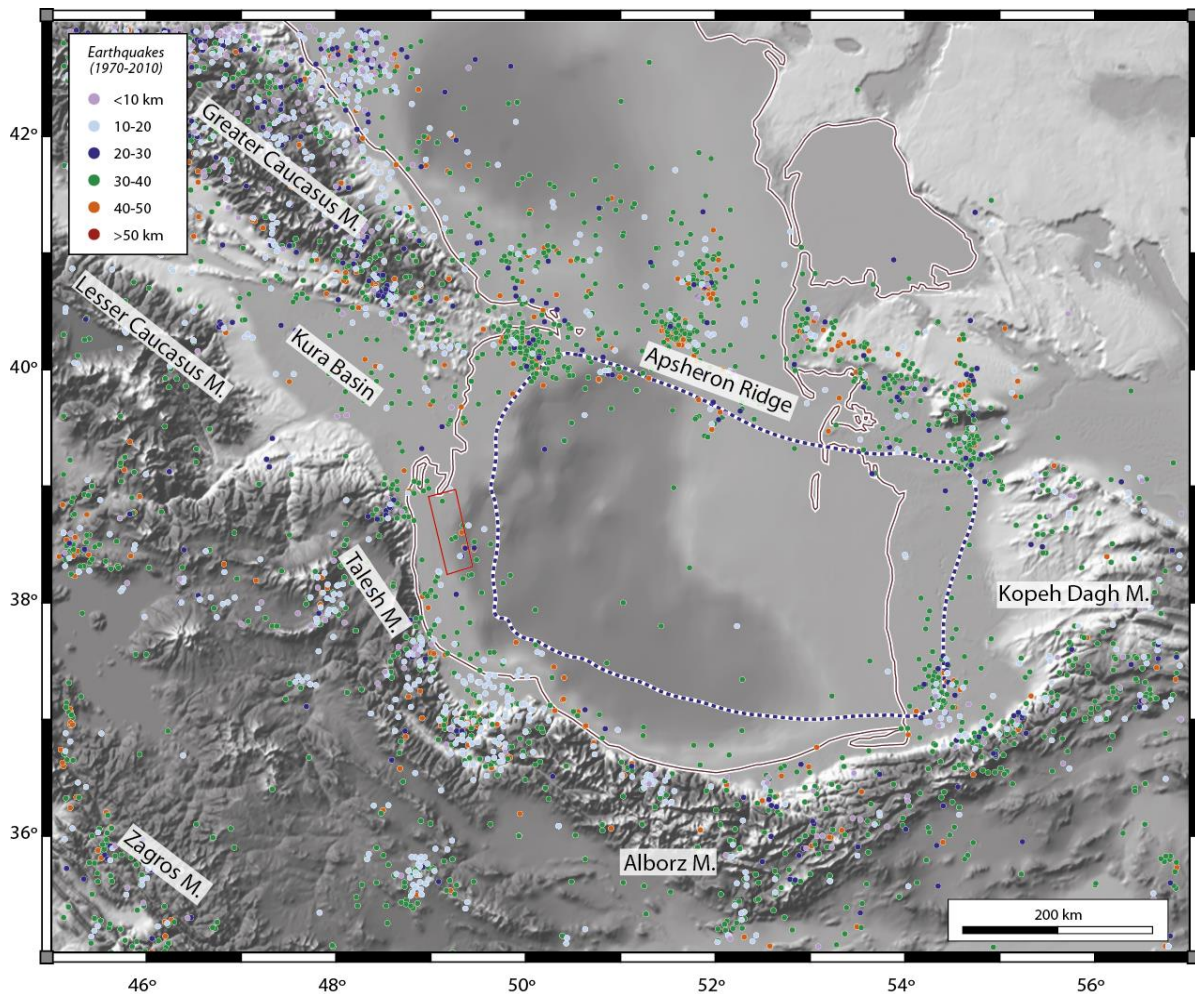


Figure 2.6: Map of earthquake activity in the CCB and SCB regions. Seismicity data are taken from the IRIS catalogue for the period 1970 to 2010. The SCB limits are highlighted in a blue-broken line taken from Berberian (1983). The red-coloured rectangle includes the study area. Topography information is taken from etopo1-usgs database. Mountains are abbreviated as M.

Hypocentres in the SCB are predominantly located in shallow depth intervals (<20 km). Earthquakes have centroids lower than 15 km in the Kopeh Dagh and the Alborz Mountains, and occasionally reaches 26 km depth in the Talesh range system (Fig. 2.6) (e.g., Jackson *et al.*, 2002). Seismological studies of Kovachev *et al.* (2006) in the southeastern Caucasus revealed earthquakes in mantle levels with hypocentres up to 150 km depth. Beneath the Apsheron Ridge intense seismic events also occur deeper than 30 km (even >80 km) distributed in a band of 100 km wide which is the offshore continuation of the Greater Caucasus and the Kopeh Dagh (e.g., Guliev and Panahi, 2004; Artyushkov, 2007; Khain *et al.*, 2007).

Multiple seismically-active faults are recognized within the SCB boundaries (Fig. 2.7) (e.g., Berberian, 1983; Priestley *et al.*, 1994; Jackson *et al.*, 2002). Most of the focal mechanisms in the Kopeh Dagh show either right-lateral strike-slip or reverse faulting on faults parallel to its NW, regional strike. In the Alborz Mountains, nodal planes are parallel to the regional strike of the belt, with pure thrust motion combined with strike-slip faults with a left-lateral component, that result in the northward thrusting of the Iranian continent over the SCB (e.g., Priestley *et al.*, 1994; Knapp *et al.*, 2004). The earthquake mechanisms in the Talesh system reveal N-S, low-angle thrusting with slip vectors directed towards the SCB that presumably represent thrusting over the SCB basement. The Caucasus Mountains

involve two conjugated planes of low-angle thrusts gently dipping towards the mountains on both sides. In the eastern Greater Caucasus shortening occurs NE-SW-directed. There are also some mantle earthquakes beneath the Caucasus, which may be interpreted as thrusting of the Turan Plate under the SE Caucasus (Kovachev *et al.*, 2006).

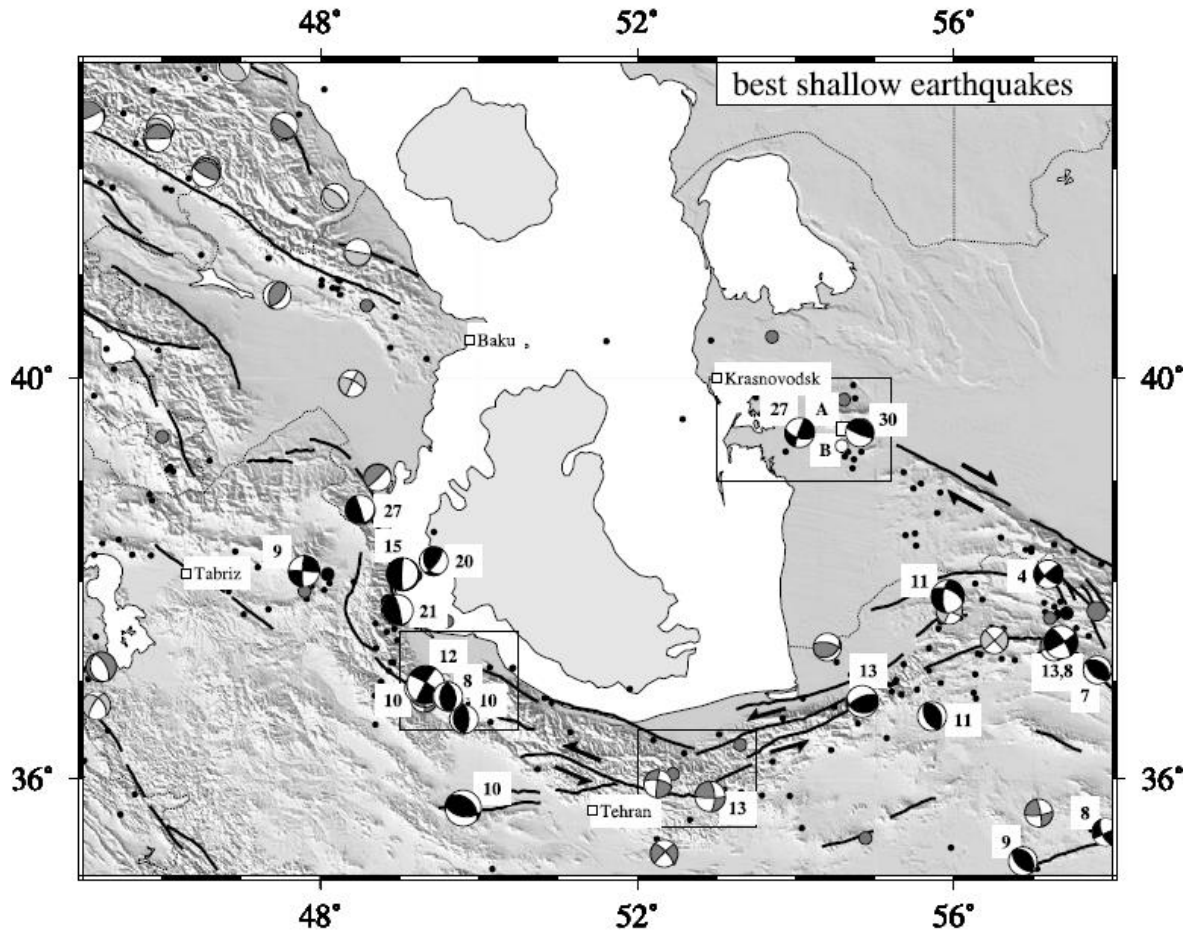


Figure 2.7: A compilation of the best-quality focal mechanisms for shallow earthquakes (<30 km of depth) around the SCB (Jackson *et al.*, 2002). The illustrated better solutions contain those based on waveform analysis (black focal spheres), additional Centroid Moment Tensor (CMT) solutions with >70% double-coupled component and $M_w > 5.3$ (grey spheres), and additional first-motion solutions detected on long-period instruments of the after catalogue in 1963 (light grey spheres). Small black-filled circles are hypocentres of 1964-1998 described by Engdahl *et al.* (1998), large grey and black-filled circles are epicentres of earthquakes of $>M_s 6.0$ ($>M_s 7.0$ for larger size) from 1900 to 1962 and post-1963, respectively. The white square A and the white circle B are the epicentres of the 1895 Krasnovodsk and the 1983 Kum Dag earthquakes, respectively. Bathymetry contours correspond to 500 m of depth.

Deep earthquakes along the Apsheron Ridge indicate normal and thrust faulting, both parallel to the ridge. Jackson *et al.* (2002) and Khain *et al.* (2007) suggested that the Apsheron Ridge is an incipient subduction zone where the SCB Block moves under the CCB in the Eurasian Plate.

In summary, active deformations in the SCB region reflect a relatively quiescent block, which is being progressively consumed by two contrasting subductions; towards the N and beneath Eurasia, in the Apsheron Ridge, and towards the S beneath Iran, in the Alborz. Thus, it is expected the disappearance of the SCB (*e.g.*, Priestley *et al.*, 1994).

2.3. Deep Structure

In contrast to the overall Caspian Sea, geophysical studies in the SCB reveal that the nature and origin of the basin basement is completely different from the expected in the Caspian Sea. The SCB is floored by a high P-wave velocity layer ($v_p = 6.8-7.0 \text{ km}\cdot\text{s}^{-1}$) (e.g., Zonenshain and Le Pichon, 1986; Mangino and Priestley, 1998) characterized by high density values ($\sim 2.9 \text{ g}\cdot\text{cm}^{-3}$) (Granath *et al.*, 2000; Knapp *et al.*, 2004). These characteristics depart from the granitic layer ($v_p = 5.8-6.5 \text{ km}\cdot\text{s}^{-1}$; $\rho = \sim 2.7 \text{ g}\cdot\text{cm}^{-3}$; Mangino and Priestley, 1998; Granath *et al.*, 2000) seen in the surrounding region and support the general assumption of an “oceanic-like” crust. This composition helps also to explain the relative stability of the SCB block and its resistance to tectonic deformation (e.g., Neprochnov, 1968; Berberian, 1983; Priestley *et al.*, 1994).

The Moho below the SCB is usually observed between 35 km and 40 km of depth (Fig. 2.8). Data compilation of Grad *et al.* (2009) shows that low depth values are concentrated in a large region that mostly covers the SCB, and departs from the gravity data in the CCB. Maximum Moho depths are registered within the Caucasus fold-and-thrust belt and in the Zagros Mountains.

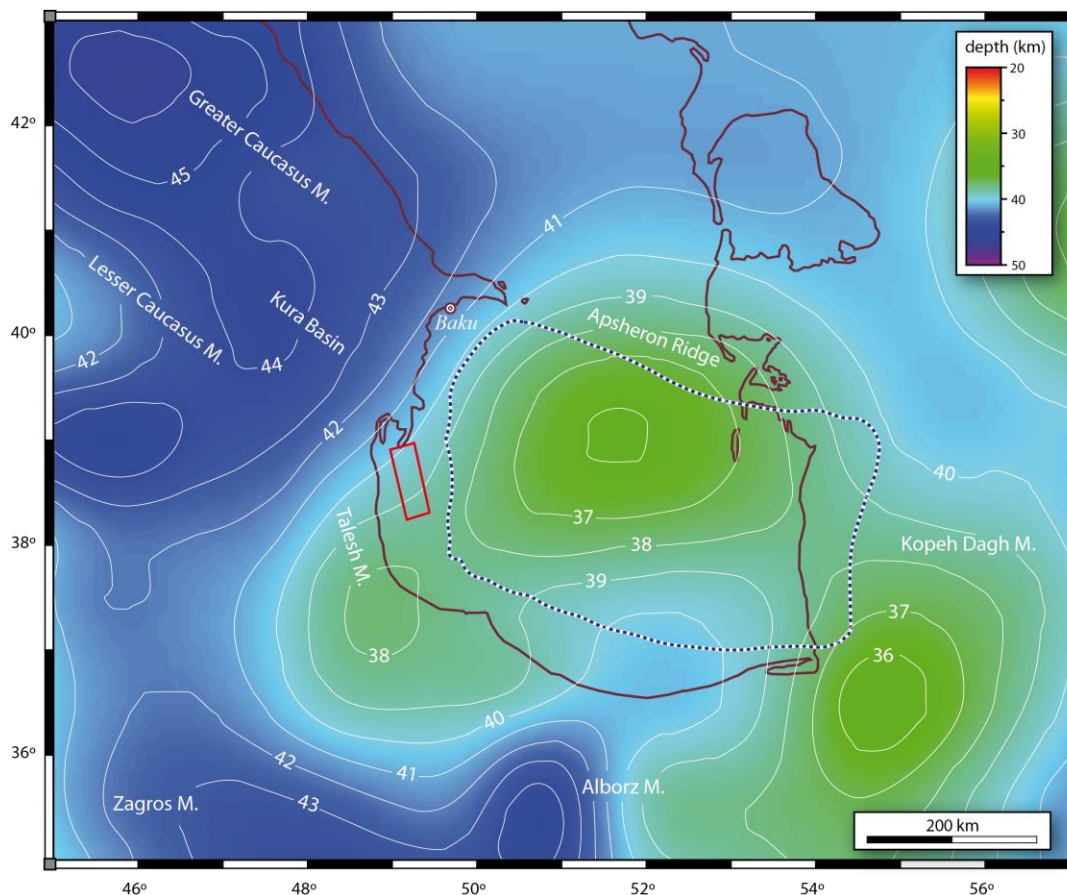


Figure 2.8: Moho depth (in km) below the CCB and SCB regions. This model has been obtained from a gravity and refraction data (Grad *et al.*, 2009). The oceanic crust of the SCB is delimited by a blue-dotted line (Berberian, 1983). A red rectangle defines the position of the study area. Mountains are abbreviated as M.

Gravity data and deep seismic profiles in the region suggest that the crystalline basement is overlaid by a thick sedimentary overburden, with a mean $v_p = 3.5-4.0 \text{ km}\cdot\text{s}^{-1}$

(Jackson *et al.*, 2002; Knapp *et al.*, 2004). Low P-wave velocities disappear at ~ 20 km depth although the prominent reflector of the basement-cover contact is still recognized at 26-28 km depth along the Apsheron Ridge (*e.g.*, Zonenshain and Le Pichon, 1986; Knapp *et al.*, 2004; Artyushkov, 2007). The Bouguer anomaly observed in the SCB reinforces the occurrence and geometry of such huge sedimentary depocentres (*Fig. 2.9*).

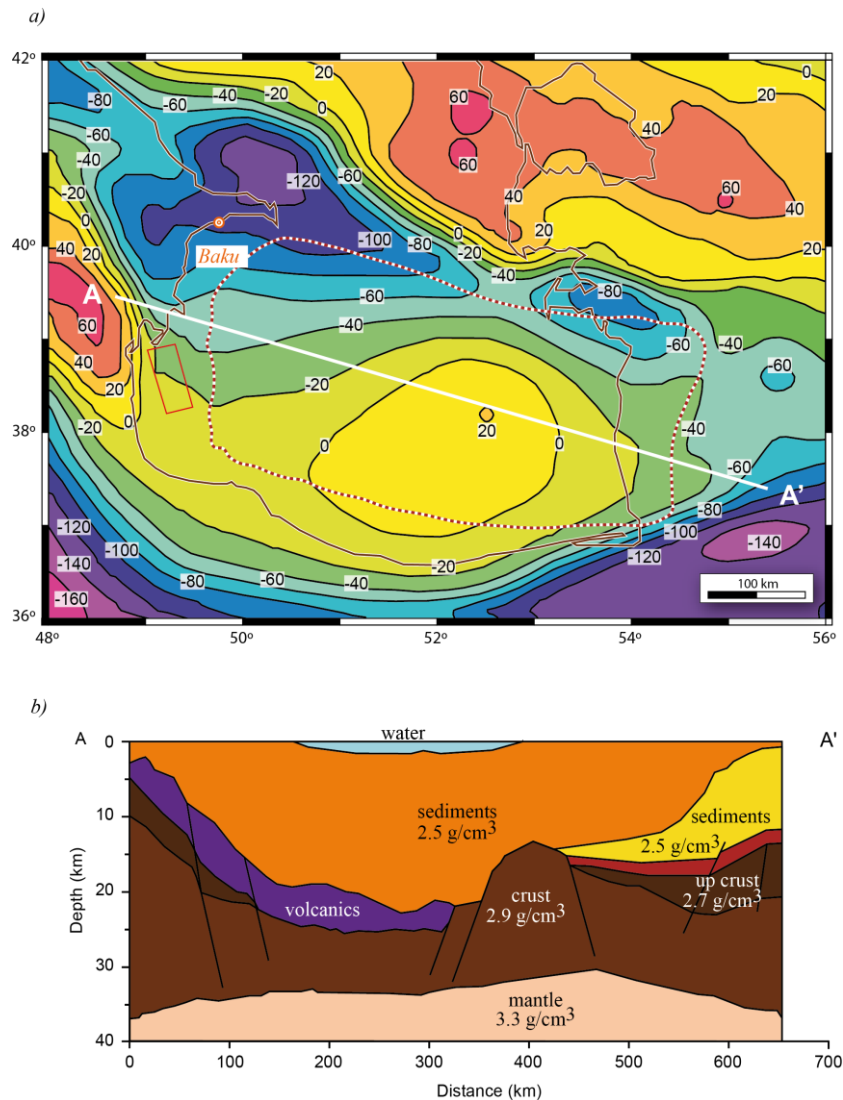


Figure 2.9: a) Map of the Bouguer anomaly (in mGal) that shows the sedimentary depocentres in the region. A linear negative anomaly is clearly marked in the Apsheron Ridge. The SCB crust is bounded by the red-coloured broken line (taken from Berberian, 1983). The study area is delimited by a red rectangle. *b)* A-A' crustal section derived by gravimetric modelling (see location in the above map). Jurassic volcanic rocks coloured in purple; Paleozoic and Cenozoic sediments are red-coloured and yellow-coloured, respectively; Pliocene sediments are coloured in orange. Density of Paleozoic is $2.5 \text{ g}\cdot\text{cm}^{-3}$. Taken from Brunet *et al.* (2003).

The previously described characteristics of the SCB are also accompanied by low heat-flow values, which are presumably indicators of a remnant piece of the Tethys ocean (*e.g.*, Berberian, 1983; Zonenshain and Le Pichon, 1986; Nadirov *et al.*, 1997). Many authors state the SCB was originated in the Early Jurassic as a relic of a marginal back-arc basin in the North of the subducting Tethys (*e.g.*, Mangino and Priestley, 1998; Brunet *et al.*, 2003).

2.4. Structure and Tectonic Evolution

The SCB is presently one of the major sedimentary basins in the World. Sediments are mainly distributed among three depocentres, as it is illustrated in the compiled map shown in *Figure 2.10* (Abrams and Narimanov, 1997; Mangino and Priestley, 1998; Smith-Rouch, 2006). The main depocentre has up to 26-28 km of sediments and runs parallel to the Apsheron Ridge. This is consistent to a northward basement bending due to subduction (e.g., Allen *et al.*, 2002; Knapp *et al.*, 2004). A second major depocentre is located NE of the Alborz Mountains, the so-called the Pre-Alborz trough with ~20 km of sediments (Brunet *et al.*, 2003). The area between both domains is occupied by a horst, the Turkmenian structural step, at 15 km depth (Brunet *et al.*, 2003). A third great depocentre occurs in the SW, nearby the Talesh system, with up to 19 km depth.

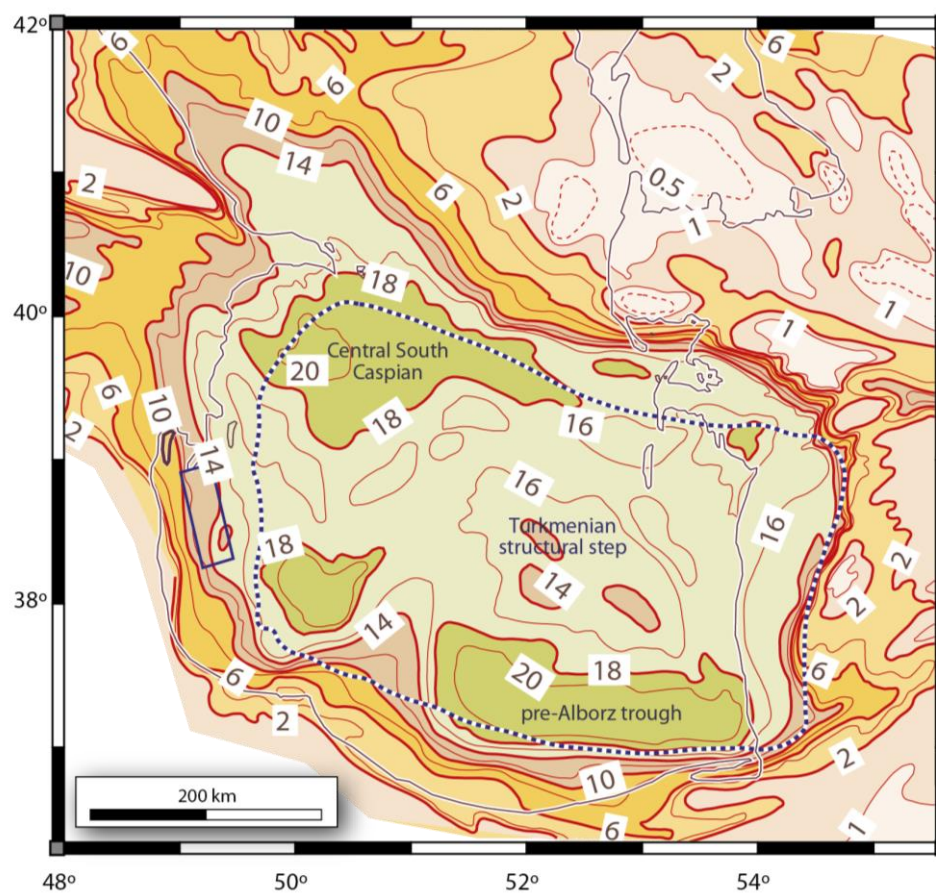


Figure 2.10: Contour map (in km) of the sedimentary infill of the SCB. In the study area (denoted by a blue rectangle) the thickness of sediment is over 12 to 14 km. The blue-broken line corresponds to the limits of the oceanic SCB crust (Berberian, 1983). Blue-rectangle boundaries coincide with the position of the studied area. Sedimentary isopach data have been compiled from Malovitsky (1970); Shikalibeily and Grigoriant (1980); Berberian (1983); Glumov (2004); Artyushkov (2007).

Major structural features in the South Caspian region are illustrated in *Figure 2.11*. A continental pericratonic basement floors the NCB that lies over the Late Proterozoic Russian shelf (Berberian, 1983; Brunet *et al.*, 2003). The floor in the CCB corresponds to the continental Hercynian Scythian platform in the West and the Turanian platform in the East. The SCB is a Tertiary depression floored by a presumable Late Jurassic oceanic crust, which comprises the South Caspian block (Zonenshain and Le Pichon, 1986;

Mangino and Priestley, 1998; Brunet *et al.*, 2003).

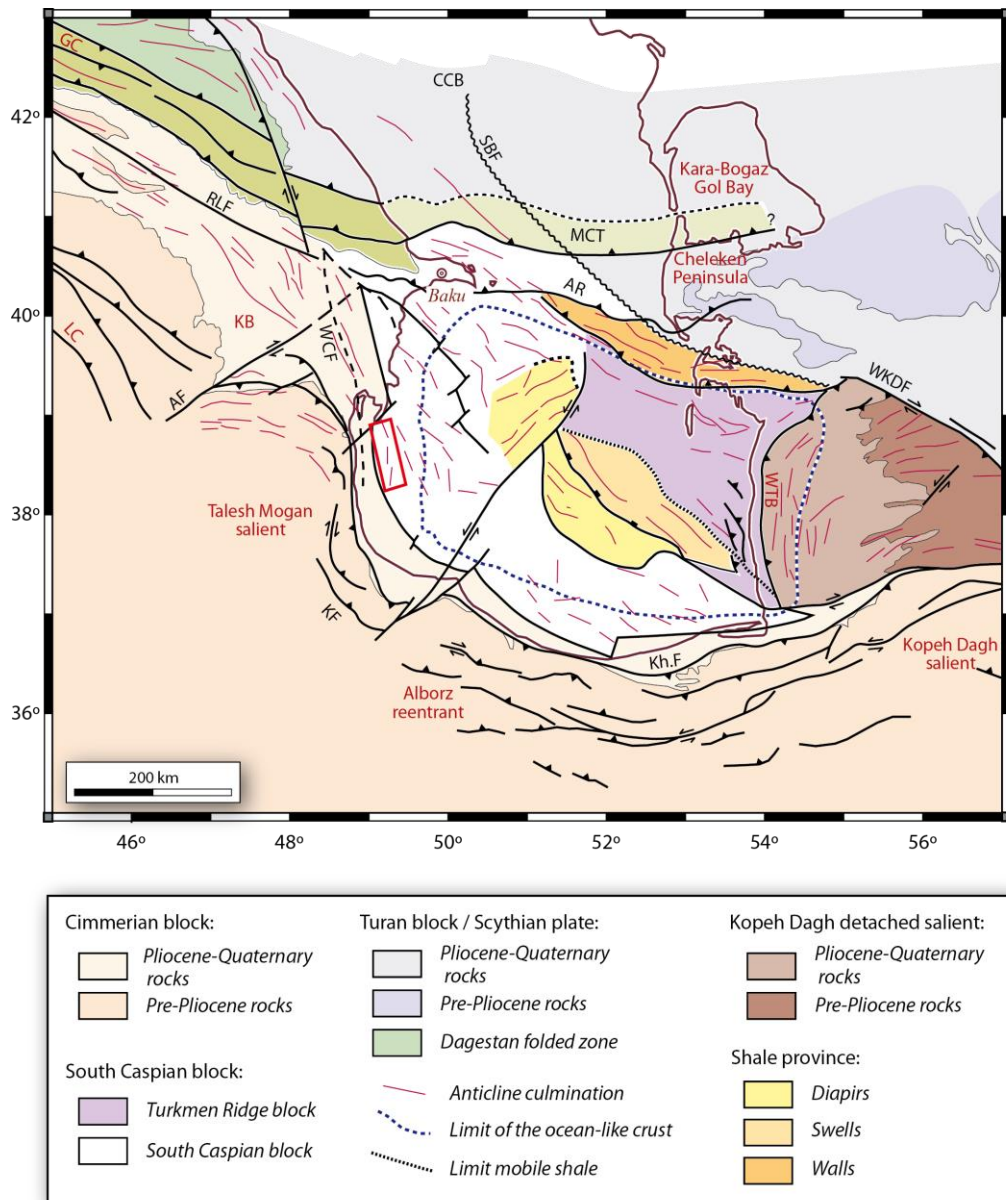


Figure 2.11: Tectonic map of the SCB. The study area is delimited by a red square situated in the non-oceanic-type South Caspian block. Notice the progressive change of the trend of Pliocene anticline folds from NW-SE in the Kura basin, South of the Caucasus mountain range, to nearby N-S in offshore Azerbaijan. Sources of the map are: Berberian (1983); Priestley *et al.* (1994); Inan *et al.* (1997); Nadirov *et al.* (1997); Tagiyev *et al.* (1997); Devlin *et al.* (1999); Jackson *et al.* (2002); Allen *et al.* (2004); Smith-Rouch (2006); Khain *et al.* (2007); Hollingsworth *et al.* (2010). Abbreviations: Araks Fault (AF), Apsheron Ridge (AR), Central Caspian Basin (CCB), Greater Caucasus Mountains (GC), Kabateh Fault (KF), Khazaar Fault (Kh.F), Kura Basin (KB), Lesser Caucasus Mountains (LC), Main Caucasian Thrust (MCT), Racha-Lechkhumi Fault (RLF), South Balkhan Fault (SBF), West Caspian Fault (WCF), West Kopeh Dagh Fault (WKDF), and West Turkmenistan Basin (WTB).

Tectonic map in *Figure 2.11* shows that the thick sedimentary sequence of the SCB is largely deformed. The SCB has been divided into fold and fault zones bordering the basin, separated from intraplate shale-diapir domains (Lebedev, 1987; Devlin *et al.*, 1999). Thrust belts and strike-slip structures are oriented NW-SE in the western and southern domains of

the SCB, N-S to NE-SW in the eastern part and WNW-ESE parallel to the Apsheron Ridge. In Azerbaijan, anticlines correspond to Pliocene, NW-trending structures, with subtle strike changes in the Talesh Mountains (NNW-SSE) following the coastline (Devlin *et al.*, 1999; Brunet *et al.*, 2003).

Tectonic movement along the Apsheron Ridge has created shale diapirs (Fig. 2.11) and mud volcanoes in the central and western parts of the SCB by forcing overpressured shales into weakness zones such as faults (Devlin *et al.*, 1999; Abdullayev, 2000). Mud pierces as single-diapir stocks or forming shale-diapir ridges and walls (Philip *et al.*, 1989; Devlin *et al.*, 1999).

Deformed rocks have been decoupled from the basement through the occurrence of a deep shale-rich layer, typically the Maykop Formation, in conditions of overpressure that usually rises in mud diapirism and volcanism (Fig. 2.12) (Allen *et al.*, 2002; Jackson *et al.*, 2002). This mud layer acts as a regional décollement surface during deformation of the sedimentary overburden (Fig. 2.13).

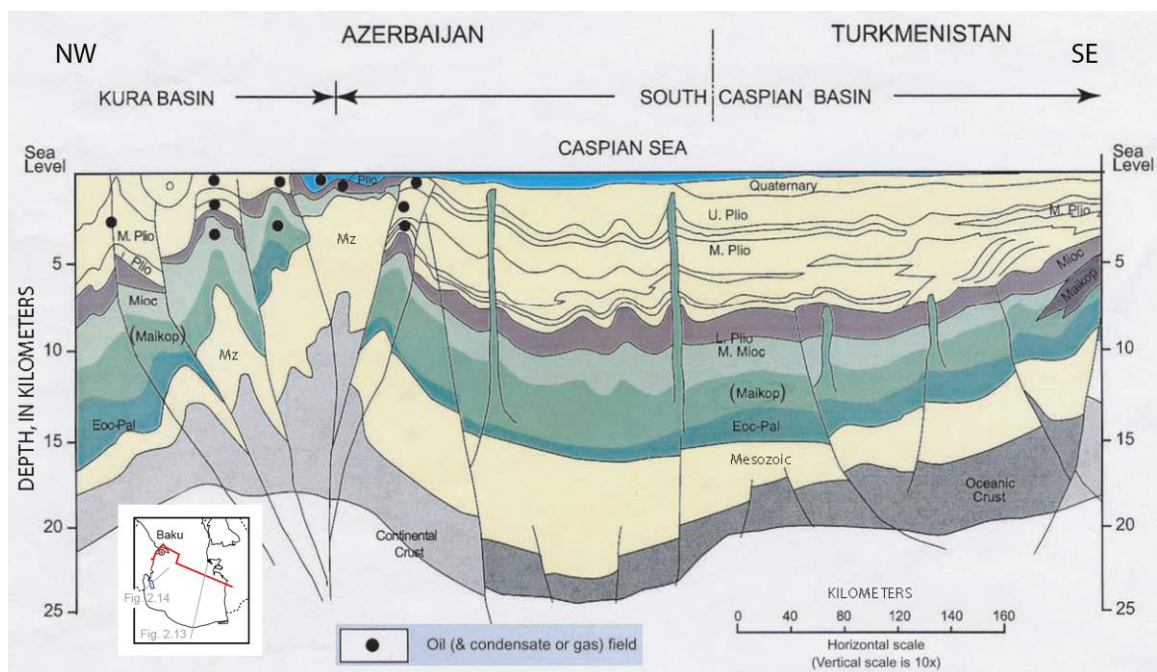


Figure 2.12: NW-SE geological profile across the northern SCB, from the Kura basin to the Cheleken Peninsula in Turkmenistan. Profile location is shown in red in the inset map. Taken from Smith-Rouch (2006) and modified from Abrams and Narimanov (1997).

The overall structure of the SCB, from the northern Iran and across the Apsheron Ridge is illustrated in Figure 2.13 (Guest *et al.*, 2007). The North-directed fold-and-thrust belt of the Alborz Mountains forms the southern margin of the SCB and consist of thick-skinned thrust sheets. The SCB itself is floored by a deep and thick oceanic crust, overlaid by a constant layer of Mesozoic sediments (~10 km thick). These authors suggest that towards the North, the Mesozoic cover, together with the oceanic floor have a gentle bend, covered by a thinner Cenozoic sedimentary sequence. This domain coincides with the area with shale diapirs and walls in the Turkmen Block (Fig. 2.11). The section shows finally the South-directed thrusting of the Apsheron Ridge with an incipient subduction of the SCB towards the North.

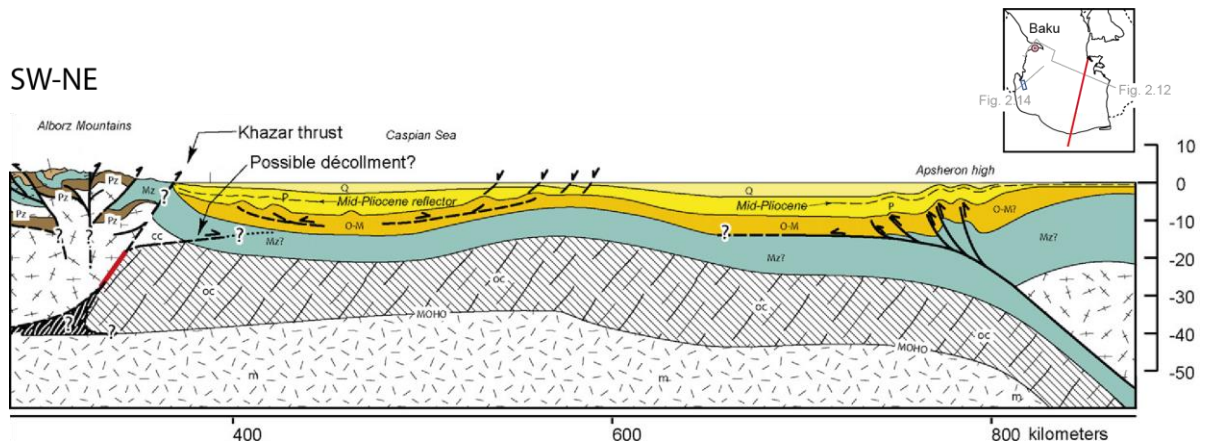


Figure 2.13: SW-NE crustal section of the SCB, from the Alborz Mountains to the Apsheron Ridge (Guest *et al.*, 2007), highlighted in red in the inset map.

Fold structural styles range from anticlines to monoclines. Folds depict symmetrical domal shapes and are locally penetrated by overpressured mud intrusions, such as diapirs and volcanoes (Fig. 2.12). The structural style of the western margin of the SCB is clearly illustrated by the deep-seismic section shown in Figure 2.14. The sedimentary section thickens progressively towards the deeper basin. Folds seem to be detached from the deep structure, shaped by the probably Mesozoic sequences. The style of folding in the Neogene cover shows a transition from deep, sub-vertical faults with a probably reverse regime, to crestal faults in the fold hinges.

Deep faults are widespread within the basin, as the major West Caspian Fault that has been postulated to occur in the East of the Kura Basin and parallel to the coast line (Fig. 2.11) (Khain *et al.*, 1966; Nadirov, 1985). These faults usually correspond to the pre-Late Cenozoic crustal structure (Jackson *et al.*, 2002). Alsop and Holdsworth (2002) suggested that folding may also reflect strong variations in the displacement of deep-seated faults.

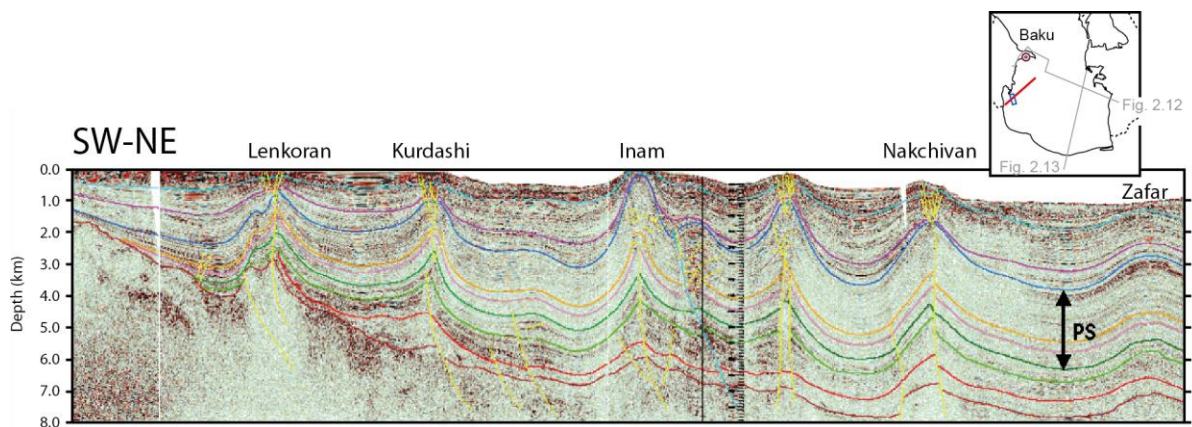


Figure 2.14: Deep crustal seismic from shallow regions in offshore Azerbaijan to the Apsheron Ridge (see inset map for location). Profile shows the overall deformation pattern of the sedimentary cover in the western margin of the SCB. Transect taken from Bertello *et al.* (2001); ENI (2002).

A complex geodynamic evolution characterizes the Caspian region, which involves different periods of rifting and compression during two main tectonic episodes (*e.g.*, Brunet, 2007). Origin and geodynamics of the NCB and CCB diverges from the evolution in the SCB. The NCB and CCB are continental-floored and relatively stable since the Cimmerian orogeny affected the Caspian Sea in the Late Triassic (*e.g.*, Berberian, 1983;

Brunet, 2007). The SCB is conversely active from the later stages of the Arabia-Eurasia convergence (Adamia *et al.*, 1977; Shikalibeily and Grigoriants, 1980; Zonenshain and Le Pichon, 1986; Mangino and Priestley, 1998; Brunet *et al.*, 2003).

The SCB has a presumable oceanic crust that was created along the southern margin of Eurasia during the Tethys subduction and closure in Mesozoic times (Zonenshain and Le Pichon, 1986; Mangino and Priestley, 1998; Brunet *et al.*, 2003). Extensional processes in the Mesozoic were replaced in the SCB by shortening during the Early Oligocene as a consequence of the collision between Arabia and Eurasia (Nadirov *et al.*, 1997; Allen *et al.*, 2003; Brunet *et al.*, 2003).

The approach of the Arabian Plate during the Late Messinian was accompanied by a dramatic fall in sea level of up to 600 m (~5.6-5.5 Ma). The Caspian Sea and the SCB were isolated from the Black Sea (Fig. 2.15) (Krijgsman *et al.*, 2010).

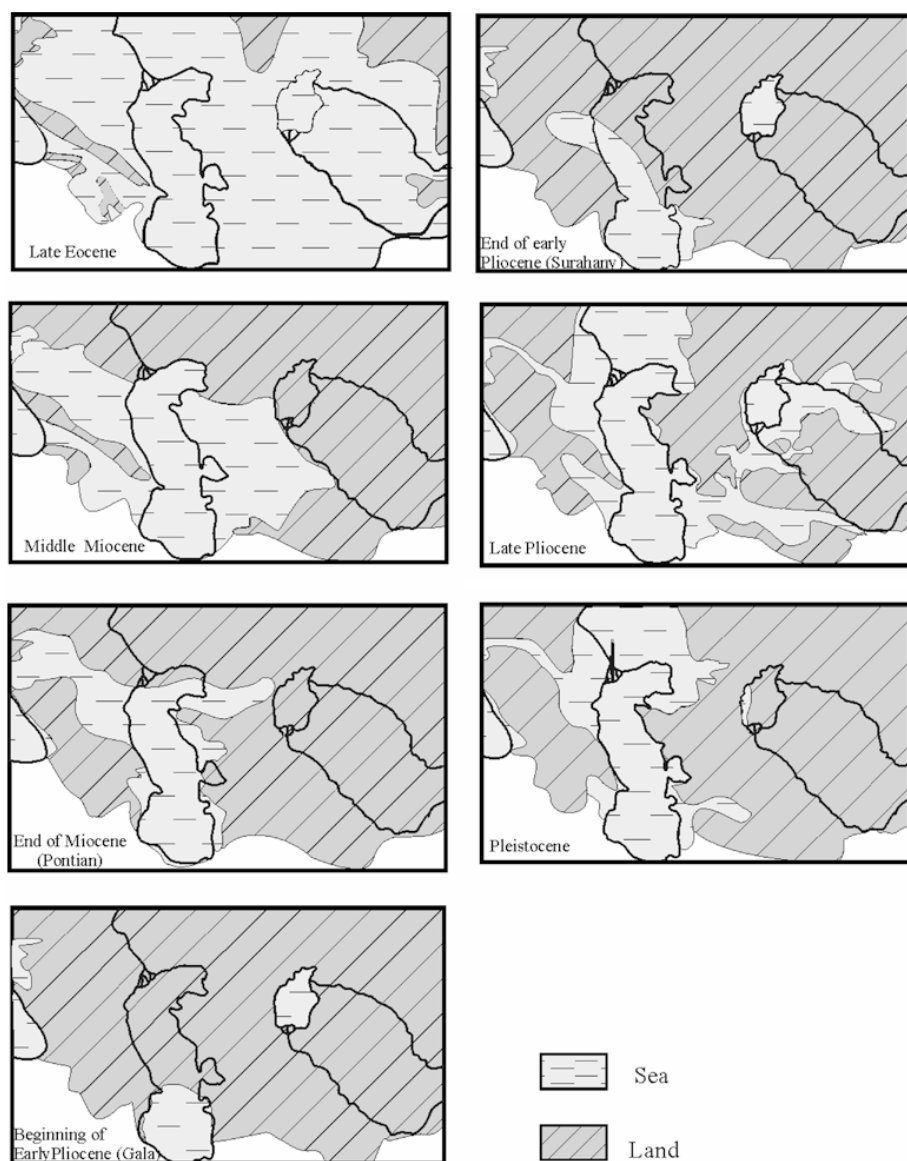


Figure 2.15: Cenozoic evolution of the paleogeography in the eastern Paratethys specifically centred in the Caspian Sea region (taken from Huseynov and Guliyev, 2004).

During the Pliocene-Pleistocene a major reorganization occurred in the SCB because shortening dominated the region at 3-5 Ma. The trend of structures due to this shortening varies significantly throughout the basin (*Fig. 2.11*). The Arabia-Eurasia collision promoted thrusting and surface uplift of the Caucasus Mountains (Nadirov *et al.*, 1997; Allen *et al.*, 2003; Brunet *et al.*, 2003). In the same epoch, the Alborz fold-belt started to grow (Axen *et al.*, 2001). The probable subduction of the SCB beneath the Apsheron Ridge might start simultaneously in this time (~5.5 Ma) (Allen *et al.*, 2002; Hollingsworth *et al.*, 2008).

Different processes shaped the marked asymmetry observed between the eastern and western sectors, because they are finally characterized by a relatively quiescent and old shelf in the East and an active, W-directed fold-and-thrust belt in the West (Kopeh Dagh) (*e.g.*, Devlin *et al.*, 1999). In the western margin, basin tilting occurs additionally towards the oceanic domain in the East. In addition, the occurrence of the West Caspian Fault produces an abrupt step of the basement in the westernmost SCB (*Figs. 2.10 and 2.11*) (Khain *et al.*, 1966; Nadirov, 1985).

The Pliocene folding in the Caucasus accelerated the subsidence of the dense, oceanic crust of the SCB that started ~160 my ago and whose wane was estimated for Pliocene times (Allen *et al.*, 2002; Jackson *et al.*, 2002; Artyushkov, 2007). Such increase in the subsidence rate combined with Late Messinian eustatic sea-level drop, promoted the ensuing establishment of large sedimentary depocentres in the basin. The Greater Caucasus uplift from ~3.4-3.1 Ma to Present contributed to the supply of sand-rich sediments to the SCB that prograded as enormous sedimentary bodies (Priestley *et al.*, 1994; Allen *et al.*, 2002; Morton *et al.*, 2003). In consequence, a huge amount of Late Miocene-to-Holocene sediments were rapidly accumulated above the pre-existent Jurassic-to-Messinian rocks. Rapid burial of the deltaic-lacustrine sediments also generated ideal conditions for a productive breeding ground: mud diapirism and hydrocarbon generation and preservation (Alizade *et al.*, 1966; Azizbekov, 1972; Berberian, 1983; Devlin *et al.*, 1999; Brunet *et al.*, 2003).

2.5. Mud Diapirs and Volcanoes

A large province of mud diapirs and mud volcanoes is recognized in onshore and offshore SCB from eastern Georgia and western Turkmenistan (*e.g.*, Guliev and Panahi, 2004; Huseynov and Guliyev, 2004; Yusifov and Rabinowitz, 2004). Mud accumulations sketch variable geometries at different scales in the SCB, both as buried and extruded structures (*Fig. 2.16*) (*e.g.*, Hovland *et al.*, 1997; Stewart and Davies, 2006). Seismic imaging of mud diapirs depicts teardrop, “hour-glass” and “Christmas-tree” structures (*Fig. 2.16a*) that express onto the surface as domes culminations (Stewart and Davies, 2006). Biconic morphologies characterize mud volcanoes profiles, in occasions fingered by overlapped wings, fed by straight chimneys or diatremes. When mud volcanoes reach the surface the edifice may consist of many morphological features (gryphons, domes) (Yusifov and Rabinowitz, 2004), whereas cones show gentle slopes and radially symmetrical geometries (*Fig. 2.16b*).

Extensive studies in the SCB manifest that mud volcanoes are usually developed on the crest of buried mud diapirs, although some examples are disconnected (Cooper, 2001a; Dimitrov, 2002; Yusifov and Rabinowitz, 2004). Approximately 75% of the mud volcanoes in the SCB coincide with the anticlines (Yusifov and Rabinowitz, 2004). Others, predominantly in the southern offshore region, occur on folds flanks of the anticlines or as

diatremes in rollover folds connected to regional deep faults (Yusifov and Rabinowitz, 2004).

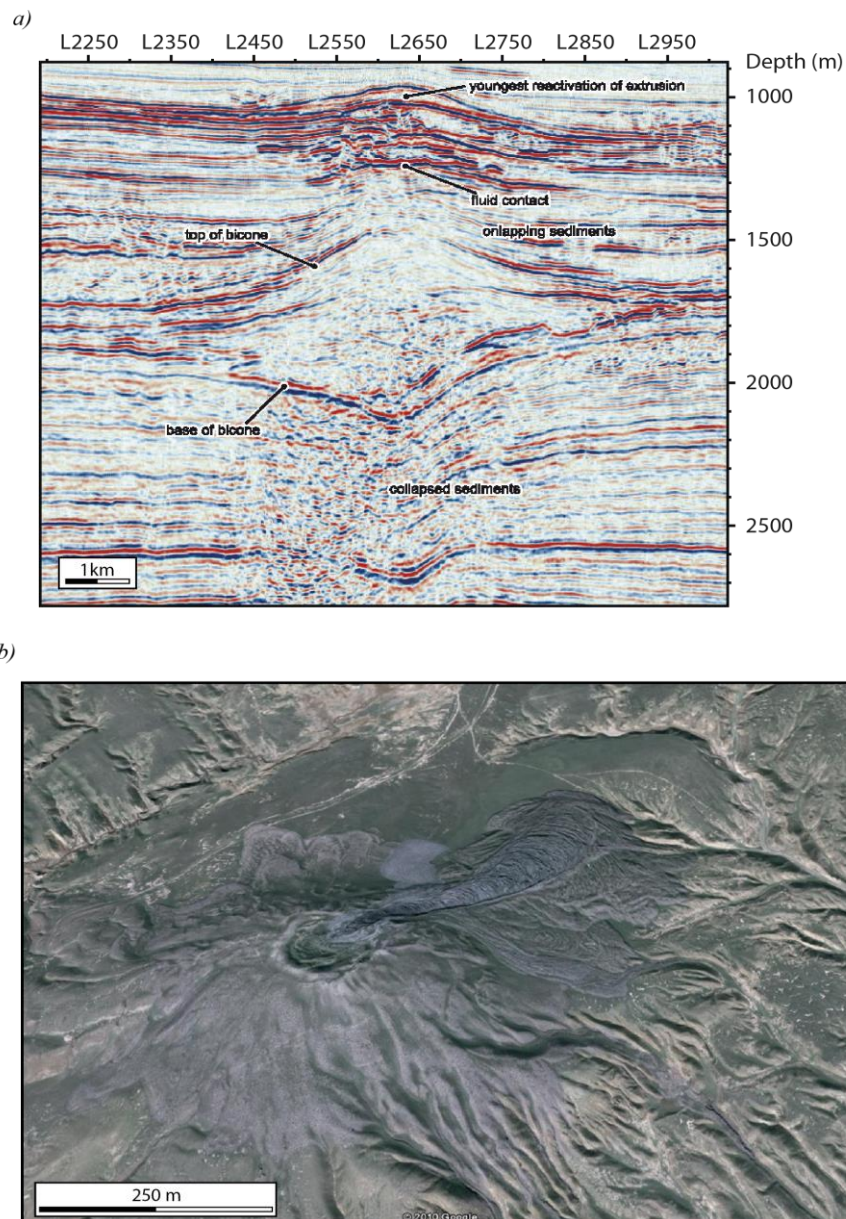


Figure 2.16: a) Typical seismic image of a buried mud volcano edifice with a “Christmas-tree” structure in the Caspian Sea (Stewart and Davies, 2006). The structure is characterized by the associated feeder channel (mud chimney), inter fingered margins and a bicone form. b) Perspective view of a large-scale mud volcano onshore Azerbaijan composed by a crater zone and numerous mud flows taken from Google Earth.

The sources of mud volcanism and diapirism are located at significant depths, between 3 and 12 km, in the Maykop Formation (see Fig. 2.12) or in other shallower rocks (Yakubov *et al.*, 1971; Lavrushin *et al.*, 1996; Cooper, 2001b; Stewart and Davies, 2006; Kopf *et al.*, 2009). Yusifov and Rabinowitz (2004) stated that mud volcano activity may not always be related to this formation. Mud processes seem to be closely linked to seismic fractures in the SCB. According to Huseynov and Guliyev (2004) mud volcanism and diapirism started in the Early Miocene and reached its highest intensity close to the Miocene-Pliocene boundary, associated with the isolation of the Caspian Sea (Fig. 2.15)

(Krijgsman *et al.*, 2010). Yusifov and Rabinowitz (2004) estimated that the beginning of the mud volcanism in the offshore SCB occurred at 4.33 My in the South of the basin, whereas it spreads towards northern areas 1.3 My ago. Intensification of mud volcanism in the overall SCB took place during the last 0.75 My.

Mud volcanism is the most visible demonstration of the overpressured nature of the sedimentary cover in the SCB (Lerche *et al.*, 1997; Nadirov *et al.*, 1997; Guliev and Panahi, 2004; Yusifov and Rabinowitz, 2004). Overpressure conditions are due to excessive fluid pressure preserved within the sediments throughout the whole SCB due to very high sedimentation rates since the Middle Pliocene (up to $1 \text{ mm}\cdot\text{yr}^{-1}$; Yusifov and Rabinowitz, 2004). Episodic loss of fluids in the associated shale diapirs by pulses of mud volcano activity may reduce the overpressure, strengthening the source layer and temporarily halting diapir growth (Yusifov and Rabinowitz, 2004). Furthermore, the occurrence of such highly plastic clay layer saturated with fluids at the level of the Maykop Formation restricts the bulk hypocentres generation at shallower levels than 10-12 km, (*e.g.*, Allen *et al.*, 2002; Glumov, 2004; Huseynov and Guliyev, 2004).

2.6. Sedimentary Sequence

The regional stratigraphy in the Caspian Sea is strongly controlled by several fluvial systems and ancient deltas (*Fig. 2.17*). As it is extensively described in the Russian literature (*e.g.*, Azizbekov, 1972), the Volga and paleo-Volga River have generated the major deltas, which discharge in the NCB. These sediments are subsequently distributed by submarine canyons into the northwestern SCB carrying sediments (*Fig. 2.17*) (*e.g.*, Brunet *et al.*, 2003). The current and ancient Kura River rise in the Lesser Caucasus and drain directly into the western SCB, in Azerbaijan, but they do not spread sediments into the easternmost SCB. By the contrary, this sector of the SCB was filled by the Paleo-Amu Darya River that supplied sediments from the Pamir Mountains in Tajikistan.

The sedimentary infill in the SCB is studied from onshore outcrops correlation and deep borehole data in offshore, but the complete sequence has not been drilled. Sediments thickness in the SCB exceeds 20 km in several depocentres (see *Fig. 2.10*) that range from Jurassic-to-Present in age, and represents the highest sedimentary package of the Caspian Sea (Zonenshain and Le Pichon, 1986; Abrams and Narimanov, 1997; Nadirov *et al.*, 1997; Mangino and Priestley, 1998; Brunet *et al.*, 2003; Smith-Rouch, 2006). About 5 km of this section corresponds to Mesozoic sediments (Brunet *et al.*, 2003). By contrast, the bulk of the sedimentary infill is younger than Oligocene, with up to 10 km of sediments deposited between the Pliocene and the Present (Berberian, 1983; Devlin *et al.*, 1999; Brunet *et al.*, 2003; Morton *et al.*, 2003).

Different contributions of major rivers systems and basin architecture have developed important variations in the depositional environment in the SCB margins (*Fig 3.9*). In the West, first sediments were supposedly deposited during the Callovian-Late Jurassic (Zonenshain and Le Pichon, 1986; Nadirov *et al.*, 1997; Knapp *et al.*, 2004), whereas in the eastern SCB sedimentation began during Cretaceous (*e.g.*, Brunet *et al.*, 2003). From the mid-Jurassic into the Neogene, the SCB was a depression on the shelf of Southern Eurasia where different episodes of marine isolation occurred (*e.g.*, Abrams and Narimanov, 1997). Several regional discordances are recognized in the sedimentary record.

Volcanoclastic sediments mainly have been identified in the Mesozoic sequence in the western onshore and offshore margin of the basin (*Fig. 2.18*) (Mamedov, 1992). Volcanic rocks coexist with Jurassic shales and sandstones from the Kinalug Formation and

limestones of the Shagdag Formation. The Cretaceous section is composed of marine, carbonate flysch and limestones (Kulunin, Kemchi, Yunun Dag and Ilkhidag formations) (ENI, 2002).

Clays and clastics interbedded with carbonates are dominant during the Paleocene, combined with an intercalation of shales and sandstones from the Sumgait Unit (Brunet *et al.*, 2003; Smith-Rouch, 2006). Above these units the Kun Formation of Eocene age consists of calcareous shales, alternating with black shales and sandstones (Brunet *et al.*, 2003; Smith-Rouch, 2006). The Eocene sediments are rich in tuff sediments and also present high content of clays and clastics interbedded with carbonates (Brunet *et al.*, 2003).

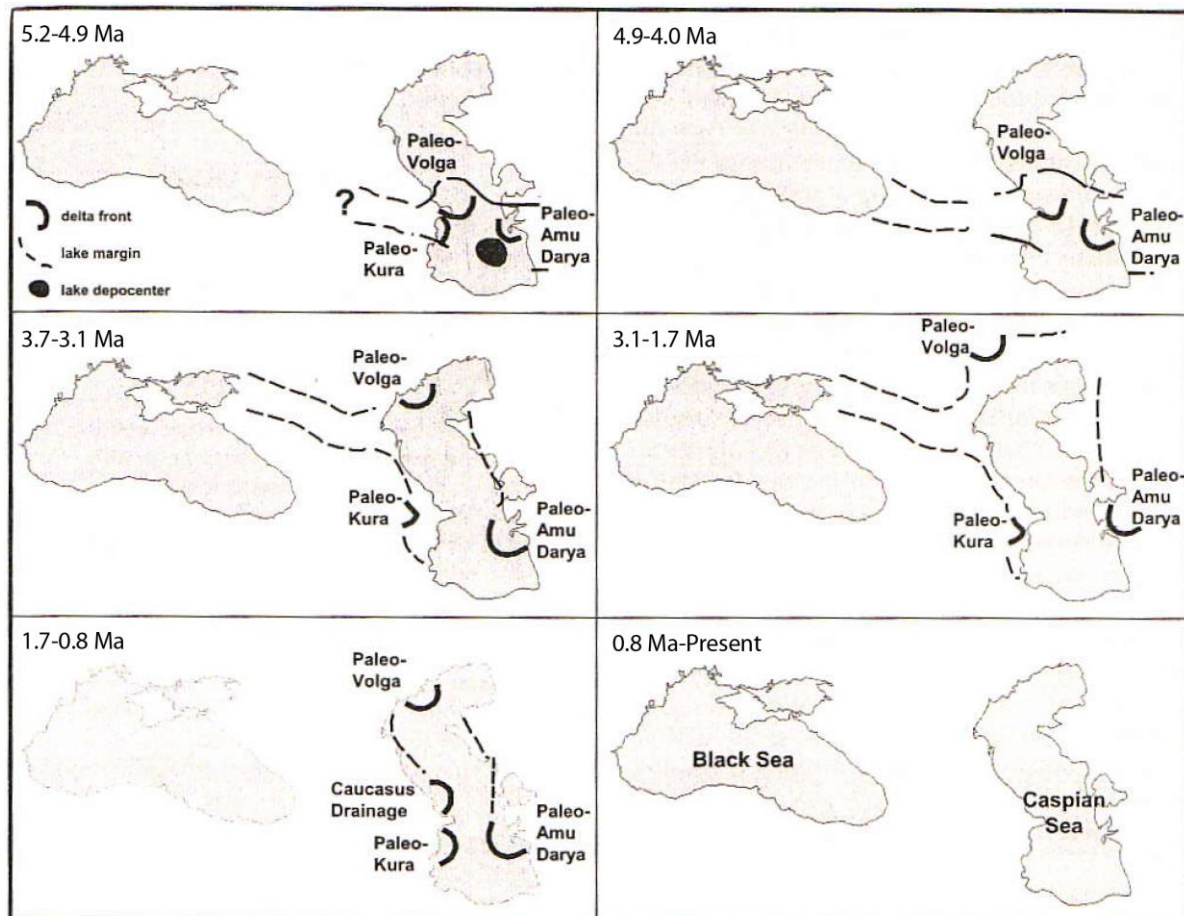


Figure 2.17: Paleogeographic reconstruction of the three main deltaic systems in the Caspian Sea from the Pliocene to the Quaternary. Possible connections between the Caspian and Black seas are also included. Taken from Abreu and Nummedal (2007). Source for ages: Jones and Simmons (1997); Abreu and Nummedal (2007); Forte *et al.* (2010).

The regional and widespread Maykop Formation was deposited during the Late Eocene-Early Miocene (~36-16.5 Ma) (Inan *et al.*, 1997; Hudson *et al.*, 2008; Afandiyeva *et al.*, 2009). This unit is formed by a monotonous series of anoxic dark-grey mudrocks deposited in a euxinic shallow-water environment. It is commonly interpreted that this formation was formed while the Caspian and the Black seas were still connected forming a large marginal sea of the Tethys marginal sea. In the Azerbaijan area, maximum thickness of the Maykop Formation is about 2-3 km (Hinds *et al.*, 2004; Smith-Rouch, 2006; Hudson *et al.*, 2008).

After the Early Miocene the marine depositional scenario of the SCB changed, favouring the deposition of thick shale- and marl-rich sediments (Smith-Rouch, 2006). They are grouped in different formations: the Tarkhanian (Early Miocene, 16.5-15.6 Ma), Chokrakian (Middle Miocene, 15.6-13.8 Ma), Karaganian (Middle Miocene, 13.8-12.5 Ma) and Konkian (Middle-to-Late Miocene, 12.5-10.5 Ma) (Jones and Simmons, 1997; Abreu and Nummedal, 2007; Forte *et al.*, 2010).

Age	Epochs	Stages		Suites	Lithology	Comments	
		Global	Local				
0.1	Recent	Ionian		Absheron		"Late Arabian" compression	
1.8	Pleistocene	Calabrian				Modern deep water South Caspian Basin established (Abdullayev, 2000)	
2.4		Gelasian					
3.4	Early Pliocene -Late Miocene ?	Piacenzian Zanclean	Klimmerian/ Balakhanian	Akchagyl		Akchagyl marine flood – reconnection to global oceans.	
				Surakhany	Productive Series		The Productive Series is composed of stacked fluviodeltaic reservoirs and lacustrine shales. Absolute age of units within the PS is uncertain because of limitations of biostratigraphy. Stratigraphic subdivisions are from summary in Popov <i>et al.</i> , 2006.
				Sabunchy			
				Balakhany			
				Fasila			
				NKG			
				NKP			
				KS			
				PK			
				KAS			
	Messinian						
6.0	Late Miocene	Tortonian	Pontian			Marine to increasingly freshwater lacustrine environment through Miocene	
		Serravallian	Pannonian	Diatom			
23.3	Oligocene	Langhian				"Early Arabian" compression during early Miocene	
		Burdigalian		Maykop			
35.4	Eocene	Chattian				Miocene–Oligocene anoxic marine source rocks of Maykop and Diatom formations (Jones and Simmons, 1996)	
		Rupelian		Paleogene			
56.5	Paleocene					Carbonate and shales in N to S shelf to basin transition	
	Cretaceous						

Figure 2.18: Summary stratigraphic column of the Azerbaijan area (taken from: Reynolds *et al.*, 1998; Devlin *et al.*, 1999; Baganz *et al.*, 2012; Green *et al.*, 2009; Abdullayev *et al.*, 2000).

During the Tortonian the Diatomaceous Formation was deposited (Late Miocene, 10.5-7.0 Ma) (Figs. 2.18 and 2.19), constituted by organic-rich calcareous and diatomaceous black shales (Abrams and Narimanov, 1997). Some authors still discuss if the Diatomaceous Unit comprises the older sediments of the Karaganian and Konkian units (Morton *et al.*, 2003; Smith-Rouch, 2006). In that case, the Diatomaceous Formation would be Serravallian to Tortonian (Middle-to-Late Miocene, 13.8-7.0 Ma) in age. The Diatomaceous Formation is interpreted as deposited due to the remnant occurrence of a marine connection between the Mediterranean and the Caspian seas (*e.g.*, Smith-Rouch, 2006). Overlying strata were deposited in progressively shallower water depths with evaporites present in the Messinian Pontian Unit (Late Miocene, 7.0-5.9 Ma) (Fig. 2.19), mainly constituted by shales with intercalated marls.

Deltaic to lacustrine conditions were predominant in the latest Miocene promoting the deposition of clastic-rich sediments with minor carbonates. Between 5.9 Ma and ~3.4-3.1 Ma (Late Miocene-Late Pliocene) the Productive Series (PS) were deposited in the SCB, which consist in an alternation of sandstones and shales of over 5-6 km-thick (Figs. 2.18 and 2.19) (Jones and Simmons, 1997; Allen *et al.*, 2002; Brunet *et al.*, 2003; Hinds *et al.*, 2004; Abreu and Nummedal, 2007). PS were deposited with sedimentation rates as high as

2 mm·yr⁻¹ (Nadirov *et al.*, 1997; Hinds *et al.*, 2004; Smith-Rouch, 2006; Stewart and Davies, 2006). The PS rocks are commonly divided into Lower and Upper PS separated by a regional discontinuity within an age of about 5.2 Ma (Fig. 2.19) (Smith-Rouch, 2006).

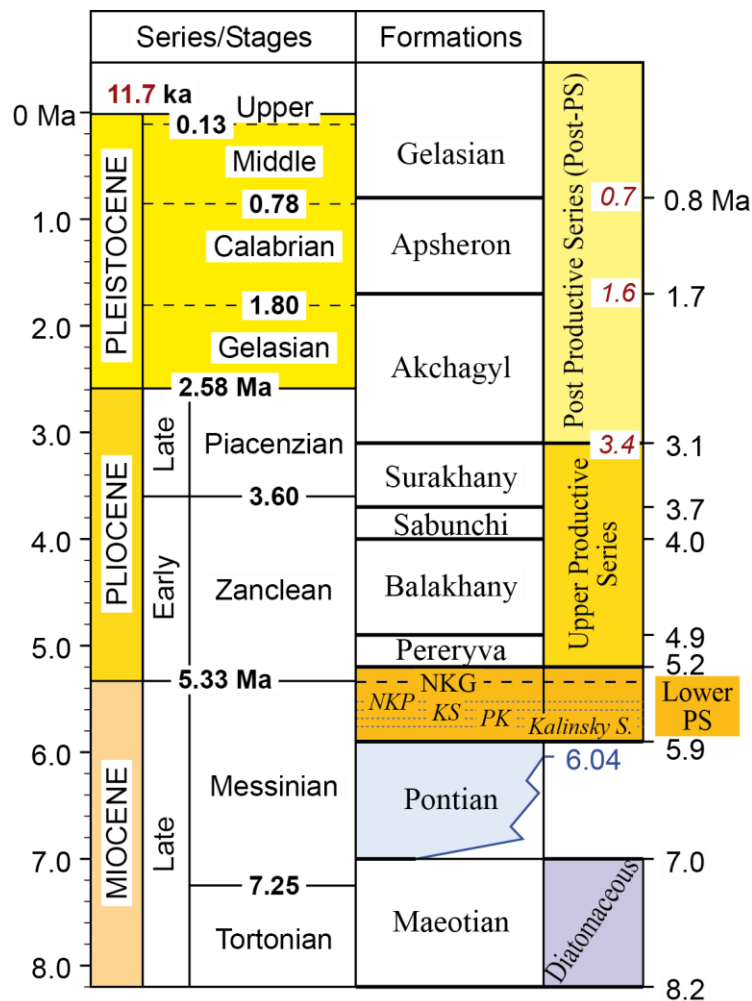


Figure 2.19: Stratigraphic table of the western SCB. The Diatomaceous Unit was deposited in the Early Tortonian (10.5 Ma). Time scale and geologic stages according to Gradstein *et al.* (2012). Sea level variations are taken from Miller *et al.* (2005). Age sources: red-coloured ages, Inan *et al.* (1997); black-coloured ages, Jones and Simmons (1997), Abreu and Nummedal (2007), Forte *et al.* (2010); blue-coloured ages, Krijgsman *et al.* (2010). Subunits of the Lower Productive Series (Lower PS; Kalinsky S, PK, KS, NKP, NKG) are detailed in the text.

The Lower PS sedimentation (Late Miocene-Early Pliocene, 5.9 to ~5.33-5.2 Ma) is controlled by a dramatic fall in base level at ~5.6-5.5 Ma ago that left the SCB as an isolated and restricted basin (Fig. 2.20) (Reynolds *et al.*, 1998; Krijgsman *et al.*, 2010). The Upper PS units (Early Pliocene-Late Pliocene, ~5.33-5.2 to ~3.4-3.1 Ma) are characterized by large fluvial-deltaic systems prograding into the basin (majorly, the Paleo-Volga and the Paleo-Kura rivers) (Morton *et al.*, 2003; Hinds *et al.*, 2004; Abreu and Nummedal, 2007). A continuous landward shift of coastal onlap marks the PS sections along the Kura delta and offshore Azerbaijan (Fig. 2.21a) (Abreu and Nummedal, 2007). In the eastern margin of the SCB, major regression of the paleo-Amu Darya marks the pronounce basinwards shift of the offlap break in the PS since the Late Miocene (Fig. 2.21b). A significant erosional unconformity crowns the top of the PS, highly evidenced on the region, followed by a major transgression along the overall basin margins (Fig. 2.21).

The Lower PS package (Late Miocene-Early Pliocene) in the Azerbaijan region mainly shows sandstone-prone intervals combined with mudstone-prone intervals (*Fig. 2.18*). This package is interpreted as channelized and sheet-flood fluvial deposits intercalated with regional short-lived lacustrine transgressions, respectively (Reynolds *et al.*, 1998; Hinds *et al.*, 2004), deposited within an alternating fluvial and lacustrine conditions presumably, in a continental basin with a low-gradient ramp, without evidence for a shelf-break (Jones and Simmons, 1997; Abreu and Nummedal, 2007). Maximum thickness estimates for the Lower PS are 1200 m (Smith-Rouch, 2006).

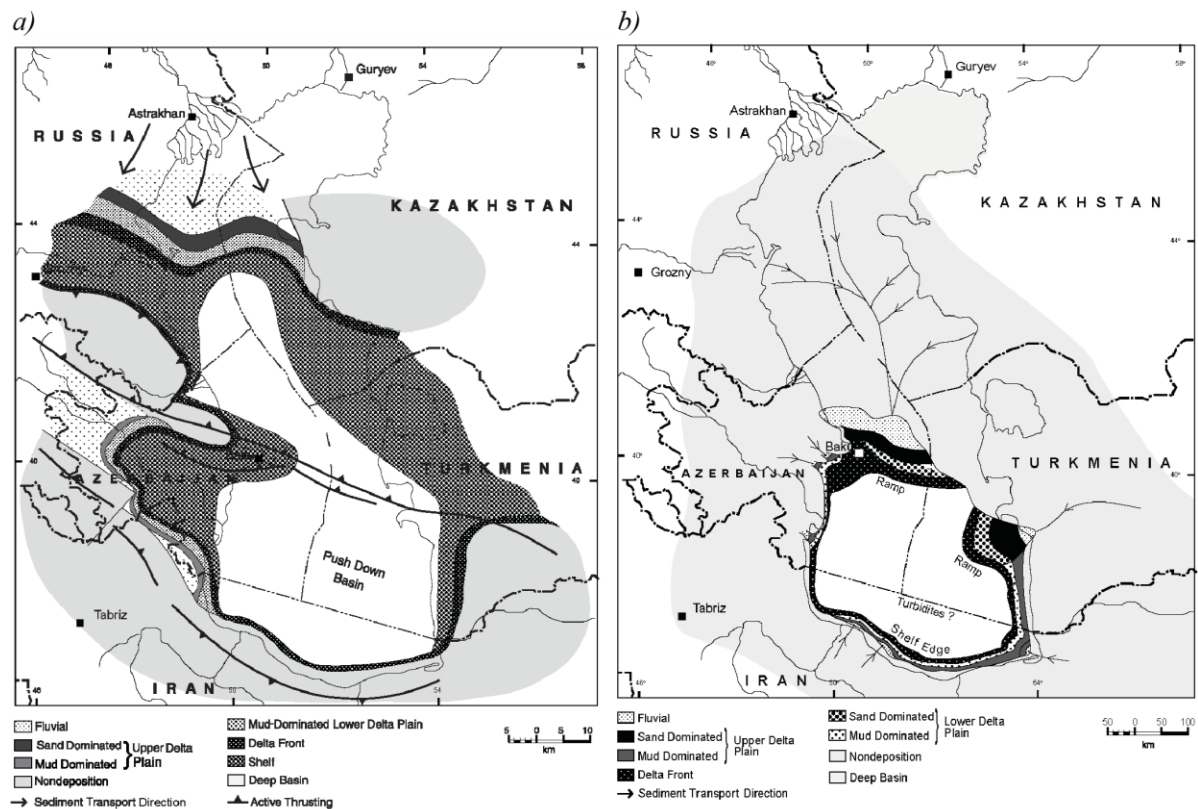


Figure 2.20: Paleogeographic maps of the Caspian Sea (a) before and (b) after the deposit of the PS (Late Miocene-Late Pliocene), initiated after a major fall in the base level ~ 5.6 - 5.5 my ago. Compiled by Reynolds *et al.* (1998) from Alizade *et al.* (1966); Zonenshain and Le Pichon (1986); Mamedov (1992); among others.

The stratigraphical sequence of the Lower PS consists into 5 units (*Fig. 2.19*) (e.g., Alizade *et al.*, 1966; Azizbekov, 1972; Reynolds *et al.*, 1998). The Kalinsky Formation (KAS) is a shale-sand sequence with inclusions of gypsum and anhydrite. The Podkirmakinskii or Pre-Kimarky Sand Formation (PK) consists of more than 90% of sandstones. Kirmaky Formation (KS) is comprised of alternating sandstones, silts and sands. The Nadkirmakinskii or Post-Kirmaky Sand Formation (NKP) contains mainly sandstones that are followed by the Nadkirmakinskii or Post-Kirmaky Clay Formation (NKG), which represents the only unit completely formed by shales. The base and the top of the NKG are represented by discontinuities.

There are fewer lacustrine evidences discernible in the sedimentology of the Upper PS (Early Pliocene-Late Pliocene), where the overall setting resembles a dry-land river system or terminal fan environments (Hinds *et al.*, 2004). Facies associations encompass a large range of paleoenvironments in a river-dominated braid delta (Reynolds *et al.*, 1998).

Lithology consists of the Upper PS sequence consists of sandstones deposited during periods of increased fluvial discharge and sediment supply, and mudstones, deposited during periods of decreased discharge and therefore coarse-grained sediment starvation. The high fluvial activity during the Upper PS conditioned a large sediment input of up to 3600 m of thickness (Smith-Rouch, 2006).

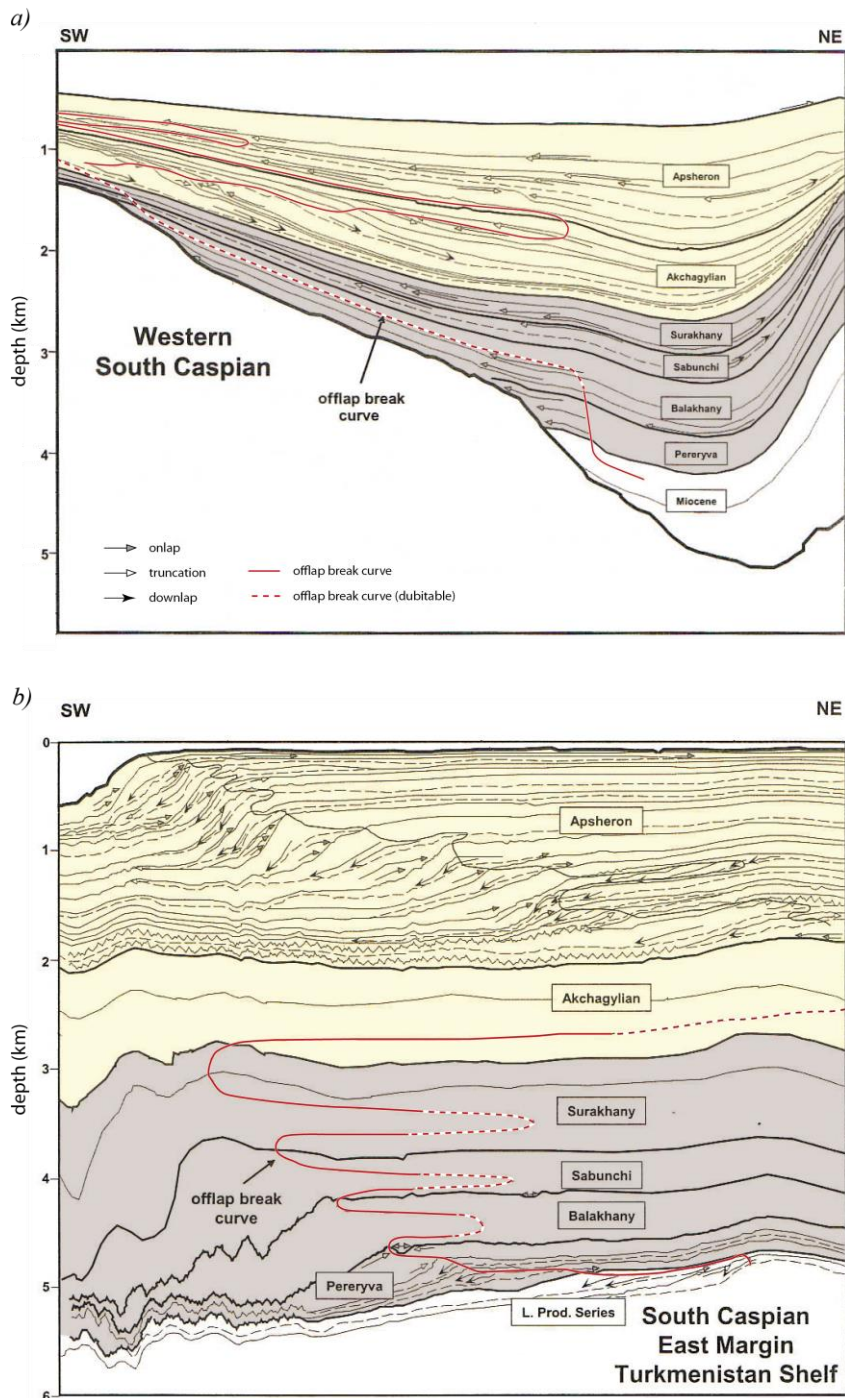


Figure 2.21: Stratigraphic architecture of (a) the western and (b) the eastern SCB margins. The Upper PS units are coloured in grey and the Post-PS sequence is yellow-coloured. Taken from Baganz *et al.* (2012); Abreu and Nummedal (2007); Green *et al.* (2009).

The Upper PS sequence is commonly divided into numerous subunits or horizons:

Pereryva, Balakhany, Sabunchi, and Surakhany units (Figs. 2.18 and 2.19) (Reynolds *et al.*, 1998; Hinds *et al.*, 2004). Pereryva Formation (~5.33-5.2 Ma to 4.9 Ma) consists of sand banks and few shale-rich intervals. Balakhany Unit (4.9-4.0 Ma) comprises coarse-grained sandstones with some interbedded shales. Sand-prone reservoir intervals in the Pereryva and the overlying Balakhany formations are interpreted as amalgamated, low sinuosity, braided fluvial sheet sandstones. Mudstone-rich intervals represent alluvial-plain and lacustrine facies. The succession displays an overall fining-up trend, which is controlled by a long-term climatic cooling, a decreased fluvial discharge and a reducing coarse-clastic input. The uppermost units present high proportion in shales. The Sabunchi Formation (4.0-3.7 Ma) is an argillaceous succession with sandstone packages in the upper parts (coarsening-upward silty sandstones and channelized sandstones). The Surakhany Formation (3.7 Ma to ~3.4-3.1 Ma) is dominated by mudstones and siltstones and comprises scarce and very thin sandstones (Reynolds *et al.*, 1998; Hinds *et al.*, 2004).

Sediments deposited after the PS sequence in the last ~3.4-3.1 Ma are here collectively grouped as the post-Productive Series (Post-PS) (Late Pliocene-Present) (Figs. 2.18 and 2.19). Lithology indicates that in the SCB, as in other closed basins with high terrigenous input, basinal deposition comes from turbidity currents and slumps generated from large shelf-edge deltas (Jones and Simmons, 1997; Abdullayev, 2000; Abreu and Nummedal, 2007; Forte *et al.*, 2010). The Post-PS strata maintain similar thickness over the SCB between 2 and 3 km (Inan *et al.*, 1997; Allen *et al.*, 2002).

The Late Pliocene-Early Pleistocene Akchagyl Unit (~3.4-3.1 Ma to ~1.7-1.6 Ma) consists of mud-rich turbidites and deepwater lacustrine deposits. The Akchagyl sediments are widely spread in Azerbaijan and are mainly represented by thin levels of grey laminated, poorly carbonaceous clay, with thin intervals of sandstones and volcanic ashes deposited in a large transgression phase (Fig. 2.21). The Apsheron sediments (Early Pleistocene, ~1.7-1.6 Ma to ~0.8-0.7 Ma) are represented by grey weak sandy clays, grey yellow-brown sandstones, shell-rich limestones, grey clays, sometimes volcanic ashes and conglomerates as non-marine, commonly brackish conditions have prevailed during deposition. The Apsheron Suite consists in prograding clinofolds packages and slumps. Slump deposits and deepwater fan systems (fan-lobes and channel-levee systems) constitutes the non-marine Gelasian sequence (Early Pleistocene-Present, ~0.8-0.7 Ma to Present).

2.7. The Petroleum System

Azerbaijan is one of the oldest oil-producing countries in the World and it stands out as the major oil and gas productive region in the Caspian Sea area. In addition to Azerbaijan, Turkmenistan, Russia, Kazakhstan, Uzbekistan and Iran are the other important oil-and-gas producing countries. The current exploration and production permits of hydrocarbon fields in the Caspian region are summarized in Figure 2.22.

The petroleum system in the SCB is characterized by hydrocarbon generation in two source rocks: the most relevant Maykop Unit and, locally, the Diatomaceous Formation (Figs. 2.23 and 2.24). Total organic carbon contents range from more than 10% in the Maykop source rock to over 1.2% in the Diatomaceous Unit (Smith-Rouch, 2006). Maykop rocks are able to generate both liquid and gaseous hydrocarbons.

The Maykop shales have been generating hydrocarbons since the Pliocene (*e.g.*, Inan *et al.*, 1997; Devlin *et al.*, 1999). The organic content and the level of maturity varied in time and space for both oil and gas (Abrams and Narimanov, 1997; Guliyev *et al.*, 2001). The

oil maturity appears to be lower than the conventional oil window but the unusually high and rapid sedimentation in the SCB, created low temperatures gradients ($14-16\text{ }^{\circ}\text{C}\cdot\text{km}^{-1}$; *e.g.*, Devlin *et al.*, 1999) ideal for hydrocarbon generation and preservation (Bagirov *et al.*, 1997; Stewart and Davies, 2006). In the SCB the kerogen-to-oil conversion probably occurs between 5 and 5.5 km depth in onshore and deeper than 8 km in offshore (Abrams and Narimanov, 1997; Guliyev *et al.*, 2001). The base of the oil window and onset of gas generation is estimated at 12-14 km (Abrams and Narimanov, 1997; Bagirov *et al.*, 1997; Inan *et al.*, 1997; Devlin *et al.*, 1999).

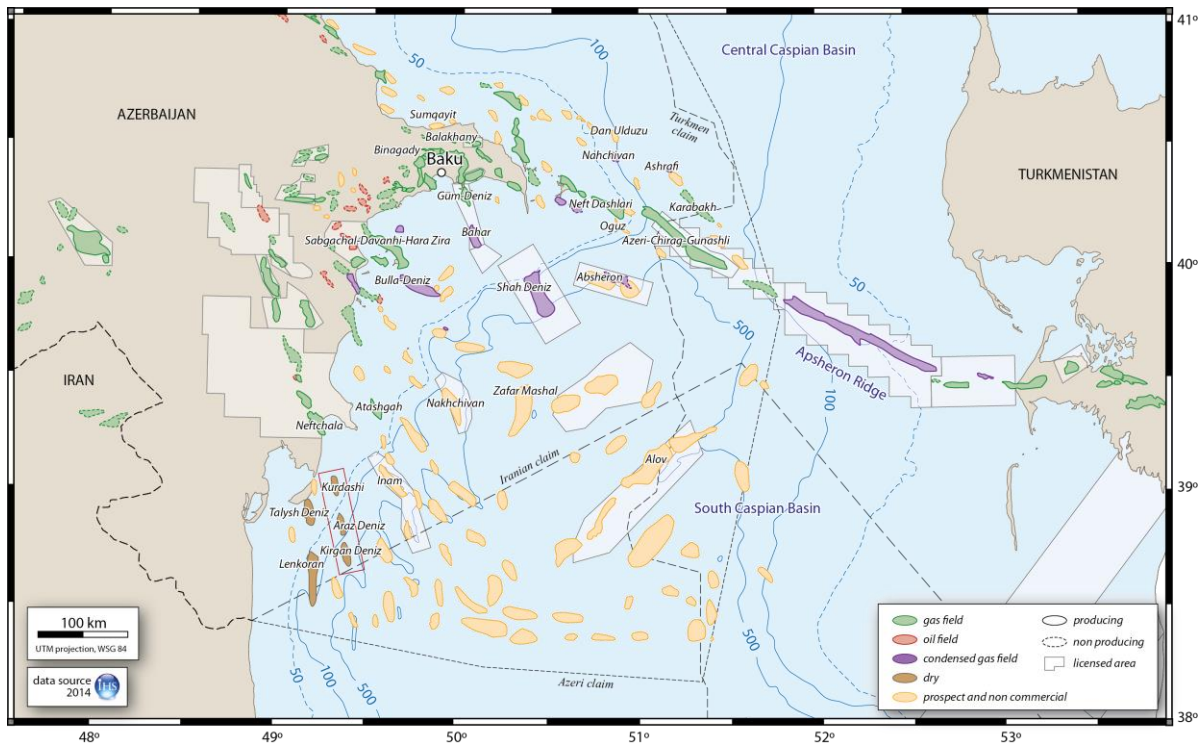


Figure 2.22: Production and exploration map of oil and gas in the Caspian Sea in 2013. The studied area is delimited by a red rectangle. Map courtesy of IHS in 2014.

The sedimentary succession in the SCB is thermally mature in gas. Reservoir gases are not from the thermal destruction of the oils, but generated from a younger more gas prone source at conventional generating temperatures (Devlin *et al.*, 1999).

Sandstones within the Late Cretaceous to Neogene succession are the principal reservoirs in the SCB (Bagirov *et al.*, 1997; Reynolds *et al.*, 1998). The main oil and gas deposits have been discovered in the deltaic PS reservoirs that encompass different deltaic environments from the fluvial and delta plain to the distal delta front (Reynolds *et al.*, 1998). Within the Lower PS, the PK sequence is an important reservoir, whereas in the Upper PS the primary reservoirs of the western SCB are located in Pereryva and especially in the Balakhany formations (*e.g.*, Smith-Rouch, 2006). Secondary targets are located in the Surakhany Unit.

Hydrocarbons are prevalent at less than ~ 3 km depth in the sedimentary sequence. Reservoir porosity is about 20%, reservoir shale content is about 30%, and reservoir permeability is about 200-300 mD (mildarcy), according to Bagirov *et al.* (1997).

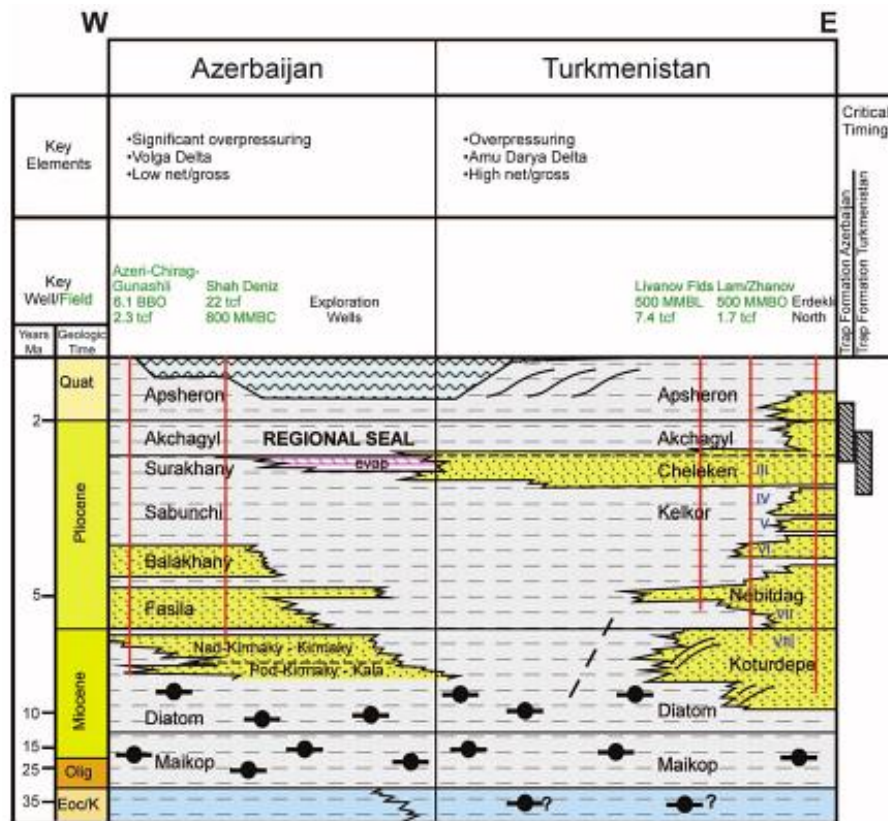


Figure 2.23: Panel of the petroleum system in the western and eastern SCB margins. Oil and gas prone-facies are represented by black circles. Taken from Baganz *et al.* (2012).

The Akchagyl and the Apshehon units in the Post-PS group constitute good-quality seals. One third of the entire hydrocarbon traps in the SCB are structurally controlled. The variety of folds and associated fractures creates favourable conditions for trapping hydrocarbons in the basin (*e.g.*, Belopolsky and Talwani, 1999). In fact, most of the proven and in production fields in the area occur in anticlines. This is also the place where overpressured sediments mobilize and escape producing mud volcanoes. According to Yusifov and Rabinowitz (2004), among others, mud volcanoes in the Caspian Sea are located in regions with an active hydrocarbon systems.

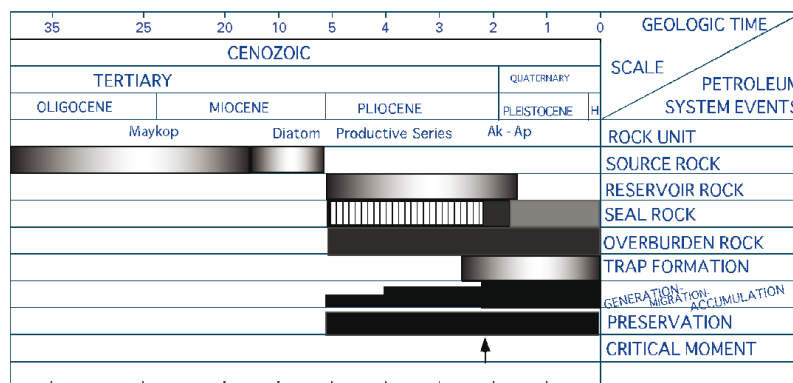


Figure 2.24: Schematic chart of the petroleum system in the SCB since the Oligocene, which includes the offshore region and adjacent narrow strips of land from Azerbaijan, Iran, and Turkmenistan (taken from Smith-Rouch, 2006). Abbreviations: Akchagyl Formation (Ak), Apshehon Formation (Ap), and Holocene epoch (H).

Oil and Gas Production

Oil fields in onshore and offshore Azerbaijan are known as early as the 4th century B.C. Economic production dates from the late 1870s and represents over the 45% of hydrocarbons production in the SCB, followed by Turkmenistan (35%) and Iran (20%) (Fig. 2.25) (e.g, Smith-Rouch, 2006). In the SCB province, oil fields are majorly located in the West whereas gas fields are encountered to the East.

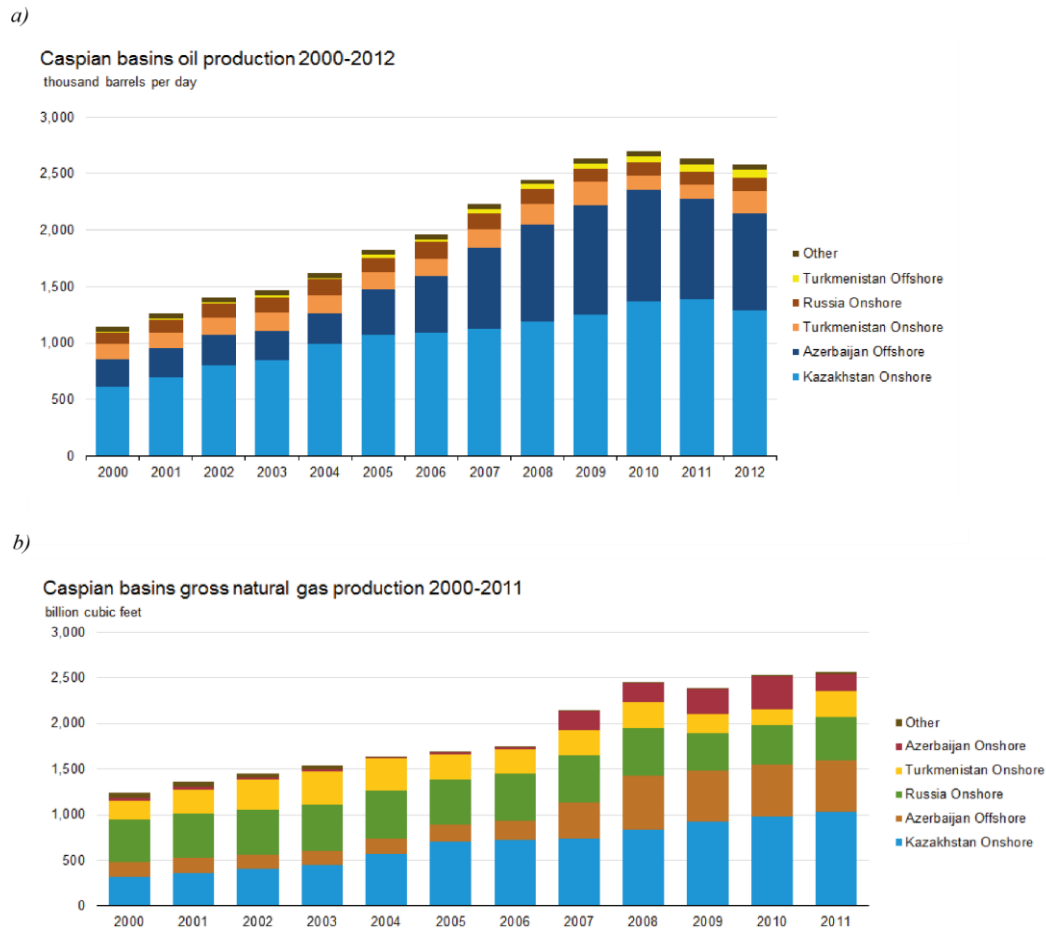


Figure 2.25: Data of (a) oil and (b) gas production from 2000 to 2012, and to 2011, respectively, taken from EIA (2013) for the Caspian region. Iran and Uzbekistan partially contribute to the offshore Caspian Sea.

In offshore Azerbaijan there are located up to 65 active oil and gas fields, more than a half part of the 105 fields discovered in the overall SCB province (Fig. 2.22). The largest oil-rich fields are parallel to the Apsheron Ridge: the giant Azeri-Chirag-Gunashli field, and the Neft Dashlari field. The giant gas field rich is Shah Deniz, in offshore Azerbaijan. These fields are currently in a mature production phase. To date, a great number of proven fields are still in the early stage of production or await development, specially, in relatively deep water.

According to the report published by the Energy Information Administration (EIA) of the United States in 2012, oil production expectations in the entire Caspian Sea region were >2.6 MMbbl (million barrels of oil; $\sim 4.13 \cdot 10^8$ litres), around 3.4% of the total World supply. Most current Caspian oil comes from onshore fields. The Azeri-Chirag-Gunashli field in offshore Azerbaijan produces over 660,000 bbl of oil per day (BP, 2014). The EIA stated in 2012 natural gas production in the Caspian region as >2.5 Tcf (trillion cubic feet;

~0.445 bbl). Gas production in the Shah Deniz field is ~260 Bcf per day (billion cubic feet) (BP, 2014; EIA, 2013) and the Azeri-Chirag-Gunashli field daily produces 110 Bcf of gas per day (EIA, 2013).

Estimations evidence that in 2012 the Caspian region roughly contained more than 48 billion bbl of proven oil reserves (*Table 2.1*) (EIA, 2013), and over 3-5 bbl are located in the Azeri-Chirag-Gunashli field (Belopolsky and Talwani, 1999; Smith-Rouch, 2006). Gas reserves in 2012 were estimated in the Caspian region to be at least of 292 Tcf (EIA, 2013). Proven world oil and gas reserves contain about 3% and 7%, respectively (Belopolsky and Talwani, 1999). The EIA estimates another 20 billion bbl of oil and 243 Tcf of gas as recoverable resources yet undiscovered in the SCB.

Country	Oil (bbl)			Gas (Tcf)		
	Offshore	Onshore	Total	Offshore	Onshore	Total
<i>Azerbaijan</i>	6.8	1.7	8.5	46	5	51
<i>Iran</i>	0.5	s	0.5	1	1	2
<i>Kazakhstan</i>	15.7	15.5	31.2	36	68	104
<i>Russia</i>	1.6	4.5	6.1	14	95	109
<i>Turkmenistan</i>	1.1	0.8	1.9	9	10	19
<i>Uzbekistan</i>	0	s	s	0	7	7
Total Caspian Sea	19.6	28.6	48.2	106	186	292

Table 2.1: Proved and probable reserves of crude and lease condensate oil and natural gas in the Caspian Sea region estimated for 2012. Units are barrels of oil (bbl) and trillion cubic feet (Tcf). Very low values are expressed as “s”. Source: EIA (2013).

In the hydrocarbon-bearing Caspian Sea gas resources are also obtained from alternative sources. On one hand, degassed fluids are erupted by mud volcanoes (Stewart and Davies, 2006), and, on the other hand, gas hydrates precipitated on the sea. Onshore and offshore volcanoes annually release >35 Bcf of gases, consisting of CH₄ (79-98%), and a small admixture of C₂H₆, C₃H₈, C₄H₁₀, C₅H₁₂, CO₂, N, H₂S, Ar, He (*e.g.*, Brown, 1990; Van Rensbergen *et al.*, 1999; Huseynov and Guliyev, 2004). Accumulations of gas hydrates are as much as 3.5-35 Tcf (Huseynov and Guliyev, 2004).

3. SEISMIC DATASET AND INTERPRETATION PROCEDURES

This thesis is based on the interpretation of a seismic volume in offshore Azerbaijan called as the Kurdashi Permit. The Kurdashi seismic survey is composed by numerous seismic profiles that represent the image of the subsurface constructed by means of the travel time of reflection seismic waves. Accurate interpretation of reflection seismic data is one of the most important elements for oil and gas exploration program. Seismic reflexion surveying consists in various interrelated steps to finally obtain a reliable geological image that make possible the interpretation of the geological structures. These stages are acquisition, processing and interpretation (e.g., Robein, 2010).

3.1. Basics of the Seismic Reflection

The seismic reflection technique is based on the study of the seismic waves that reflect along a surface or interface that bounds two materials with different properties. (Fig. 3.1). This interface is called a seismic horizon (e.g., Hölt *et al.*, 2011).

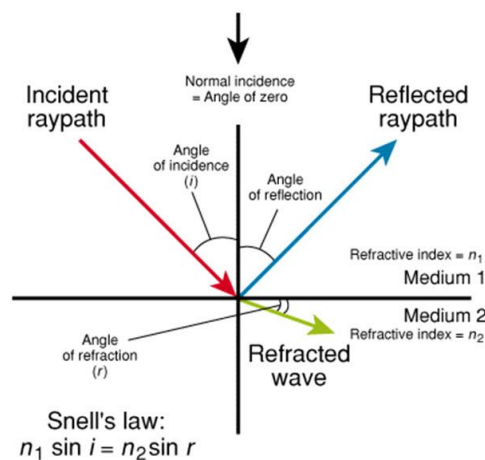


Figure 3.1: Explicative diagram of the Snell's Law assuming the Fermat's Principle. A seismic wave is reflected back at exactly the same angle as the incident angle (i) defined in the normal plane of the interface between both layers.

The energy reflects with an angle of reflection defined by the Snell's Law [4-1] and derived from the Fermat's Principle [4-2]:

$$\sin \theta_1 / v_1 = \sin \theta_2 / v_2 \quad [4-1]$$

$$n_1 * \sin \theta_1 = n_2 * \sin \theta_2 \quad [4-2]$$

$$n = c/v$$

Where, n is the reflexion index within the medium 1 (n_1) and medium 2 (n_2); c is a constant; v is the velocity in both mediums (v_1 and v_2 , respectively in medium 1 and 2). Thus, the angle of reflection (θ_2) is equal to the angle of incidence (θ_1), because both rays travel at the same velocity (v_1).

Reflection of the transmitted energy occurs when there is a contrast in velocity or density at the interface. The product between both parameters is called the acoustic impedance ($AI = v * \rho$) (Fig. 3.2) (e.g., Robein, 2010; Schlumberger, 2014). Variations of the AI may result from different conditions such as lithological changes, variations in porosity and/or in the pore fluids, or cementation changes, because all of them modify the rock strength. A detailed description on how the different rock conditions might affect the acoustic impedance is summarized in Table 3.1.

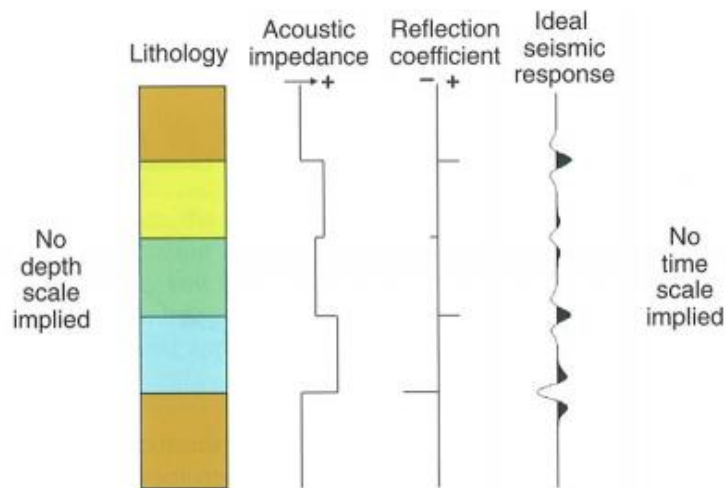


Figure 3.2: Scheme of the construction of a seismic trace during reflection campaigns from rock physical properties. Taken from Herron (2011).

Seismic energy is artificially generated by different sources in offshore and onshore regions. The emerging echoes of the sound waves are detected over the time by an array of receivers (Figs. 3.3 and 3.4). Each receiver records the arrival time of the different seismic waves. Each record is called as a seismic trace and it is plotted as a function of time. Seismic traces are usually condensed in groups that have collected reflections around the same point on the geological interface, even if they are generated from different shots. So it is possible to construct the interface responsible of the repeated signal in the subsurface. Each common point of reflection is termed as a common mid point (CMP) and represents a conventional method applied in seismic surveying because it facilitates determination of seismic velocities used in following processing and interpretation. Reflections recorded in the same position are summed to construct a single trace in the CMP (Fig. 3.4b). The number of times each CMP is sampled determines the “fold coverage” for the survey.

Geologic Condition	Impedance Effect
Lithological interfaces	A common cause of impedance contrasts. Generally ρ and V change whenever there is a change in lithology.
Porosity variations	ρ and V are porosity dependent. Gradual changes in porosity generate modest impedance contrasts. Abrupt changes in porosity can create large reflection coefficients.
Changes in pore fluid	Pore-fluid density affects bulk density ρ and velocity V . A change of pore fluid from water to oil creates a small impedance contrast that can be detected seismically only in ideal signal-to-noise conditions. A change from liquid (either water or oil) to gas can produce large impedance contrasts and robust seismic reflections.
Overpressure	ρ and V decrease in overpressure zones. If the onset of overpressure is gradual, the impedance contrasts may be too small to create detectable seismic reflections. Abrupt onsets of overpressure can produce strong reflections.
Cementation	Cementation affects the mechanical strength of rocks. V generally increases as mechanical strength increases (assuming a constant rock type). In some instances, variations in cementation can create impedance contrasts sufficient to result in seismic reflections.

Table 3.1: Summary table of the most common geological influences on acoustic impedance (Hart, 2008).

Fold coverage and seismic resolution are strongly linked to the number of receivers and they are also dependant of the survey design. Widely spaced lines of the receivers group or shotpoints generate a poor coverage of data and numerous gaps, whereas a denser grid formed by closely-spaced lines takes a real volume approach of the subsurface. The 3D acquisition method advent in early 1980s provided a high spatially sampled measure of subsurface reflectivity and, therefore, increased resolution and higher quality of data, with no significant gaps in the subsurface coverage (Fig. 3.5) (Cartwright, 2007). The powerful 3D seismic methodology is directly attributable to its better ability to illuminate structures and stratigraphic features in detail (Fig. 3.6) (e.g., Sheriff, 1992; Cartwright, 2007).

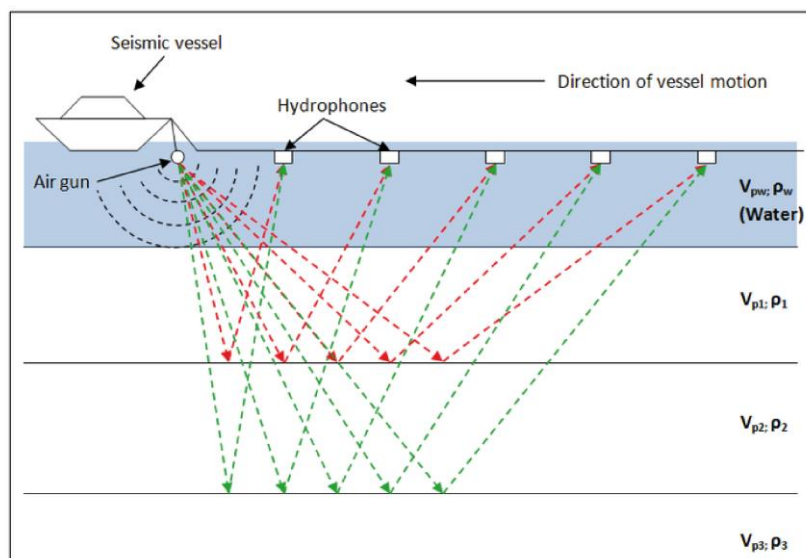


Figure 3.3: Diagram of a marine towed streamer seismic survey with the raypaths that result from a single shot by an airgun into a streamer containing 5 hydrophones. Red, dashed lines correspond to raypaths to first reflector, whereas the green ones are used for the second reflector.

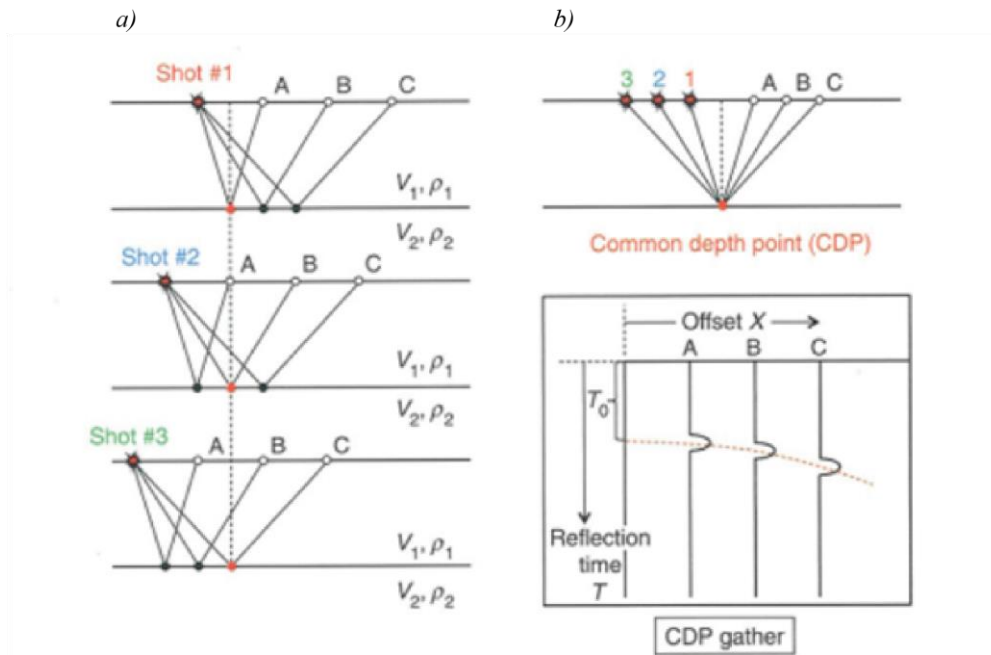


Figure 3.4: a) Scheme that explains how to obtain the geometry of the common depth point (CDP) and the common mid point (CMP) considering a simple seismic reflection survey with 3 shots, 1 to 3, and 3 receivers, A, B and C. As the survey progresses the source-receivers devices are displaced in steps of one interval toward the left. b) Seismic traces recorded on the same receivers in the three different shots, from the CDP construction to the final CMP.

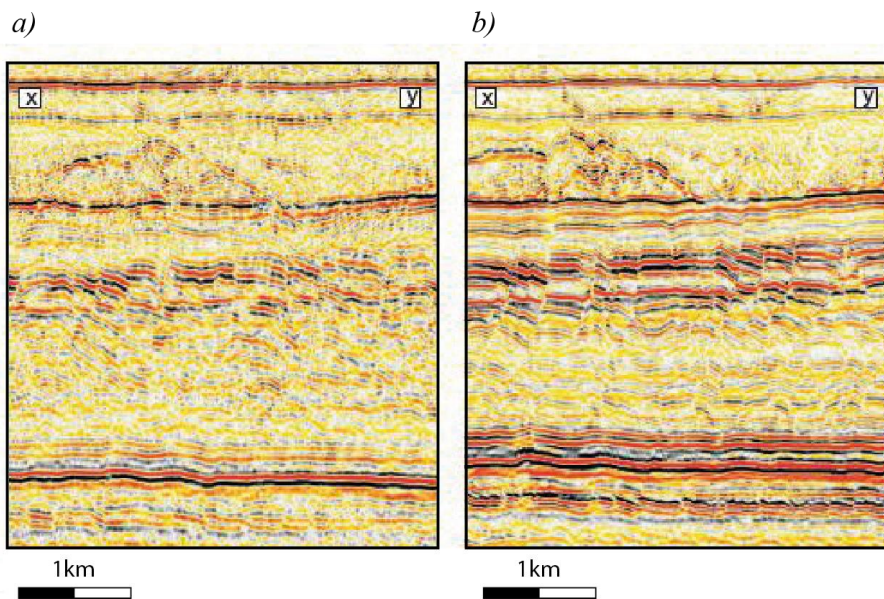


Figure 3.5: Seismic image of the same polygonal faulted interval imaged by (a) 2D and (b) 3D seismic profiles (Cartwright, 2007).

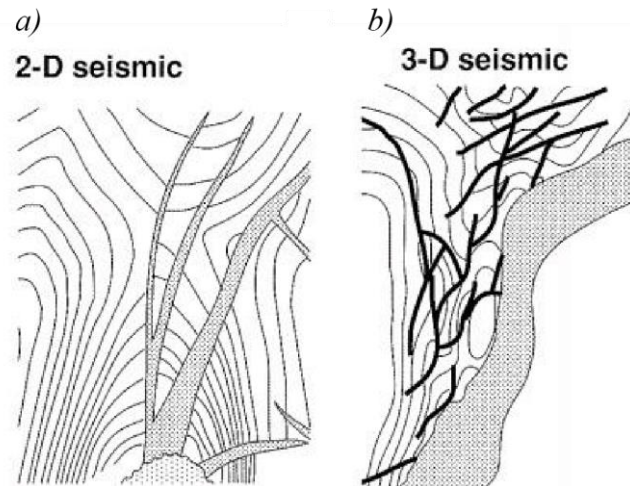


Figure 3.6: Cartoons to compare interpretation of the same area conducted by a (a) 2D vs. (b) a 3D seismic dataset. Notice the density of faults detected within the 3D example. Taken from Bacon *et al.* (2007).

3.1.1. Marine Acquisition

In 3D seismic programs the array distribution defines a seismic volume that contains three sets of close and regularly-spaced sections usually displayed in three orthogonal directions (*e.g.*, Brown, 2003). In-line (IL) direction is parallel to the receiver lines where data are acquired (Schlumberger, 2014), and cross-line direction (XL) is parallel to the source lines and perpendicular to ILs (*e.g.*, Cordsen *et al.*, 2000). The horizontal slice is called a horizontal section, time slice or depth slice. As a result, the 3D dataset can be “cut” in any direction but it still displays a well sampled seismic section without significant interpolation (Schlumberger, 2014).

In marine campaigns a vessel tows the source-receiver dispositive along a neutrally buoyant streamer (*Fig. 3.7*). The 3D seismic survey is acquired by sending sound waves provided by an air gun source that generates successive shots on the sea surface.

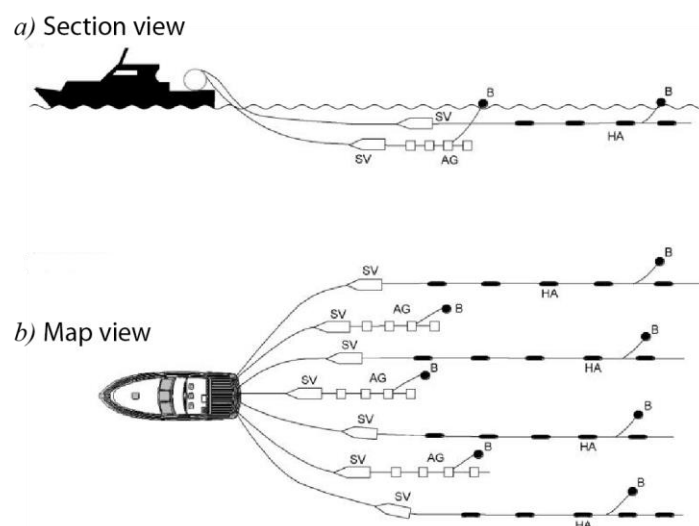


Figure 3.7: Basics scheme for marine seismic acquisition in (a) section and (b) plan views. The boat tows 3 airguns arrays (AG) that every few meters emit a sound wave into the water. The back reflected sound waves are captured by strings of hydrophones within 4 long cables or streamers (HA). The separation of seismic cables and general disposition of the source-receiver system is fixed by different buoys and floats (B). The steering vane is abbreviated as SV. Source: Cairn Energy (2014).

Seismic reflections are recorded by a string of hydrophones located 10-20 m below sea level behind and offset from the air gun source. The receivers transmit the recorded signal back to the vessel where it is stored on tape to be processed in following stages. In offshore areas, the direction of the vessel movement defines the two vertical sections of the volume: ILs and XLs. Configuration of the dispositive, and even the direction of the vessel movement, depends on the aim of the project.

Seismic equipment used in 3D data offshore acquisition is usually configured with 2 to 6 sources and between 3 and 12 regularly spaced arrays of hydrophones (streamers) (*Fig. 3.7*). Streamer length oscillates commonly between 4 and 9 km that may carry up to 3000 hydrophones.

3.1.2. Signal Processing

Seismic data need to be processed to maximize the useful signal and provide a correct image. Three main stages are included in the seismic processing workflow: deconvolution, stacking and migration. Other auxiliary processes such as specific filters and corrections are also used to increase the effectiveness of the former ones in complex 3D seismic surveys (*e.g.*, Yilmaz, 1987).

The deconvolution process tries to rebuild the original spectrum of the signal through an inverse filter. It is therefore obtained a higher temporal resolution of the seismic trace, and it also removes multiples of the traces. Multiple reflections or multiple scattering could appear as artefacts on the seismic image (*e.g.*, Robein, 2010).

The stacking phase consists in piling the traces recorded in the same CMP. This work is based on the analysis of the velocity field (*e.g.*, Cordsen *et al.*, 2000; Robein, 2010). As the same reflexion in CMP is detected with different arrival, an increasing delay is suffered by each wave proportionally to the separation to the air gun. In consequence, and before traces could be stacked, a normal move out correction (NMO) needs to be applied. Once, reflectors are aligned, traces are summed to create a single trace at a central location in a stacked sequence where reflector multiples are attenuated (*e.g.*, Robein, 2010; Schlumberger, 2014).

Stacking may be done over selected offset ranges when AVO (amplitude variation with offset) effects exist in the data. AVO is a technique used to determine rock properties as, for example, fluid contents and composition, or hydrocarbon occurrence (*e.g.*, Bacon *et al.*, 2007; Schlumberger, 2014).

The migration phase is developed after stacking procedures and it is the principal technique for improving horizontal resolution. During the migration stage the geophysicist try to relocate reflections recorded at the surface at their right position in the subsurface. Migration is performed by three distinct functions: 1) relocate reflections out-of-place because of dip (for example, CMP converts to CRP, or common reflection point); 2) consider the Fresnel zone to separate intersection events; and 3) remove diffraction waves from points and edges remove. The latter two processes make the wave amplitudes more accurate (*e.g.*, Brown, 2003).

Migration is indispensable for seismic imaging because seismic information is converted from the time domain to the depth domain, and it is therefore required an accurate velocity model. Typically, time migration uses average values for velocity in areas with minor structural complexities, whereas depth migration use the full velocity model, which leads to a much better image. In time imaging, the vertical axis of the image is in double travel-time units (twtt), whereas in depth imaging, the relocated

reflection coefficients are at their true depth (Yilmaz, 1987; Robein, 2010).

Seismic processing in time requires an implicit and smooth velocity model to obtain the pre-stack time migration (Pre-STM), whereas an explicit velocity model building and a full waveform inversion are used in any pre-stack depth migration (Pre-SDM). Pre-SDM is required in areas of complex lateral velocity variation attempting to move events with potential stacking conflicts to finally determine a unique stacking velocity (see Bacon *et al.*, 2007). *Figure 3.8* illustrates four different types of stacking procedures. Two main traditional approaches to pre-SDM exist: the Kirchhoff method, which consists of modelling a single ray path, and the wave equation method, which models the entire wave front. Kirchhoff, phase-shift and full-wave migration are among the most common types of seismic migration procedures. A third method has recently been developed, the beam algorithm method, which analyses seismic data for coherent events (Eisley and Tieman, 2010).

Seismic interpretation comprises the ultimate stage of seismic surveying in a marine campaign and in onshore projects. Many geological aspects are enhanced and a realistic view is offered for the subsurface structures.

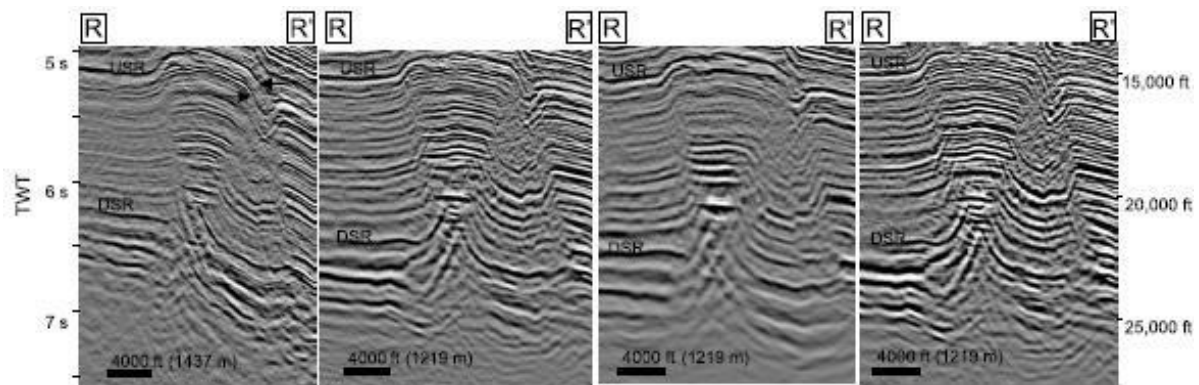


Figure 3.8: Comparison of the same seismic section R-R' obtained through different stacking procedures. From left to right: post-stack time migration (full stack), near-angle stack time migration, far-angle stack time migration and pre-stack depth migration (full stack) (Camerlo and Benson, 2006).

3.2. The Kurdashi Seismic Dataset

This thesis studies a seismic survey conducted in the Kurdashi Permit in territorial waters of Azerbaijan (see *Fig. 2.2*). This permit encompasses a folded structure with three separated culminations: Kirgan Deniz (420 km²), Araz Deniz (355 km²), and Kurdashi itself (290 km²) domains, sited from the South to the North, respectively. Our analysis is focused on the Kirgan Deniz structure and the southern sector of the Araz Deniz domain, referred in this thesis as Southern and Northern culminations, respectively. This anticline zone is called in this study as the Kirgan-Araz Deniz (KAD) anticline of ~653 km². REPSOL has provided us the dataset through an academic agreement.

Seismic data consist in a Pre-stack 3D processed seismic cube migrated in depth. The seismic analysis is combined with the drilling information from a commercial exploration well: Araz Deniz 1X (AD-1X) (*Fig. 3.9*). To the North of the studied area in the Kurdashi Island, a second exploration well was also drilled, the Kurdashi 1X well. The stratigraphic information of both wells has been used in this study, although the seismic interpretation of this thesis has not been extended to the area of the Kurdashi 1X well.

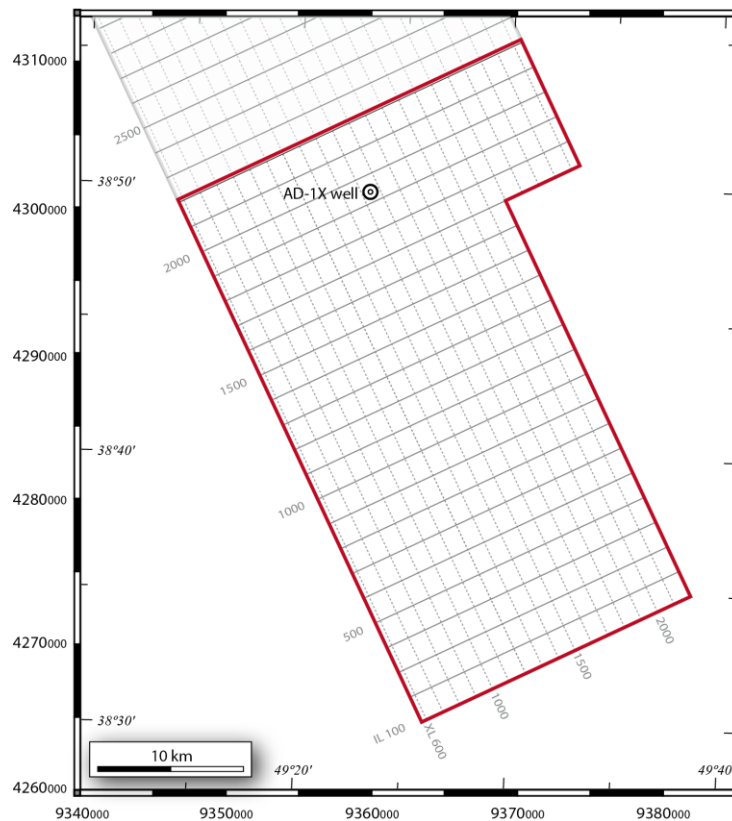


Figure 3.9: Seismic survey used for this study within the Kurdashi Permit, showing also the position of the AD-1X well. The perimeter of the permit is coloured in red and delimitates the studied KAD area. This location map, like the rest of the figures presented in this thesis, corresponds to UTM projection (Gauss-Kruger, Pulkovo 1942, coordinate system and the Krassovsky 1940 ellipsoid).

Seismic acquisition operations started in November 1998 and were completed in April 1999. The vessel was equipped with 3 streamers of 5100 m cable-long in the deepwater region, whereas one cable of 5100 m was used in shallow waters. Two sources were used in both regions. The vessel towed the dispositive to the East with 65° of azimuth.

The Kurdashi exploration block covers approximately 1660 km² between 38° 30.4' N – 39° 10.4' N and 49° 4.5' E – 49° 38.75' E. The Kurdashi Permit is sited over 140 km South of Baku and 25 km South of the Kura River mouth (Fig. 3.9). The water depth ranges between 0 to 700 m. Over 4200 seismic lines comprise the studied KAD area (Fig. 3.9). ILS were displayed with an space of 18.5 m, whereas XLs spacing is 12.5 m. Depth range is 8990 m with 900 samples per trace. Sample interval is 10 m and storage format, 8 bits. Seismic data are displayed according to SEG normal polarity, meaning that a positive increase in acoustic impedance across an interface is shown in black (for black-and-white seismic images) or blue (for the coloured seismic images). The average vertical resolution (quarter of the wavelength) is 20 m in the interval of interest (approximately 0-2000 m), although resolution decreases with depth.

Seismic processing in the Kurdashi seismic project was performed between 1999 and 2000 subdivided in two phases (Pre-SDM). Phase I consists in depth imaging of the Araz Deniz area, and Phase II comprises the Kirgan Deniz and the Kurdashi areas.

During Phase I Vertical Seismic Profile (VSP) data were fundamental to generate an initial velocity model, whereas a comprehensive 3D velocity field was generated and used during Phase II for conducting the 3D Pre-SDM methodology. After the determination of an initial velocity model, a velocity update and geometry interpretation phase was

conducted layer by layer to finally build a more robust velocity model for the next iteration. This method is also known as the “layer stripping technique”. At the end, this procedure builds up an accurate velocity model with vertical and horizontal velocity gradients for each layer (Fig. 3.10) (ENI, 2002; Schlumberger, 2014).

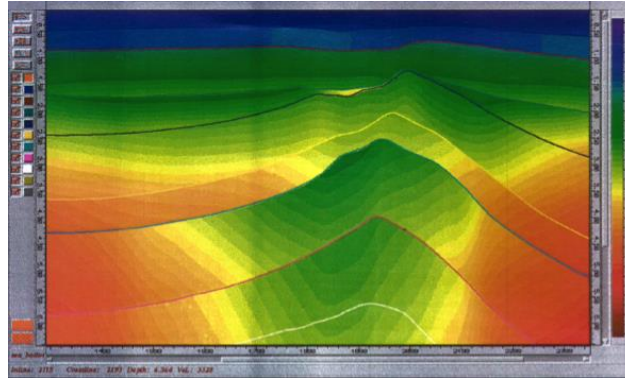


Figure 3.10: 3D Pre-SDM velocity section in the studied area. Source: ENI (2002).

Pre-SDM was implemented using Kirchoff algorithm (Yilmaz, 1987). Radon filter and spiking deconvolution were also applied for multiple removal during the Pre-SDM processing. As a result, the Pre-SDM dataset used in this thesis has a much better image with respect to the original time-migrated cube, with a higher accuracy and resolution, making therefore possible a more detailed and precise reconstruction of the structure in the depth scale (e.g., Fig. 3.11).

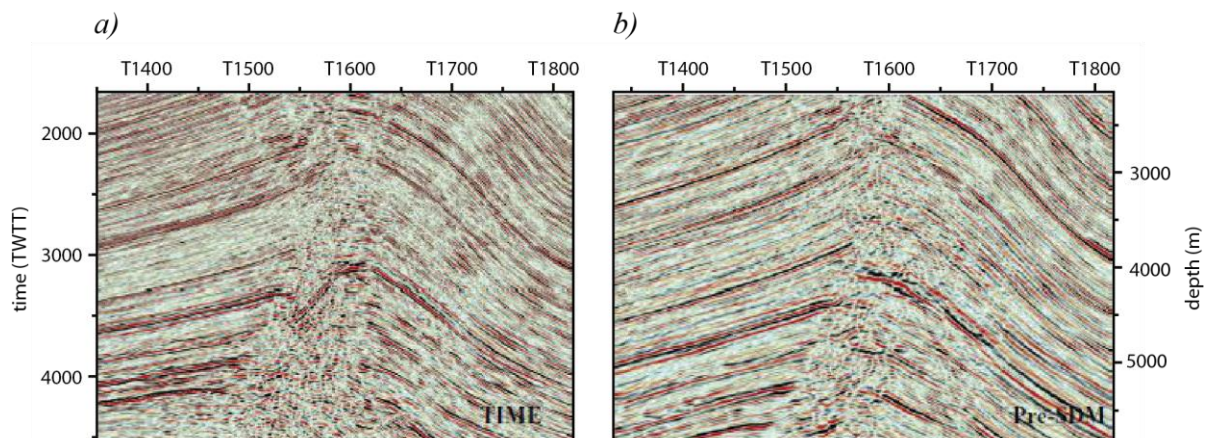


Figure 3.11: A comparison between (a) conventional time-processed and (b) Pre-SDM for a 3D vertical section in the Kurdashi cube (taken from Bertello *et al.*, 2001).

3.3. Seismic Interpretation

This study is based on the interpretation of the seismic response throughout the KAD structure by means of different techniques. The initial step consisted in the horizons interpretation in some master ILs and XLs by integrating stratigraphic and biostratigraphic data from the AD-1X well. This approach was then extended throughout the seismic cube by using different specific softwares for 3D interpretation and visualization. The secondary, complementary objective was interpreting the fault and mud structures in the

survey. This analysis has been also completed with a detailed inspection of the seismic facies that might correspond to gravitational-instability deposits.

This work is mainly based on the geometrical reconstruction of the Productive Series (PS). We have conducted a comprehensive interpretation of the seismic cube through the analysis and correlation of twelve seismic horizons, locally implemented by intermediate horizons. In addition, the most recent sedimentary package (Post-PS) has been studied using mainly two regionally consistent seismic horizons. A detailed study of the seismic attributes through the seismic cube has not been carried out in this thesis, although this type of analysis has been used to characterize the internal structure of the most-recent mobilized sediments.

3.3.1. Softwares

The Pre-SDM seismic cube has been loaded and interpreted by using numerous softwares: Kingdom Suite, Landmark and Petrel (Table 3.2). However, the interpretation obtained through the automatic tracking tools of these softwares have been always revised and checked manually. Golden Surfer has been used to complement the visualization and contouring.

SOFTWARE	 Kingdom Suite v. 8.3	 Petrel v. 2011.1	 SeisWorks v. 5000.01.0	 Golden Software Surfer v. 8.05
SEISMIC INTERPRETATION HORIZONS	2d/3dPAK v. 8.3 to 8.6 <i>Horizons</i> <i>Polygons</i>	Seismic interpretation <i>Geophysics:</i> -Seismic interpretation <i>Utilities:</i> -Make surface (TST,TVT) -Make grid	Seisworks <i>SWhorizons</i> GeoProbe 5000 <i>Horizons</i>	
STRUCTURES	2d/3dPAK <i>Faults</i> <i>Polygons</i>		Seisworks <i>SWfaults</i> GeoProbe <i>Volume</i> <i>Bodies</i> <i>Geobodies</i> <i>Tools</i>	
MTCs		Multitrace attributes <i>Geophysics:</i> -Volume attributes -Surface attributes	GeoProbe <i>Tools</i> Power Calculator	
3D VISUALIZATION	2d/3dPAK <i>Grids</i> <i>Contours</i> VuPAK v 8.6	Seismic volume rendering and extraction	GeoProbe <i>Volume</i> <i>Tools</i> <i>Probe</i> Power View	<i>Contours</i> <i>Thickness maps</i>

Table 3.2: Workflow of the procedures followed in this thesis from the data loading, interpretation to visualization stages.

Kingdom Suite and Petrel have been used by means of academic agreements obtained by the University of Granada, respectively with ancient SMT and currently IHS, and Schlumberger. Landmark was employed as part of the research realized by the author in the Imperial College of London through collaborations with Halliburton.

The first stage consisted in revising the seismic interpretation conducted by data providers (REPSOL, among others). These preliminary results were checked with the AD-1X well and were implemented with additional seismic horizons. We also interpreted the fault structures, the mud-diapir limits, and gravitational bodies, among other tasks.

Kingdom Suite has been mainly used to trace horizons and faults features in the 3D volume and also to generate structural maps from amplitude data. A preliminary interpretation of mud diapirs was also conducted with this program through the 2d/3dPAK interpretation package. Interpretation of horizons and faults was later revised in Landmark by using various modules within the SeisWorks package. New intermediate surfaces were also created in Landmark, especially within the Post-PS sequence. Fault and diapir structural interpretation were accomplished with different attributes using various Landmark modules within the GeoProbe5000 package. We used the Geobody tool to enhance the interpretation of diapiric bodies, and the Power Calculator module was employed to study some of the sediments mobilized by topographic instabilities. Petrel was also used to analyse the seismic attributes by means of the Multitrace Attributes package (Geophysics module), through the volume and surface attributes tools. The Seismic Interpretation package was also employed in Petrel to measure the true stratigraphic thickness of the seismic units by the Utilities tools.

The 3D visualisation has been possible with the combination of the VuPak module display contained in Kingdom Suite and the Seismic volume rendering and extraction package in Petrel. We especially used Surfer to implement the graphic output of the seismic interpretation packages.

3.3.2. Seismic Interpretation Workflow

In this thesis we analysed the Post-PS horizons (~3.4-3.1 Ma-to-Present), focusing on the recognition of the top of the shallower horizons, especially the Akchagyl (~3.4-3.1 Ma to ~1.7-1.6 Ma) and the Apsheron units (~1.7-1.6 Ma to ~0.8-0.7 Ma), and also the seafloor. A revision of the pre-interpreted horizons tops is also conducted, evaluated from the Lower PS, which includes the PS-bottom (5.9 Ma) and the NKG (~5.33-5.2 Ma), to the Upper PS that consist in the Pereryva (~5.33-5.2 Ma to 4.9 Ma), Balakhany (4.9-4.0 Ma), Sabunchi (4.0-3.7 Ma), and Surakhany (3.7 Ma to ~3.4-3.1 Ma) units, crowned by the PS-top (~3.4-3.1 Ma). We have completed the inherited seismic horizons through the analysis of the continuity of reflections.

The seismic interpretation was tied with drill data from the AD-1X well. Horizon interpretation was developed through the intersection of formation tops penetrated in the AD-1X well in Kingdom Suite. The tops of the Akchagyl and Apsheron formations and the seafloor were correlated with the well data in several intersection lines. We then used them to expand our interpretation to the remainder volume and finally obtain seismic horizons. We extended initial data along some key ILs, XLs, arbitrary lines and depth sections. The seismic horizons were firstly extracted based on semi-automatic depict tools and continuously checked manually. The overall workflow of Post-PS horizon picking consists of the identification of Akchagyl and Apsheron tops in every 10 ILs and 10 XLs sections by means of cross-cutting correlation. We also interpreted horizons in correlative depth slices. The workflow is very dynamic since continuous updates of horizons are accordingly realized in other views. PS horizons tops were also studied with the same 2D-3D technique to finally match the complete volume.

Horizon revision in Landmark was realized to smooth the zig-zag effect delineated by Kingdom Suite during horizon interpretation. We reinterpret critical seismic horizons

through the establishment of a signal tracking feature in the already picked amplitude value within the reflector (see Fig. 3.12). Then, this signal tracking feature or seed was propagated through the 3D volume by the software through a small voxel track designed for the same value and character of the amplitude in the studied horizon; in intense reflections, propagation reach wider areas. Where the extrapolation was not sufficient, conventional 2D picking was accomplished. Horizon seed picking was also conducted to create intermediate horizons within the Post-PS package in locally constrained areas with 3D techniques. We set a seed in a key point of each intermediate horizon top and software algorithms propagated this seed in small frames we selected.

The density of interpreted dataset favoured the creation of reliable 3D surfaces from the picked horizons in the different seismic sections. Surfaces gridding consists in the interpolation of all the horizon points along the complete cube. The nearest neighbour algorithm in the Kingdom Suite was mostly used to fill the voids between profiles and also to interpolate the horizon position in problematic areas. This method was chosen because it employs triangulation as a gridding technique in areas with high density in discrete points without extrapolation where there are no sample data. This algorithm provides a smoother approximation of the underlying function so the final image is more realistic, in comparison to the, *e.g.*, flex gridding or kriging interpolations. As a difference with other algorithms the gridding remained within the data coverage.

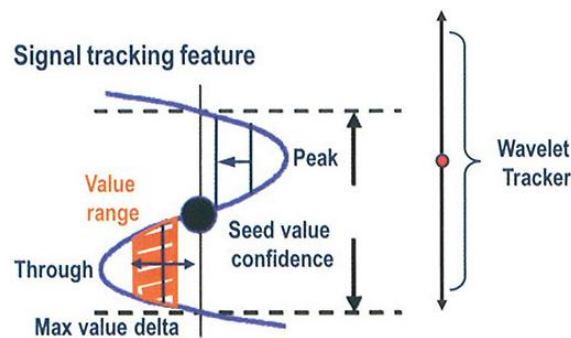


Figure 3.12: Scheme of signal feature tracking.

Gridded was also completed and revised in Landmark. This task was conducted through a dense network formed by horizons picked in Kingdom Suite and in Landmark. The preferred gridding algorithms were nearest and natural neighbour. Surfer was also employed to smooth these surfaces. Contouring was finally conducted with Kingdom Suite and Surfer to build up the different structural maps shown in this thesis.

The careful inspection of seismic horizons has shed light on the occurrence of faults and mud structures. Marked disruption and displacement of packages of reflectors have been used to evaluate faults through a lowly spaced cross-cutting correlation. Both vertical and horizontal correlation was done in Kingdom Suite along 10 seismic sections. The recognition of faults along the seismic volume is completed through the combination of the previously described workflow and the analysis of some key seismic attributes in Landmark (see *ap.* 4.3.3). Contouring of fault surfaces was also accomplished to characterize fracture geometries and cross-cutting relationship between faults.

The analysis of the shale structures was more difficult. The conducted seismic interpretation requires a separate description because it also requires an inspection of the seismic attributes (see *ap.* 4.3.4).

The detailed study of some seismic bodies has been conducted every 5-to-10 lines both in Landmark and Petrel, using conventional interpretation tools and also different seismic attributes analysis.

In this study, it has been also calculated the total vertical thickness (TVT) and the total stratigraphical thickness (TST) of different seismic units and packages. We used specific algorithms contained in Petrel. TVT is obtained from the depth difference between two surfaces, whereas TST represents the accepted geological thickness of each formation. In the TST, the thickness is measured perpendicularly from the upper surface to the lower surface. It has not been accomplished any decompaction study, and in consequence, any of the TVT or TST maps that are included in this thesis should be considered as minimum values for the original thickness of the unit during its deposition (*e.g.*, Allen and Allen, 2005).

3.3.3. Seismic Attributes

A seismic attribute is a quantitative measure of a seismic characteristic of interest and the analysis is developed since 1930s (Chopra and Marfurt, 2005). Seismic attributes make seismic reflection data to resemble surface geology and make easier the visualization of structural complexities. Attributes extraction transforms the seismic slice into an image that fosters geological intuition by relating stratigraphical or geophysical information to its structural context (Nissen *et al.*, 1999; Barnes *et al.*, 2011). The original seismic data are often treated like a stratigraphic attribute but there are more than 50 distinct seismic attributes that can be calculated. Stratigraphic and geophysical attributes are very common, such as reflection strength, impedance, and spectral decomposition attributes. Structural attributes include discontinuity or coherence or semblance, dip, azimuth, curvature, seismic shaded relief, and relative amplitude change (*e.g.*, Fig. 3.13).

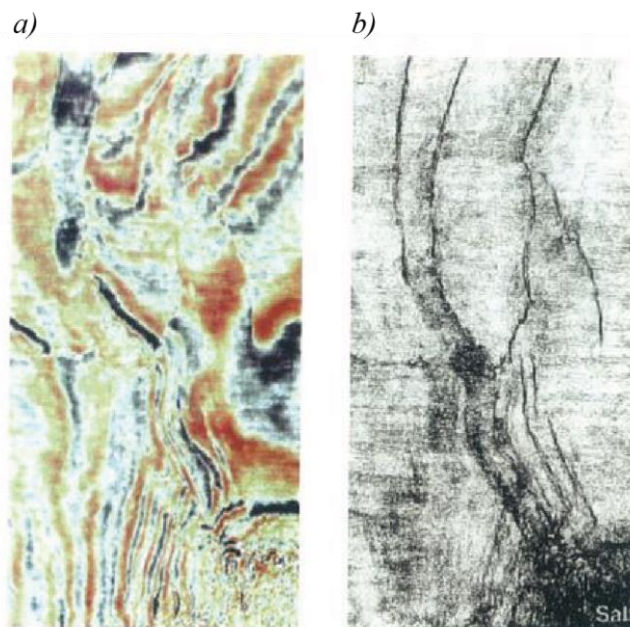


Figure 3.13: Comparison between (a) seismic reflection data and (b) coherence display in a time slice (Herron, 2011).

Seismic attributes are directly extracted from single reflections (Dalley *et al.*, 1989) and also from intervals of reflections (Sonneland *et al.*, 1989). Interval attributes are

usually referred as volume attributes and exhibit characteristics not easily observed on the vertical and horizontal seismic sections. The areal variation in reflection characteristics are usually related to paleogeographic elements while the amplitude extractions of single seismic reflections revealed features directly related to stratigraphic events (*Fig. 3.14*) (Brown and Robertson, 1985; Brown, 1986; Thadani *et al.*, 1987; Chopra and Marfurt, 2005).

In this thesis, we have focused our attributes analysis on the complete identification of fault structures and mud diapirs (see *ap. 4.3.4*), as well as on the accurate reconstruction of mass-transport complexes (MTCs) in the youngest sedimentary sequences. Semblance, dip and edge mapping shows, for example, the orientation of faults (Chopra, 2001).

Seismic signature of MTCs corresponds to disaggregated facies sited between tabular layers. These bodies have been studied in detail by combining two methodologies: amplitude analysis and attribute extraction in surfaces and volumes (Posamentier *et al.*, 2007). We extracted windowed root mean square (RMS) attributes from the selected packages. Their bounding, upper and lower (basal or shear), surfaces have been studied analysing their seismic amplitude and dip magnitude (*e.g.*, Weimer and Shipp, 2004). To better characterize their internal fabric, it has been used volume-based attribute mapping, such as edge detection and semblance analyses.

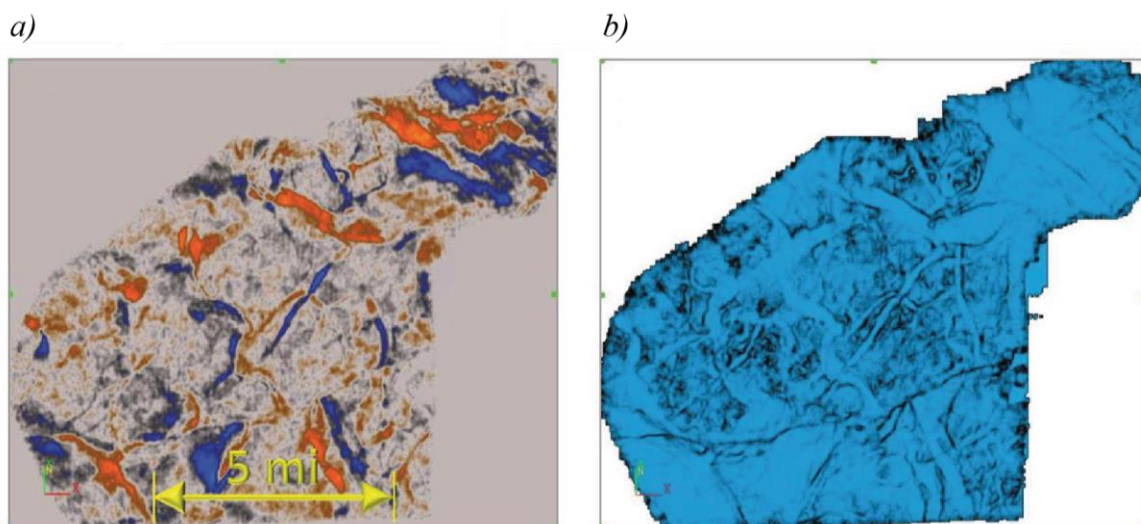


*Figure 3.14: a) Original seismic data in a time slice section that highlights fluvial channels. b) Discontinuity computed with nine traces in a window of length eleven samples along the time slice shown in (a). Data from southern Louisiana from Barnes *et al.* (2011).*

3.3.4. Mud-diapir Signal

Salt diapirs are well-known structures described in many geological settings (*e.g.*, Hudec and Jackson, 2007), whereas mud diapirs are exclusively found in basins with thick sedimentary accumulations (*Fig. 3.15*). This type of diapirs is well known from the Caspian Sea (*e.g.*, Hovland *et al.*, 1997), the Barbados accretionary wedge (Brown and Westbrook, 1988), the Niger delta (Cohen and McClay, 1996), the Gulf of Mexico (Bruce, 1973), and the Alboran Sea (Jurado and Comas, 1992; Talukder *et al.*, 2003). Proper interpretation of mud diapirism needs a correct understanding of the triggering factors. Some authors have used the concept of shale tectonics to encompass the different processes and mechanisms controlling shale and mud mobilization in the subsurface (*e.g.*,

Wu and Bally, 2000; Camerlo *et al.*, 2004; Soto *et al.*, 2010). This is a term equivalent to salt tectonics (*e.g.*, Jackson and Talbot, 1991).

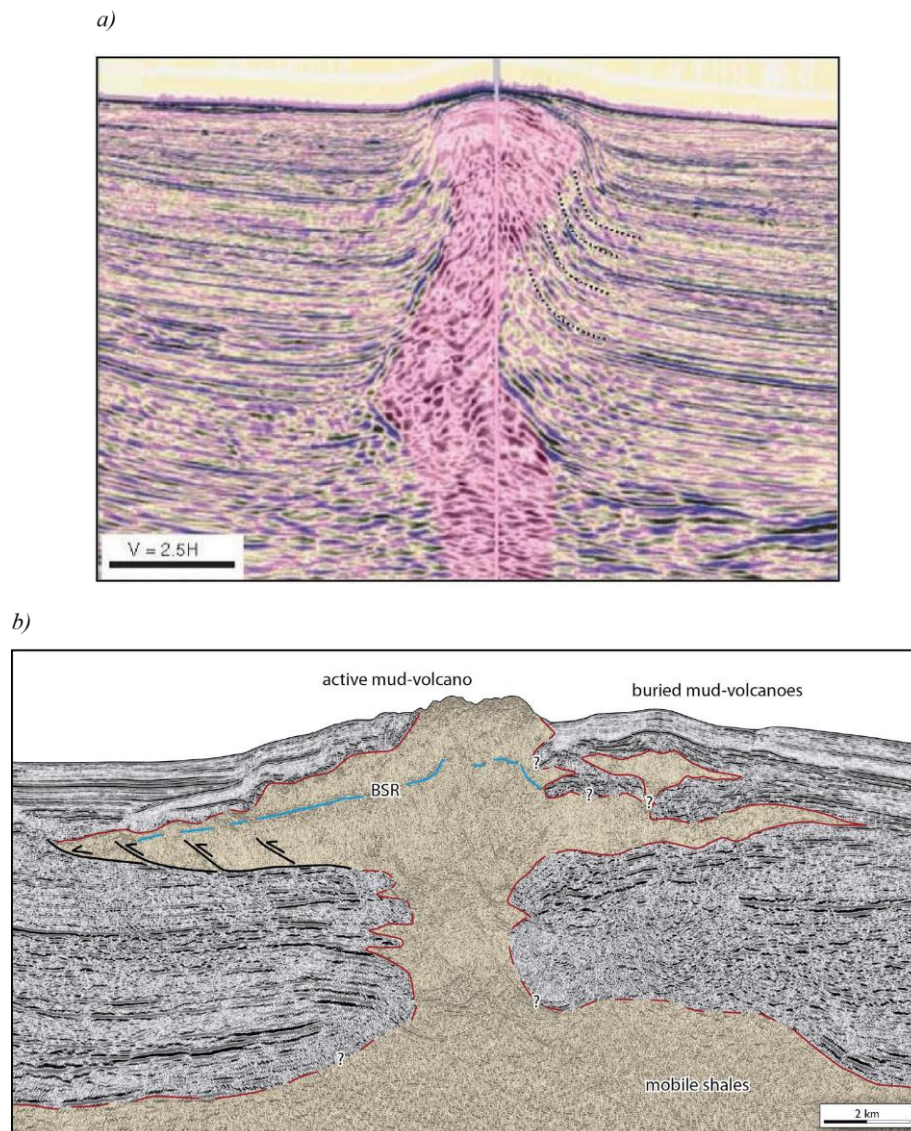


Figure 3.15: a) Seismic image of a salt diapir (coloured in pink) in Gulf of Mexico taken from Stewart (2006). Rise of plastic material causes seafloor convex topography and sinks the adjacent sediments. b) Example of a *Christmas tree* mud diapir that includes some active and buried mud volcanoes. Notice a bottom simulating reflector (BSR), as an artefact that copies the seafloor. Source: Soto *et al.* (2014), data courtesy of REPSOL.

Homogeneity and low strength values favour salt to remain weak and, therefore, potentially mobile throughout the entire history of diapirism. However, mobilization of mud structures depends on shale characteristics, such as clay composition, density, fluid content and plasticity (Murton and Biggs, 2003; Mondol *et al.*, 2008). Singularity of mud diapirs also lies on the variation of all these parameters during diagenesis and burial, which accompanied by tectonic deformation, could promote variability of mobilization processes through time. Thus, mud diapirs may depict variable geometries and may even penetrate the adjacent sediments sketching “*Christmas-tree*” structures, which are exclusive for mud diapirs (Fig. 3.15b).

Seismic expression of shale diapirs shows a response that differs from salt diapirs

(Table 3.3) (Morley and Guerin, 1996; Soto *et al.*, 2014). Main effect of overpressured shale diapirs on the seismic image is the reduction of the seismic velocities and the loss of seismic resolution (*e.g.*, Graue, 2000; Day-Stirrat *et al.*, 2010; Eislely and Tieman, 2010). The escape of fluids also tends to distort the seismic signal of the mud diapir and neighbouring rocks (Fig. 3.16). Mud diapirs are characterized by internal chaotic seismic facies constrained by feeble limits, with the lack of a mud carapace usually present in salt diapirs (Fig. 3.15a). Conventional interpretations sketch diapir boundaries where adjacent layering terminates against the chaotic mass, although some layered packages of the country rock are occasionally integrated, with amplitudes loss. Common lateral seepages of fluidized mud usually occur (*e.g.*, in *Christmas-tree* structures), which are not observed in salt structures, and usually obstruct the illumination of underlying sediments (Fig. 3.15b). Their base is rarely observed and the common pull-up effect developed beneath salt bodies is absent in mud diapirs. Frequently, mud depleted chimneys are erroneously interpreted as faults but the absence of displacement usually depict the existence of a shale weld. Mud accumulations generally develop mud volcanoes, which can be seen on the surface or even buried (Fig. 3.15b).

Tipo de Observación	Descripción
Carácter de la cima	No se observa una reflexión continua de fuerte amplitud (<i>e.g.</i> , Fig. 3).
Carácter de los límites laterales	Es frecuente que las reflexiones de los sedimentos circundantes se adentren (perdiendo continuidad) en el diapiro (<i>e.g.</i> , Figs. 1 y 3).
Geometría de los límites laterales	Es común que haya superposiciones múltiples de láminas o lentes del diapiro en los sedimentos circundantes. Normalmente con contactos concordantes entre ellos (<i>e.g.</i> , Fig. 1).
Facies sísmica	Caótica con algunas reflexiones aisladas de baja continuidad y reflectividad, que pueden disponerse según la orientación de la fábrica de los sedimentos circundantes (<i>e.g.</i> , Fig. 2). En ocasiones se pueden encontrar difracciones laterales o generadas fuera de la sección sísmica.
Estructuras definitorias	“ <i>Christmas trees</i> ” (<i>e.g.</i> , Fig. 1), diatremas (conductos subverticales con gran desarrollo vertical y con una sección pequeña de tipo elíptico o circular).
Estructuras no definitorias	Volcanes de lodo (<i>e.g.</i> , Fig. 1) y estructuras debidas al escape de fluidos (“ <i>mud pipes</i> ”, “ <i>pockmarks</i> ”, “ <i>gas chimneys</i> ”, etc.). Aunque muchas veces acompañan a los diapiros de arcilla, también se encuentran en campos con diapiros de sal.
Otras observaciones en las sucesiones infrayacentes	Pérdida de reflectividad y ausencia de efectos de tipo “ <i>pull-up</i> ”

Table 3.3: Chart to explain the characteristics of the seismic signal of mud diapirs taken from Soto *et al.* (2014).

During interpretation procedures it is important to consider that the intrinsic complexities for the interpretation of shale diapirs could be enhanced by the use of inaccurate seismic velocities. Complexities are also enhanced by variable shale characteristics. Seismic attributes analysis of diapiric bodies is usually needed to facilitate interpretation. Attributes exhibit characteristics that are not easily observed on the vertical and horizontal seismic sections. Semblance or coherence volumes and other structural attributes are useful to map multiple lateral extrusions, sub-vertical segments that obstruct the seismic illumination below the diapiric body, and structures due to fluid escapes that

distort the seismic image also.

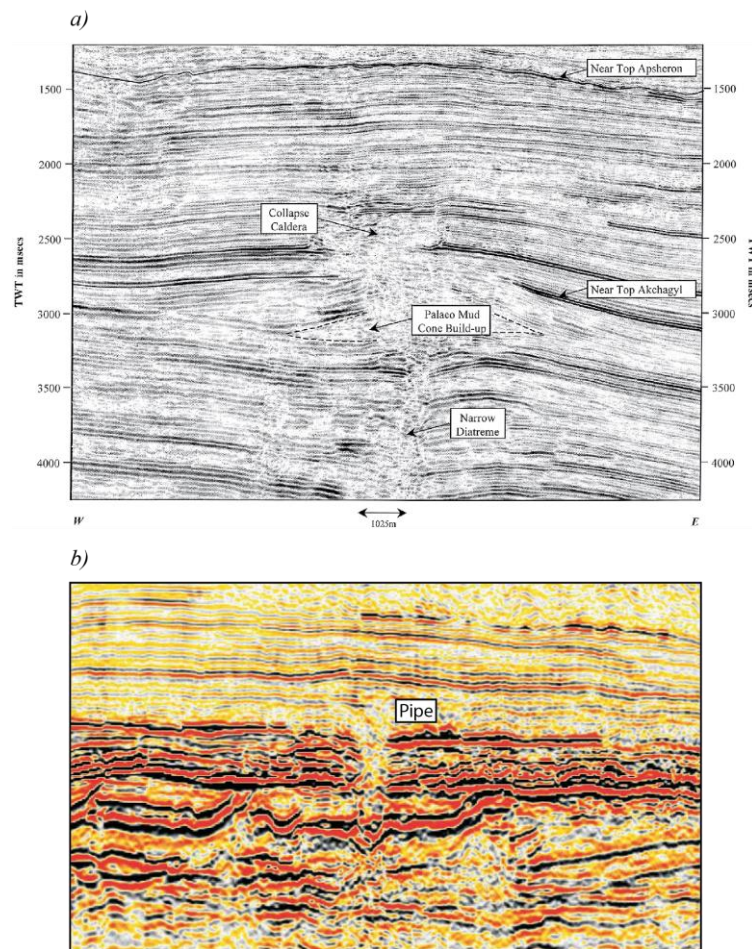


Figure 3.16: a) Seismic buried mud volcano in the crest of an anticline in offshore Azerbaijan. Notice the underlying small diameter diatreme through which fluidized muds flowed to the paleo-seabed taken from (Fowler *et al.*, 2000). b) Pipe formed due to evaporate dissolution over collapsed cavities in the Eastern Mediterranean (Cartwright, 2007).

3.3.5. Reconstruction of Mud Diapirs

Our interpretation of mud diapir geometries in the studied KAD fold follows a conventional methodology collected from different displays. We have delineated two mud diapirs through a detailed inspection of the seismic amplitudes accomplished by attribute extraction. Study is conducted to locate diapir limits where irregular seismic chaotic attitude departs from nearby and organized beds without any displacement. We committed a specially detailed analysis to infer feeding channel mud fingering, fluid escapes and extrusion features, such as mud volcanoes. Internal seismic reflections usually present low-to-intermediate amplitude values contained in small wavy features, and occasionally accompanied by remnant reflections from adjacent sediments with less reflectivity. The basal boundary is usually characterized by the physical and marked intersection between surrounding layers, as a result of a depleted and extinguished mud channel usually described as a shale weld. Occasionally, the roof of the diapir is hardly depicted due to the abundance of fluids that deforms the overlying Post-PS sediments that even pierce the seafloor as local gas seepages but any active mud volcanoes is distinguished.

Initial interpretation of diapirs was realized in Kingdom Suite, following a slightly

coincident workflow as for faults. Preliminary methodology was based on the recognition of structural boundaries by means of crossing ILs and XLs to laterally extend these borders. However, due to software limitations, we could not generate diapir surfaces because algorithms do not allow the junction of points with the same X value. To surpass this problem, the complex boundaries of the mud diapirs have been split into different surfaces that never have overhangs or points with two depths (e.g., Fig. 3.17).

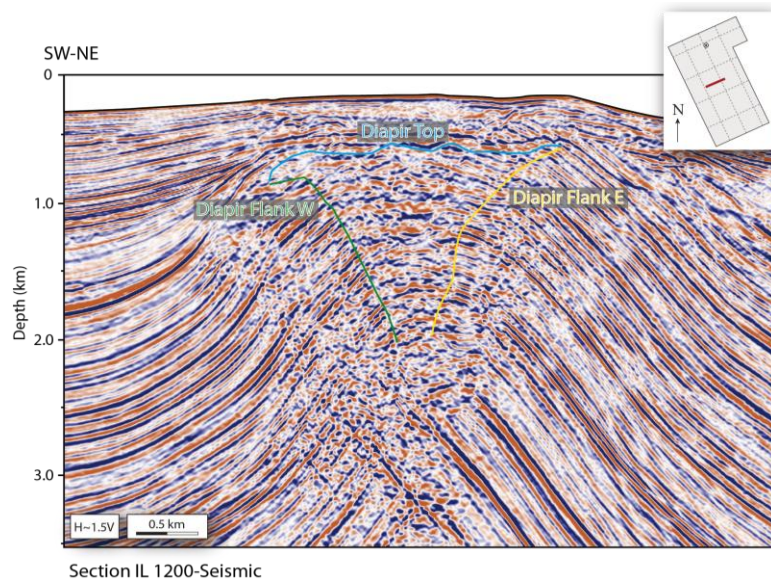


Figure 3.17: 2D image of a mud diapir picked in the IL 1200 in Kingdom Suite. We used up to 3 surfaces to delimitate diapir margins. For reference, the inset map shows the position of the section in the Permit as a red-coloured line. The location of the AD-1X well is also illustrated dash and grey-coloured lines correspond to SW-NE ILs (500, 1000, 1500 and 2000) and NW-SE XLs (1000, 1500 and 2000).

The final interpretation of the diapirs geometry was conducted in three dimensions with the Landmark Geobody module. Picking of diapir limits resulted in complex shapes like the 3D bulb illustrated in Figure 3.18.

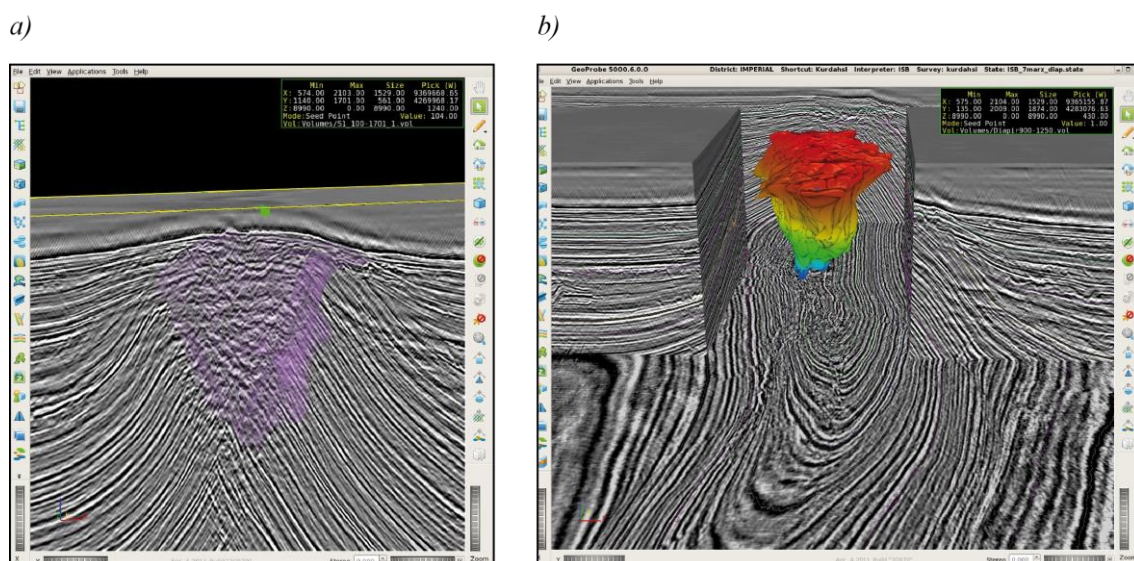


Figure 3.18: Screenshots from Landmark showing: a) delineation of a shale diapir in a seismic section generated from a seed point in Landmark and b) the final three-dimensional geobody. Geobody is coloured according to depth intervals (increasing depths from red to blue).

To delineate diapir geobody we extracted several attributes along the seismic cube, focused on the pierced area. Semblance or coherence volumes were the main useful tools for our purposes as these attributes emphasize stratal discontinuities in mud diapir system and traces similarity, ideal for the correct establishment of the diapir terminations. Other relevant structural attributes were studied with the dip/structure cube tool, which approximates covariance discontinuity to detect abrupt lateral changes in seismic character caused by diapirs and faults, by the recognition of traces with the same shape though their magnitudes may differ (*Fig. 3.19a*). Dip and azimuth maps established the correct orientation of the structure. Extraction of dip magnitude attributes was useful to define shale welds, as it is illustrated in *Figure 3.19b*. Some difficulties took place where structure limits coexisted with faults, making impossible the correct recognition of the discontinuity origin. Other volume attributes, such as dip-edge variation, or RMS were also obtained but without satisfactory results. Nor salt tool in Landmark was useful.

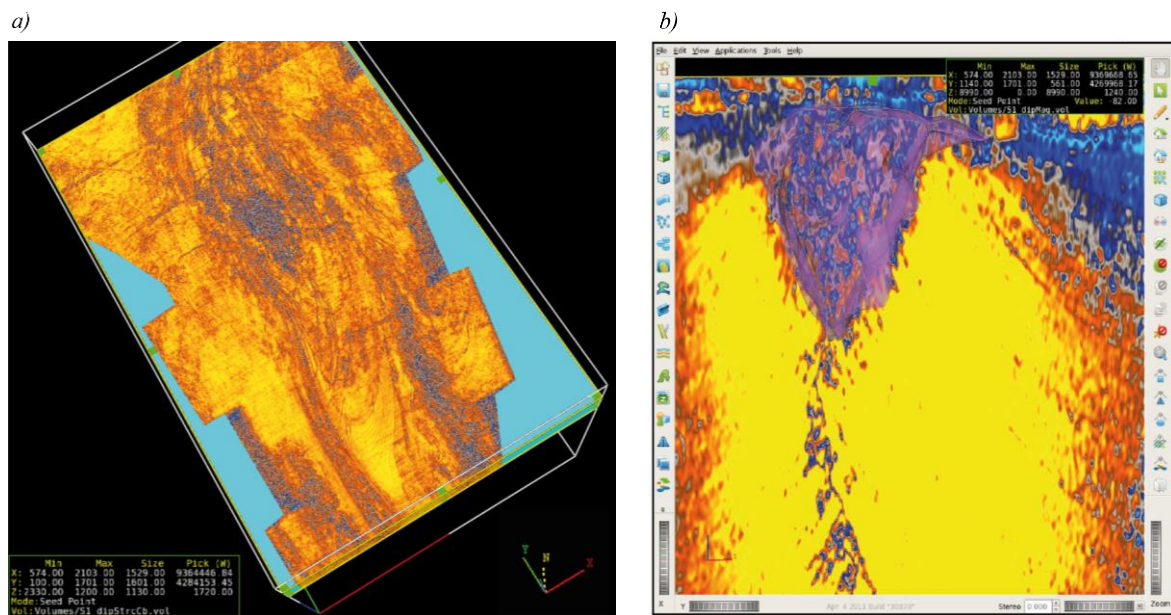


Figure 3.19: Screenshots from Landmark to illustrate some of the key attributes used to depict shale bodies in the KAD: (a) the dip-structure cube attribute and (b) the dip-magnitude module seen in a selected IL section.

4. WELL DATA AND SEISMIC UNITS

4.1. The Araz Deniz Well

A unique well has been analysed for this thesis: the Araz Deniz 1X well (AD-1X). The exploratory AD-1X was drilled for the oil and gas exploration program in the Kurdashi Permit from April to June 2000. The well is sited in the North of the study KAD area, sited in the intersection between the In-line (IL) 1940 and the cross-line (XL) 1540 of the 3D seismic survey (*Fig. 4.1*). The well lies on the southwestern sector of the Araz Deniz or Northern Culmination at about 1 km to the West of the crestal line. Geographic coordinates of the surface location corresponds to $38^{\circ} 49.8' \text{ N} - 49^{\circ} 23.15' \text{ E}$ and bottom hole location is $38^{\circ} 49.35' \text{ N} - 49^{\circ} 23.23' \text{ E}$.

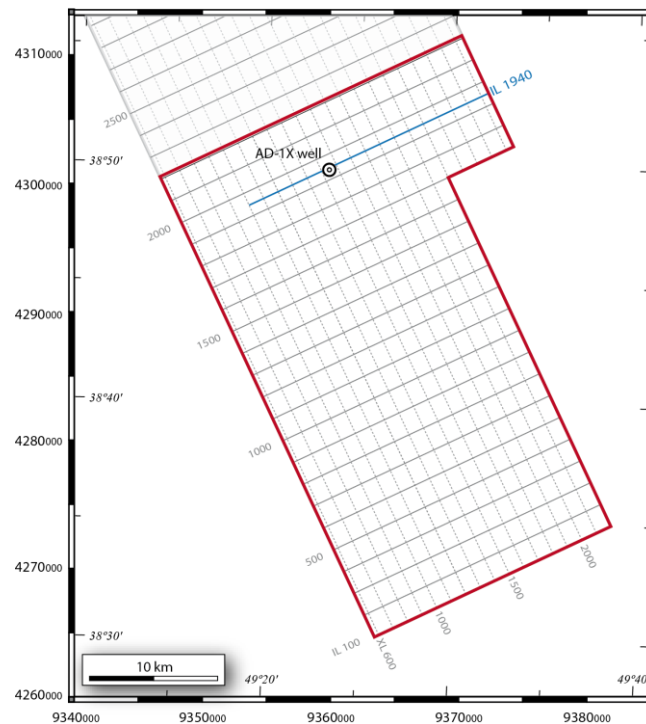


Figure 4.1: Seismic survey of the KAD area. Blue-coloured line corresponds to the IL 1940, which runs through the AD-1X well.

The AD-1X is a deviated vertical well which drilling end is sited at 4225 m depth. This

depth corresponds to the final total depth measured from the rotary table Kelly Bushing (KB; *i.e.*, MDRT or MDRKB), which was elevated 22.6 m above the sea level (*Fig. 4.2*). The sea level is located at 103.4 m above the seafloor. If measurements are calculated along vertical planes, the final depth of the well corresponds therefore to 4216 m TVD (measured in total vertical depth) and 4193.4 m TVDSSL (measured from the seafloor). The well is slightly deviated from the vertical over 11 m toward the North and 126 m toward the East, with a maximum inclination of 10°, and the final azimuth was 83.82°N (see *Fig. 4.2*).

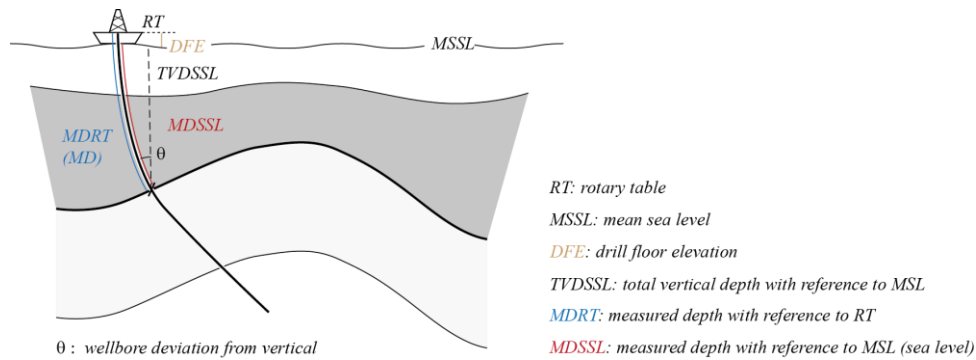


Figure 4.2: Scheme of a deviated well that includes different well measures. Depth measurements along deviated wells are referred as measured depths (MD).

Well drillings extract lithological and chronostratigraphic data and valuable geophysical information that allow us to tie seismic interpretation with precise age determination and to correlate seismic facies with lithofacies. Most of the common types of logging are listed in *Table 4.1*. Well log data are especially useful when performing time-depth conversion which can be used to correct the position of the main seismic reflectors and improve seismic interpretation (*e.g.*, Asquith *et al.*, 2004; Hölt *et al.*, 2011).

Groups	Type of log	Main measured property	Objective	Units
ACOUSTIC	Sonic	Velocity of seismic waves	Porosity, fractures, lithological contacts	ms/m
ELECTRICAL	LL	Resistivity of rocks and conductivity of WF	Lithological contacts, permeability	ohm/m
	Short normal, large normal	Real resistivity and conductivity of WF	Lithological contacts, permeability, thin layers	ohm/m
	SP	Difference of potential between shales and sands and conductivity of WF	Water and salt content, permeability	mV
GEOCHEMICAL	FLO	Velocity of the flow of water	Direction of water flow	-
	Salinity	Conductivity and resistivity of rocks and of WF	Identification of fluids	S/m
	T	Temperature of fluids	Fluid gradient, identification of aquifers, density	-

Table 4.1: Summary chart of the most common types of logs, accompanied by the main measured property and objectives. Abbreviations: caliper (CAL), flowmeter (FLO), gamma-gamma (γ - γ), gamma-ray (GR), laterolog (LL), neutron (N), nuclear magnetic resonance (NMR), spontaneous potential (SP), temperature (T), and water formation (WF). *Continuation in the next page.*

Groups	Type of log	Main measured property	Objective	Units
GEOMETRICAL	CAL	Diameter of the borehole	Ripability, fractures	cm
	Well Deviation	Direction and inclination of the well	Spatial position of the well	-
	Dipmeter	Strike and dip of the rock layers	Spatial position of the rock layers	-
MAGNETIC	NMR	Polarization of hydrogen particles	Porosity, permeability	T/(A/m)
RADIOACTIVE	GR	Natural radioactivity	Shales and organic materia, lithological contacts	API
	γ - γ	Density	Fractures, and density	g/cm ³
	N	Porosity	Porosity (alteration), gas-oil contact	-

Table 4.1: Continuation.

Drilling operations in the AD-1X well consisted in the integration of LWD/MWD (logging-while-drilling and measurements-while-drilling, respectively) and wireline logging with a total combination that is described in detail in Table 4.2. The wireline logs were performed by the Schlumberger Company.

Depth interval (m MDRT)	Logging tools	Logging data
140-4200	VSP-Checkshot	C1, C2, DT, GR, NPHI, RHOB
246-1119	BGT-GR	C1, C2, CRB, DEVI, DT, GR, HAZI, NPHI, RHOB
1214-1962	BGT-GR-DSI	BS, C1, C2, CRB, DEVI, DSI, DT, DT, DT, GR, HAZI, NPHI, PSR, RHOB
1956-2680	BGT-GR-AMS	C1, C2, DRHO, DT, DT, DT, GR, NPHI, RHOB, TNPHO
1956-4233	LDL-CNL-GR-AIT-DSI	AT _n , BS, C1, C2, DSI, DT, DT, DT, GR, NPHI, RHOB
2009-2657	RFT-HP-GR	C1, C2, DT, GR, NPHI, RHOB
2590-3443	CBL-VDL-CCL-GR	C1, C2, DT, GR, NPHI, RHOB
2670-3440; 3515-4162	MDT-GR	C1, C2, DRHO, DT, GR, NPHI, RHOB, TNPHO

Table 4.2: Summary chart of the wireline logging operations realized along the AD-1X well. Depth ranges are measured from the rotary table (MDRT), with maximum reached at 4233 m, whereas the end of the driller procedures was 4225 m. Logging tools abbreviations (1): array induction imager tool (AIT), auxiliary measurement sonde (AMS), borehole geometry tool (BGT), cement bond log amplitude (CBL), casing collar locator (CCL), compensated neutron log (CNL), digitizer sample interval (DSI), gamma-ray (GR), high pressure elemental capture spectroscopy sonde (HP or ECS-HP), litho-density log (LDL), mud delta-T (MDT), repeat formation tester (RFT), variable density log (VDL), vertical seismic profile (VSP). Logging data abbreviations (2): resistivity (AT_n), bit size (BS), caliper 1 (C1), caliper 2 (C2), calibrated relative bearing (CRB), deviation (DEVI), bulk density correction (DRHO), digitizer sample interval (DSI), delta-T (DT), delta-T compressional (DTCO), delta-T shear (DTSM), gamma-ray (GR), hole azimuth (HAZI), thermal neutron porosity (radio method) (NPHI), uncorrected phase shift resistivity (PSR), bulk density (RHOB), thermal neutron porosity (TNPHO). Mnemonics correspond to the Schlumberger codes.

4.2. Borehole Stratigraphy

The study of the stratigraphy in the KAD area is mainly based on well logs correlations

accompanied by cuttings, as well as biostratigraphic data. Drilling procedures in the AD-1X well were committed to identify the tops of individual units within the PS (both Lower PS and Upper PS) and the Post-PS sequences. The end of the well is located within the NKG Unit, which is the top of the Lower PS, whereas the PS-bottom is not achieved by the well and lies below 4.225 km of depth (MD in *Figure 4.2*).

The AD-1X well penetrated up to 22 regional seismic horizons. Key formation tops used in this thesis are 15, which are mostly summarized in *Table 4.3*. They represent the upper and intermediate boundaries of 8 different units detectable on a seismic scale: Lower PS, Pereryva (Per), Balakhany (Bk), Sabunchi (Sab) and Surakhany (Sk) in the Upper PS, Akchagyl (Ak), Apsheron (Ap) and Gelasian in the Post-PS. The NKG top crowns the Lower PS, whereas the upper limits of the different Upper PS sequences are represented by particular horizons: the Pereryva-Old (also referred as XX surface), the Balakhany-Upper, the Sabunchi (originally recognized as Horizon XIII), and the PS-top for the Surakhany Unit. We have also detailed some internal horizons, such as the Pereryva-New, the Balakhany-Lower, and, within the Surakhany Formation, the horizons Sk XII (or Sk 12), Sk IX (or Sk 9), Sk VI (or Sk 6) and Sk II (or Sk 2). Intermediate horizons and formation tops let us to divide the studied sequences into 14 subunits, partly described in *Table 4.3*, and completely presented in *Figure 4.3*. They are named homonymously to their tops, except the subunits Lower PS, Sk I (Sk 1, Upper PS), and Gelasian (Post-PS).

Sedimentary sequences	Horizon tops	MDRT (m)	MDSSL (m)	TVDSSL (m)	Thickness (m)
Post-PS	Seafloor	126	103.4	103.4	254
	Apsheron	380	357.3	357.4	477.3
	Akchagyl	858	835.4	834.7	153
Upper-PS	Surakhany (H. II)	1093	1070.4	1069.7	150
	Surakhany (H. VI)	1561	1538.4	1537.7	87.9
	Surakhany (H. IX)	1822	1799.4	1798.6	49
	Surakhany (H. XII)	2215	2192.4	2191.6	155
	Sabunchi (H. XIII)	2370	2347.4	2346.6	229.9
	Balakhany Upper	2958	2935.4	2934.2	379.2
	Balakhany Lower	3338	3315.4	3313.4	519.4
Pereryva (H. XX)	3860	3837.4	3832.6	324.1	
Lower-PS	NKG	4188	4165.4	4156.9	-

Table 4.3: Depth estimations in meters of most of the geological formations tops studied in this thesis and penetrated by the AD-1X well, according to cuttings and data logs. Measures are realized along the deviated well (MD) and the vertical plane (TVD), expressed from the rotary table (RT) and from the seafloor (SSL) (*Fig. 4.2*). Thickness of formations is measured in TVD, and it is apparent due to the strong dip of the units and the draft of the well at the bottom. Abbreviations: horizon (H), Productive Series (PS).

The aim of the exploration well was to prospect the Upper PS, both Balakhany (horizons XVIII-XIX) and Pereryva (Horizon XX) formations. Secondary targets were the Surakhany Unit (horizons I-XII or 1-12, but especially VI-VII, or 6-7), Sabunchi Unit (horizons XIII to XV) and horizons XVI-XVII within Balakhany Unit.

As it is observed from the seismic record of *Figure 4.3*, the well was drilled in a collapsed area. In the borehole, the PS units lie between ~1.0 km and 4.23 km of depth,

and the Post-PS start at 126 m depth and terminate at <1.0 km depth, with thickness that ranges between >3.23 km in the PS and <1.0 km in the Post-PS. Values of GR oscillate around 50-130 gAPI in both packages along the complete record, whereas resistivity logs start at 1.9 km depth and show that ATR is generally 0.5 ohm·m, except in the uppermost Post-PS that grows up to 3.0 ohm·m.

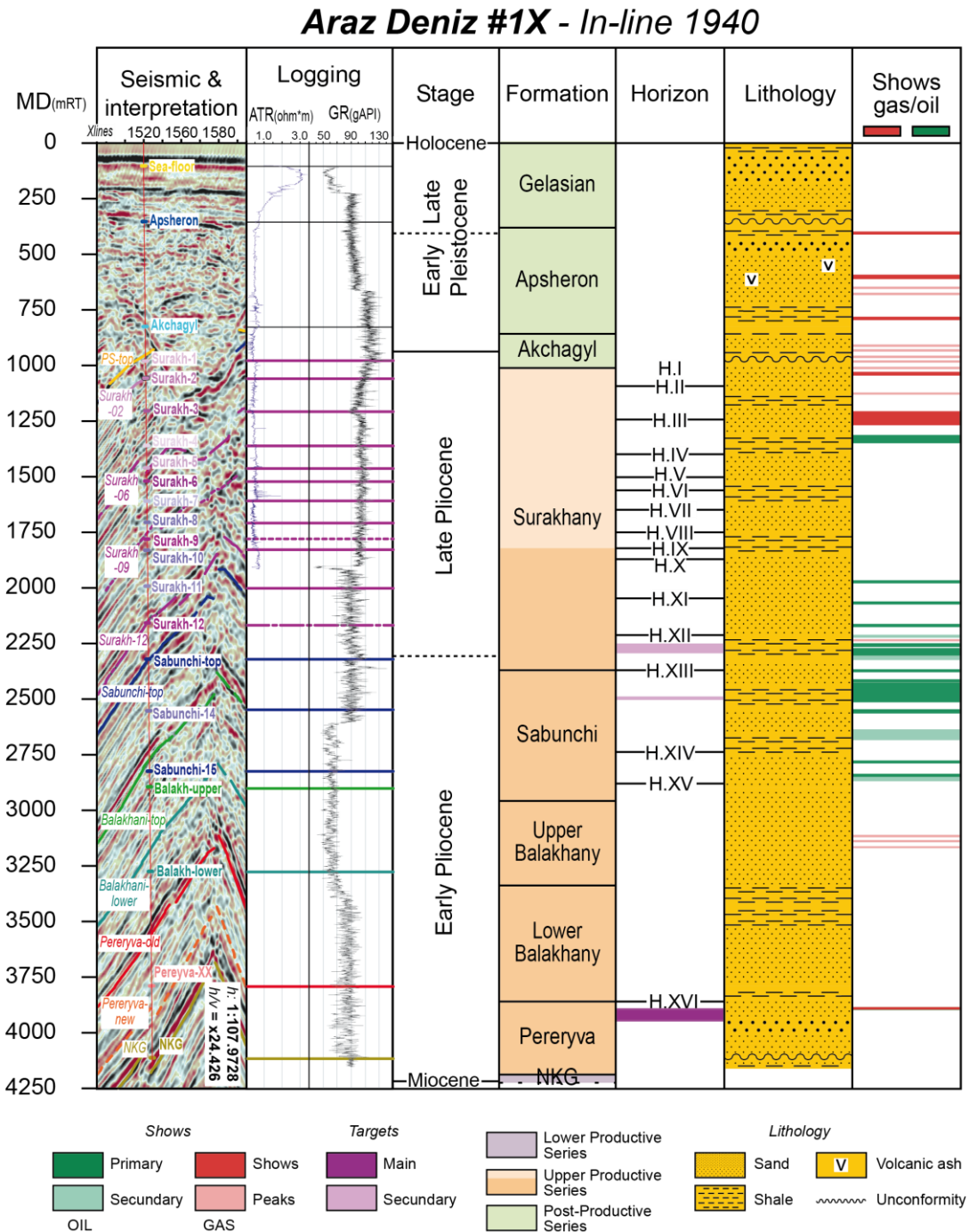


Figure 4.3: Borehole seismic image and stratigraphy in the AD-1X well in IL 1940 accompanied by GR and ATR logs, lithology and shows of oil and gas for each formation. Geological stages are taken from Gradstein et al. (2012).

In the borehole, only the upper boundary of the Lower PS sited in the top of the NKG Unit (Late Miocene) is clearly recognized from cuttings at ~4.2 km depth (cf., Table 4.3

and *Fig. 4.3*). GR logs in the Lower PS register a sharp change from marked 90 gAPI to 70-110 gAPI upwards. Any resistivity logs reach so deep levels.

Above the NKG horizon, it is identified the thick sequence of the Upper PS (from the Pereryva Unit to the Surakhany Unit) (*Fig. 4.3*). The lowermost Pereryva XX or Pereryva-Old top is located at 3.86 km depth. The Pereryva Unit (Early Pliocene) is 325 m-thick and is characterized by a relatively a constant GR window of 60-110 gAPI (*cf. Table 4.3*). The Pereryva Formation represents a low velocity sandy package with an overall fining upward trend characterized by a blocky SP/GR shape at the base and finally into a shaly interval at the top. This vertical stacking pattern can be interpreted with an overall transgressive trend starting with fluvial deposits and finally evolving to marine sandstones and shales.

Interpreted top of the overlying 900 m-thick Balakhany Unit (Early Pliocene), the Balakhany-Upper horizon, is sited at 2.96 km depth, whereas the intermediated top of the Balakhany-Lower subsequence was cut at 3.34 km depth (see *Table 4.1* and *Fig. 4.3*). Most of the Balakhany sediments express 50-70 gAPI, although they become up to 70-100 gAPI in the base of the Balakhany-Lower subunit. The stratigraphy of the Balakhany Formation is similar to the Pereryva package, characterized by a lower section with sandy layers and a mud-prone upper part. Facies change is interpreted as a result of a transition between fluvial and marine conditions. Near the Balakhany top, the depositional unit is overlaid by a shaly package of low velocity that corresponds to a maximum flooding event.

Three horizons of the Sabunchi Unit (Early Pliocene) are cut in *Figure 4.3*, but they do not appear in the *Table 4.3*. They correspond to horizons XV, XIV and XIII, respectively from the bottom to the top. The Sabunchi stratum is ~590 m-thick and its top lies at 2.37 km depth, coincident with the Horizon XIII (referred as Sabunchi top) described in *Table 4.3*. The base has similar results of GR as the underlying unit (50-70 gAPI), but they noticeably increases towards the top, in the proximities as the Horizon XIV, as much as 70-110 or >110 gAPI. In the Sabunchi Unit a fining upward vertical trend is detected as a result of an overall transgressive pattern. The uppermost section coincides with a remarkable shaly interval (both traceable on logs and seismic) located on the top of a low-velocity shaly package. The well-delineated interval is interpreted as marine in origin and associated with a maximum flooding surface occurring at the end of the overall transgression. The flooding event corresponds to the maximum concentration of shales detectable on logs and should represent the top of the Sabunchi Formation.

The Surakhany Formation (Early to Late Pliocene) is over 1.37 km-thick and is contained between 1 km and 2.37 km depth (*Fig. 4.3*). GR values are comprised between 70 gAPI and 110 gAPI for the lowermost Sk 12 and part of the Sk 11 units. The trend sharply decays to 40 gAPI in the middle of the Sk 10 Unit and suddenly recovers to a constant tendency of 90-120 gAPI until the overlying Sk 3 Unit, followed by a down-break in the Sk 3 top. The uppermost subunits slightly rise to maximum ranges of 110 gAPI to >130 gAPI. Logs of resistivity also crosscut the Surakhany Formation from the Sk 10 subunit, which is characterized by 1.0 ohm·m. Mean ATR values are 0.7 ohm·m but, 0.5 ohm·m are also registered. Surakhany sequences are characterized by vertically stacked fining upward. This trend is remarkable in the lowermost sequence. This lower section is characterized by a strong facies variation in a package of shales where the acoustic response changes from low frequency and medium amplitudes below. This facies variation is evidenced by the gradual decrease of the silty-sandy intervals southwards, followed by a concentration in the uppermost section. Upper sequences show abundant onlap terminations.

Above the Sk 1 top, which coincides with the top of the PS (PS-top), it is observed the

lowermost formation of the Post-PS group, which corresponds to the 150 m-thick Akchagyl Unit (Late Pliocene-Early Pleistocene) (*Table 4.1*). GR oscillates between 100 gAPI and 130 gAPI along the sequence. The upper boundary is coincident with the crosscut formation top sited at ~860 m depth, with the highest resistivity (0.8 ohm·m) in a 0.4 ohm·m sequence (*Fig. 4.3*). The Akchagyl Unit is characterized by numerous facies changes with mobilized sediments. Thin levels of shales, sandstones and volcanic ash are the most common alternation in their stratigraphy.

The ~480 m-thick Apsheron Unit (Early-to-Late Pleistocene) comprises the interval between 860-380 m of depth, detailed in both displays of *Figure 4.3* and *Table 4.1*. The Apsheron Formation is characterized by a constant resistivity (0.8 ohm·m) and two different domains of GR. In the proximities of the base, GR = 100-130 gAPI, and GR = 80-100 gAPI towards the top. Within the Apsheron Formation numerous mass deposits combined with large clinofolds coming from the continent are identified. Grey clays and ash deposits are abundant.

The Present-day seafloor lies at 126 m below sealevel on the top of the youngest Gelasian Unit, which presents increasing values of ATR, from 0.8 ohm·m in the contact with the underlying Apsheron top, and up to 3.0 ohm·m nearby the seafloor (*Fig. 4.3*). By the contrary, GR parameters sharply decrease in the uppermost part from maximums of 100 gAPI to minimum of 50 gAPI. Unit thickness is 250 m (*Table 4.3*). Lithology evidences gravitational deposits due to slope breaks.

4.3. Seismic Units

In this study we have analysed the seismic response of the seismic volume in order to recognize the principal reflections packages. We have grouped packages with similar seismic facies in seismic sequences, which differ from adjacent facies, such as in the configuration of the reflectors (geometry, boundary relationships) or reflectors continuity, amplitude and frequency (*e.g.*, Brown Jr. and Fisher, 1979). Sequence description highlights the geological and structural characterization and timing that helps us to recognize the regional setting and to understand sedimentary geometries, in terms of the erosion-depositional scenario, structural approaches and fluid contacts, used to define the geological significance.

4.3.1. Chrono-Stratigraphy

Age of units and tops was established by using different types of sources. As an initial base, it has been used the chronology proposed for the PS and the Post-PS units in the SCB and the surrounding regions by numerous authors (*e.g.*, Jones and Simmons, 1997; Abreu and Nummedal, 2007; Forte *et al.*, 2010). The age of the different lithostratigraphic formation tops drilled in the AD-1X well was taken from the internal and confidential well reports, which contain micropaleontological data with foraminifera, ostracods, nannofossils and palynology observations.

In this research, we have dated several internal horizons within the Pereryva (Early Pliocene), Balakhany (Early Pliocene) and Surakhany units (Early to Late Pliocene). We have also interpreted extra Akchagyl (Late Pliocene to Early Pleistocene) and Apsheron (Early to Late Pleistocene) horizons. These additional surfaces are: Pereryva-Old, Balakhany-Lower, and horizons 12, 9, 6 and 2 in the Surakhany Formation. Within the Post-PS sequences, additional horizons are Akchagyl 1 (Ak.1) and Apsheron 1 (Ap.1)

(Table 4.4). Akchagyl 1 and Apsheron 1 are also referred in this thesis as the Akchagyl and Apsheron tops of their homonymous units. Our estimations were realized in a selected section in the South of the studied survey: the IL 240. This estimate assumes the relative thickness of the studied units measured along a vertical plane in the western domain. Dating was linearly interpolated from the well-known age of the upper and lower boundaries of each formation.

We have considered the different ages established regionally for the PS and the Post-PS; e.g., 5.2 Ma for the NKG top, 4.9 Ma for the top of the Pereryva Unit, taken as the Pereryva-New horizon, 4.0 and 3.7 Ma for the top of the Balakhany and Sabunchi units, 3.1 Ma for the PS-top, 1.7 Ma for the upper boundary of the Akchagyl Unit, and 0.8 Ma for the Apsheron top (Jones and Simmons, 1997; Abreu and Nummedal, 2007; Forte *et al.*, 2015; *cf. Fig. 2.19*). The ages for the Pereryva-Old horizon and the different Balakhany subunits are extrapolated linearly using the reference ages of 4.9 and 4.0 Ma. Akchagyl 1 and Apsheron 1 are also estimated by extrapolating the well-known ages of the Akchagyl and Apsheron units (1.7 and 0.8 Ma). The extrapolated ages are shown in brackets in Table 4.4. With this approach, the Pereryva-Old horizon is 4.5 Ma, the Balakhany-Lower is 4.2 Ma and the resulting ages for horizons Sk 12, 9, 6 and 2 are 3.6, 3.5, 3.4, and 3.2 Ma. Using the same approach for the Akchagyl 1, extrapolated age corresponds to 1.6 Ma, and 0.7 Ma, for the Apsheron 1 horizon.

Sedimentary sequences	Horizon tops	Age (Ma)	Stage
Post-PS	Seafloor	0	Holocene 0.01 Ma
	Apsheron 1	[0.7]	
	Apsheron 2	0.8	Pleistocene 2.8 Ma
	Akchagyl 1	[1.6]	
	Akchagyl 2	1.7	
Upper-PS	PS-top	3.1	Late Pliocene 3.6 Ma
	Surakhany II	[3.2]	
	Surakhany VI	[3.4]	
	Surakhany IX	[3.5]	
	Surakhany XII	[3.6]	
	Sabunchi	3.7	Early Pliocene
	Balakhany-Upper	4.0	
	Balakhany-Lower	[4.2]	
	Pereryva-Old	[4.5]	
	Pereryva-New	4.9	
Lower-PS	NKG	5.2	Late Miocene 5.3 Ma
	PS-bottom	5.9	

Table 4.4: Ages of geological units estimated in this study are in brackets. Rest of the ages are taken from Jones and Simmons (1997); Abreu and Nummedal (2007); Forte *et al.* (2010). Geological time scale according to Gradstein *et al.* (2012). Akchagyl 1 and Apsheron 1 correspond to the tops of homonymous units analysed in this thesis, also labelled as Akchagyl and Apsheron (see Fig. 4.4).

4.3.2. Seismic Units

Evaluation of the acoustic facies in the KAD fold is based on the seismic image illustrated in *Figure 4.4* and regional reports. The line shown in *Figure 4.4* is the IL 1940 that transects the studied structure in the North, where the well was drilled (*cf. Figs. 4.1* and *4.3*). The key section has been chosen because it shows several distinctive seismic events with a fairly constant character and expression through the seismic cube.

As the drilled area is collapsed, special attention should be paid to the accurate calibration of the location of the seismic units according to their formation tops. Limits of the seismic horizons of the PS and the Post-PS sequences usually depart slightly from the formation tops obtained from the AD-1X well. This deviation is particularly evident in the Pereryva-Old top. Seismic stratigraphy of the PS and the Post-PS groups are here separately described according to its characteristics. According to our inspection of IL 1940 (*Fig. 4.4*) sequences get thicker towards flanks, which are 4.5 km- thick in the PS and 2 km-thick in the Post-PS, in the western limb, against 5.3 km-thick in the eastern PS and 2.2 km-thick in the eastern Post-PS. The different seismic expressions recognized are classified in diverse geological processes: folding, faulting, diapirism and sedimentation (pre-, syn- and post- tectonics).

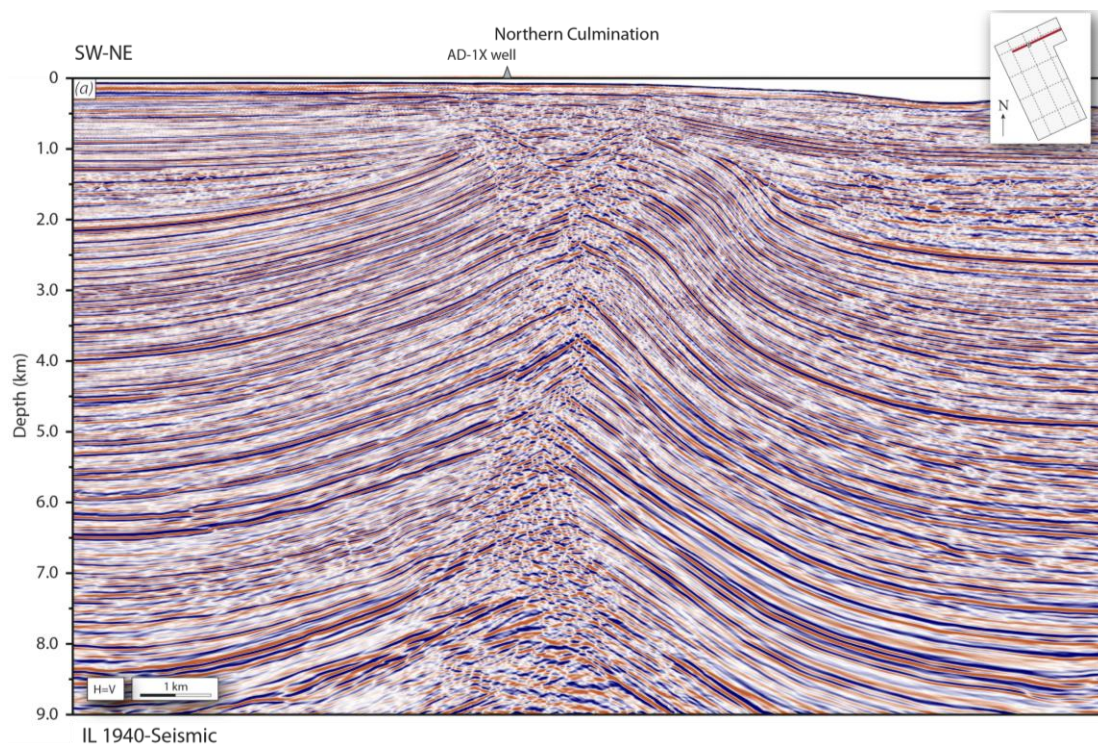


Figure 4.4: a) Seismic line IL 1940 penetrated by the Araz Deniz 1X well (AD-1X) in the Northern Culmination. b) Interpreted line shown in (a) highlights the 22 formation tops reached by the well, and the 14 selected subunits. Inset map shows the IL position in the cube coloured in red, whereas other dash and grey-coloured lines are included for reference (SW-NE ILs 500, 1000, 1500 and 2000; and NW-SE XLs 1000, 1500 and 2000). The amplitudes polarity convention corresponds to red-coloured reflectors equivalent for negative amplitudes (shale-rich units) and blue-coloured, for positive values (sand-rich units). Seismic horizons and chrono-stratigraphic information are summarized in *Tables 4.3* and *4.4*. Akchagyl and Apsheron horizons correspond to the Akchagyl 1 and Apsheron 1 tops presented in *Table 4.4*. Overlapping features are depicted within the Post-PS along the fold crest. Unlabelled horizons correspond to internal reflections that are included to better illustrate the structure and which have not been followed throughout the seismic cube. Abbreviations: Balakhany (Bk), Pereryva (Per), Productive Series (PS). Surakhany horizons are named as Sk. *Continuation in the next page.*

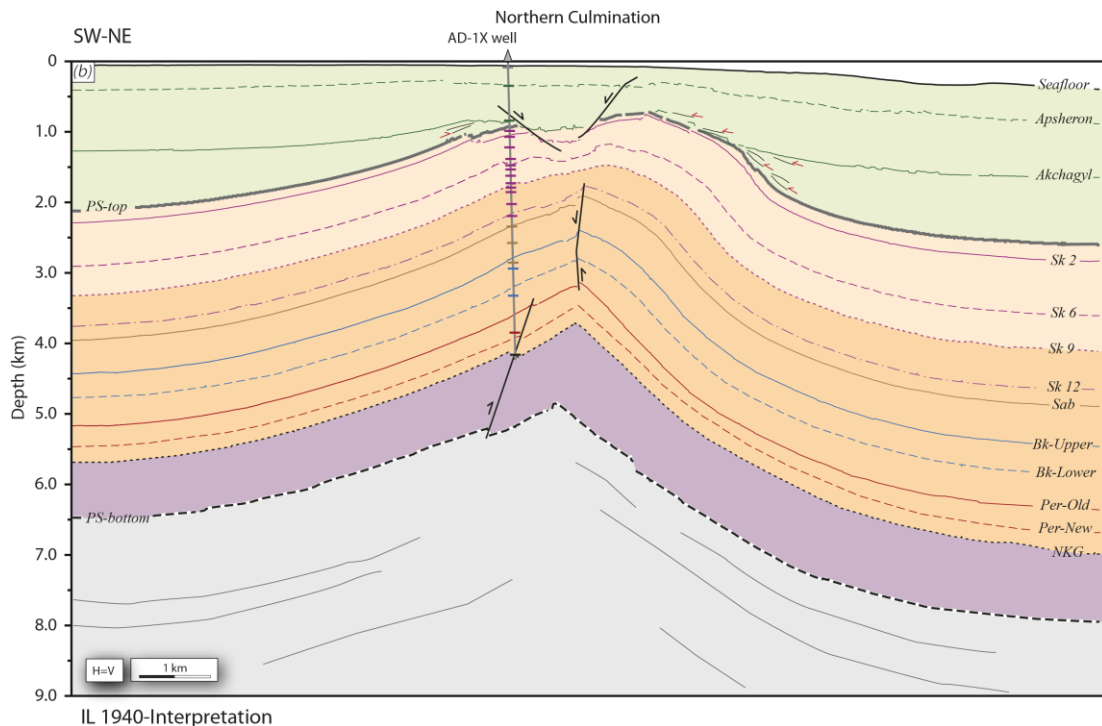


Figure 4.4: Continuation.

The seismic reflectivity of PS horizons observed in *Figure 4.4* corresponds to clastic sediments, compacted and undercompacted, affected by layers bending and sometimes being interrupted by faults and intruded by vertical material that shows chaotic seismic expression also because of the presence of fluids. Whole PS package shows similarities in regard to the aggradational pattern and the very good continuity of the reflections. Internally, the geometry of the PS geological formations is monotonous and lateral facies change is not clearly observed due to the absence of clear geometrical evidences.

Reflections continuity in the PS departs from the abundant disruptions and irregularities within the Post-PS sequence (*Fig. 4.4*). The study of lateral variations of the seismic character of the most contemporaneous reflectors (from the Akchagyl Formation towards the seafloor) during the seismostratigraphic interpretation is related to changes in the geometry of strata and the presence of channels. Irregularities within the Post-PS group show common features of unstable deposits, occasionally accompanied by sigmoidal bodies prograding into the basin.

Three seismic sequences have been identified in this research separated by relevant discontinuities. The study of the Lower PS (Late Miocene-Early Pliocene, 5.9-5.2 Ma) is focused on the interval between the bottom of the PS (PS-bottom) that coincides with the base of the KAS Formation, and the NKG top. Intermediate units within the Lower PS, such as KAS, PK, KS or NKP are not seismically inspected. The Upper PS units (Early to Late Pliocene, 5.2-3.1 Ma) are analysed conscientiously and comprise a detailed description of the Pereryva, Balakhany, Sabunchi and Surakhany units. The separation between the PS and the Post-PS sequences is coincident with an unconformity located on the top of the Surakhany Unit, which is the PS-top. The Post-PS units are formed by the Akchagyl and Apsheron horizons, crowned by the seabed layer (Late Pliocene-Holocene, 3.1 Ma-to-Present).

Lower PS

The Lower PS (5.9-5.2 Ma) is interpreted between the clearly depicted PS-bottom and the top of the NKG Unit (~5.33-5.2 Ma) (*Fig. 4.4*). The condensate sub-sequence is up to 800 m-thick, but homonymous horizons in both flanks occur at different positions, which suggest a thickness change along the SW-NE section. General patterns of the seismic sub-sequence evidence a package delimited by relative continuous horizons and mainly highlights as a low velocity interval within a thick shaly package. The sequence is disrupted in the central areas by seismic markers that cut divergently each other because of the occurrence of diffractions and disruption due to faulting. Layer bending is also observed.

Internal fabric of the seismic group is characterized by several events of high amplitude and continuous, intercalated with less intense reflectors. The seismic horizon of the PS-bottom corresponds to strong negative amplitudes with high values usually distinguished as a regional unconformity. The seismic marker of the top of the NKG presents low, positive amplitude values, and high seismic velocities characterize it, occasionally interpreted as a paraconformity without any evidences of truncations and onlaps and without a univocal seismic character.

Upper PS

The Upper PS (5.2-3.1 Ma) is a sequence of more than 3.5 km of thickness, but thickness varies between the western and the eastern limb (*Fig. 4.4*). Equivalent facies in both flanks are located at different depths. Main seismic facies observed are characterized by parallel intervals of low and high amplitudes. The sequence is composed of laminated to transparent reflections that display high lateral continuity. Seismic horizons are affected by layers bending and usually they are crosscut and interrupted by faults and by vertical intrusive material.

Distinctive seismic events are characterized in the Upper PS sub-sequence according to a fairly constant seismic character and expression. We differentiate two portions in the sub-sequence separated by the top of the Sabunchi Formation (3.7 Ma) that has strong positive amplitudes with high continuity.

In the lower part, the Pereryva-Old, the Balakhany-Upper and the Sabunchi horizons are the solely well-depicted reflectors. Internal fabric between the Pereryva-Old and the Sabunchi is characterized by thick intervals of low amplitudes and transparent facies, more abundant in deeper areas, intercalated with highly expressed reflections of stratified layering that get thin to the upper limit. Continuity of horizons decreases towards deeper positions.

The Pereryva-Old is the top of a thick package of about ~200-250 m composed by two strong events with negative amplitudes which encompass a thin and marked positive event: the Pereryva Unit (5.2-4.9 Ma). The Pereryva-Old is always placed at the base of the upper negative event. The Balakhany Formation (4.9-4.0 Ma) is crowned by a marked positive top in a 800 m-thick unit, and constituted by numerous subtle internal reflections. The horizon top in the Sabunchi Unit (4.0-3.7 Ma) is commonly interpreted along a very thin and positive interval, at the top of a strong and thick event with negative amplitudes (~100 m-thick), which is limited below by an event with high, positive amplitudes (~40-50 m-thick).

The upper interval between the Sabunchi top and the PS-top is characterized by the

clearly remarkable PS-top seismic horizon. Numerous thin events stand out within the Sabunchi and PS-top that present maximum and minimum amplitudes. Subtle onlap geometries are recognized towards the fold crest observed through a meticulous study. A detailed analysis also evidences a progressive thinning of the sequences on the fold core and noticeable differences in both flanks.

In the upper portion of the PS three thin positive events are observed within the Surakhany Unit (3.7-3.1 Ma) in *Figure 4.4*. These events correspond to coherent and continuous reflexions: the horizons Sk 9 (3.5 Ma), Sk 6 (3.4 Ma) and Sk 2 (3.2 Ma) (*cf. Table 4.3*). They are located at about 3.3, 2.8 and 2.3 km depth in the western domain of the structure, and at about 4.1, 3.6 and 2.8 km depth in the eastern area, respectively. These events are limited above and below by two, relatively thick intervals with moderate negative amplitudes (≤ 40 -50 m-thick). In the eastern domain the Surakhany Unit shows commonly wavy-events with abundant, moderate diffractions above the Sk 12 (3.6 Ma) and Sk 6 horizons (*e.g.*, at 4.2 km and 3 km depth in the vicinities of the Eastern Line).

The acoustic signal of the upper PS-top boundary (3.1 Ma) corresponds to a high-amplitude (positive) reflection with a large continuity. This reflection is partially absent in central areas of the seismic block. The seismic horizon shows strong acoustic contrast and it is easily traceable on seismic. This surface shows local erosional features and a clear onlapping relationship with the overlying sequences. The PS-top is an unconformity more pronounced in the fold core that erodes the top of a condensate sequence of continuous and parallel layers.

Post-PS

The Post-PS (3.1 Ma-Present) package is a near 2 km-thick sequence delimited by two intense reflections with high continuity in the PS-top and the seafloor (*Fig. 4.4*). Seismic analysis in the Post-PS sequence lets us to differentiate the Akchagyl and Apsheron horizons as the respective formation tops. The architecture of the Post-PS sequence is formed by two wedges oppositely disposed with significant thinning in the central region of the KAD structure. The seismic group is locally truncated and has a variable acoustic response with abundant wavy events and scarce stratified reflections. Seismic horizons are occasionally displaced by faults and even disappear in the central region of the KAD anticline due to intruding material. Disruption is frequently accompanied with the absence of the Akchagyl and Apsheron horizons. In contrast, towards the flanks, channel geometries and some lens-shaped bodies with chaotic seismic facies are widely identified. Lateral variations of the seismic character of the surfaces are related to changes in the strata geometry or sediments remobilization. Some large clinofolds are detected along the Post-PS units, especially within the Apsheron Formation in the northernmost sectors close to the basin margins (*Fig. 4.5*).

Seismic top of the Akchagyl Unit (3.1-1.7 Ma) is a positive to intermediate-amplitude reflection. Onlap features toward the central areas of the KAD anticline generally truncate the Akchagyl sequence, whereas towards the flanks, horizons commonly disappear or become rugose (*Fig. 4.4*). The Akchagyl Unit contains numerous facies changes, with intervals of transparent acoustic facies that usually present internal disorganization as a result of gravitational sediments mobilization. Mobilized sediments are embedded between highly reflective layers.

A continuous reflection with positive and intermediate amplitudes characterizes the Apsheron top. Reflections within the Apsheron Unit (1.7-0.8 Ma) are irregular, commonly

non-planar that present numerous mobilized mass-transport deposits. Usually, in the northern domains the Apsheron Formation depicts sigmoidal bodies internally stratified that correspond to large clinoforms prograding southwards from the basin margins (Fig. 4.5). Occasionally, the Apsheron base also shows an erosive geometry.

The youngest seismic unit corresponds to the Gelasian Unit (0.8 Ma-to-Present). This unit has numerous concave reflections with high amplitudes and they might indicate the occurrence of scars associated to up-slope breaks in gravitational deposits.

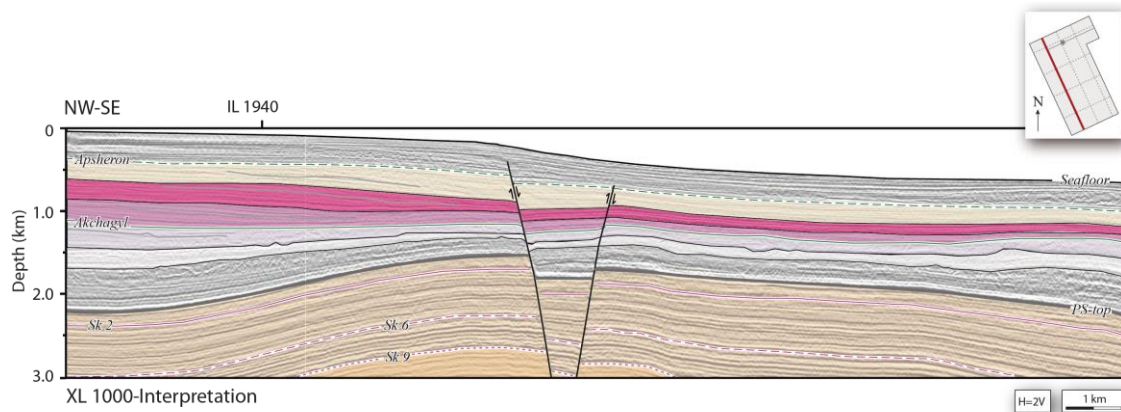


Figure 4.5: Seismic interpreted profile XL 1000 where it is observed numerous clinoforms are dominant in the NW of the studied area. The inset map shows in red the location of the seismic section, intersected by the IL 1940, represented by a grey-coloured continuous line (Fig. 4.4). Colour code for the seismic signal is positive amplitudes in black and negative amplitudes in white. The PS-top is the top of the Productive Series. The Surakhany horizons are abbreviated as Sk. Seismic horizons and chrono-stratigraphic information are summarized in Tables 4.3 and 4.4.

4.3.3. Mass-Transport Complexes

According to numerous authors, the geodynamics evolution of the SCB has triggered a great number of gravitational processes from the unstable paleo and seafloor that promoted the accumulation of mobilized masses of sediments downslope (Fig. 4.6). Different triggering mechanisms for these processes have operated along the SCB: folding, high and/or rapid sedimentary loading, changes in the sea level, mud volcanism, and seismic activity, among others (e.g., Morton, 1993; Reynolds *et al.*, 1998; Abdullayev, 2000; Sultan *et al.*, 2004; Abreu and Nummedal, 2007; Harders *et al.*, 2011; Abdullayev *et al.*, 2012; Imbert *et al.*, 2014).

Mass-movement processes can be classified as slump, rock fall, debris flow, block gliding and turbidity current, whereas several general terms define submarine mobilized deposits, e.g., debrite, turbidite, flow and slide (e.g., Posamentier and Martinsen, 2011). In this work, for simplicity, we use the name mass-transport complexes (MTCs) to indistinctly refer to failed deposited mass with no implication of specific mass-wasting process or geological setting (Gee *et al.*, 2007; Beaubouef and Abreu, 2010).

We have carried out our seismic interpretation in the KAD anticline to produce a comprehensive inventory of mass-wasting structures registered in the Post-PS group; *i.e.*, during the last 3.1 my (Santos Betancor *et al.*, 2013a). This sequence is mainly composed by mud-rich turbidites and deepwater lacustrine deposits (e.g., Abreu and Nummedal, 2007). We have recognized up to 50 mass-wasting deposits in the 3D volume usually characterized by varied-scaled seismic bodies (e.g., Frey-Martínez *et al.*, 2006;

Posamentier and Martinsen, 2011). In this thesis, we present some seismic examples of MTCs by using vertical and horizontal seismic sections and attribute maps. *Figure 4.7* shows the position of the selected vertical slices and their position in the seafloor surface (Santos Betancor *et al.*, 2013a). This surface is clearly deformed and eroded and evidences the intense gravitational activity along the present-day marine platform.

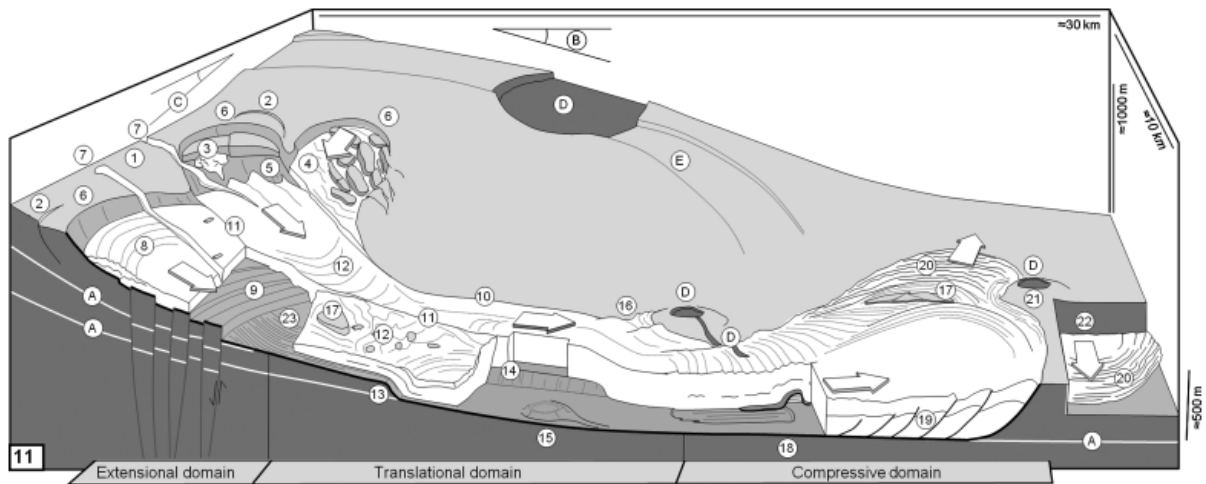


Figure 4.6: Cartoon of the morphology of the western SCB seafloor. Taken from Richardson *et al.* (2011).

Numbers are used to refer to: headwall scarp (1), crown cracks (2), rotated blocks and residual debris (3), rafted blocks (4), detached portion of the flow exposing evacuated basal shear surface (5), arcuate scarps (6), headless canyons (7), convex upslope lineations (8), normal ramps in the basal surface (9), lateral transport deposits (10), longitudinal shear zone (11), flow fabrics (12), normal ramp (13), lateral ramp (14), strain shadow behind obstacle (15), restraining bend (16), translated blocks (17), blocks and basal shear surface scours (18), thrust sheet (19), pressure ridges (20), obstacle at mass transport deposit toe (21), older mass transport deposit travelling along the old layer of weakness (22), grooves (23). Letters mean: weak layer (A), slope created by basin margin (B), slope created by fold uplift (C), mud volcano crater (D), curved grabens (E).

Mobilized sediments are accumulated in both fold flanks of the KAD anticline and are included in the Akchagyl, Apsheron and Gelasian units. Our classification lists three types of MTCs, based on well-known seismostratigraphic criteria, such as seismic facies, internal structures, thickness, and run out distances and direction. They are labelled as: types A, B and C (Santos Betancor *et al.*, 2013a). Their variation and distribution suggest different instability processes or mass-transport processes (MTPs) that can be categorized in slides and plastic debris flows. Types A and B correspond to different slided deposits, and Type C results due to numerous debris flows.

Type A bodies are usually thick masses characterized by internal structures that correspond to the original stratified sediments. These complexes are constrained by net limits both in vertical and in planar sections. MTCs of Type B are thin complexes with relative low run out distances. They are majorly recognizable in plan view with a fan shape; head focus is not easily identified but amalgamated lobes are clearly depicted in distal areas. Examples of Type C correspond to deposits with chaotic and transparent facies that run large distances among rectilinear walls. These MTCs are specially identified in horizontal slices.

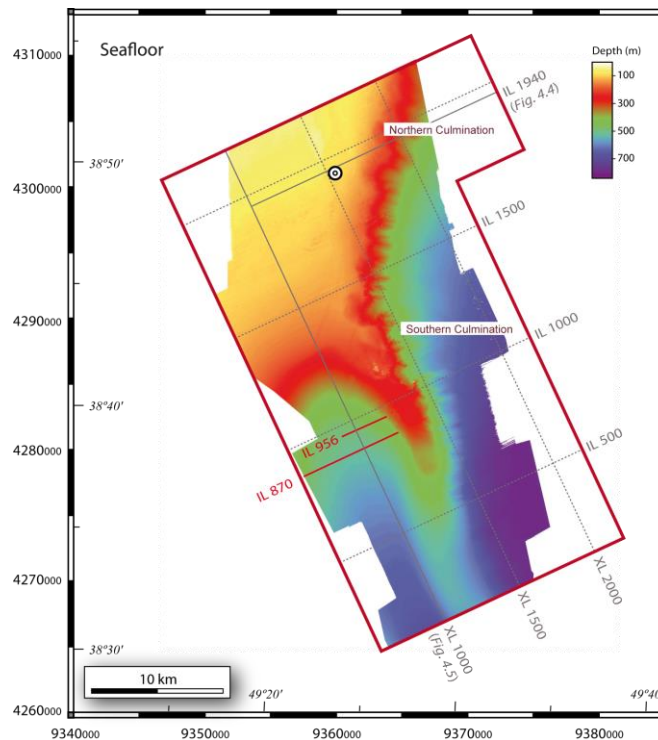


Figure 4.7: Seafloor map within the studied seismic survey marking the position of the seismic profiles (red-coloured lines) presented in this study to illustrate MTCs. Continuous grey-coloured lines represent the previous sections shown in Figures 4.4 and 4.5.

Type A

The example shown in Figures 4.8 and 4.9 corresponds to the largest Type A body identified in the KAD. This deposit has a U-valley-like profile, with a planar net base enclosed by a highly dipping eastern margin.

Internal facies makes the studied MTC to be separated into three sectors of similar dimensions: extensional, translational and compressional domains, easily distinguished in Figure 4.8 (see Santos Betancor *et al.*, 2013a). The extended domain is characterized by high positive markers above transparent facies that are steep and crosscut by normal faults. These are tilted blocks that usually evidence original stratigraphy (Fig. 4.8a). Subpackages of intense white-black-white reflectors above transparent facies dominate the central translational region, piled over the eastern sector, where markers became tilted on thrust structures in the compressional domain. Significant internal bedding distortion is recognized in the frontal thrust imbricates, although, any individual thrust involves an isolated flow unit with low block disintegration. Nevertheless, primary stratigraphy is recognized in overlapped structures.

The top of the mobilized package is shown in seismic as a black and continuous reflection. Occasionally, towards the West, the geometry of the upper surface changes to irregular or hummocky. The lower surface is depicted by a moderate and continuous reflection in the translational and compressional domains that becomes eroded in the extensional region. The upper boundary runs horizontally and wedge towards the crest of the anticline, whereas the basal surface is parallel to the PS-top surface.

Figure 4.9 is built as a horizontal section extracted from a RMS amplitudes map of 300 m of thickness. In this display morphological seismic expression of mobilized sediments is characterized by a front of linear to convex-shaped seismic lobes that occurs westwards

with variable low and high amplitudes. Parallel ribbon systems depict alternate blues and green-to-red features and advance from the seismic survey boundaries following a SW-NE direction. These linear and subparallel strips correspond to the tilted blocks distributed in the extended domain in *Figure 4.8*, whereas compressional structures depict convex arcs in horizontal sections (*Fig. 4.9*). Frontal termination of the mobilized mass depicts a triangular body constrained by sharp edges that markedly coalesce into the same point in the western limb of the KAD anticline.

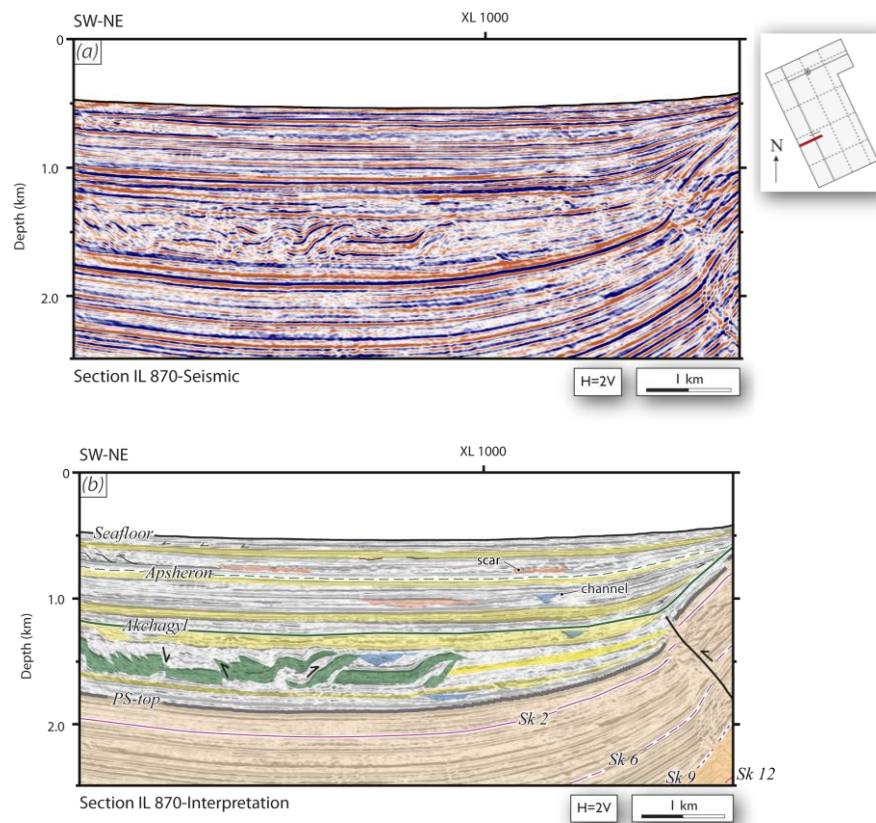


Figure 4.8: a) Representative seismic profile IL 870 to show the largest example of Type A MTC (Santos Betancor *et al.*, 2013a). Interpretation in (b) shows in green the studied example within the Akchagyl Unit. Non mobilized tabular layers are yellow-coloured, channels are depicted in blue and paleoscars are coloured in salmon. The inset map on the upper right corner marks in red the position of the profile in the KAD area. Other seismic lines shown in this thesis are marked as continuous grey-coloured lines (IL 1940, *Fig. 4.4*, and XL 1000, *Fig. 4.5*).

The failed mass covers an area of approximately 24 km² in the North of the western syncline within the Akchagyl Unit (~3.4-3.1 Ma to 1.7~1.6 Ma), sited ~150 m above the PS-top surface and ~350 m below the Akchagyl top. The studied case is about 300 m-thick and mass spreads up to 5.5 km run out distance, although the whole structure is not completely seen within the studied survey.

MTCs of Type A are abundantly identified in both flanks within the Akchagyl Formation, and isolated examples are observed within the eastern Apshteron Unit (1.7~1.6 Ma to ~0.8-0.7 Ma) and western Gelasian Formation (~0.8-0.7 Ma-Present). Gravitational deposits are characterized by large run out distances and low internal distortion with variable scales (between 50m and 350m-thick). These mobilized deposits usually moved W-E, perpendicularly to the Present-day anticline axis. The western examples are more numerous and they usually advance towards an ancient and Present-day syncline pond

coming from out-data boundaries (Figs. 4.8 and 4.9). In those cases, the origin of these deposits may be located in a neighbour structure to the West as any scar is recognized in the headwall area (Santos Betancor *et al.*, 2013a). The toe domain of the mobilized mass appears buttressed against surrounding undisturbed strata, and usually is frontally confined by a sharp edge along the KAD crest (Fig. 4.8; Frey-Martínez *et al.*, 2006). Interpretation of Type A bodies is consistent with large-scale submarine slides that majorly mobilized sandstones and shales.

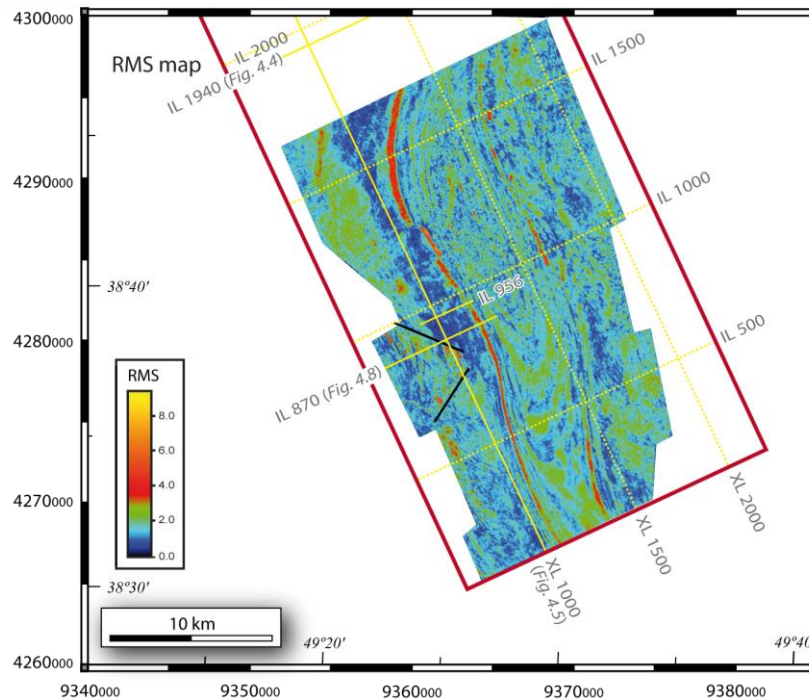


Figure 4.9: RMS amplitudes map extracted within the Akchagyl Unit between the interval from 1450 and 1750 m depth. The slide of Type A illustrated in the IL 870 in Figure 4.8 depicts a triangle shape with black-colour limits.

Type B

The deposit shown in Figure 4.10a is asymmetrical and concave-shaped with margins oppositely inclined. The western termination abruptly terminates against a highly-dipping limit.

Margins of the body of Type B shown in Figure 4.10a enclose facies without visible internal structures. Semicontinuous reflections dominate the deposit but when weak layering is depicted, seismic markers are mostly parallel to the strata. Some undulant character is illuminated in the centre of the deposit. The studied MTC lies straight in a black-white-black seismic pair that fades upslope. The toe terminates in a well-define tight black-white reflector, which is highly-dipping. Any imbricate thrusts are observed, but may be inferred from the reflector in the toe area, as the thrust front.

High negative reflections are defined in the headwall through horizontal seismic analysis, that gradually incorporate transparent facies and zero-to-high positive reflectors in the toe region, without a net separation (Fig. 4.10b). The highly dipping reflector of the toe region in vertical sections (Fig. 4.10a) depicts the net circular geometry of the MTC in plan view (Fig. 4.10b), whereas the failed area in the headwall is suggested from the

disruption of layering on the anticline flank. The upper surface covered totally the MTC, with some irregularities in the toe area.

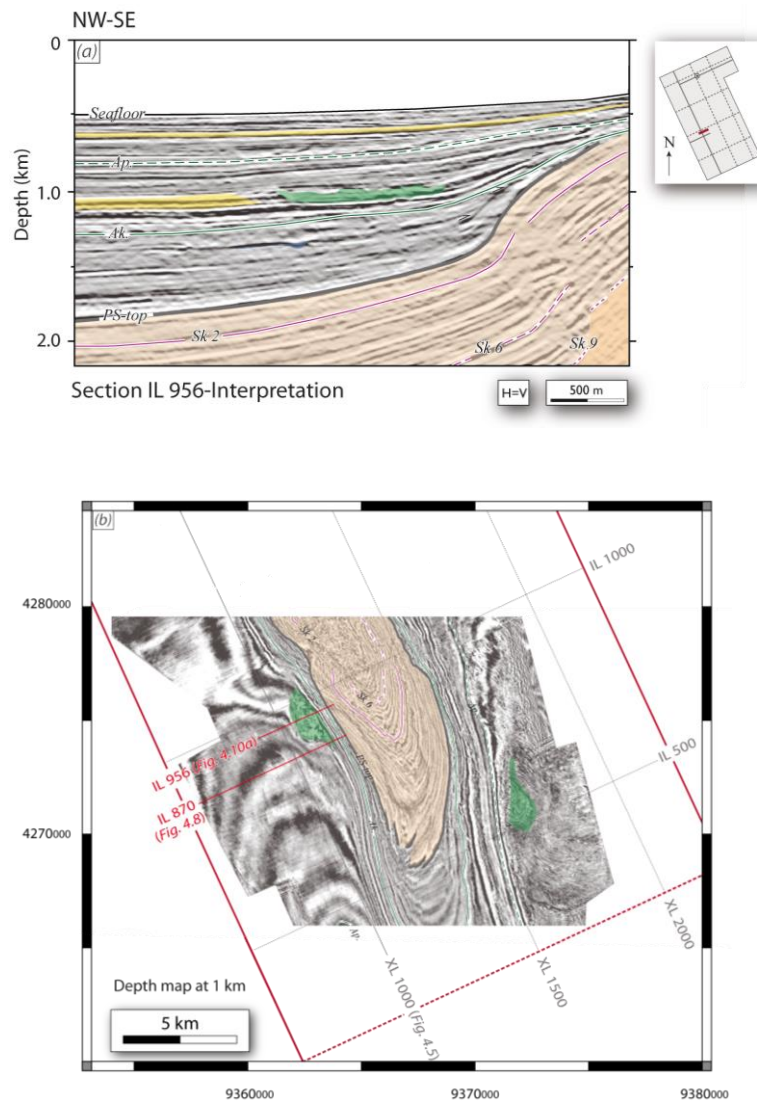


Figure 4.10: a) Seismic profile section of the IL 956 (red-coloured line in the maps) where is observed a western MTC of Type B in the base of the Apsheron Unit. The location of previous Figures 4.4, 4.5 and 4.8 is depicted in the inset map as continuous grey-coloured lines, coloured in yellow in (b). b) Depth section at 1 km depth illustrates the plan view of MTC seen in (a) and another example of Type B distinguished in the eastern limb within the Gelasian Unit. Abbreviated horizons: Akchagyl (Ak.) and Apsheron (Ap.).

The studied MTC has a lobed pattern in plan view characterized by the disruption of seismic layering (Fig. 4.10b). Toe boundaries depict a net curved edge, whereas the eastern limit in the headwall is presumed a slightly linear feature, consistent with a flow from the NE to the SW.

The example of failed mass of Type B presented in Figure 4.10a is located in the western flank in the proximities of the example of Type A shown in Figure 4.9. The deposit spreads by a maximum area of 1.2 km x 2.3 km within the Apsheron Formation (1.7-0.8 Ma) and lies in an interval between 800 m and 1080 m depth. Maximum thickness of the body ranges between 20 m in the headwall and 100 m in the toe.

MTCs of Type B are very scarce in the structure, with small representations within the Apsheron Unit in both flanks, and in the eastern limb within the Gelasian Formation (*Fig. 4.10*). We identify small bodies as thin deposits that cover low flow distances. General thickness is usually <100m and extension is <2.5 km. These MTCs run following a NE-SW direction from the anticline crest in the West, and NW-SE in the eastern limb (*Fig. 4.10b*). The headwall scar of the failed bodies is not clearly observed due to their size and seismic resolution, but it may truncate towards the smooth anticline topography, which follows the regional dip direction of the limb. The seismic characteristics of the studied Type B agree with small slides along instable slopes triggered by the uplift of the KAD fold (Santos Betancor *et al.*, 2013a).

Type C

Geometry of MTCs of Type C is majorly established through their recognition in depth slices, as they are hardly identified through vertical sections. They show curved updip scars (*Figs. 4.11* and *4.12a*) and linear walls downdip (*Fig. 4.12b*) that terminate in a slightly convex area.

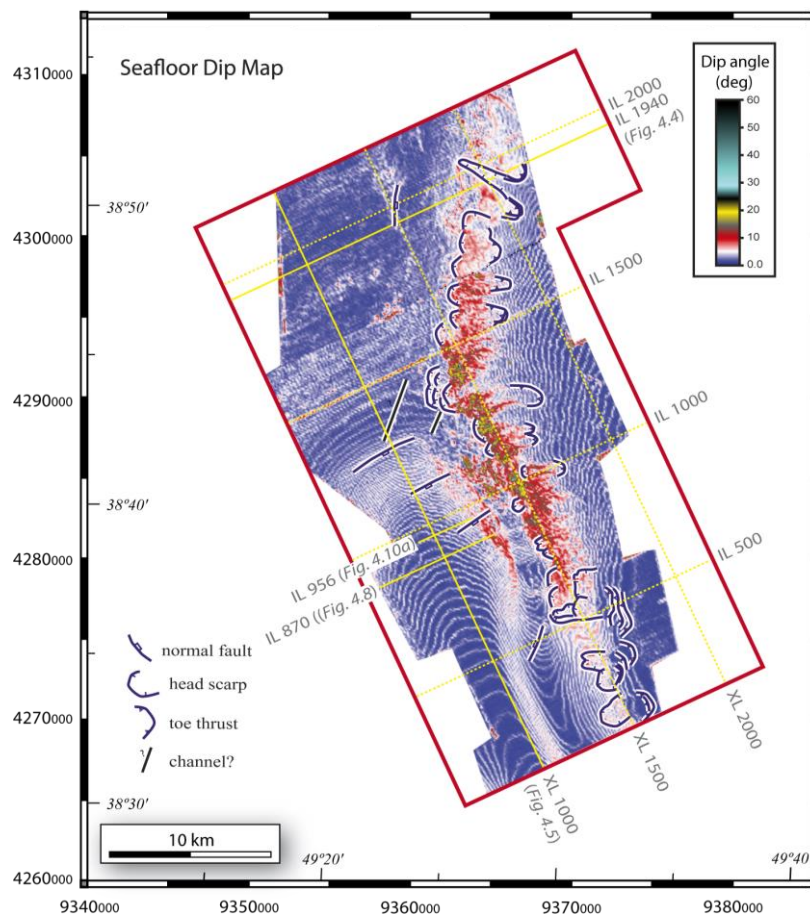


Figure 4.11: Dip map of the Present-day seafloor. Notice the abundance of “cookie bites” along the actual topography that correspond to numerous MTCs of Type C. Numerous scars control the eastern slope of the KAD anticline, and locally, the western part. Black-white-red colour scale indicates a progression of low dip angles to high dips. Contour lines coloured in white represent an exaggeration of original seafloor deepening.

MTCs of Type C are depositional bodies integrated by disaggregated sediments with

intermediate amplitude values that camouflage in the surroundings (*Fig. 4.12b*). Facies are rugose and chaotic. Discontinuous reflectors are present towards the head, whereas some pairs float in the suggested translated domain. Some internal architecture of deformed strata is observed in the compressional region.

The upper boundary is usually a bright white reflection that underlies the seabed response. The lower boundary is generally disrupted and it corresponds to a black reflection, only observed in the transitional domain.

Studied MTCs sediments of this category depict concave headwall scars with very high dips (*Fig. 4.11*), that resemble “cookie bites” in the Present-day seafloor surface (*Figs. 4.7* and *4.12a*). Mobilized deposits generally run basinwards flanked by steep and divergent walls to convex lobe-shaped downdip (*Figs. 4.11* and *4.12b*).

In this thesis we present a representative case of MTC of Type C coloured in dark green in *Figure 4.12*. This body occupies over 7 km² in the eastern syncline within the youngest rocks of the Gelasian Unit. The MTC is described from 500 m (*Fig. 4.12a*), to 750 m (*Fig. 4.12b*) below the sealevel, with a maximum thickness of 120 m. The deposit has an abrupt and concave head observed at 500 m depth and divergent internal and terminal parts.

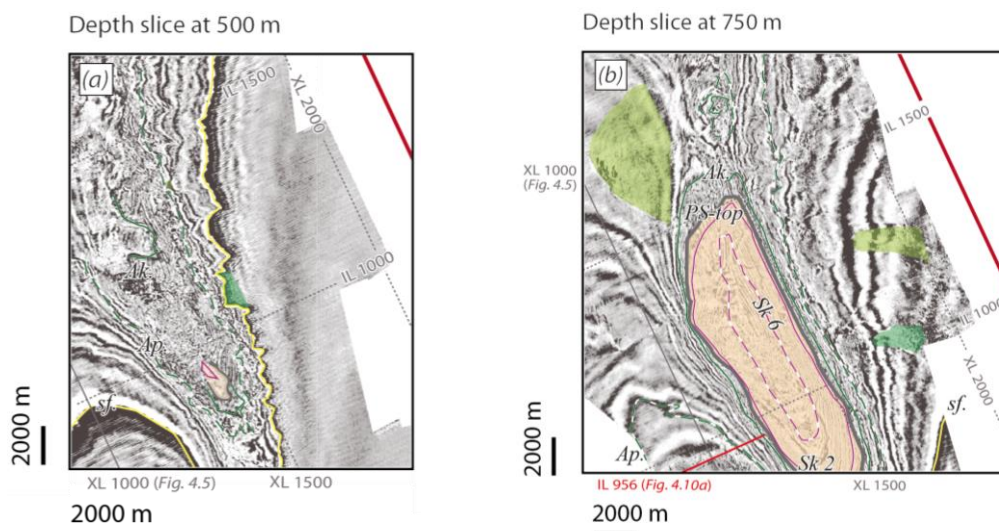


Figure 4.12: Seismic section of depth slices of (a) 500 m and (b) 750 m that show the evolution in depth of the studied MTC of Type C with a dark-green colour. The headwall of the mobilized mass is observed in (a) whereas the mature channelized flow is distinguished in (b). (b) Two deposits of Type C are highlighted within the Apsheron Unit in the eastern domain of the anticline at 750 m depth; one MTC of Type A is detected in the western area (coloured in light green). Abbreviated horizons: Akchagyl (Ak.), Apsheron (Ap.), top of the Productive Series (PS-top), the seafloor (sf.) and horizons within the Surakhany Unit (Sk 2, Sk 6).

Failed deposits of Type C are numerous; they are sited within the Apsheron and most population is concentrated in the Gelasian packages. Failed mass is variably scaled with relative large dimensions, and usually stops outside the 3D cube. MTCs run obliquely to the fold strike in the eastern domains and parallel to the fold axis in the West. Apsheron unstabilized deposits occur in the southwestern domains following a NW-SE direction, whereas Gelasian deposits are widespread with variable flow source directions (W, and N). These deposits may initiate by continuous slope failures in different periods that, when triggered in the same area, promoted amalgamation of Type C bodies (*Fig. 4.11*). They

moved along tight flow paths as a channelized flow very penetrative confined by linear sharp edges separated 1 km until it diverges and spills in the termination region (*Fig. 4.12b*). The accumulation area is located in the mouth of the channel without the definition of a net terminus. Seismic analysis suggests that incoherent mass of sediments flowed very rapidly as a result of a release of material upslope in the KAD anticline triggered by debris flows. These bodies may be a result of unstable slopes due to fold growth and or prograding clinoforms to the inner SCB (Santos Betancor *et al.*, 2013a).

5. 3D GEOMETRY

This study is based on the reconstruction of the geometry of the KAD anticline through seismic interpretation procedures. We focused on the spatial analysis of the seismic signal expression across the structure to evaluate the fold shape, with special distinction between pre- and syn-growth sediments, faults distribution and mud occurrence. The study evidences the evolution of the seismic response of reflected horizons affected by layers bending and sometimes being interrupted by normal and reverse faults and by vertical intrusive material that also deforms the sedimentary overburden. Careful evaluation evidences different folded sequences along the PS and Post-PS units related to changes in the geometry of strata. The different seismic expressions recognized are grouped in diverse geological processes: folding, faulting, diapirism and gravitational sedimentation (pre-, syn- and post- tectonics).

5.1. Vertical Seismic Sections

Seismic sections presented in this thesis are both vertical and horizontal profiles. Vertical profiles correspond to seven representative seismic lines: In-Lines (ILs) 540, 1140, 1640 and 2000, and arbitrary lines named as Western, Central and Eastern sections. Selection of lines has been based on the interest to illustrate a general view of the evolution of the KAD anticline geometry from South to North. Selected profiles are shown as interpreted and non-interpreted images. The location of the selected seismic profiles in the 3D seismic survey is shown in the map of *Figure 5.1*.

Key ILs are SW-NE directed whereas the arbitrary lines are composite profiles with mostly NW-SE-directed segments, and intersect all the ILs. 2D vertical seismic slices are illustrated in the following *Figures 5.2 to 5.8*.

Seismic interpretation of 2D profiles is conducted in three-dimensions conjointly tied by using both, the X-Line (XL) seismic dataset and crosscutting transects accompanied by the stratigraphic information derived from the Araz Deniz well (AD-1X). Our results are extracted from the post-stack depth-migrated volume with a vertical scale corresponding to the real depth (in meters). It should be taken into account that the complete interpretation during this study is focused on the PS and Post-PS packages, because deeper seismic units are not clearly imaged by the seismic penetration and processing.

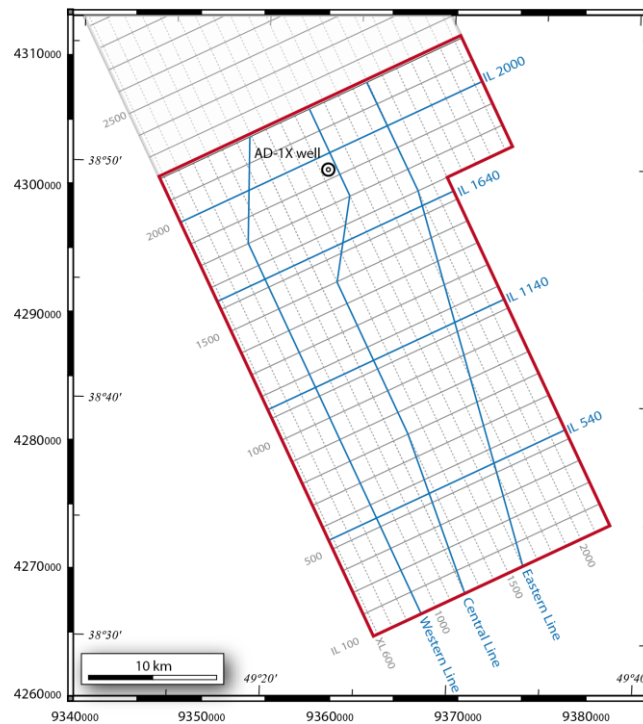


Figure 5.1: Surveyed area of the study including the main seismic lines presented in this chapter highlighted in blue.

5.1.1. IL 540

The first seismic line shown in this thesis corresponds to the southernmost section of the studied structure named as IL 540 (Fig. 5.2); this profile is extensively detailed in Santos Betancor *et al.* (2013b) and Santos Betancor and Soto (2015). Seismic section of IL 540 shows a continuous, double hinge anticline that deforms the complete sedimentary record depicted in the seismic cube. The structure resembles a box-like geometry with a fold wavelength of ~6-7 km and ~0.7 km of fold amplitude measured along the PS-top surface. The Late Miocene-to-Late Pliocene PS sequences describe a symmetric anticline which geometry evolves from a narrow, angular fold hinge in the PS-bottom (at 5.5 km depth), to a rounded hinge with a wide and sub-horizontal fold culmination in the PS-top (~4 km-long at 1.2-1.4 km depth). Fold culmination limits two narrow and planar limbs, dipping 30°W, and 45°E, in the western and eastern limbs, respectively (measured in the PS-top as relative values). The interlimb angle is ~105° corresponding to an open to gentle anticline (Fleuty, 1964). The axial surface is a single and vertical surface in the PS-bottom, corresponding to an upright fold (Fleuty, 1964), which branches up-section into two convergent surfaces dipping oppositely. The fold shape described in the PS (horizons 1 to 10) resembles a kink-like anticline. In the PS-top, the axial plane dips 80°W and fold vergence is East-directed.

Several multiple reflectors of the seafloor are still remnant in the processed seismic image. For example, a bottom simulating reflector (BSR) is observed at 1.5 km depth in the western fold limb, and another is shown at ~2 km depth to the East. Some seismic diffractions are also present at higher depths.

Stratigraphic thickness of the folded PS sequence in the western flank is ~4.6 km-thick facing the 5.15 km in the East, whereas minimum thickness is achieved in the fold crest area, with ~4.4 km. This tendency is also observed in the Post-PS series. The Post-PS sequences describe two sedimentary wedges with progressive thinning towards the

anticline crest. The sequence changes progressively from 1.4 to 1.6 km-thick, from West to East, respectively, whereas above the anticline crest they achieve a minimum thickness of ~ 0.5 km. The progressive thinning is particularly evident above the planar fold limbs and it is seen throughout the Akchagyl and Apsheron units, and also up to the seafloor surface.

The transition of thicknesses within the PS rocks from West to East is different in the oldest units, in comparison to the uppermost horizons. In detail, the PS sequences limited by the PS-bottom and the top of the Surakhany 9 subunit (Sk 9) evidence a progressive thickening: 3.3 km measured in the West, 3.3 km in the anticline culmination, and 3.7 km in the eastern flank. By contrast, significant thinning within the fold hinge is registered from the Sk 9 to the PS-top, where the observed thickness achieves 1.1 km, whereas in both sides of the anticline culmination thickness is 1.3 km and 1.45 km, respectively in the West and in the East.

Dips within the PS sequences are majorly $<10^\circ$ registered in distal areas of fold flanks and in the fold crest in the uppermost horizons ($<5^\circ$ in the PS-top). Maximum dips are measured in the eastern parts of the KAD fold (40°E in the PS-bottom and 45°E in the PS-top) whereas the flank dip is nearly constant in the western limb ($\leq 30^\circ\text{W}$). Post-PS beds are sub-horizontal in both flanks.

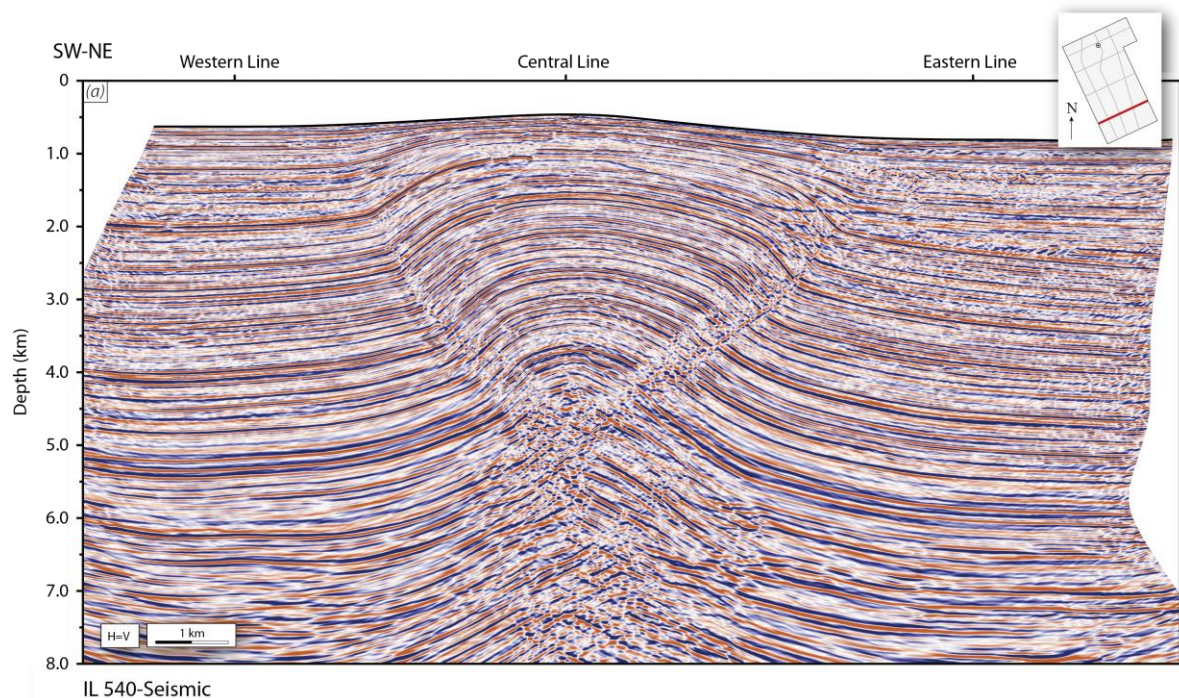


Figure 5.2: Seismic IL 540, (a) non-interpreted and (b) interpreted with no vertical exaggeration (Santos Betancor and Soto, 2015). Inset map in (a) shows the IL position in the KAD cube, whereas the remainder interpreted lines in this chapter are coloured in grey (cf. Fig. 5.1). The AD-1X well is also located in the map. The amplitudes polarity convention corresponds to red-coloured reflectors equivalent for negative amplitudes (shale-rich units) and blue-coloured, for positive values (sand-rich units). Seismic horizons and chrono-stratigraphic information is summarized in Tables 4.3 and 4.4. Onlapping features are depicted within the Post-PS along the fold crest. Unlabelled horizons correspond to internal reflections that are included to better illustrate the structure and which have not been followed throughout the seismic cube. Abbreviated horizons correspond to: Balakhany (Bk), Pereryva (Per), Productive Series (PS), Sabunchi (Sab), and Surakhany (Sk). *Continuation in the next page.*

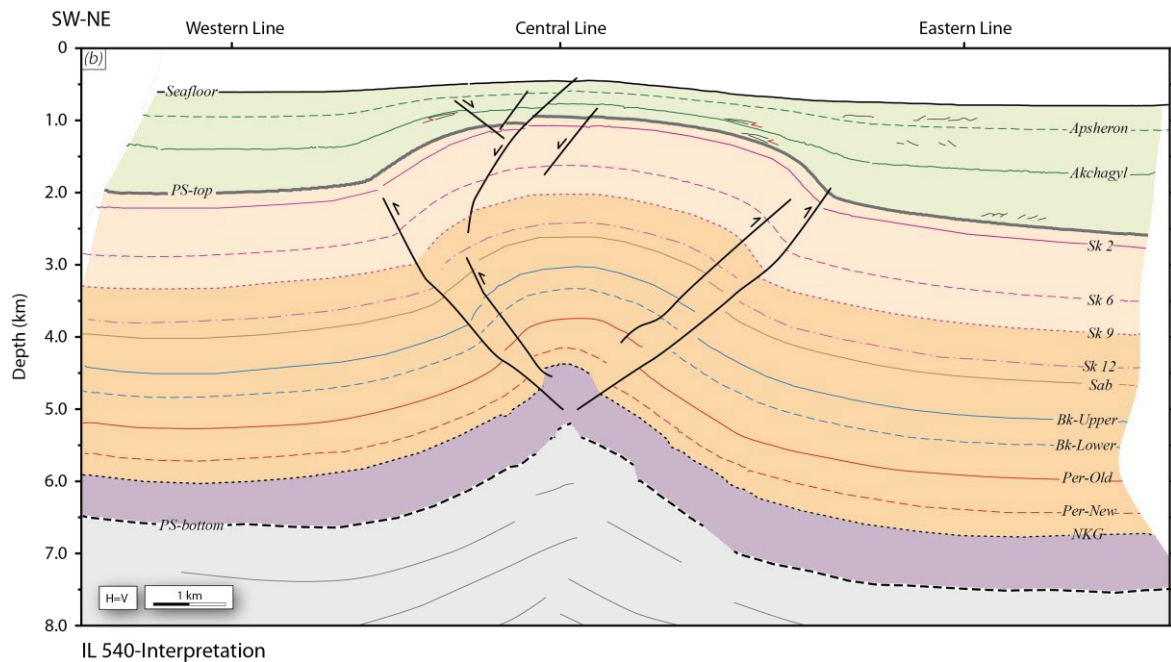


Figure 5.2: Continuation.

Two contrasting fault families displace the sedimentary folded sequence. One family affects only the PS sequences, which is sealed by the PS-top unconformity, and is clearly linked to the fold structure. It is formed by two, double-vergence, reverse faults developed along the two, kink-like anticline axial zones (dipping 45-60°; *i.e.*, high-angle faults) that depict a pop-up structure. The most significant fault is internally located on the eastern flank and is ~15 km-long, whereas the opposite western fault is over 12 km-long.

The other family corresponds to normal faults with high dips (~50°) and mutual cross-cutting relationships that evidence their conjugate origin (*e.g.*, Ferrill *et al.*, 2000). These faults cut mainly the sequences above the PS-top surface, although some of the master normal faults extend both upwards (affecting up to the seafloor) and downwards (displacing up to the Sk 9).

5.1.2. IL 1140

The IL 1140 (*Fig. 5.3*) is located in the central positions of the surveyed area over 11 km to the North from the IL 540 (*Fig. 5.2*). This section crosscuts the Present-day Southern Culmination, locally entitled as the Kirgan Deniz dome. The structure is a single-hinge fold. Fold wavelength is 5.2 km-long and the fold crest elevates up to 0.7 km. Geometry within the PS depicts an anticline with markedly asymmetrical fold limbs and an angular-to-rounded fold hinge. Western fold flank dips up to 35°W, whereas the eastern limb dips ~30°E. The anticline in this section is an open to gentle structure (the interlimb angle remains fairly constant, ~110°), and an upright fold (axial surface is totally vertical).

A chaotic seismic body, typical of mud facies, is present in the fold-core area mainly constrained by the PS units, with low interaction in the Post-PS. Mud structure depicts a teardrop diapir within the culmination domain of the KAD. Diapir margins correspond to fade surfaces except on the western boundary. Blur limits are probably due to the high fluid content in the mobilized muds.

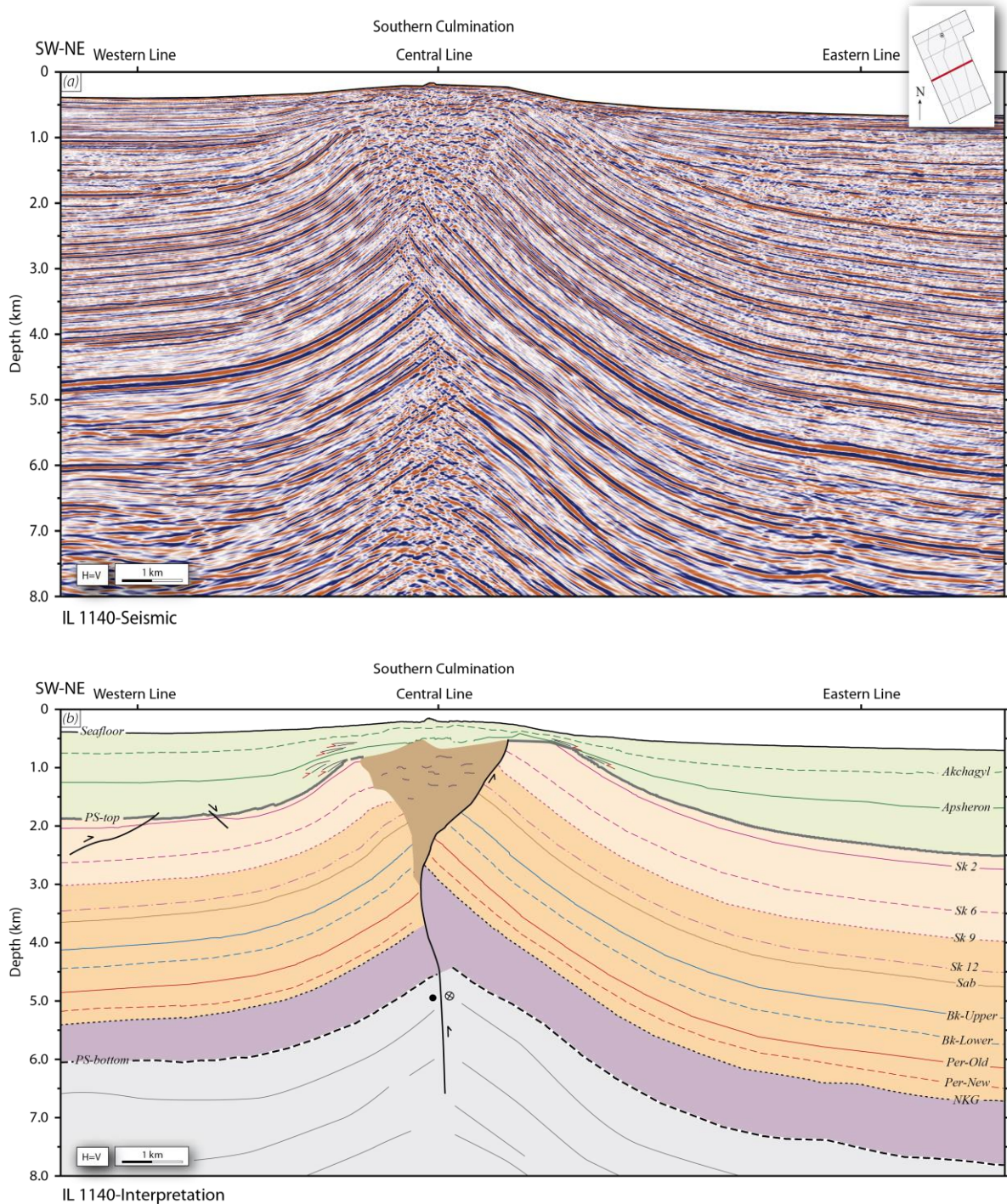


Figure 5.3: Seismic IL 1140, (a) non-interpreted and (b) interpreted. Inset map in (a) shows IL position. Abbreviations and symbols as are summarized in Figure 5.2.

The diapir presents on the top a flat crest ~ 2.25 km-long. At 2 km depth the vertical structure gets narrow and becomes less than 0.3 km wide. The neck of the diapir is located at ~ 3 km depth. Downwards, mud structure terminates and appears disconnected from the feeder source layer with no presence of a shale pedestal. The termination of the vertical edifice is coincident with a vertical weld, seen up to 7 km at depth. This surface shows a clear reverse and probably strike-slip displacement for the Lower PS, whereas the complete Upper PS sequence has a normal displacement. It is interpreted that this structure corresponds to a pre-existent feeder-channel of a teardrop diapir that was latterly depleted

and shortened during folding. Mud diapir promotes the interruption of the majority of the PS horizons (from the Balakhany Lower top) and the unconformity at the PS-top.

Onlapping features are clearly seen in the Akchagyl and Apsheron units in the fold crest. The eastern limb, comprising all the sedimentary sequences and the seafloor, is tilted slightly towards the East, to the inner basin and this geometry is more evident in the PS.

The PS series stratigraphic thickness is 4.15 km-thick and 5.2 km-thick in the western and eastern flanks, respectively. A minimum value of 4.4 km is inferred to occur in the fold hinge. The Post-PS have 1.45 km and 1.65 km of thickness, in the West and East, respectively. On the fold hinge, the Post-PS sequences reach minimum thickness values of 0.4 or 0.5 km. Thinning is especially evident in the Akchagyl Formation.

The thickness changes observed in both flanks within the PS-bottom to the Sk 9 package comprise 3.05 km of sediments in the West, and 3.75 km in the East. For the overlying Sk 9 to PS-top units, variation measurements are 1.1 km in the West and 1.45 km in the East.

Dips for the PS sequence in the eastern sector change upwards from 35°E to 30°W (measured from PS-bottom to PS-top), whereas the western flank shows a reverse tendency, increasing to the PS-top (changing from 30°W to 35°W, for the same surfaces). These dips vanish outwards from the anticline limbs, achieving minimum values of 5°. Post-PS units have very low dips, increasing locally towards the vicinities of the fold crest (~15° to the East and to the West).

In the western flank there are two oppositely-dipping faults affecting only the Sk 2 and the PS-top interval. These fractures have a limited displacement of both, normal and reverse regime.

5.1.3. IL 1640

The IL 1640 (*Fig. 5.4*) is located in the northern sector of the studied survey, over 9 km to the North from the previous IL 1140 (*Fig. 5.3*), between the Southern and Northern (also named as the Araz Deniz domain) culminations. The fold wavelength is higher here than in previous profiles, and achieves over 9 km. The fold amplitude is 0.7 km. The western fold flank dip is around 10°W, whereas in the East it dips ~15°E. The interlimb angle is ~155°, thus depicting a very gentle anticline. The axial surface dips ~70° W, corresponding therefore to a very inclined anticline without a marked vergence to the East (Fleuty, 1964).

The overall PS sequences thicken across the structure, from ~4.1 km-thick in the western fold domain, 4.5 km-thick in the fold hinge to ~5.2 km thick in the eastern limb. This tendency changes within the Post-PS series, with values of 1.85 km in the western flank, 1.0 km in the crestal domain and 1.9 km-thick eastern limb.

Within the PS series, there is a noticeable thickness variation between the lowermost and uppermost sequences. The interval between the PS-bottom to the Sk 9 sequence thickens towards the eastern syncline, from 3 km to 3.7 km, whereas the upper Surakhany (including Sk 6 and 2 strata) change from 1.1 to 1.5 km-thick. In the fold hinge is 3.8 km-thick in the lower package, whereas it is 0.7 km-thick in the uppermost Surakhany Unit.

Bedding of units varies from West to East. PS units dip congruently diminishes from 15°-to-10°E to shallow depths, whereas in the West the average dip is 15° W. Maximum dips of the Post-PS are registered in the Akchagyl Unit with over 5°E.

Faulting is widespread in shallow crestal positions with a normal regime, whereas reverse faulting is predominant in the deepest levels. The family of normal faults crosscut

the sequence between the Sabunchi and the Apsheron units and evidences conjugated origin (*e.g.*, Ferrill *et al.*, 2000). The reverse family is mainly located below the Pereryva-Old Formation. Therefore, in this section, the Balakhany package represents a region comparable to the neutral surface where deformation regime changes from layer-parallel extension above to layer-parallel shortening below.

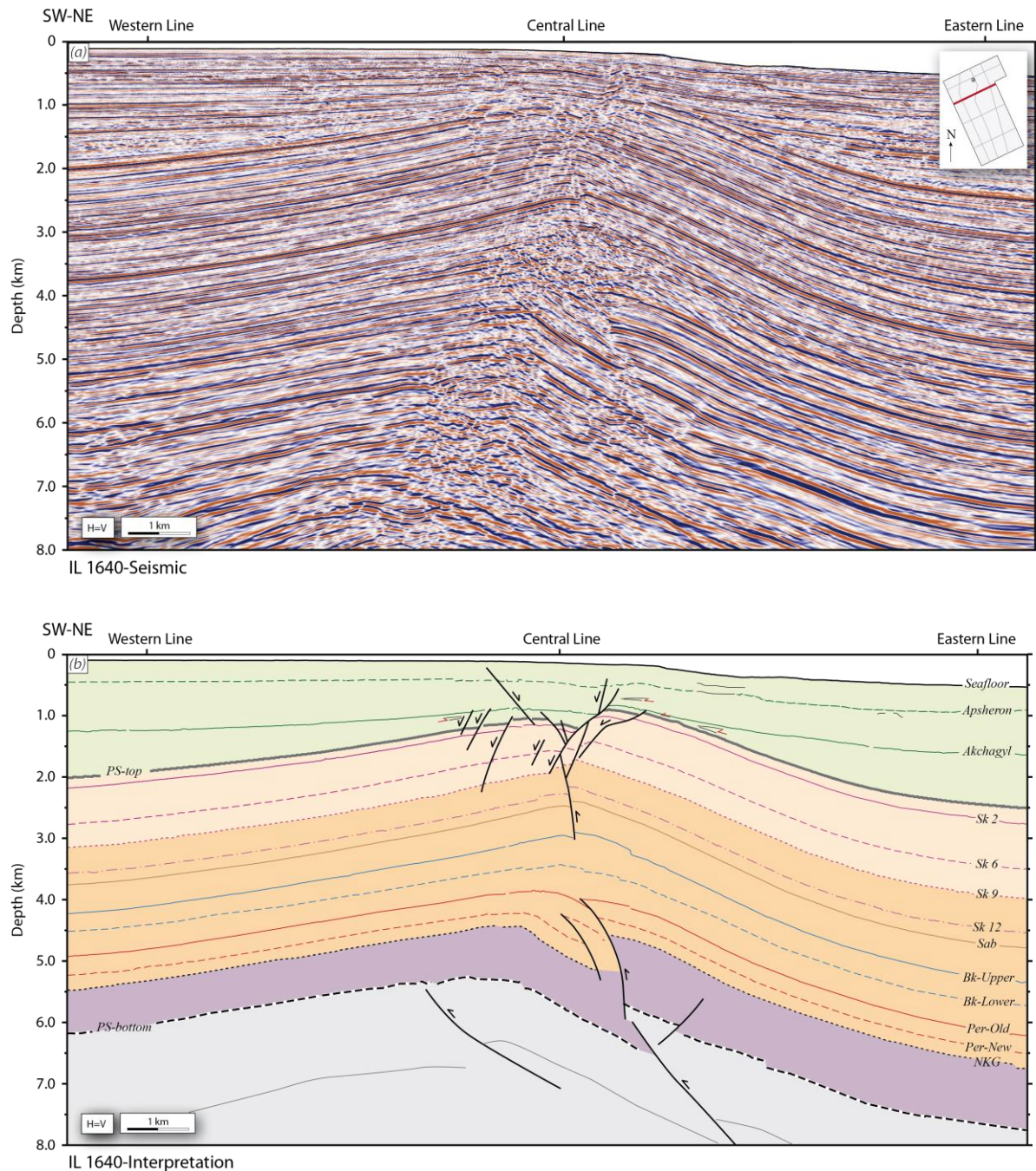


Figure 5.4: Seismic IL 1640, (a) non-interpreted and (b) interpreted. Inset map in (a) shows IL position, located within the saddle domain of the KAD fold. Abbreviations and symbols as are summarized in Figure 5.2.

5.1.4. IL 2000

The IL 2000 (*Fig. 5.5*) represents the best example of the northernmost sector of the KAD structure, close by the AD-1X well, which transversally crosscuts the Northern Culmination (Santos Betancor and Soto, 2015). The wavelength of the anticline in the northern sector is ~5.2 km and the fold amplitude is 0.6 km. The inspection of the attitude of the fold flanks evidences a clear asymmetry within the deformed sequences. The fold structure presents long flanks that dip 20°W and 30°E. The fold shows a gentle structure (the interlimb angle is ~125°), and a steeply inclined to upright anticline vergent to the East (axial surface dips 85°W).

The fold culmination is pierced by a mud structure that corresponds to a collapsed diapir. Geometry corresponds to a teardrop diapir highly symmetrical, approximately 2.3 km-wide and 2.5 km-tall. Mud structure presents well-defined boundaries that correspond to normal faults. The crest of the diapir is wavy-shaped, of ~2.2 km length, and it is broken by planar normal faults that progressively converge downwards up to 2 km depth. From 2 km to 3.5 km depth the neck of the diapir considerably squeezes and disappears without any evidences of the shale pedestal or the source layer in this section. A sub-vertical motion plane is recognized in deeper levels with a moderate reverse displacement and probably a strike-slip component. This fault zone is interpreted as a weld structure.

PS units, from the PS-bottom to the Pereryva-Old, constitute an antiformal with a sharp hinge. The hinge becomes more rounded, cored by the mud teardrop, in the shallower positions. A subtle onlap pattern is recognized in the PS-top clearly evident to the East. The Akchagyl Unit is fractured and almost absent on the crestal domain, above the mud diapir, also accompanied by onlap pattern, especially evident in the eastern limb. Overlying reflectors are continuous in the complete section. The Apsheron Unit as well as the seafloor are also displaced downwards on the crest of the structure and dips to the East towards the deeper basin.

The PS multilayer is, respectively, 4.35 and 5.2 km-thick to the West and East. The Post-PS units are constituted by 2.2 km of sediments in the western domain, which progressively thins towards the crestal area (0.85 km-thick) and again thickens up to 2.2 km in the eastern limb. The Akchagyl Unit is almost absent on the top of the diapir.

In detail within the PS units, the sequence between the PS-bottom to the Sk 9 top is 3.15 km-thick and 3.8 km-thick, respectively, in the western and eastern flanks. Upper units to the PS-top constitute 1.2 and 1.4 km-thick packages.

In the anticline limbs, the lower and upper boundaries of the PS dip constantly 20°W in the West, whereas in the East layer dip diminishes upwards, from 40°E to 25°E. The Post-PS sequence dips usually <10° (E and W). High dips are mainly located in the eastern flank. The seafloor is majorly flat, except in the transition towards the inner SCB, that becomes 4°E dipping.

A pair of normal faults limits both margins of the mud diapir in the anticline crest. They depict a symmetric graben constituted by conjugated high-angle faults (dip is over 65°) that progressively converge downwards up to 2 km depth along the top of the Sk 12, interpreted as a result of crestal collapse. Most significant structure propagates up to 0.1 km of depth in the West, whereas the eastern fault has been sealed at ~1 km depth. Both faults reach the top of the Sabunchi Unit. Normal fault displacement is also detected in the seabed. The inner parts of the KAD anticline are crosscut by a high-dipping fault without a significant displacement.

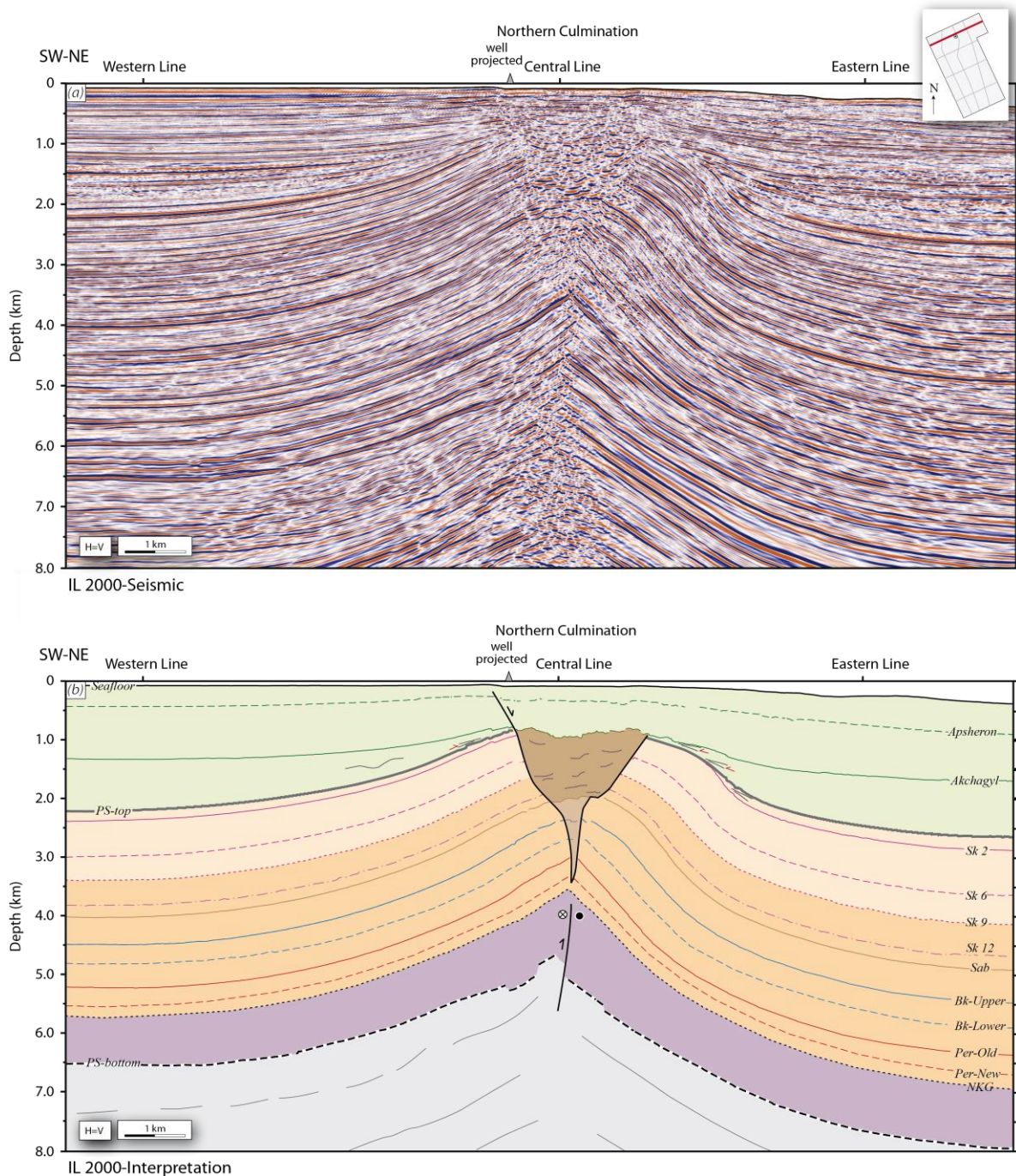


Figure 5.5: Seismic IL 2000, (a) non-interpreted and (b) interpreted (Santos Betancor and Soto, 2015). Inset map in (a) shows IL position. Abbreviations and symbols as are summarized in Figure 5.2.

5.1.5. Western Line

The Western Line is a composite section that crosscuts the studied dataset and the already describe ILs in the western domains (Fig. 5.6). Two fragments with different directions compose the arbitrary section. The northern area is a N-S directed section whereas it becomes NW-SE southwards. In this section, the uplifted area in the PS coincides with the Present-day Southern Culmination.

The Western Line depicts a contrasting geometry to the PS and Post-PS. Taking for reference the PS, the section shows an apparent homogenous structure, with parallel layers that depict a wide anticline with 20 km of wavelength and 0.3 km of fold amplitude,

accompanied by a broad syncline in the North. Flanks dips are $<10^\circ$ to the North and South. The angle between fold limbs is $<170^\circ$ (very gentle anticline) and the axial plane is sub-vertical (upright fold). By contrast, the Post-PS shows a bathymetric slope that falls down towards the South with a talus break located around the IL 1140. The lower strata of the Akchagyl Unit onlap the PS-top surface. The Apsheron layers show abundant downlapping geometries. In the platform area, the Apsheron reflection corresponds to a truncating surface with toplap terminations (see Fig. 5.6).

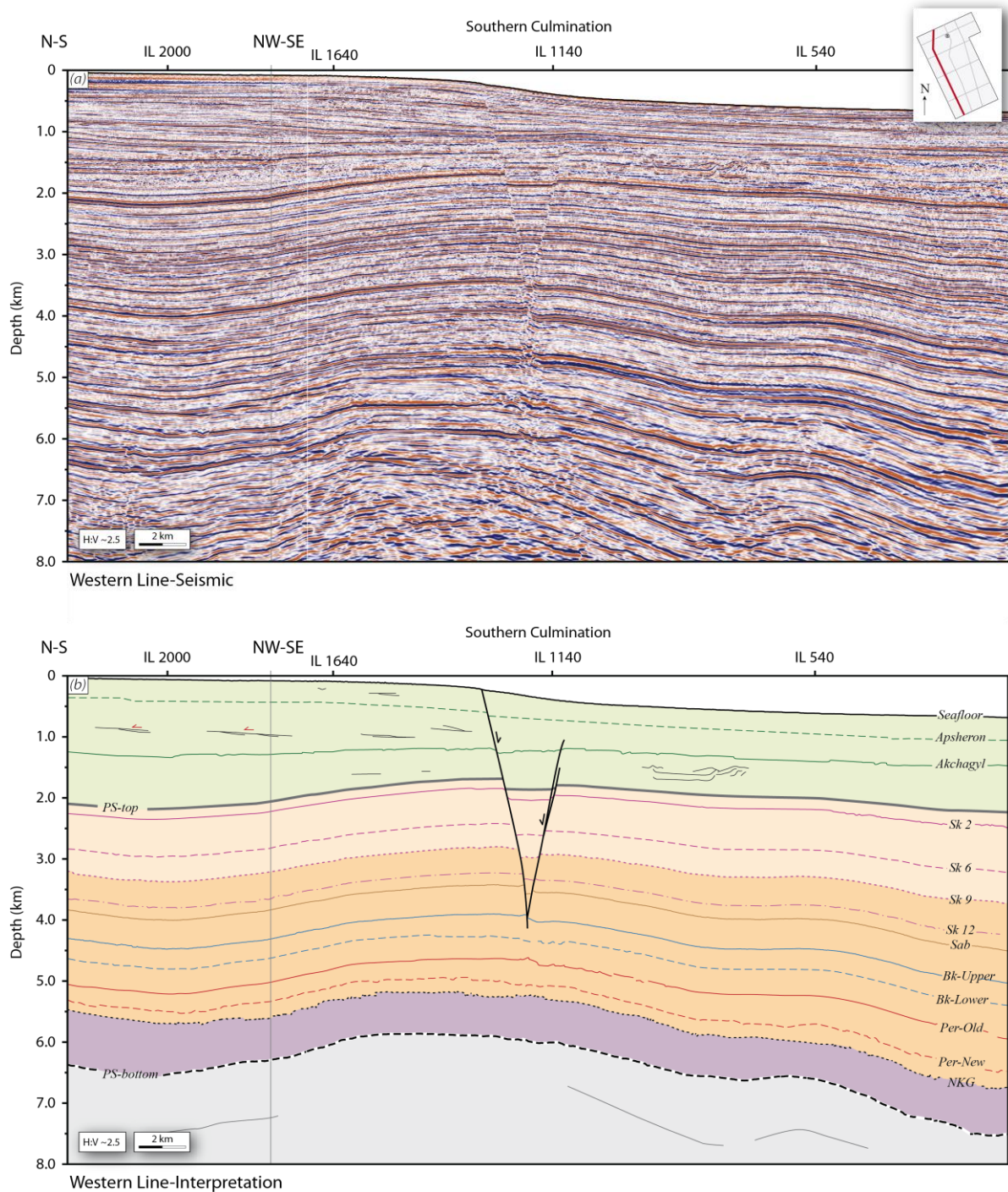


Figure 5.6: Seismic arbitrary Western Line, (a) non-interpreted and (b) interpreted. Inset map in (a) shows IL position. Some internal structures are recognized within the Akchagyl Unit that correspond to mobilized bodies. Abbreviations and symbols as are summarized in Figure 5.2.

A marked change in thickness is observed in *Figure 5.6b*, compiled from previous data presented in seismic inlines (see *Figs. 5.2 to 5.6*). Thus, the stratigraphic thickness of the PS is higher in the North (4.35 km, 4.1 km, 4.15 km and 4.6 km, from ILs 2000 to 540, respectively). Nevertheless, the Post-PS appearance evidences higher thickness in the Northern Culmination (2.1 km-thick, in the IL 2000), whereas it decreases to 1.85 km, 1.45 km (coincident with the Southern Culmination dome) and 1.4 km, respectively southwards. Maximum thickness in the Post-PS units occurs above the PS syncline.

In detail, the sequence between the PS-bottom and the Sk 9 varies from 3.15 km-thick in the IL 2000, to 3 and 3.05 km-thick in the central lines (ILs 1640 and 1140), and finally, 3.3 km-thick in the IL 540. By contrast, the uppermost PS sequences are 1.2 km-thick in the position of the ILs 2000 and 1640, 1.1 km of thickness coincident with the IL 1140 and 1.3 km in the IL 540.

An isolated pair of antithetic normal faults is present in the centre of the seismic profile. Faulting affects the top of the Balakhany Unit and progress upwards up to the seafloor in the Southern Culmination domain.

5.1.6. Central Line

The Central Line is composed by three segments in the central sector of the seismic survey (*Fig. 5.7*). The composite section majorly crosscuts the structure in a NW-SE direction and partially it follows a N-S strike in the saddle zone between culminations (Santos Betancor and Soto, 2015).

The overall structure corresponds to an open-to-gentle anticline, and the Central Line shows both fold culminations (*Fig. 5.7*). Within the PS, the Lower PS to the Sk 9 top, units are a tabular package; whereas the upper Sk 6 and Sk 2 units show a subtle thinning and onlapping along fold culminated domains. Marked wedge geometry is observed within the Post-PS group, especially along the Southern Culmination, whereas flat strata are predominant northwards. Onlap geometries are particularly well-developed in the Akchagyl and Apsheron units within the Post-PS package. The anticline geometry is intensely affected by diapirism and faulting, especially within the PS layers, and therefore, the resultant fold geometry is conditioned by these structures.

Fold wavelength is <4 km and 17 km in the Northern and Southern culminations, respectively, whereas fold amplitude is 0.55 km in both domains. Both culminations are asymmetric. Average dips within the PS are <10°N-S with maximum values of 25°S in the Southern Culmination. This is an upright fold.

Mud diapirs pierce each culmination domain, as were illustrated in IL 1140 and IL 2000 (*Figs. 5.3 and 5.5*, respectively). In both cases, they correspond to teardrop structures. The northern diapir (*cf. Fig. 5.5*) is a collapsed structure, limited by normal faults and is buried below the PS-top at 1 km depth. The horizons above the diapir depict an almost flat crest of over 3.5 km length. Collapse faults in the diapir margins fracture the sequence up to 2.5 km depth where the diapir disappears. In this section, there are no evidences of mud feeder channels or shale pedestals or even welds. The southern diapir extrudes up to the Akchagyl Unit. It does not have net boundaries with the surrounding sediments, which even seem to continue within the mud diapir. These observations might indicate a high fluid-content of the mud. The top of the structure is undulated and 1.75 km-long. The diapir neck is sited at 2.5 km depth within the Pereryva Unit, with any connection to underlying features.

Thickness estimations for the PS sequences correspond to 4.2 km (IL 2000), 5.2 km (IL 1640), 4.3 km (IL 1140), and 4.8 km (IL 540), from North to South, respectively. In northern sectors, Post-PS are 0.85 km-thick (IL 2000), 1 km occur in the centre of the image (IL 1640), whereas values change southwards to 0.5 km-thick (ILs 1140 and 540).

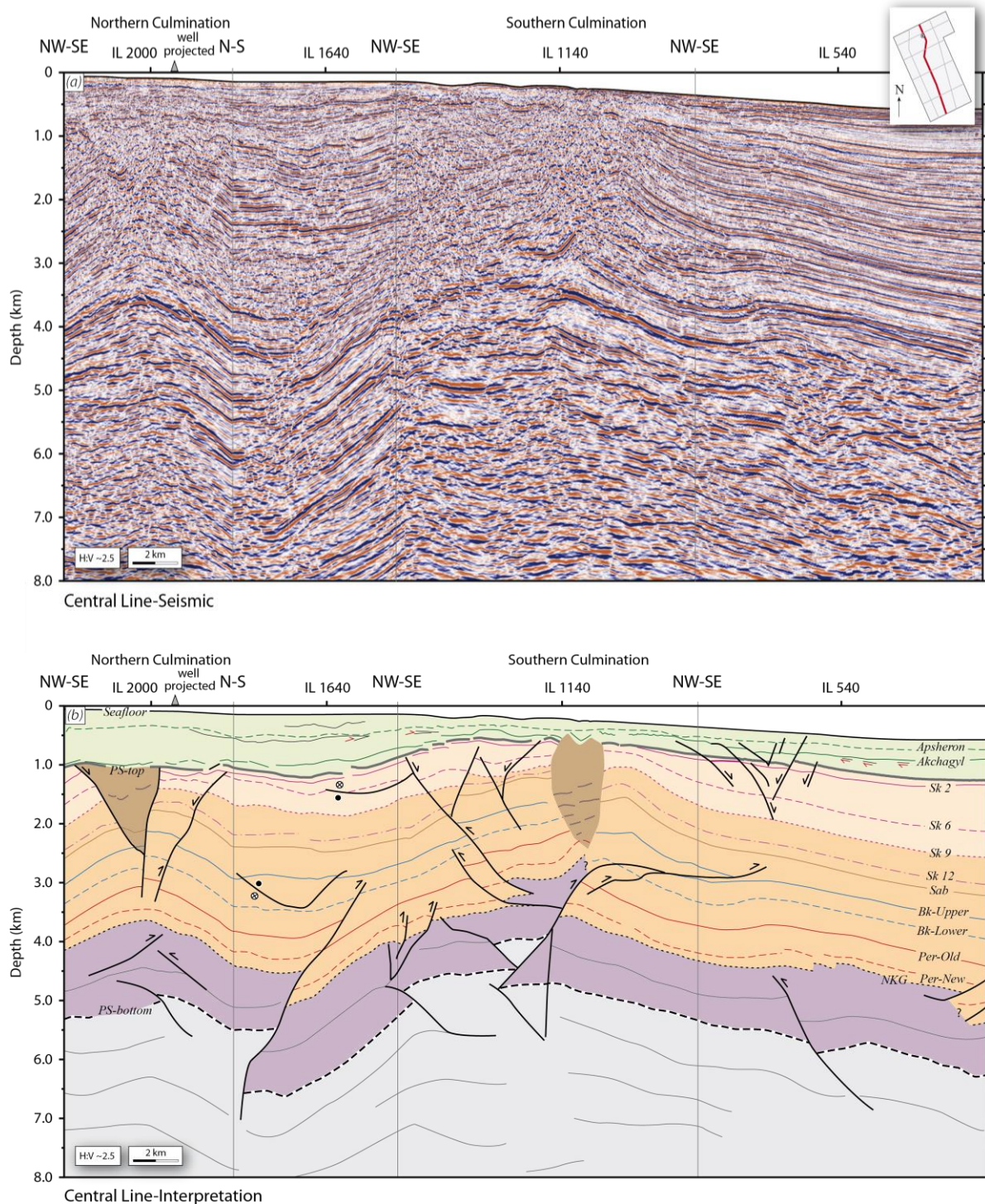


Figure 5.7: Seismic arbitrary Central Line, (a) non-interpreted and (b) interpreted (Santos Betancor and Soto, 2015). Inset map in (a) shows IL position. Abbreviations and symbols as are summarized in Figure 5.2.

Stratigraphic thickness variations within the PS units are really noticeable. The interval between the PS-bottom and the Sk 9 Unit is: 3.7 km-thick measured in the IL 2000, 4.55

km-thick in IL 1640, 3.7 km-thick in the IL 1140, and 3.6 km-thick in IL 540. Upper units to the PS-top (Sk 6 and Sk 2 formations) constitute: 0.5, 0.65, 0.6, 1.2 km-thick, respectively in the same positions, from North to South.

Central Line is intensely affected by faulting. Reverse faulting is widespread in the deeper levels, coinciding with the two fold cores. Reverse faults affect mainly the Lower PS interval, but they even extend upwards up to the Sabunchi Unit. Normal faults also occur in this section and tend to concentrate in the outer arc areas of the two fold culminations. Most of these fractures are probably conjugate faults and affect the youngest sediments, from the Pereryva Formation towards almost the Present seabed. Some of these normal faults extend downwards and change to have reverse displacements. Two of these faults occur at: 1) from 1 to 3.5 km depth at the Northern Culmination, close to the well position; and 2) between 0.75 and 3.25 km depth in the Southern Culmination.

5.1.7. Eastern Line

The Eastern Line shown in *Figure 5.8* is composed by two major sectors. In the North, the direction of the seismic transect is NW-SE up to IL 1640, and continues southwards with a NW-SE orientation.

PS formation depicts a very broad folded geometry, whereas the Post-PS group shows wedge geometry, with maximum thickness in the North. This section is an open and symmetric anticline, wide (17 km of fold wavelength), with very low amplitudes (0.25 km). Fold limbs along the top of the PS are mostly planar, smooth and sub-horizontal. This is a very gentle and upright fold. Some scars of gravitational mobilized bodies in the top of the Apsheron Unit are recognized, and in similar positions in the proximities of the seabed, which is also affected.

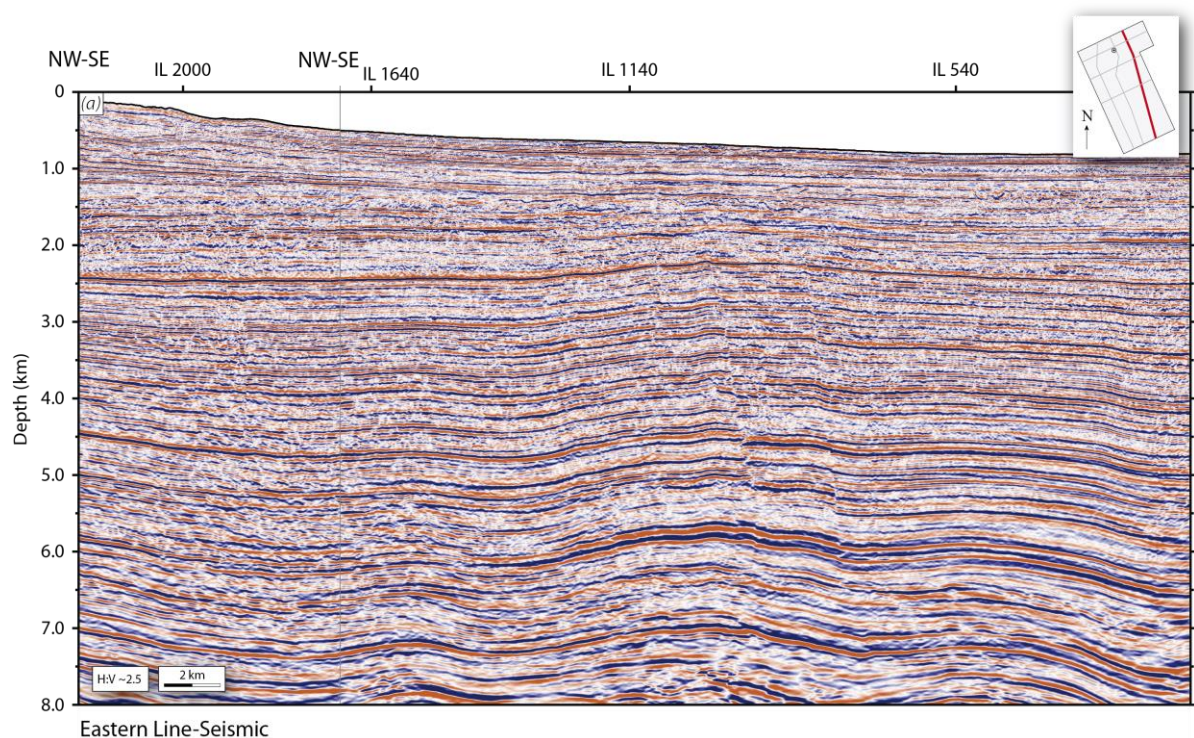


Figure 5.8: Seismic arbitrary Eastern Line, (a) non-interpreted and (b) interpreted. Inset map in (a) shows IL position. Some concave scars are distinguished in the top of the Apsheron and Gelasian formations. Abbreviations and symbols as are summarized in *Figure 5.2*. Continuation in the next page.

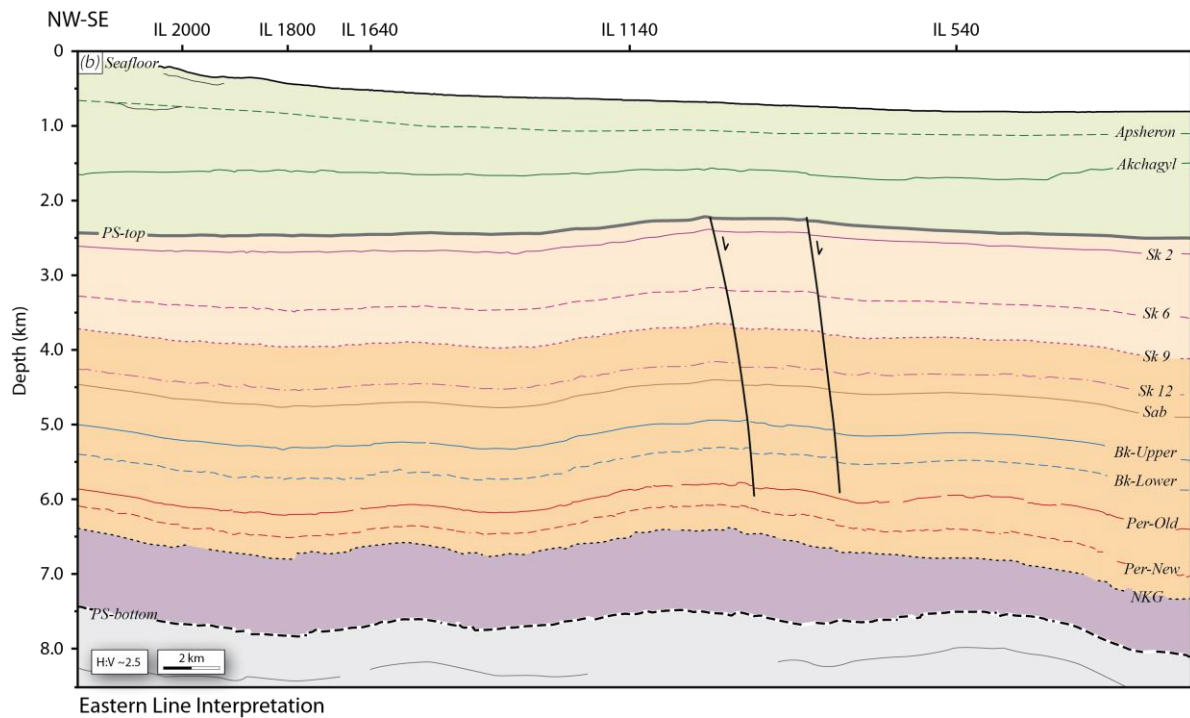


Figure 5.8: Continuation.

Stratigraphic thickness variation along the Eastern Line evidences low discrepancies between northern and southern sectors. Thickness of the PS is mostly constant, with subtle thinning to the S: from 5.35 km in the vicinities of the IL 2000, 5.3 km in the IL 1640, 5.25 km in the IL 1140, to 5.15 km coincident with the position of the IL 540. The Post-PS series are quite thick in the vicinities of the IL 2000, with up to 2.2 km but decreasing is observed in central (1.9 and 1.65 km-thick, in the ILs 1640 and 1140, respectively) and southern areas (1.6 km-thick in the IL 540).

In detail, the package between PS-bottom and the Unit Sk 9 decreases southwards. Measurements correspond to 3.95 km-thick in the IL 2000, 3.9 km-thick in the IL 1640, 3.8 km-thick in the IL 1140, and 3.75 km-thick in the IL 540, whereas the overlying units from the Sk 9 to PS-top have 1.4 km as a mean and rather constant thickness value (only in the IL 1140 reaches up to 1.45 km).

A pair of S-dipping normal faults is recognized in the central sector. Faults are large and crosscut the interval between the top of Pereryva-Old Unit to the PS-top, although substantial displacements are not observed.

5.2. Horizontal Slices

To support the interpretation of the overall structure vertical slices are accompanied by two key horizontal sections that crosscut the KAD anticline at 4 and 2 km depth, also described in Santos Betancor and Soto (2015). We have chosen 4 km and 2 km slices due to their relevance in the geometrical description and due to the continuity of horizons at that depth. Selected slices are shown in *Figures 5.9* and *5.10* as interpreted and non-interpreted images.

5.2.1. Depth Slice at 4 km

The general geometry of the KAD in *Figure 5.9* corresponds to an elongated and tight anticline closely flanked by neighbour synclines. The axial trace is sigmoidal and trends NW-SE (Santos Betancor and Soto, 2015). The structure has an elliptical shape of ~11 km wide and ~40 km long along NW-SE. At 4 km depth, both Northern and Southern culminations are clearly observed in two different domains, intersected by ILs 1140 and 2000 (*cf. Figs. 5.3* and *5.5*, respectively) and the arbitrary Central Line (*Fig. 5.6*). The IL 1640 separates both culminations through a small saddle zone (*cf. Fig. 5.4*).

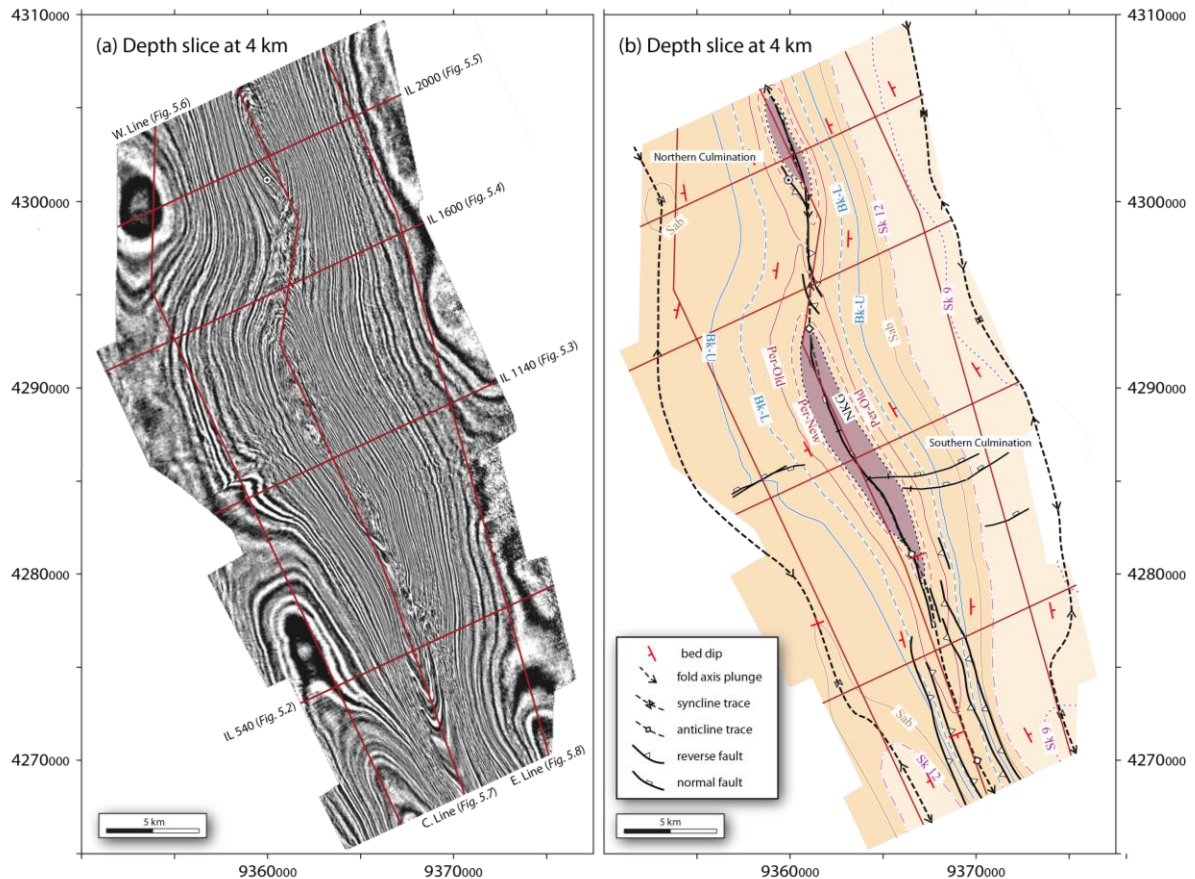


Figure 5.9: Seismic depth slice of the KAD area at 4 km depth, (a) non-interpreted and (b) interpreted (Santos Betancor and Soto, 2015). Colour code for the seismic signal is positive amplitudes in black and negative amplitudes in white. Arbitrary lines are denoted as C, E, and W. Line for Central, Eastern and Western lines, respectively. Balakhany Unit is divided into Lower (Bk-L) and Upper (Bk-U). Abbreviations are summarized in *Figure 5.2*.

The Southern Culmination extends approximately 7.5 km along NW-SE, and integrates the IL 1140 in the centre. The IL 2000 constitutes the centre of the visible part of the Northern Culmination, which measured length of ~2.8 km is minimum restricted by the end of the dataset. Fold width in the southern and northern domains at 4 km depth is 0.5 km and 0.3 km, respectively. The crest of the Southern Culmination is strangulated in the southernmost sector closely to the position of the IL 540 (*Fig. 5.2*).

The KAD anticline has periclinal areas that correspond to the hinge intersection of the fold with this horizontal section that accompany both culmination domains. Double-plunge orientation changes consistently in the periclinal domains, dipping both to the NW and to the SE. Due to the dimensions of the studied area it is not possible to identify the northern

prolongation of the fold hinge in the Northern Culmination. The dip of the anticline axis diminishes progressively to the SE in the Southern Culmination.

The anticline is flanked by two synclines and four elongated depocentres grouped in pairs that correspond to rim synclines. Synclines dimensions are difficult to establish because the studied block does not illuminate completely their flanks. The western syncline is more evident, where also a smoothed culmination area separating two depression domains is subtly identified, coinciding with the Southern Culmination. In the eastern syncline, a culmination domain is also inferred between both depocentres, although it is not completely illuminated by the seismic dataset. Both synclines run parallel to the Northern to the Southern culminations.

According to our interpretation, numerous faults crosscut the PS series at 4 km depth (*Fig. 5.9b*). The most significant fault is a NW-SE normal fault located along the KAD fold crest in the Southern Culmination coincident with the position of the axial trace. The fault extends ~17 km along the fold core and is a curve-to-planar normal structure that locally changes to a vertical fault. Dip oscillates between 30-40°E in the South and to 70-60°W northwards.

The Northern Culmination is also crosscut by a sigmoidal NW-SE 8 km-long fault with variable regime and dip orientation. Fault is reverse and highly-dipping (60°E) in the vicinities of the IL 1640, becomes vertical northwards and finally it turns into a normal fault in the northernmost regions dipping 70°E.

Two pairs of planar NW-SE reverse faults occur in the southernmost area and run parallel and along the fold limbs, with a maximum distance of 12 km. These faults correspond to conjugate and reverse faults accompanying the kink-like fold shown in *Figure 5.2*.

SW-NE-directed faults are observed in both fold flanks. They are planar, normal faults that usually converge towards the fold core at the Southern Culmination. As they approach to the fold core in the eastern flank, they become sub-vertical faults. In the western flank, two conjugated antithetic faults are immediately located to the North of the IL 1140 merging at this depth.

5.2.2. Depth Slice at 2 km

The image of the folded structure at 2 km depth in *Figure 5.10* evidences a wider anticline (fold wavelength of 7.5 km) than in the horizontal section at 4 km depth (*Fig. 5.9*). Fold width at 2 km depth is 14 km measured across the Southern Culmination (IL 1140, in *Figure 5.10*) and 7 km in the Northern Culmination (IL 2000, in *Figure 5.10*). Fold amplitude was measured along the Sk 12, and values correspond to ~5.5 km and ~3.7 km in the southern and northern domains, respectively (Santos Betancor and Soto, 2015).

Mud structures are locally present in the KAD fold at 2 km depth in the centre of both culmination zones, as it was previously seen in ILs and composite sections of *Figures 5.3, 5.5 and 5.6*. In the Northern Culmination mud diapir depicts an elongated shape in horizontal section with 2 km-long and ~0.75 km wide. In the Southern Culmination the mud structure is a relative rounded structure in plan view, with around 0.75 km of diameter, and is limited by faults. It is important to notice that mud structures are not present in the southernmost areas (for example, in the IL 540, *Fig. 5.2*) or in the surroundings of the saddle zone.

Four synclines are recognized parallel disposed to the anticline axe. The reflectors within the eastern clearly depict two synclines, both composed by two depocentres.

Numerous faults previously described in *Figure 5.9* extend upwards and affect the folded sequence at 2 km depth. New structures are observed at this depth and correspond to different crestal faults. These faults have a distinctive orientation and structural position identified over the crest of both anticline culminations. They show a nearly radial distribution, as WSW-NNE and NNW-SSE structures, convergent into the fold crest that does not extend downwards. They are normal faults with planar and curved traces, up to 5 km-long that converge towards culmination domains and show occasionally complex crosscutting relationships that change along strike. This type of mutual crosscutting relationships is typically developed under conjugate normal faulting conditions (*e.g.*, Ferrill *et al.*, 2000). A clear example is illustrated in the Southern Culmination in *Figure 5.2* around 1.4 km depth, and it is partly observed in the Northern Culmination.

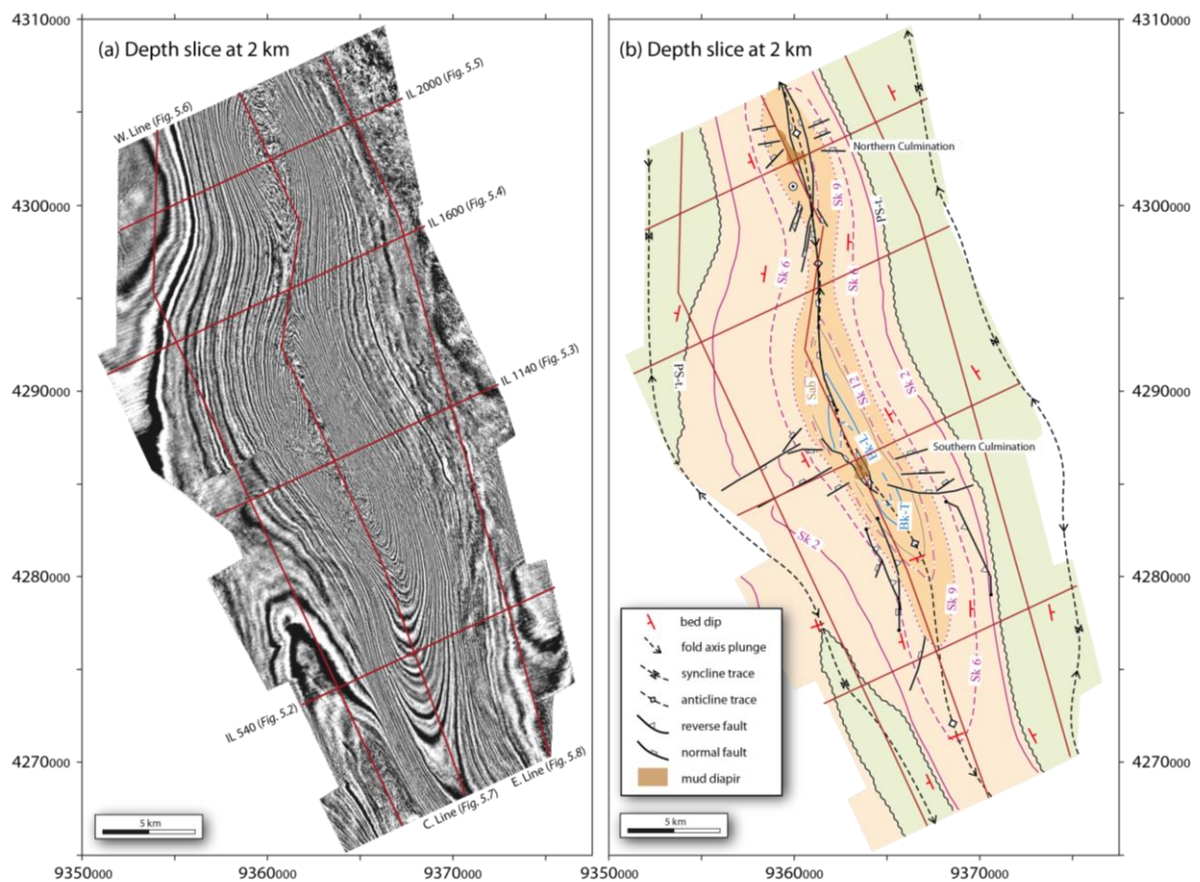


Figure 5.10: Seismic depth slice of the KAD area at 2 km depth, (a) non-interpreted and (b) interpreted (Santos Betancor and Soto, 2015). Black-filled circle represents the tip line of fault structures. Colour code for the seismic signal is positive amplitudes in black and negative amplitudes in white. Abbreviations are summarized in *Figures 5.2* and *5.9*.

In the Southern Culmination in *Figure 5.10*, a large NW-SE normal fault runs along the fold crest, similarly to the observations done at 4 km depth (*Fig. 5.9b*). This structure is a single fault with a total length of 9-10 km. In the Northern Culmination, it diverges into two splay normal faults around the northern mud diapir. In the saddle zone, it corresponds to a curved fault that dips 60° W. In the vicinities of the northern diapir, the two fault branches are antithetic fractures dipping $<40^{\circ}$.

NW-SE faults locally affect fold flanks. They are planar fractures and occur between ILS 540 and 1140.

Perpendicular SW-NE structures observed at 4 km depth (Fig. 5.9b) achieve the Sk 2 Unit at 2 km depth (Fig. 5.10b). These fractures affect the Surakhany Horizon and do not crosscut the fold culmination or the trace of the western syncline. In the western limb, these faults bound a symmetrical graben with a total length of 5 km.

5.3. Structural Maps

A selection of eight structural tops maps (Fig. 5.11) are presented in this thesis as key horizons surfaces to complement the interpretation previously shown for selected lines and depth sections (Figs. 5.2 to 5.10) and to progress into the 3D description of the structure. Maps are displayed in pairs from the oldest units to the Present-day surfaces. We present both limits of the PS (PS-bottom and PS-top; Figures 5.11a and 5.11c), some tops within the Upper PS rocks (Pereryva-Old, Sabunchi and Sk 6, Figs. 5.11a, 5.11b and 5.11c), some tops in the Post-PS units (Akchagyl, Apsheron, Figures 5.11f and 5.11g) and the seafloor (Fig. 5.11h). The tops of the Sabunchi Unit and the PS multipackage is also presented in Santos Betancor and Soto (2015). Structural maps are accompanied by depth contours (in m).

The study of the selected structural surfaces let us to establish fold shape evolution in relevant time intervals combined with the structural relationships with mud diapirs. Our selection of surfaces looks for evaluating intermediate stages of the folding history.

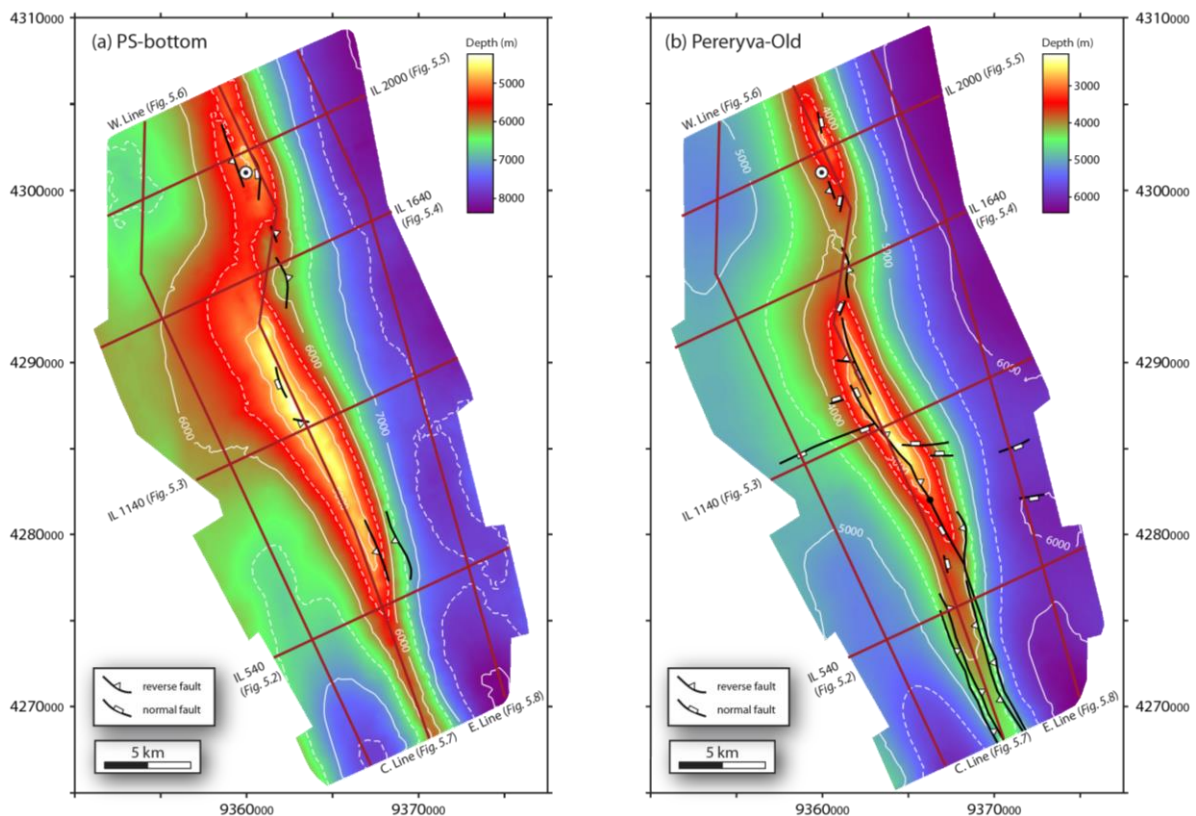


Figure 5.11: Contour maps expressed in meters (m) for (a) the PS-bottom, (b) the Pereryva-Old, (c) the Sabunchi (Santos Betancor and Soto, 2015), (d) the Surakhany 6 (Sk 6), (e) the PS-top (Santos Betancor and Soto, 2015), (f) the Akchagyl, (g) the Apsheron and (h) the seafloor surfaces. Black-filled circle represents the tip line of fault structures. The AD-1X well is shown in the North. Seismic lines names are abbreviated as in Figure 5.9. Continuation in the next page.

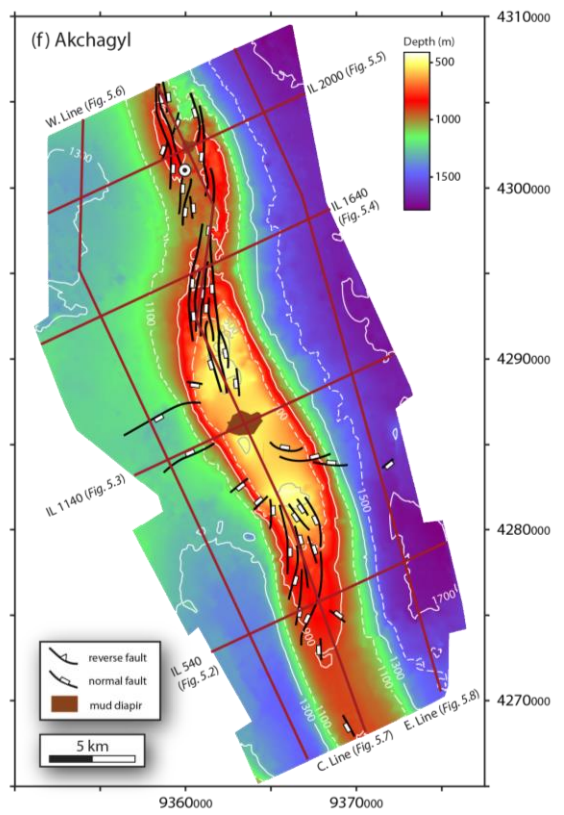
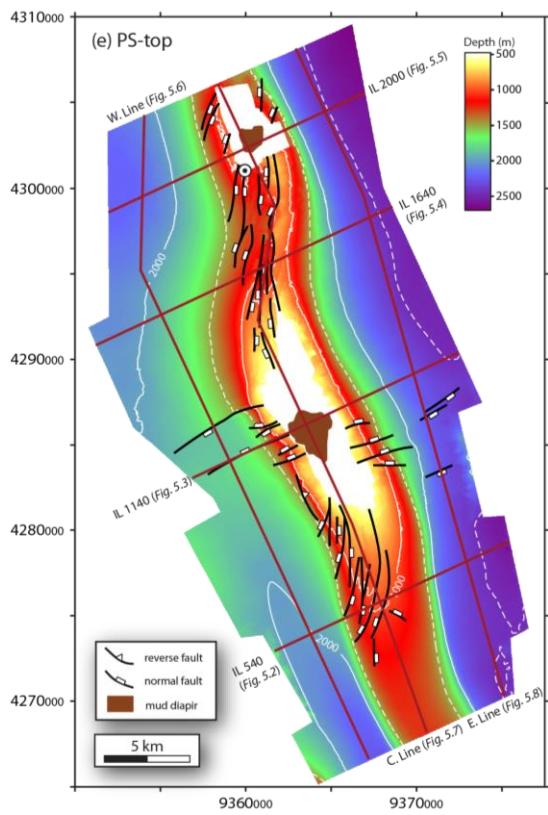
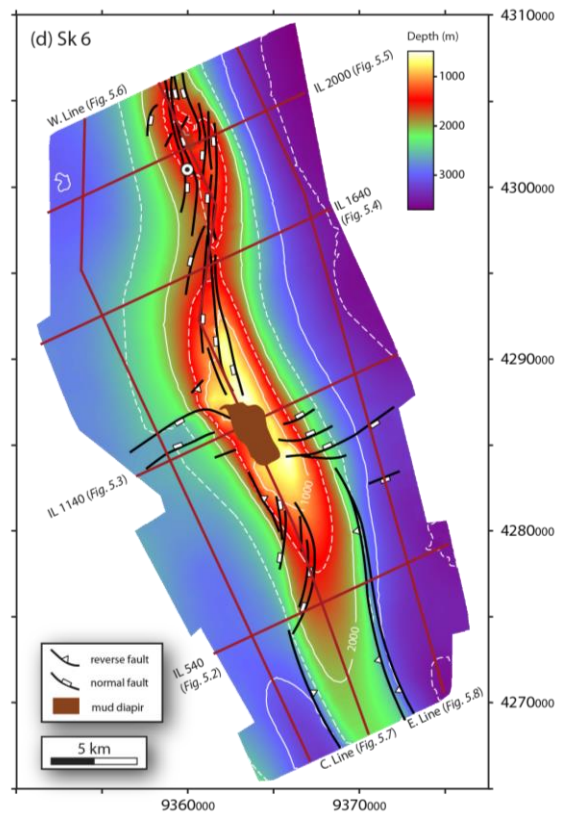
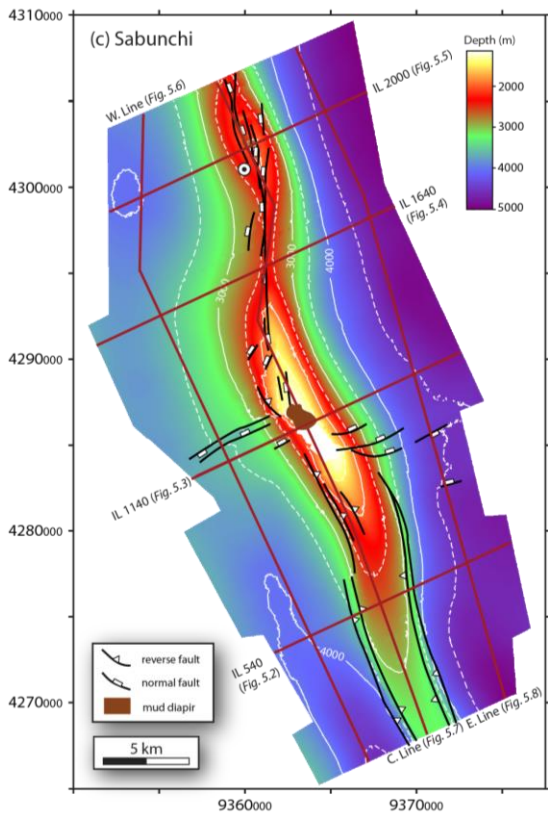


Figure 5.11: Continuation in the next page.

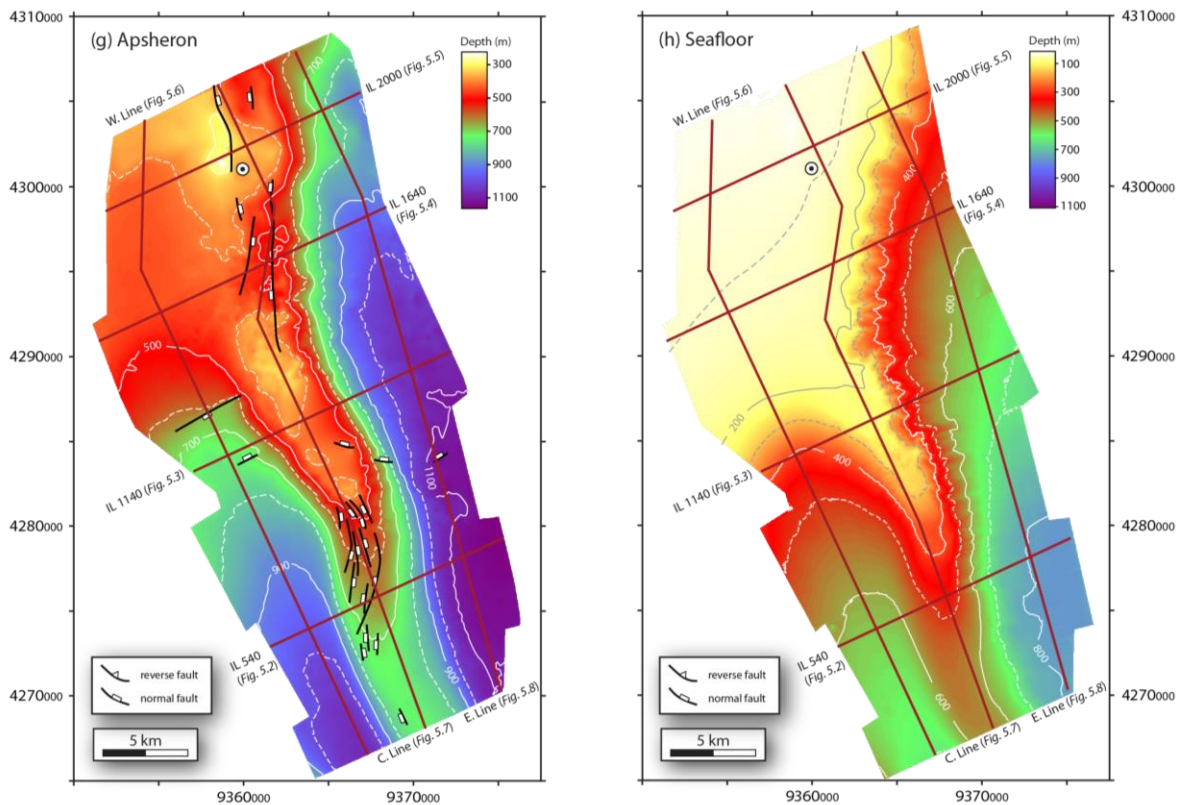


Figure 5.11: Continuation.

The PS-bottom has been selected to show the lowest and oldest boundary of the KAD anticline and the deformation pattern at that age. The Pereryva-Old shows an intermediate stage between the PS-bottom and the upper Sabunchi top. The latter surface evidences a change in the fold geometry. Evolution of shale-cored anticline is appreciated in the Sk 6 map, and in the PS-top surface, which is a key stratigraphical discontinuity in the region. The top of the Akchagyl Unit has been chosen due to its relevance for the folding history. The Apsheron top and the seafloor maps show an evident geometrical and structural variation of the structure and its most recent evolution.

5.3.1. PS-bottom

The PS-bottom surface evidences a double-culminated anticline with an elongated geometry very tight in the South. The surface clearly shows a non-cylindrical fold markedly asymmetrical (Fig. 5.11a). The axial trace is sigmoidal and NW-SE directed. The Northern Culmination depicts a small ellipsoid that connects with the southern domain via a N-S narrow path of over 5.5 km depth. The southern crest in the Southern Culmination is a large, shallower and elongated feature that becomes linear towards the South. Both culmination domains reach up to 5 km of depth. To the South, both flanks converge in a major periclinal closure. With this dataset, it cannot be established if this closure marks a major saddle domain or if it corresponds to a domain where the fold vanishes. The overall structure is double-plunged anticline dipping to the South and North in both culminations.

This surface evidences dissymmetrical limbs along the KAD-anticline strike, with a shallow western limb faced against a deeper eastern fold flank. Geometrical observations along the western limb show that it is longer and less dipping than the eastern flank. Wide fold flanks are observed in the North, whereas highly dipping and tight limbs are

developed in the South flank the anticline. In the proximities of the IL 240, the KAD anticline is bounded by two parallel synclines. The western depocentre is less deep than the eastern one and terminates close northwards (*cf.* Western and Eastern lines in *Figs. 5.6* and *5.8*).

Two NW-SE synclines accompany fold flanks, with a noticeable variation in their depth range with a shallower western trough with respect to the deeper, eastern syncline. The position of syncline and anticline culminations is coincident in the North although in the South, the depocenter is separated from the Southern Culmination, which is sited southwards. In this zone the PS-bottom is located at over 7.5 km depth, in contrast to 6.5 km depth in the North. The eastern syncline contains three troughs linearly disposed along the syncline trace that progressively turns N-S in the southernmost depocentres. These areas register the largest depths (up to 8 km) in rounded-to-elongated depocentres.

Few faults are recognized along the anticline crest in the PS-bottom surface. Most of the fractures are NW-SE directed. They correspond to planar and slightly curved faults in plan view (*cf. Fig. 5.7*), with varied regimes. Some reverse faults dip between 35°-65°W in the eastern fold flank and in the Northern Culmination, whereas in the saddle region they dip oppositely and achieve 70°. Most of these faults extend upwards, as it is shown in the depth slice at 4 km depth (*Fig. 5.9*).

5.3.2. *Pereryva-Old*

The structural map of the Pereryva-Old (*Fig. 5.11b*) highlights a more accentuated and symmetric fold geometry than previously described in the PS-bottom map (*Fig. 5.11a*). Fold is a tight, double-culminated anticline surrounded by tight and parallel synclines, mostly coincident with the fold trace established at 4 km depth (*Fig. 5.9*). Both culmination domains are closer. Minimum depths are reached in these zones with 3 km and over 2.5 km in the North and South, respectively.

The Pereryva-Old map depicts a continuous, highly dipping eastern limb against a less dipping western fold flank. The western limb is wider along both culminations whereas it becomes narrow towards the South. This evolution is similar to the one observed in the eastern limb.

The structural pattern of this surface contrasts with the PS-bottom. Faulting is widespread in the Pereryva-Old structural map, especially in the Southern Culmination and propagates, both to the saddle zone and southwards. The contour map is similar to the horizontal slice at 4 km, related to fault structures and their geometry, regime and position (*Fig. 5.9*).

Different NW-SE-directed faults run along the fold crest and run parallel to the fold axis. They are well developed in the Southern Culmination and correspond to planar fractures, with both normal and reverse regimes that predominantly dip to the East. Maximum dips are reached in the Southern Culmination with up to sub-vertical planes. Towards the South, it is distinguished two pairs of NW-SE reverse conjugate faults. They occur at both fold flanks as large and planar fractures that dip oppositely over 45° (*cf. Fig. 5.2*).

There are also normal faults trending perpendicular to the fold axis. These surfaces are SW-NE and were also identified in the horizontal seismic slices (*Figs. 5.9* and *5.10*). They occur in the surroundings of the Southern Culmination in central areas of the fold and extend to both synclines. These faults are planar to slightly curve and dip in average 65°.

5.3.3. Sabunchi

The geometry observed in the structural map of the Sabunchi surface (*Fig. 5.11c*) shows a wider fold compared with the previous surfaces (*Figs. 5.11a* and *5.11b*), especially in the southern region (see Santos Betancor and Soto, 2015). Sabunchi is intruded in both crestal domains by mud diapirs. The Northern domain in the Sabunchi surface depicts a non-bulged region that faces against the previously shown in the Pereryva-Old surface (*Fig. 5.11b*). The Southern Culmination increases its size. The anticline crest is well defined in the complete survey with a clear sigmoidal axis trace. The southern dome lies on over 1.5 km depth. Maximum hinge elevation in the Northern and Southern culminations varies between 0.5 km and 0.75 km, respectively.

Characteristics of fold flanks attitude and periclinal closures are similar to the ones described in the Pereryva-Old surface (*Fig. 5.11b*): eastern narrow limb against a generally wider western flank. Geometrical observations are consistent with a longer and less dipping western limb except in the vicinities of central areas, whereas the transition towards the Southern Culmination results in a short and highly dipping western limb.

Synclines are quite different from the deepest surfaces, with a noticeable necking of the south-western structure and the generation of a large unique depocenter along the eastern syncline. The deepest region is detected along the eastern syncline (>4.5 km) and also in the southernmost part of the western syncline, where depths are 4.5 km, against the 4 km in the northwestern depocenter.

Mud diapirs occur in both fold culminations as it was previously described at 2 km depth (*Fig. 5.10*). The northern diapir is elongated and narrow (~0.5 km-wide), and it is bounded by high-angle faults. The southern diapir has a rounded shape and is probably formed by fluid-rich mud. The limits of the Sabunchi reflection are here difficult to established, due to the abundance of scatter and discontinuous reflections. The resulting map reflects these interpretations in the Southern Culmination, with a narrow mud-diapir surrounded by a larger area without surface contours.

Faulting increases in the Sabunchi surface, and new fractures are also recognized. The NW-SE-oriented planar faults, which occurred along the saddle zone and parallel to the axis trace, have now a normal regime. Therefore, they change upward from reverse to normal faults (*cf. Fig. 5.11b*). They mainly occur in the saddle domain, with a total length of 13 km and dip around 55°W. In the Northern Culmination, these faults evolve as N-S symmetric graben with conjugate, concave fractures that dip in average 60°. They correspond to a crestal collapse structure (see *Figs. 5.5* and *5.7*). Southward of the Southern Culmination, the NW-SE reverse faults identified in the Pereryva-Old map along the KAD anticline flanks, diverge upwards in the Sabunchi surface.

SW-NE perpendicular fractures occur in the western fold limb as planar and conjugate extensional faults. The master fault in this narrow graben seems to be here the South-dipping fault. In the eastern flank, similarly-oriented faults are mostly dipping to the North and have a concave shape.

5.3.4. Sk 6

The main geometrical difference in the Surakhany 6 (Sk 6) map is the width of the KAD anticline along the complete trace (*cf. Fig. 5.11d*). Elevation difference between both culminations varies up to 1 km because in the northern domain it is over 1.5 km, whereas, the Southern Culmination is at 0.5 km depth. Syncline geometry is rounded in the western

case in comparison to the shape in the Sabunchi map (*Fig. 5.11c*). Disparity between depths is maintained.

Piercing of overpressured muds is widespread and interrupts the Sk 6 in the core of both culmination domains. Northern and southern mud diapirs geometry noticeably varies from the Sabunchi surface (*Fig. 5.11c*) and between the two, diapir and fold culminations. In the North, the mud diapir has changed its geometry as a rounded bulge with <0.75 km of width, whereas the southern diapir has noticeably increased its size. The southern structure is the largest and extends up to 55 km^2 of the Sk 6 surface.

Faulting is maturely developed in the Sk 6 surface. All N-S, NW-SE and SW-NE systems are widespread. New faults are grouped in the Southern Culmination as curved and normal faults that follow a SSW-NNE direction and do not affect the southern diapir. Comparing to the geometry depicted at 2 km depth, these faults prolong toward the fold crest (*Fig. 5.10*). These structures are observed in the *Figure 5.2* in the surroundings of IL 1000 as conjugate pairs over the fold crest with dips $<55^\circ$ with low displacements.

The NW-SE and N-S directed faults between both culminations are more numerous and extend southwards. These faults also observed in the Sabunchi surface (*Fig. 5.11c*) as normal and planar structures that become sigmoidal towards the Northern Culmination. In this surface, reverse faults in fold flanks are less important. A pair of fractures affects the eastern limb of this surface, whereas a single fault occurs in the West.

The size of the SW-NE faults is higher (>10 km-long). The western pair reaches the fold with two curved segments. In the eastern flank, the faults occur similarly to the geometry depicted in the Sabunchi surface.

5.3.5. PS-top

The folded PS-top is not present in the crestal domains of the Southern and Northern Culminations due to two different processes (*Fig. 5.11e*). These zones are characterized by piercing mud diapirs (Santos Betancor and Soto, 2015). It is also the focus of large erosive processes associated to this regional unconformity.

Maximum depths in the rim synclines are different between the western and eastern troughs. Both depocentres in the West reach the same depth of 2 km, whereas the eastern fold achieves 2.5 km. A deeper eastern fold limb is still recognized, but the western syncline is still more accentuated. Two elongated depocentres occur in the West at the same depth in the position of the southernmost and northernmost seismic lines. The eastern becomes narrower to the South (*i.e.*, fold wavelength decreases southwards).

Mud piercing is vastly developed in both culminated domains in the PS-top surface, particularly the southern diapir, which is $\sim 40 \text{ km}^2$. The northern structure is larger than in deeper levels (*Fig. 5.11d*) and occupies over 5 km^2 .

Most of the normal fractures observed in the Sk 6 map (*Fig. 5.11d*) extend upwards and displace more intensely the PS-top, both crestal and fold-flank structures. Normal faulting controls the PS-top surface.

Previous NW-SE axial faults are solely expressed as a single, large fault that connects with the N-S normal faults developed in the Northern Culmination. Contrasting dips with constant angles are maintained alike the observations done in the Sabunchi surface (*Fig. 5.11c*). Commonly, faults terminate towards the areas interrupted by erosional features in both culmination domains. Geometry of normal faults is here sigmoid. Maximum crestal fault displacement occurs in the saddle area, where the main normal fault creates a marked

surface displacement. This fault extends further, achieving a maximum length of 15 km with an average dip of 65°W.

The number of SW-NE, normal fault segments increased with respect to the underlying surfaces, appearing new and small fractures along fold flanks. They occur also as isolated fault strands located in the culminated domain of the eastern syncline.

Crestal faults recognized along the Southern Culmination have a SSW-NNE direction that changes to S-N. They are very abundant and curved and correspond probably to keystone-like collapse faulting in the fold crest shaped by different conjugate, normal faults.

5.3.6. Akchagyl

The Akchagyl structural map shows fold geometry with two broad culminations, more open than the geometry depicted by the PS-top surface (*Fig. 5.11e*). The Northern Culmination is collapsed, with low topography than surroundings (>1 km depth). This domain is largely flat with local bulges located at 500 m depth. The Southern Culmination is still affected by mud diapirism, but majorly the Akchagyl surface is disturbed by fluids.

Synclines have subtly changed their shape and relative depth. Now, the northwestern depocenter is less elongated than in the PS-top surface and the culmination domain between this and the southwestern depocenter has increased its size, developing local sinking. The eastern syncline is 400 m deeper than the western depocentre.

Faulting occurrence is similar that took place in the PS-top surface. A relevant difference is that N-S large and sigmoidal faults in the saddle domain become planar in the Akchagyl Unit. Perpendicular SW-NE structures are more curved and almost disappeared in the eastern limb (*cf. Fig. 5.8*). N-S crestal faults in the South are less abundant.

5.3.7. Apsheron

The Apsheron surface markedly departs from previous maps (*Fig. 5.11g*). The anticline trace decreases considerably its dimensions. Fold is buried in the northwestern sector and individual culminations are not easily recognized. The geometry of the anticline has become a sub-horizontal, shallow platform (~100 m depth) in the North that connects southwards with a partially buried fold with a sigmoidal trend. The anticline hinge occurs northwards beneath a NNE-SSW escarpment or talus, coincident with the Southern Culmination.

Synclines are hidden but its possible prolongation to the North occurs beneath the flat platform. In the South, deepening of the structures is produced simultaneously, with major depths of 0.95 km in the western syncline and 1 km in a large and single eastern depression. The fold crest in that position separates both depocentres at 0.85 km.

Faults are now concentrated in restricted areas along the anticline. Curved crestal faults only affect the southern sectors of the Southern Culmination in the S-N system, whereas extensive N-S faulting is almost vanished in the North. In this domain, conjugated normal faults crosscut the saddle region and isolate the Araz Deniz sector in the Northern Culmination. In both cases, planar and crestal faults, they crosscut the anticline in the same position as in the Akchagyl surface. Fold-flank faults which occurred with SW-NE directions during the deposit of the Pereryva-Old Unit (*Fig. 5.11 b*) are still active but with less relevance, especially in the East. In any case, these faults have a long-lived history of deformation because they extend upward deforming the Post-PS.

5.3.8. Seafloor

The northern area of the seafloor surface shows clearly a morphology not affected by folding (*Fig. 5.11g*). Advance of burial over the shelf extends southwards, but the geometry of the eastern slope reflects a steep fold flank. The slope talus is irregular as a result of instabilities along the seabed.

Depression domains are solely sited in the southernmost sectors in both synclines, whereas ancient synclines are disappeared. Depth differences are again high in the southern depocentres where depth oscillates between 600 m and 800 m, respectively in the West and in the East.

The Present-day surface deepens southwards, from a building up platform settled in the North. The platform seems to have grown up to Present, with a sedimentary progradation towards the E-ESE.

5.4. The KAD Structure

The figures used in this section are chosen to illustrate the fold and fault geometries in 3D, to determine the axial trace of the folds and to characterize diapir shapes and faults distribution along the seismic cube. The inspection of these images is also useful to reconstruct the evolution of the structures and to infer the locus of the mud conduits to feed the diapiric bodies.

5.4.1. 3D Fold and Faults Geometries

We have created some figures by combining seismic sections and some key contour maps (*Figs. 5.12 to 5.16*). Selected surfaces are displayed in three-dimensions and are illuminated from the East. They correspond to the PS-bottom (*Fig. 5.12*), NKG (*Fig. 5.13*), Sabunchi (*Fig. 5.14*) and PS-top (*Figs. 5.15 and 5.16*) surfaces.

PS-bottom

The 3D geometry of the PS-bottom surface is illustrated in *Figure 5.12* in combination with seismic ILs 240, 1000, 1640 and 2200. The contour map describes a tight, double-culminated anticline surrounded by parallel synclines. KAD anticline has a single-plane along the complete survey. The crest geometry is narrow and extends also to the South of the survey. The PS-bottom depicts an asymmetrical surface with a deeper eastern flank.

The southern IL 240 shows that the PS-bottom is in the core of the kink-like fold, similarly to the IL 540 (*Fig. 5.2*). Folded PS-bottom geometry in the Southern Culmination depicts a sharp anticline limited by steep flanks (*cf. Fig. 5.3*), which is shale-cored in upper parts. Along the Southern Culmination, fold trace is sigmoid and NW-SE, and deviates to N-S in the IL 1640 (*cf. Fig. 5.4*). Vergence changes from W-dipping to E-dipping. Finally, the IL 2200 above the PS-bottom illuminates a gentle anticline in the Northern Culmination.

Faulting in the PS-bottom is scarcely developed with predominance in the anticline crest of reverse faults, in agreement to the observations conducted in *Figure 5.11a*. *Figure 5.12* shows also significant changes of the faulting pattern from deeper levels to shallower positions in the KAD fold.

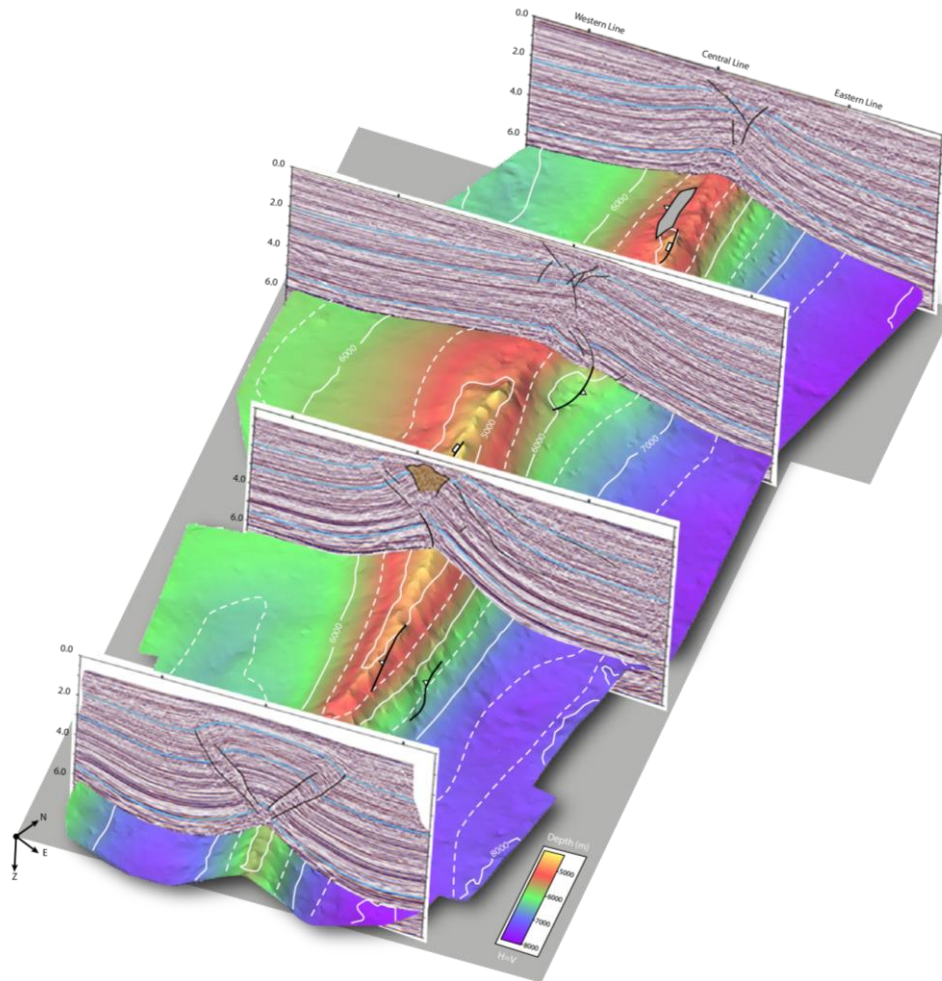


Figure 5.12: 3D panel of the PS-bottom surface intersected by vertical ILs 240, 1000, 1640 (Fig. 5.4) and 2200. Seismic horizons included in the seismic lines are NKG, Sabunchi and PS-top. Surface contour interval is 500m.

NKG

The 3D NKG surface is shown in Figure 5.13 in combination with the horizontal seismic slice at 5 km depth. The interpretation of vertical profiles is also included at both extremes of the dataset, partially in the IL 100 and along 9 km in the IL 2214. The NKG map depicts an asymmetric anticline with a single axial plane, with a marked plunge to the South. Northwards immersion also occurs in the northern termination of the Southern Culmination. Both culminations are continuously traced separated by a noticeable saddle zone. The Southern Culmination is topographically higher located at 3 km depth. Interpreted seismic lines in Figure 5.13 evidence how the fold anticline changes its geometry from a chevron structure in the South to a more rounded anticline in the North. Fold crest is narrower and sharper in the South and it becomes wider and more rounded-like to the North.

Accordingly to the image of the depth section, KAD-bounding synclines depict the classical shape of cuvettes, especially in the square-like south-western structure. Synclines are mostly rounded-to-elongated, linked by narrow path zones. The western syncline has a curve trace that runs parallel to the NW-SE anticline fold, with a more marked sigmoidal step within the synclines uplift. This syncline is composed by two depocentres separated by a narrow culmination. In the East, the syncline depicts a slight concave NW-SE-

directed trace. Eastern syncline is partially decoupled from the KAD anticline; the northern depocentre and the culminated area are slightly displaced southwards. Seismic layering suggests highly dipping sequences with minor dips in the synclines.

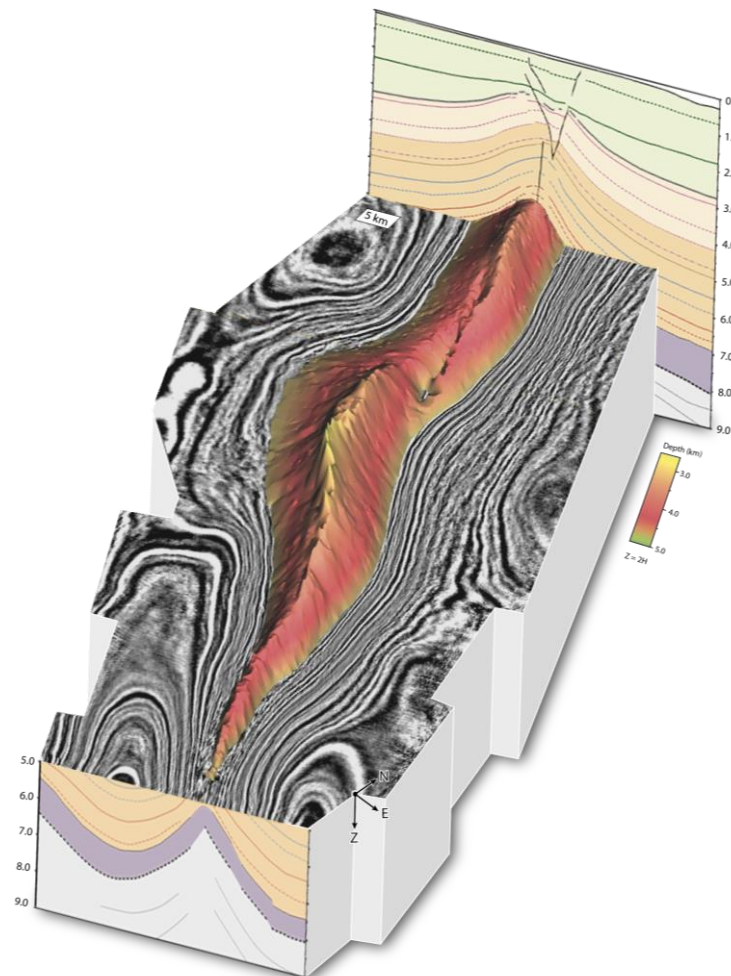


Figure 5.13: 3D seismic cube combining the depth slice at 5 km with the NKG surface. The interpretation of the IL 100 (in front) and IL 2214 (behind) are also included. Vertical scale is exaggerated two times in comparison to horizontal scale.

Although any fault trace is included in *Figure 5.13*, faulting also occurs in the NKG surface, as it is evident from the surface topography in the saddle area and our previous descriptions (*Figs. 5.2 to 5.8*). The relevant topographic high is planar and does not connect both culminations. This structure may continue northwards as is shown in the interpreted vertical section, where the NKG is lowly displaced. Accordingly to the 2D maps of the PS-bottom (*Fig. 5.11a*) and the Pereryva-Old units (*Fig. 5.11b*), this structure may have a reverse regime and dip to the West. We infer that it has also a strike-slip component (see *Discussion Chapter*).

Sabunchi

The perspective shown in *Figure 5.14* complements the previous description done with the Sabunchi structural contour map (*Fig. 5.11c*). This perspective view of the Sabunchi

PS-top

The 3D geometry of the PS-top surface is summarized here by two complementary figures. The first one, *Figure 5.15*, presents in perspective the PS-top surface accompanied by two depth slices located at 1.95 km in the South and at 1.14 km in the North. This panel includes also for reference two, bounding vertical sections, corresponding to ILs 100 and 2214. The second figure used to illustrate the PS-top geometry in 3D is *Figure 5.16*, which shows the same perspective of this surface but includes four seismic sections (ILs 240, 1000, 1640, and 2000).

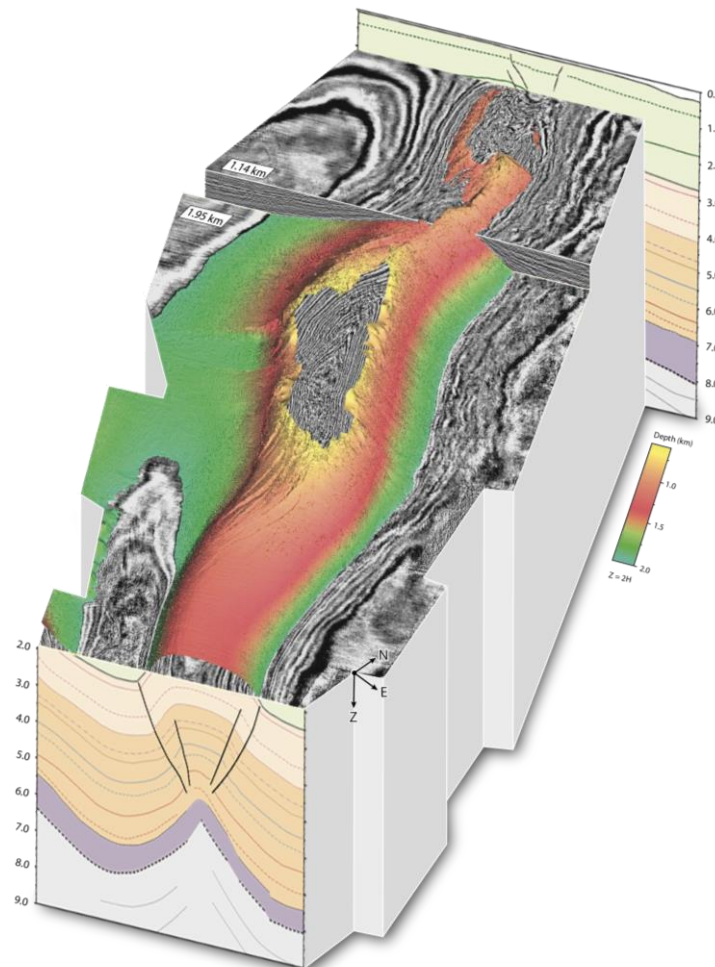


Figure 5.15: 3D seismic cube combining the depth slices at 1.95 km and 1.14 km with the PS-top surface. The interpretation of the IL 100 (in front) and IL 2214 (behind) are also included. Vertical scale is exaggerated two times in comparison to horizontal scale.

The folded PS-top surface has a rounded hinge in the South, with a sub-horizontal fold crest, and is limited by a highly dipping eastern limb and a low-dipping western flank. The PS-top surface is eroded in most of the Southern Culmination. This observation indicates most probably that erosion occurred in the post-PS epoch, coinciding with fold uplift. This surface is preserved in the Northern Culmination, which remains deeper probably because it was collapsed. This domain contains numerous, conjugated N-S-trending normal faults. Between both culminations, the saddle domain is intensely faulted and we interpret that the master fault there is a W-dipping normal fault that bounds an asymmetric graben.

Two mud diapirs and numerous faults deform the PS-top surface (*cf.*, Fig. 5.11e). Mud diapirs piercing the PS-top surface have an elongated and rounded shape and occur at both, the Southern and Northern culminations.

Kink-band structures in the South are sealed by the PS-top, according to our observations in the IL 100 (Fig. 5.15). The southern crest of this surface is cut by numerous concave, conjugate normal faults. These faults advance southwards from the hinge to the western flank domain and show limited fault displacements.

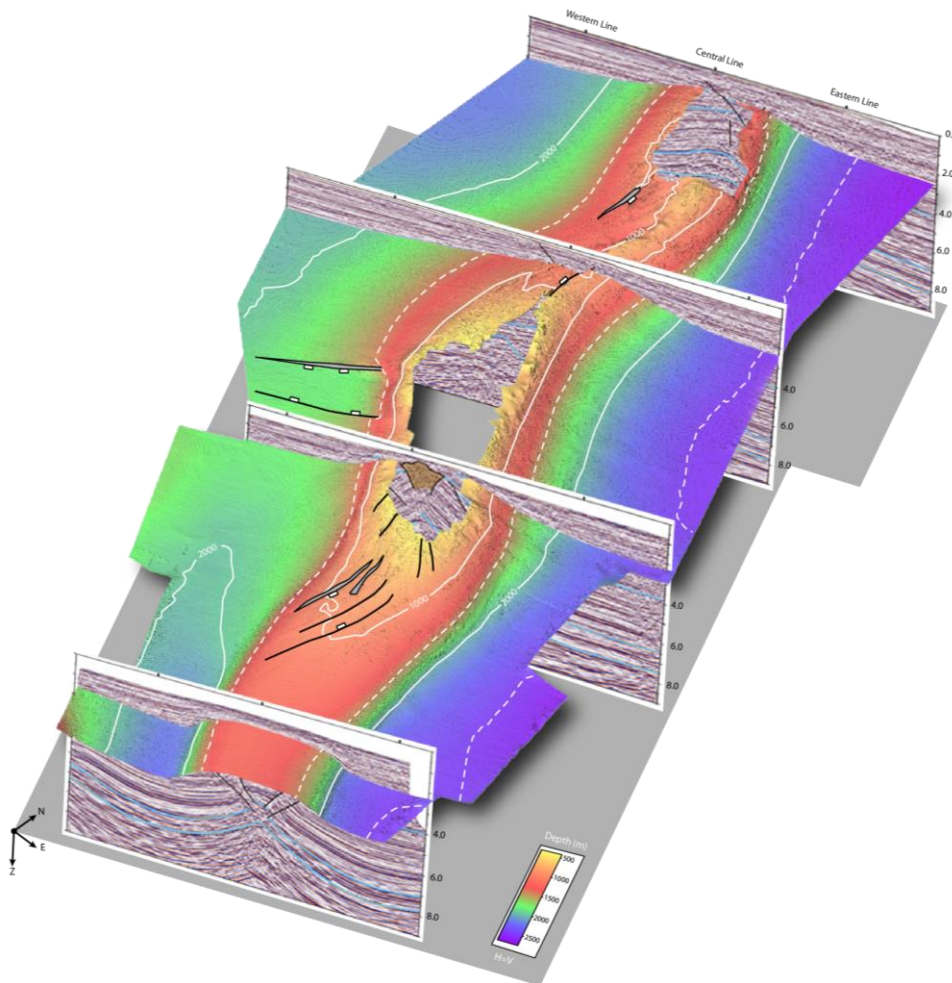


Figure 5.16: 3D panel of the PS-top surface intersected by vertical ILs 240, 1000, 1640 (Fig. 5.4) and 2200. Seismic horizons included in the seismic lines are PS-bottom, NKG and Sabunchi. Surface contour interval is 500m.

5.4.2. Mud-diapirs

We have reconstructed the 3D geometry of the two well-delineated mud diapirs that correspond to mostly symmetric teardrop diapirs located in both culmination domains. The southern structure is detailed in Figure 5.17. Mud structures are shaped as vertical reverted drops in profile, characterized by a relative small bulb with a wide top and necking pattern towards the deeper base. The upper termination of the structure is planar in collapsed areas of the Northern Culmination, whereas pierce print is irregular in the Southern Culmination (*cf.* Fig. 5.7). In the southern sectors, the shallow boundary intrudes the overlying Post-PS. Necking of the mud diapirs in depth connects with a 1 km-long vertical-to-sub-vertical shale weld. The preservation of a feeder channel is not clearly depicted in the seismic cube

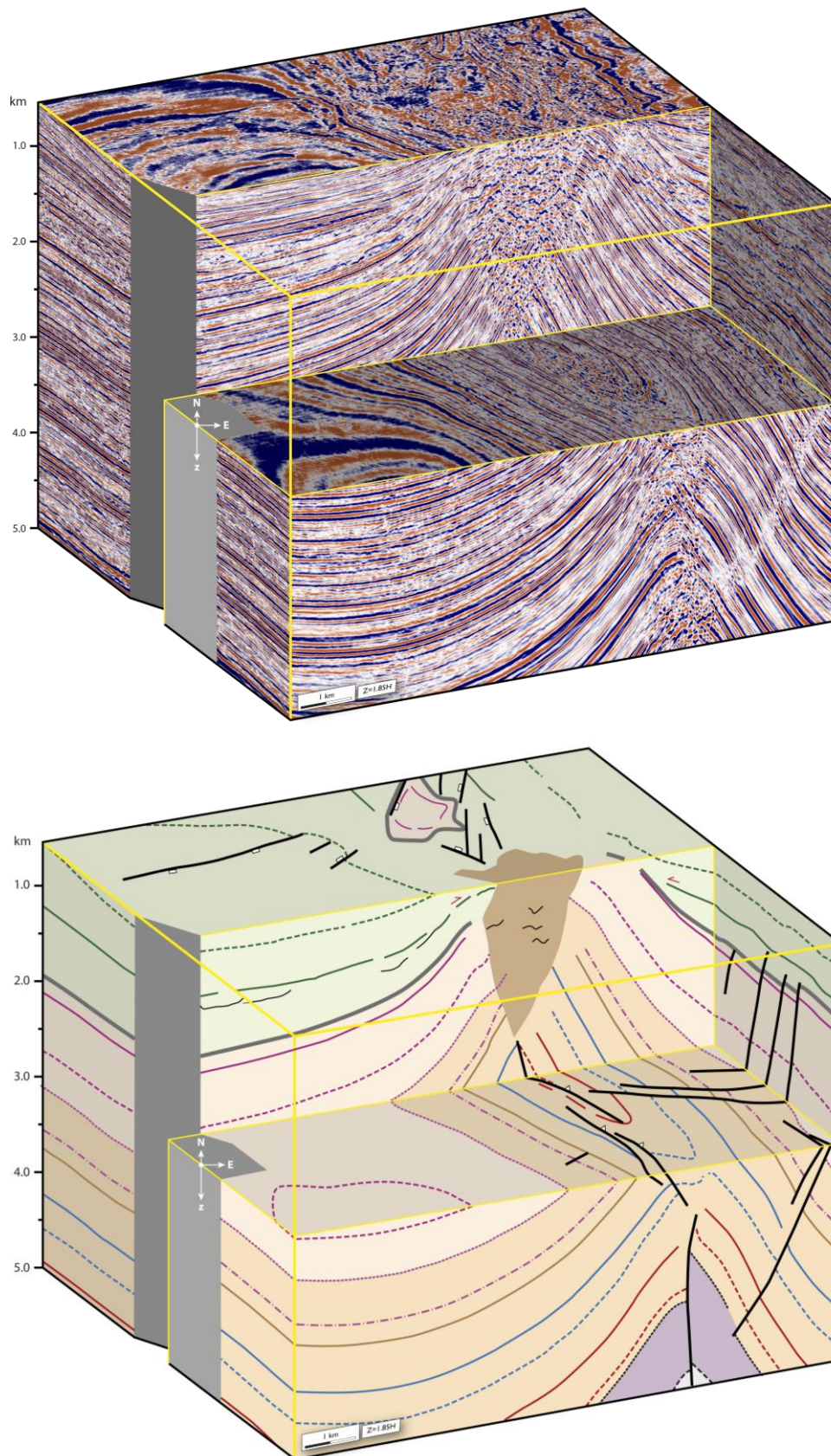


Figure 5.17: Chair-cut seismic cube to show mud diapirism in the KAD anticline in the Southern Culmination as (a) non-interpreted and (b) interpreted. Depth ranges between 0.55 km to 5 km. At front, horizontal slice of 2.7 km depth intersects the cube to highlight the structural evolution from shallow mud diapirism to deep faults. This small cube is bounded by the ILs 820 and 1110 (frontal and back panels, respectively), whereas the left- and right-hand limits correspond to the XLs 700 and 1600, respectively.

but this interpretation should be taken with care due to the abundant diffractions and a poor resolution of the signal in these depths. Presumably, welds represent the prolongation of migration paths from the source rock, which is located at more than 9 km depth, according to seismic image.

Coherently with previous description, plan view of diapirs depicts local accumulations of mud in deep sections that become larger and elongated in upper sectors until the PS-top, especially within the Sk 6 Unit. Within the Post-PS the northern diapir disappears and the southern structure is scarcely recognized with an irregular mud occurrence.

6. DEFORMATION ESTIMATE

Different theoretical and experimental models have been developed to estimate deformation magnitudes in Chamberlin (1910), Dahlstrom (1969); Mitra and Namson (1989). Much or all of fold kinematics can be deciphered through the geometrical analysis of the folded layers. Shortening information is recorded in the spatial distribution of thicknesses and dips (*e.g.*, Suppe, 1983), syntectonic microstructures and mesostructures (Fisher and Woodward, 1992) and growth stratal patterns (Hardy *et al.*, 1996). Balanced structural restoration is also a basic strategy to unravel fold kinematics.

In this study, we have applied both geometrical estimations and proper numerical approaches to establish shortening values in the KAD anticline. The geometrical analysis has been realized along the complete survey, whereas we have chosen selected seismic lines to apply a statistical study to estimate detachment depth, shortening values and fold growth (*Fig. 6.1*). We have focused on the detailed analysis of the IL 540, as it represents an ideal example of a kink-band fold. This work also presents our evaluation in IL 720, 1140 and 1640 as they correspond to true fold profiles used to compare the spatial and time variations of the KAD anticline (Ramsay and Huber, 1987).

6.1. Detachment Folds

Deformation of a sedimentary sequence may trigger folding and/or faulting. In many cases, folds are triggered as a consequence of blocks displacement along a fault structure, called as fault-related folds (*e.g.*, Poblet *et al.*, 2004). Three major types of fault-related folds related to thrusts have been recognized in fold-and-thrust belts: detachment folds, fault-bend folds and fault-propagation folds.

Detachment or “*décollement*” folds are located in the termination of a thrust plane, above the tip line or within the interior of a thrust sheet where a sharp decrease in faulting rate occurs (*Fig. 6.2a*) (*e.g.*, Dahlstrom, 1969; Poblet and McClay, 1996). Geometry is independent of the fault shape and usually correspond to buckle folds bounded by detachment horizons above, below or both (*e.g.*, Homza and Wallace, 1995). Shortening is accommodated along the bedding-plane fault or *décollement* surface which is commonly located within incompetent layers as salt or shale (Dahlstrom, 1969). The ductile underlying unit acts as a lubricant during deformation and its behaviour promotes more complex geometries in the upper block than fault-bend or fault-propagation folds. Kinematics of detachment folds is decoupled from underlying deformation (*e.g.*, Chamberlin, 1910). According to the direction of

movement, the leading flank is named as the forelimb, and the dragged flank corresponds to the backlimb. Anticline structures of this type usually constitute effective hydrocarbons traps.

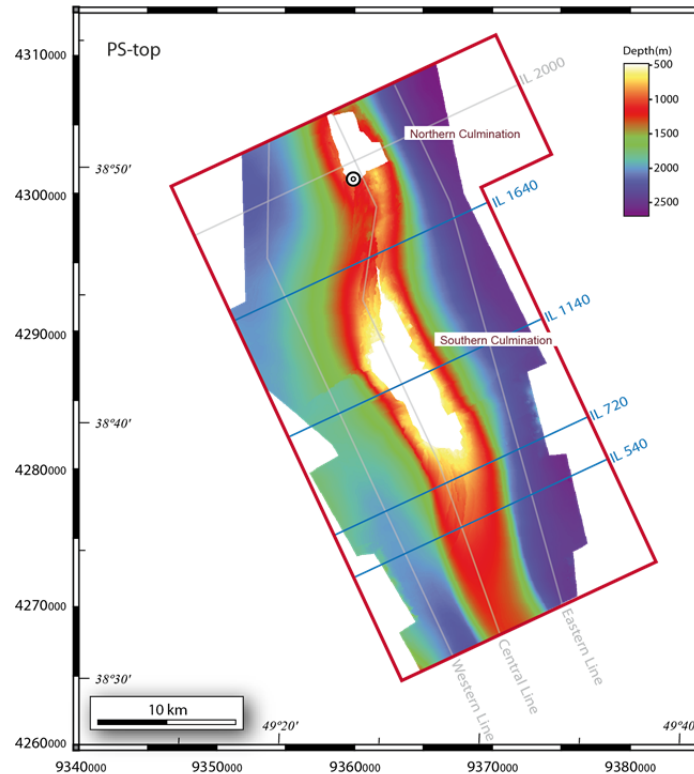


Figure 6.1: Display of the PS-top surface to show the seismic survey in the Kurdashi Permit and the position of the AD-1X well. Fold sections used for statistical approaches are blue-coloured. The IL 2000 and the arbitrary lines interpreted in this thesis are also included as grey lines (*Figs. 5.5 to 5.8*).

Fault-bend folds or ramp-flat folds are caused by bending of a fault block as it moves over a non-planar fault surface (*Fig. 6.2b*) (Rich, 1934; Suppe, 1983; Jamison, 1987). Suppe (1983) modelled ramp-flat folds with the assumption of flat and horizontal layers and constant thickness. Fold layers are affected by flexural slip and deformation produces dissymmetrical fold limbs. Back limb is parallel to the ramp and is less dipping than frontal, leading flank.

Fault-propagation folding results from compression in front and above a fault tip during fault propagation (Mitra, 1990; Suppe and Medwedeff, 1990). Fault-propagation folds occur in the inflection domain between a flat and a ramp along the fault thrust (Suppe and Medwedeff, 1990). Dip of frontal limb is higher than back limb if the ramp is low-dipping, and vice versa if the ramp is highly-dipping because back flank is not parallel to the ramp.

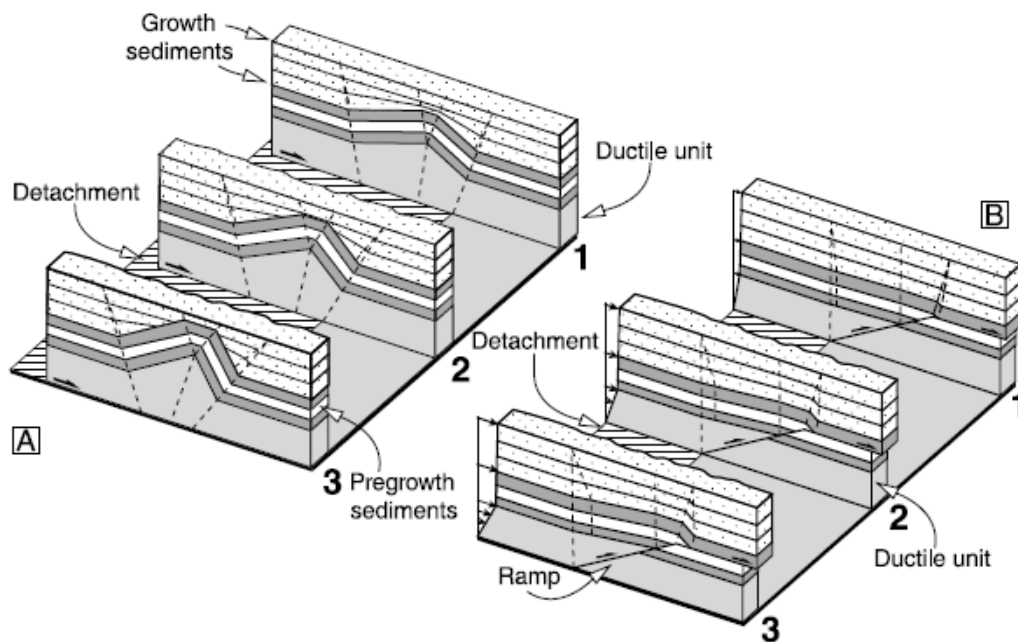


Figure 6.2: Three-dimensional kinematic models of (a) a detachment anticline and (b) a fault-bend fold. In both cases, shortening promotes increasing displacement from sections 1 to 3. Notice the variable geometry of the growth strata as deformation occurs. Taken from Guzowski *et al.* (2009).

6.1.1. Pre- and Syn-growth Sequences

A significant tool to identify the folding kinematics is based on the geometry study of the deformed sedimentary sequence. Syn-deformation strata are sediments deposited over the top or against the flanks of growing structures, both folds and diapirs. Geometry of growth sediments is a function of the axial surface activity, the fold uplift history, the limb lengthening and/or rotation, and the sedimentation-erosion rates (*e.g.*, Hardy and Poblet, 1994; Poblet *et al.*, 1997; Poblet, 2012). Conversely, pre-growth or pre-kinematics sequences are those sediments deposited before folding or diapirism, characterized by parallel sequences with constant thickness above the fold or diapir.

Thickness is variable in the syn-growth sequence due to simultaneous deformation, as for example, thinning above relatively rising structures, and development of offlap, truncations or onlap terminations (*Figs. 6.2, 6.3 and 6.4*). Offlap geometries occur against the diapir border or in the contact with the pre-growth sequences because of a high uplift to sedimentation rate. If low uplift-sedimentation rates exist, syn-growth sediment presents onlap geometries above the structure (*e.g.*, Giles and Lawton, 2002).

Strata deposited after tectonic processes are post-growth sediments and cover the whole structure with an approximately constant thickness. Post-growth sequence can be deformed locally by late, collapse structures developed at diapir or fold culminations.

Three different kinematic models have been proposed to explain the evolution and amplification of detachment folds (Epard and Groshong, 1995; Homza and Wallace, 1995; Poblet and McClay, 1996): (1) hinge migration, (2) limb rotation, and (3) a mixed mode of folding due to a combination of both hinge migration and limb rotation.

For example, folds generated by gradual limb rotation (upper right and lower panels in *Figure 6.3*) present wedge geometries in both flanks with an upward decrease of

layer dip (Poblet, 2004). Conversely, if the fold grew by hinge migration it is produced an upward narrowing of the fold panel (upper left and lower panels in *Figures 6.3* and *6.4*).

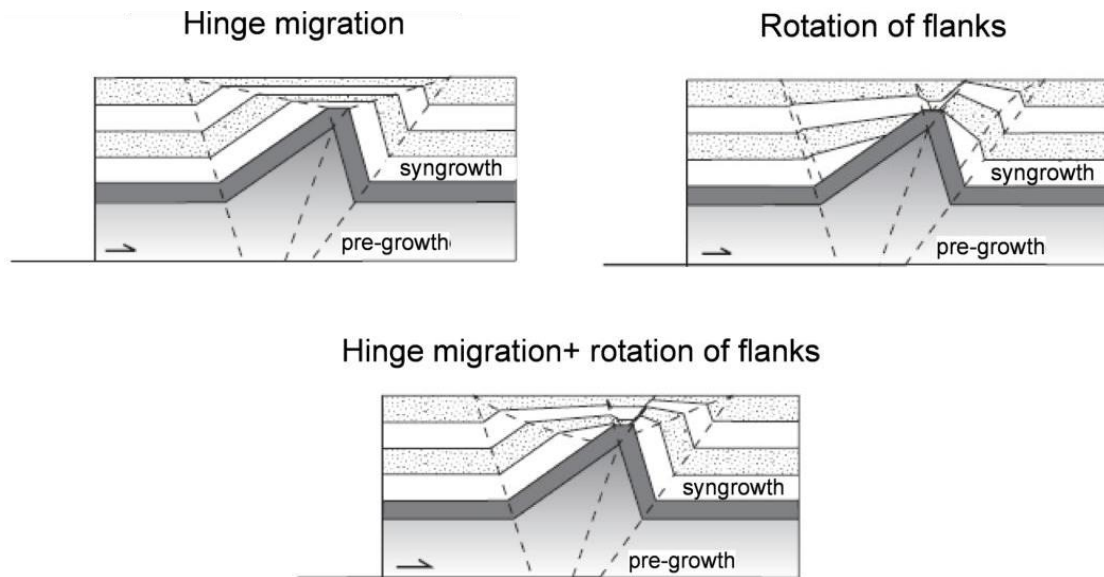


Figure 6.3: Kinematic models to describe geometry of syn-tectonic sediments in detachment folds with a high ratio of sedimentation with respect to fold uplift (taken from Poblet, 2004). Shortening and sedimentation rates keep constant during fold amplification.

The detailed analysis of the shape of the syn-growth sequences also let us to recognize different evolutionary stages during folding, such as pulses of deformation or epochs with a variable rate between vertical fold growth and sedimentation (*Fig. 6.4*).

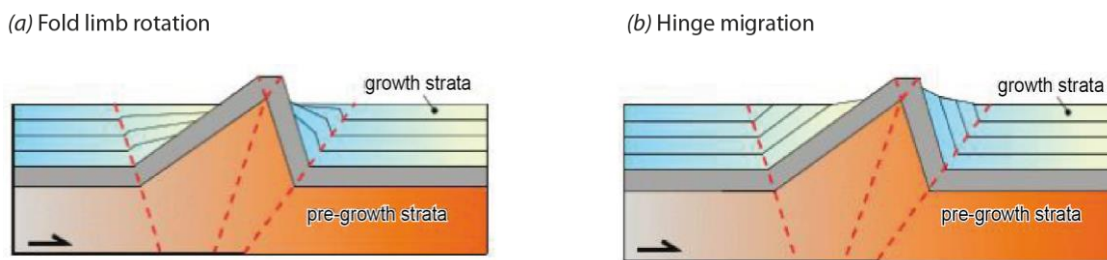


Figure 6.4: Comparison of detachment folds created under sedimentation rates lower than fold uplift rate. It is illustrated for the two-labelled models of kinematic detachment folding: fold limb rotation (*a*) and hinge migration (*b*) (Poblet, 2012).

6.1.2. Shortening Estimate

There are different approaches to reconstruct quantitatively the geometric and kinematic evolution of detachment fold systems (*e.g.*, Poblet, 2004). Detachment folding seems conceptually very simple from a mass-balance perspective, because all the shortening is associated to folding consumed. Most of the methods determine the depth of the detachment level and compute the amount of shortening (*e.g.*, see Bulnes and Poblet, 1999; Gonzalez-Mieres and Suppe, 2006).

The first approach to reconstruct these parameters was developed by Chamberlin

(1910), using the pre-growth strata. This author considered an anticline formed by plane strain and parallel folding of a competent unit; *i.e.*, it assumes a constant bed-length and thickness above an incompetent unit of constant area and with a given undeformed stratigraphic thickness (Homza and Wallace, 1997). With these assumptions and based on Dahlstrom (1990), the depth of the detachment surface (Z) beneath a fold is given by:

$$Z = A/S \quad [6-1]$$

where, A is the displaced area of the incompetent layer due to folding and S is the shortening magnitude (*Fig. 6.5*). Displaced or shortened area (A or A_s in *Figure 6.5*) can be considered equal to the uplifted area within the fold, that is, the deflection area of the same horizon above its undeformed regional level (structural relief, A_{sr} in *Figure 6.5*) (*e.g.*, Gonzalez-Mieres and Suppe, 2006, 2011). Both areas can be slightly different if deformations like layer parallel simple shear or pure shear occur during folding (*e.g.*, Gonzalez-Mieres and Suppe, 2006, 2011).

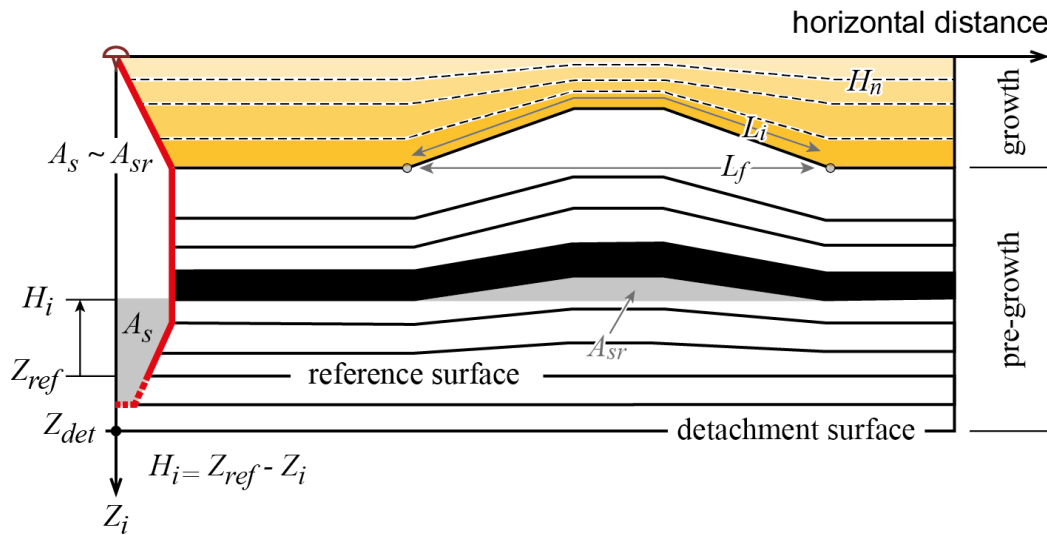


Figure 6.5: Geometrical estimations of shortening in a simple detachment fold with pre- and syn-growth sequences. In this scheme folding is accompanied by layer parallel simple shear in the lower part of the pre-growth folded sequence. Further details are in the text. Figure taken from Sánchez-Borrego *et al.* (submitted) and inspired in Gonzalez-Mieres and Suppe (2006, 2011).

Traditionally shortening has also been estimated from the difference between the initial longitude of the bed (L_i) and the deformed bed length or final length (L_f) measured along the regional between the same end points, based on the assumption of conservation of bed length (*Fig. 6.5*) (Laubscher, 1961). This is called curvilinear, linear or bed-length shortening (S_C):

$$S_C = L_i - L_f \quad [6-2]$$

The value S in [6-1] has been called planimetric or areal shortening (S_A) by Laubscher (1961) in [6-3] and studied by numerous authors (Mitra and Namson, 1989; Epard and Groshong, 1993; Mitra, 2003; Gonzalez-Mieres and Suppe, 2006). S_A is a function of the area of structural relief of the deformed horizon (A_{sri}) and the relative elevation of the deformed horizon above a reference surface (H_i) (*Fig. 6.5*):

$$S_A = dA_{sri}/dH_i \quad [6-3]$$

Plotting the areas of structural relief for a number of horizons (A_{sri}) against their relative elevation above any reference level (H_i), Epard and Groshong (1993) demonstrated that the slope of the best-fit linear distribution defines the amount of shortening (S_A). Additionally, the height (H_{det}) and depth to detachment (Z_{det}) can be estimated from the intersection of this trend with the abscise axis; *i.e.*, where the area of relief is 0 (Fig. 6.6). S_A computed by this method therefore increases with the slope of this relationship in a A_{sri} - H_i plot.

This graphical method has been revised by Gonzalez-Mieres and Suppe (2006, 2011) (Fig. 6.6). Gonzalez-Mieres and Suppe (2011) implemented the areas versus height analysis partially based on Hubert-Ferrari *et al.* (2007) findings, where the area of relief is measured in the thickness domain instead of the depth domain. In both cases, shortening estimations assume vertical simple shear in non-compacted sediments.

Our analysis in this thesis follows the method developed by Gonzalez-Mieres and Suppe (2011) to reconstruct the growth history of a fold for the syn-growth section. The equation [6-3] is then modified to the following expression:

$$S_A = \left(\frac{dA_{sri}}{dH_i} \right)_{growth} + H_{det} \frac{dS}{dH_i} \quad [6-4]$$

In this case the height should be measured with respect to the detachment surface (H_{det}). The dS_A/dH_i corresponds to the ratio between the shortening rate (dS_A/dt) to the sedimentation rate (dH_i/dt). dS_A is computed using the S_A estimated through the area-to-depth relationship (Fig. 6.6).

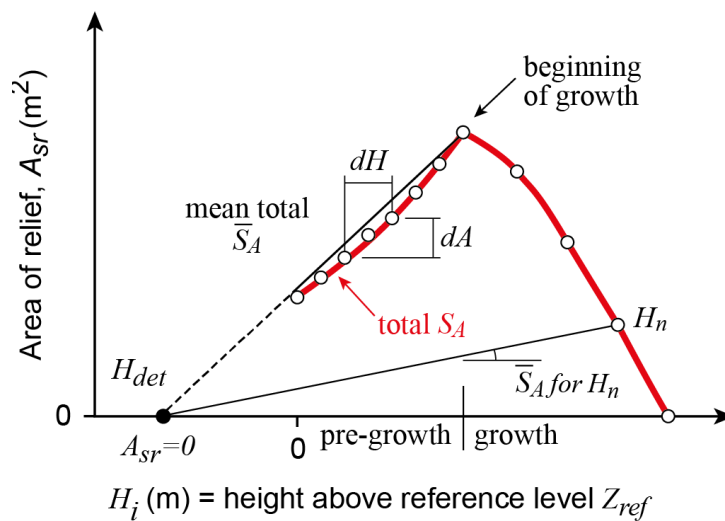


Figure 6.6: Approximated plot of A_{sr} against relative heights H_i corresponding to the scheme shown in Figure 6.5. This relationship illustrates how S_A can be estimated both in the pre- and syn-growth sequences (following Gonzalez-Mieres and Suppe, 2011, and equations [6-3] and [6-4]). For simplification, it is assumed that the beginning of fold growth occurs at the maximum of this plot. Along the A_{sr} - H_i trend, $A_{sr}=0$ locates the height of the detachment surface with respect to the reference level (H_{det}). Figure taken from Sánchez-Borrego *et al.* (submitted).

Most fault-related fold reconstructions assume a constant depth to the décollement level during folding (Suppe, 1983; Jamison, 1987; Mitra and Namson, 1989; Dahlstrom, 1990; Suppe and Medwedeff, 1990). Nevertheless, this assumption is not necessarily true for detachment anticlines because weak units where detachment occurs can change thickness during folding (Homza and Wallace, 1995). Some authors have also found

balancing problems between the measured, uplifted area (A_{sr}) and the computed, displaced area (A) as a result of sinking of the nearby synclines below the regional level (Mitra, 2003), volume changes during deformation, existence of internal deformation or compaction in the fold (*e.g.*, Poblet, 2004; Guzowski *et al.*, 2009). Mitra and Namson (1989) developed a modification of the method of Chamberlin (1910), including the effects of layer-parallel shear in detachment anticlines. The occurrence of such penetrative strain (ΔA) causes discrepancy between the uplifted (A_{sr}) and the displaced areas (A), because the relative elevation of every horizon (H_i) would be a function of:

$$H_i = (A_{sri} \pm \Delta A) / S_A \quad [6-5]$$

6.1.3. Fold Elements in the KAD Anticline

To compute the amount of shortening in the KAD we have applied two methods: the curvilinear shortening (S_C) and the planimetric shortening (S_A) (*e.g.*, Santos Betancor *et al.*, 2013b). Our research is based on the statistical analysis applied in a master section, the SW-NE IL 540, to estimate geological values in the KAD. This section shows a kink-band fold, where the eastern limb is the forelimb and the dragged, western flank corresponds to the backlimb (*Fig. 6.7*). We have selected this anticline profile because it shows a complete and continuous structure, and it lacks of any significant fault and of any of the abundant mud diapirs occurring in the area. This image is similar to the *Figure 5.2*, accomplished by the delineation of the Akchagyl 1 (Ak 1) and Apsheron 1 (Ap 1) horizons as the tops of the homonymous units.

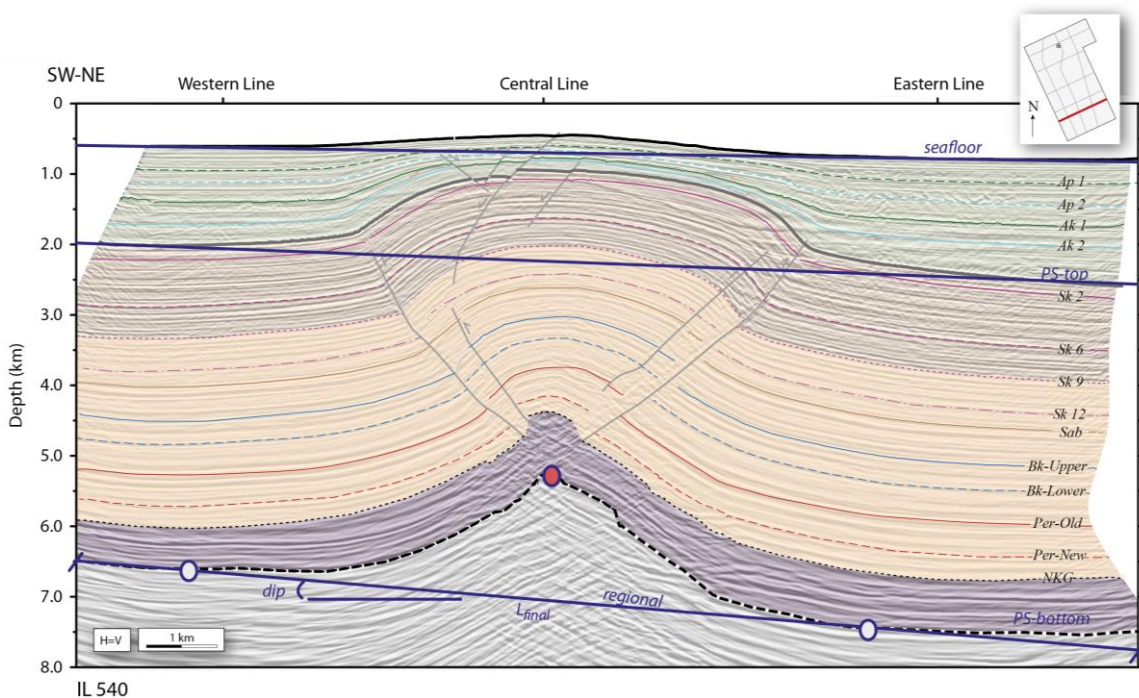


Figure 6.7: Schematic view of the IL 540 (see also *Figure 5.2*). The inset map shows the same sections as in *Figure 6.1*, and the position of the IL 540 is highlighted in red. Regional lines are depicted for the seafloor, and both boundaries of the PS sequence, and correspond to their undeformed elevations. Red-filled circle corresponds to maximum inflection point, whereas white-filled circles correspond to minima values. The tops of the surfaces are abbreviated as: Balakhany (Bk), Pereryva (Per), Surakhany (Sk), Productive Series (PS). Horizons within the Akchagyl Unit are named as Ak 1 and Ak 2, and Ap 1 and Ap 2 are interpreted in the Apsheron Unit.

The different parameters we have used to calculate shortening magnitudes are illustrated in *Figure 6.8* and described in *Table 6.1*. According to equations [6-3] and [6-4], we have considered the uplifted areas (A_{sr}) as those measured below and above the regional level of each horizon (*Fig. 6.8*) (Gonzalez-Mieres and Suppe, 2006). Positive values correspond to the uplifted area above the regional level (A_2), and negative areas are constrained below the regional surface (A_1 and A_3) (*Fig. 6.8*).

The regional line for each horizon is the line in two-dimensions that constitutes the lower boundary of the fold, which is orange-coloured in *Figure 6.8a*. In agreement with Mitra (2003), the regional level defines the limits of the anticline and syncline areas. For any geometrical analysis of the folding history, it is crucial to reconstruct accurately the position of the regional surface because it conditions the shortening magnitudes (S_C and S_A) and also the depth of the lower detachment surface (*e.g.*, Wiltschko and Groshong, 2012).

In our study, after exploring different fits to this line in the fold section, the regional level for each horizon is built by computing the best linear regression fit between the two-syncline domains (*Fig. 6.8*). We have analysed the first 100 observations from both extremes (SW and NE); this domain is denoted by a red colour in *Figure 6.8a*. For every folded surface, we have registered the Pearson correlation coefficient of the linear regression (r^2).

Our deformation estimates are built from the position and depth of the different seismic horizons previously interpreted within the PS. We have individually exported the overall seismic horizons as X (longitude), Y (latitude) and Z (depth) data.

Figure 6.8a shows the continuous distribution for one surface in the key IL 540. Two examples of discontinuous distributions are also presented in a pierced section (*Fig. 6.8b*) and a faulted fold profile (*Fig. 6.8c*). Distributions have been fitted by nonparametric methods because any parametric approaches satisfactorily fit the studied distribution (*Fig. 6.8a*). Additionally, nonparametric counterparts can avoid singularities of individual reflections, such as disruptions, gaps or faults in other fold sections, (*Figs. 6.8b and c*).

The length of the regional line constitutes the final length (L_f) of each respective folded surface in *Figures 6.7b and 6.8a*. When horizons have been partially pierced (*Fig. 6.8b*) or displaced (*Fig. 6.8c*) the final length (L_f) is calculated through the addition or subtraction of extra lengths. In both cases shown in *Figure 6.8*, we need to extract the length of the domain where the horizon is disrupted along its regional line to the final length (L_f), that is, L_{diap} (*Fig. 6.8b*) and L_{fault} (*Fig. 6.8c*).

Similar procedures are used to measure the initial length or L_i of folded surfaces in continuous (*Fig. 6.8a*) and discontinuous distributions (*Fig. 6.8b and c*). L_i^* represents a relative maximum length for the studied horizon; L_i results from the difference of L_i^* and the Present-day surface gaps due to diapirism (*Fig. 6.8b*) and faulting (*Fig. 6.8c*).

The dip of every regional level (α) is calculated for each surface, which is always compared to the dip of the reference surface (α_{ref} in *Figure 6.8*). The regional surface of the PS-bottom is used in this thesis as the absolute reference level for the complete sequence.

For every surface, we estimate the position and magnitude of the maximum (*max*) and minima (*min*) of the distribution (*Figs. 6.7b and 6.8*). They correspond to the highest values of the distribution located in the fold crest in the anticline and in the through domain in the nearby synclines. It has been subsequently estimated the position

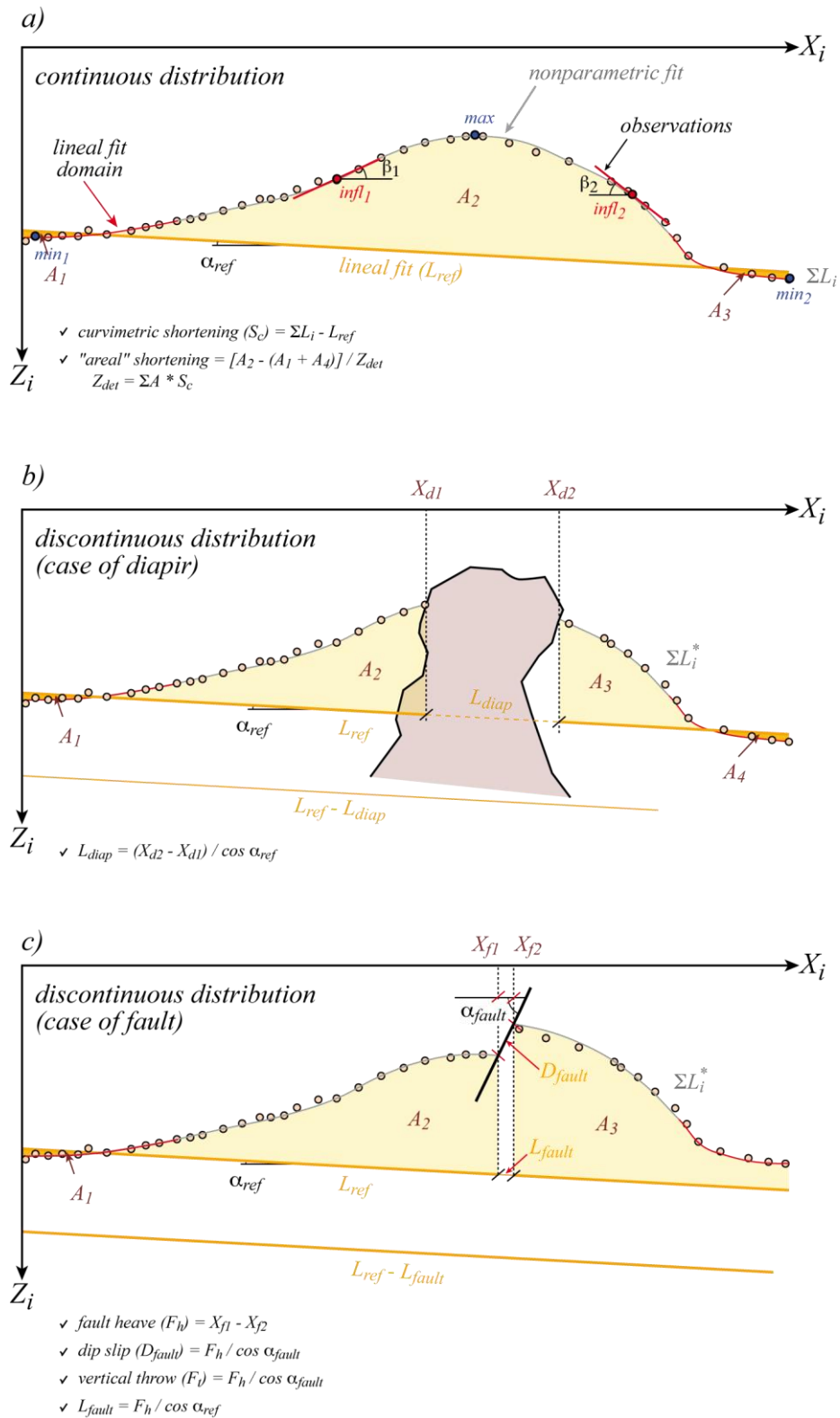


Figure 6.8: Diagram of fold elements for a single horizon used for nonparametric estimations of shortening. It is represented the procedures used to work with (a) a continuous folded surface (as in Figure 6.7; Sánchez-Borrego *et al.*, submitted), (b) a surface pierced by a mud diapir, and (c) a faulted horizon. Areas A_1 , A_2 , and A_3 correspond to the domains defined by the folded surface above (A_2) and below (A_1 and A_3) the regional level coloured as an orange line. L_{ref} is the reference length of the Present-day folded horizon that is equal to the final length (L_f) in (a) (Fig. 6.7b) and higher in (b) and (c). The nonparametric fit is depicted by grey-coloured lines; in (a) its length corresponds to the initial length (L_i) of the horizon before folding. Abbreviations and further details are described in the text and in Table 6.1.

of the inflection points (*infl*) between them, which define the inflection domain between both structures and coincide with the regions with a change in the concavity of the fold flank. Around these inflection points, we have calculated the best linear fit of the distribution and its angle to the horizontal; they are considered a good estimate of the attitude of the fold flank (β_i ; Fig. 6.8a).

We have implemented our nonparametric function with additional fold elements to analyse diapiric and faulted sections (Figs. 6.8b and 6.8c). In both cases, horizon disruption is interpreted as a discontinuous distribution limited by diapir piercing (X_{di} ; Fig. 6.8b) and fault displacement (X_{fi} ; Fig. 6.8c). Additionally, fault vertical displacement (D_{fault}) and fault dip (α_{fault}) are also considered in fold profiles affected by faulting.

List of magnitudes	
Z_i	Horizon depth from the sea surface
H_i	Horizon height from the PS-bottom surface (reference surface)
L_i	Initial length of the folded surface
L_f	Final length of the surface in the deformed situation
r^2	Linear correlation coefficient for the regional lines fit
α_{ref}	Angle between the regional line and the horizontal axis (regional dip)
β_1	Angle between the tangent to the estimated surface at the first inflection point and the horizontal axis (dip of the W-fold limb)
β_2	Angle between the tangent to the estimated surface at the second inflection point and the horizontal axis (dip of the E-fold limb)
S_C	Curvilinear shortening
S_A	Planimetric shortening

Table 6.1: List of magnitudes of fold elements also detailed in the text. Graphical illustrations of these elements are given in Figures 6.5 and 6.8. Taken from Sánchez-Borrego *et al.* (submitted).

6.2. Nonparametric Estimation

Statistical tests can be divided into two groups: parametric and nonparametric tests. Conventional and unconventional statistical techniques are applied in a wide range of settings and areas of research (Ruppert and Wand, 1994; Fan and Gijbels, 1996; McKillup and Dyar, 2010; among others). In our case, we preferred nonparametric estimations due to the complexity of fold shape in the studied section and because none of the standard functions of parametric statistics reproduces satisfactorily the horizons shape of the complete folded surface (Fig. 6.7).

The precision on the fit of the regression function is essential from a geological point of view as it establishes the position of the different fold elements and, therefore, compromises any classification of the fold structure leading to an accurate computation of the S_C and S_A values. In consequence, fit accuracy affects the reconstructed folding and deformation histories. It is also important from a mathematical point of view, because the nonparametric estimation conditions any further analysis of the folded surface, as for example the position of the fold hinge and inflection line in fold flanks.

We have extended our statistical approach specified in IL 540 to other fold sections (Fig. 6.9). In this work we also show our estimations and results in IL 720, IL 1140, and

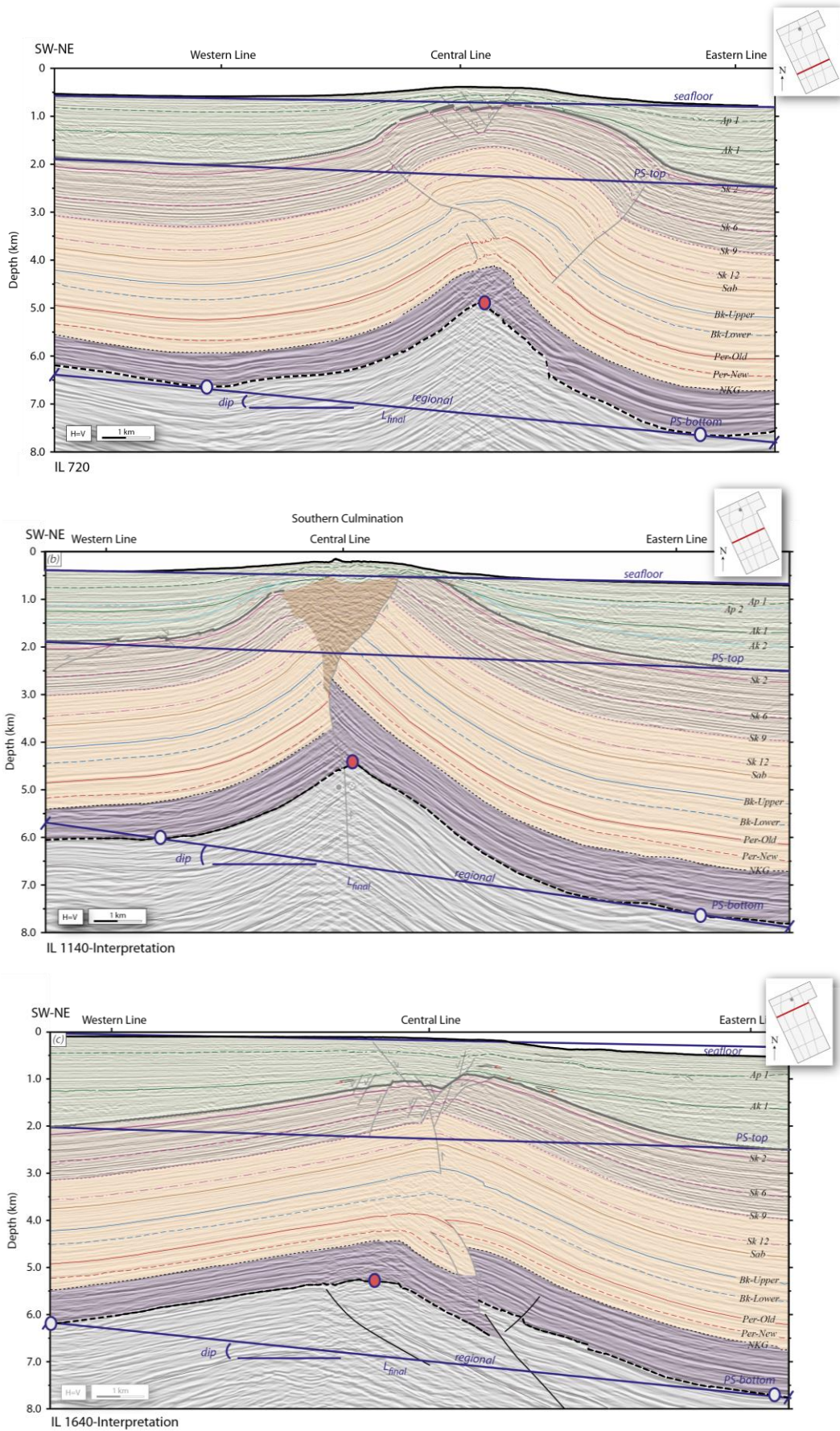


Figure 6.9: Schematic illustrations of seismic lines (a) 720, (b) 1140 and (c) 1640. Abbreviations as in Figure 6.7.

IL 1640. We believe that this approach provides robust statistical tools to analyse easily other fold sections from different geological settings or scale.

The unknown nonparametric function $m(\cdot)$ can be approximated by a polynomial. Local polynomial regression is used in this research since it is well known for its good practical and theoretical properties (e.g., Loader, 1999; Sánchez-Borrego *et al.*, 2006). Selected method can be easily precise the geometry of the folded surfaces adapted to the presence of discontinuities (Ruppert and Wand, 1994; Fan and Gijbels, 1996). Our method of estimation works under the assumption that regression functions are smooth. To estimate the horizons depth of the anticline we have considered the adapted to discontinuities kernel smoother as the best parametric approach in a finite population with jump points (Sánchez-Borrego *et al.*, 2006). This method is the result of combining a modified projected observations procedure (classical parametric function; Wu and Chu, 1993) and the piecewise local linear kernel estimator (Fan and Gijbels, 1996; Ruppert and Wand, 1994). Our selection is based on terms of the coefficient of determination value, making sure that relevant coefficients involved in the model are significantly non-zero (Sánchez-Borrego *et al.*, 2006). Thus, we need to add new observations in the scatter data by reusing the available jump points to calculate the discontinuous regression function of the depth data and balance the fit.

The choice of the bandwidth parameter (h) of the nonparametric regression estimator (\hat{m}_{np}) is critical when smoothing techniques are applied. In this thesis we have selected the bandwidth parameter (h) by minimizing the cross-validation score used to detect jump points (Bowman *et al.*, 2006) to estimate the regression function ($m(\cdot)$). This method is proposed by Sánchez-Borrego *et al.* (2006) and takes into account the square root of the mean squared error (MSE) of the estimator and the length of the estimated folded surface. According to Sánchez-Borrego *et al.*, (2006), the best filter must depict the most precise fold geometry, including antiform and synform shapes, by satisfying the lowest error measurements (E)

$$E_1(h) = \sqrt{\frac{1}{n} \sum_{i=1}^n (Z_i - \hat{m}_{np}(x_i))^2} \quad [6-6]$$

and

$$E_2(h) = \sum_{i=1}^{n-1} |\Delta_{1i} + \Delta_{2i}| \quad [6-7]$$

over a grid of values of the bandwidth parameter, with Δ_{1i} and Δ_{2i} the distances mentioned in equations [6-11] and [6-12] (Table. 6.2; Sánchez-Borrego *et al.*, 2006).

Figure 6.10 graphically illustrates the effect that the bandwidth parameter has on the depth data estimates. As an example, we show part of the statistical fit in the seafloor (Fig. 6.10a) and in the PS-bottom (Fig. 6.10b) distributions for values of h equal to 0.02, 0.3 and 0.5 (cf. Table 6.2). Both graphs evidence the marked effect of the different values into the estimation of horizons geometry; this is transcendental to the surface reconstruction of continuous (Fig. 6.10a) and discontinuous surfaces (Fig. 6.10b). We have chosen a bandwidth parameter, $h = 0.02$, as the best parameter by minimizing E_1 and E_2 scores in equations [6-2] and [6-3].

Estimator	h	sf		PS-b	
		E_1	E_2	E_1	E_2
\hat{m}_{np}	0.02	2,196	17,393	5,480	348,030
	0.03	2,393	17,760	5,737	374,595
	0.04	2,660	17,759	10,714	389,783
	0.05	3,038	17,970	11,147	400,677
	0.06	3,497	18,075	11,535	411,474
\hat{m}_{par}		120,823	23,219	479,167	1,274,604

Table 6.2: Bandwidth parameter h selection for the seafloor (sf) and the PS-bottom (PS-b) surfaces in the IL 540 (Sánchez-Borrego *et al.*, submitted). Selected parameter is $h = 0.02$ by minimizing errors scores. Parametric values are included for comparison. Further details are described in the text.

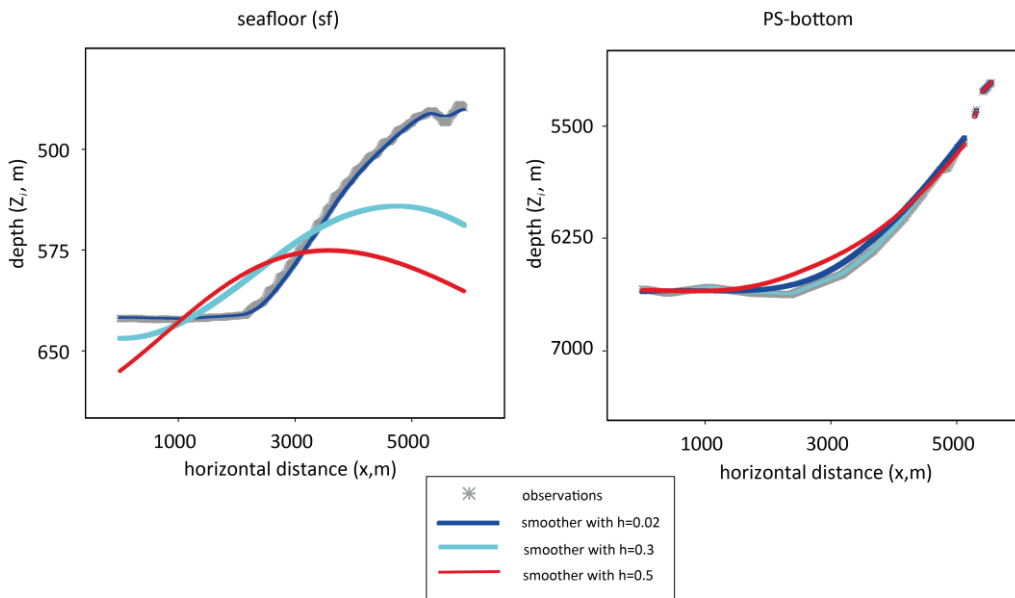


Figure 6.10: Examples of the effect that different values of the bandwidth parameter has on the estimation of depth data for the (a) seafloor and the (b) PS-bottom folded surfaces in the selected IL 540. Figure taken from Sánchez-Borrego *et al.*, (submitted).

The nonparametric local polynomial regression (\hat{m}_{np}) is expected to be the preferred estimator, since it does not place any restriction on the relationship between the auxiliary and the study variable. In this thesis, we also present our results obtained by classical parametric regression (\hat{m}_{par}) as the best parametric estimator for comparison and error estimations. Both methods are compared in terms of the gain in efficiency through the R_1 and R_2 percentages, which are given by:

$$R_1(\hat{m}_{np}) = \left(\frac{\sqrt{\frac{1}{n} \sum_{i=1}^n (Z_i - \hat{m}_{par}(x_i))^2}}{\sqrt{\frac{1}{n} \sum_{i=1}^n (Z_i - \hat{m}_{np}(x_i))^2}} - 1 \right) \times 100 \quad [6-8],$$

and

$$R_2(\hat{m}_{np}) = \left(\frac{E_2(\hat{m}_{par})}{E_2(\hat{m}_{np})} - 1 \right) \times 100 \quad [6-9],$$

in where $E_2(\hat{m}_{np})$ and $E_2(\hat{m}_{par})$ are the length of the estimated folded surface,

$$E_2(\hat{m}_{np}) = \sum_{i=1}^{n-1} |\Delta_{1i} + \Delta_{2i}| \quad [6-10]$$

with Δ_{1i} and Δ_{2i} given by

$$\Delta_{1i} = \sqrt{(x_{i+1} - x_i)^2 + \left(\left(\hat{m}_{np}(x_{i+1}) \right) - \hat{m}_{np}(x_i) \right)^2} \quad [6-11],$$

$$\Delta_{2i} = \sqrt{(x_{i+1} - x_i)^2 + (Z_{i+1} - Z_i)^2} \quad [6-12].$$

6.3. Shortening Results

The application of mathematical observations and the results of the deformation estimates are here illustrated in detail for the master line IL 540 (Fig. 6.7). We present the estimate of S_A and S_C together with other results, *e.g.*, our reconstruction of the geometries of the regional surfaces for every deformed horizon, and the dip variation of both anticline fold limbs. These results will be compared with three additional sections, IL 720, 1140, and 1640 (Fig. 6.9), to have a general distribution in 3D of the deformation associated to folding.

6.3.1. IL 540

We have fitted with nonparametric statistics the folded surfaces in the IL 540 as it is summarized in Figure 6.11 (*cf.* Fig. 6.7). Abbreviations used in this figure are described

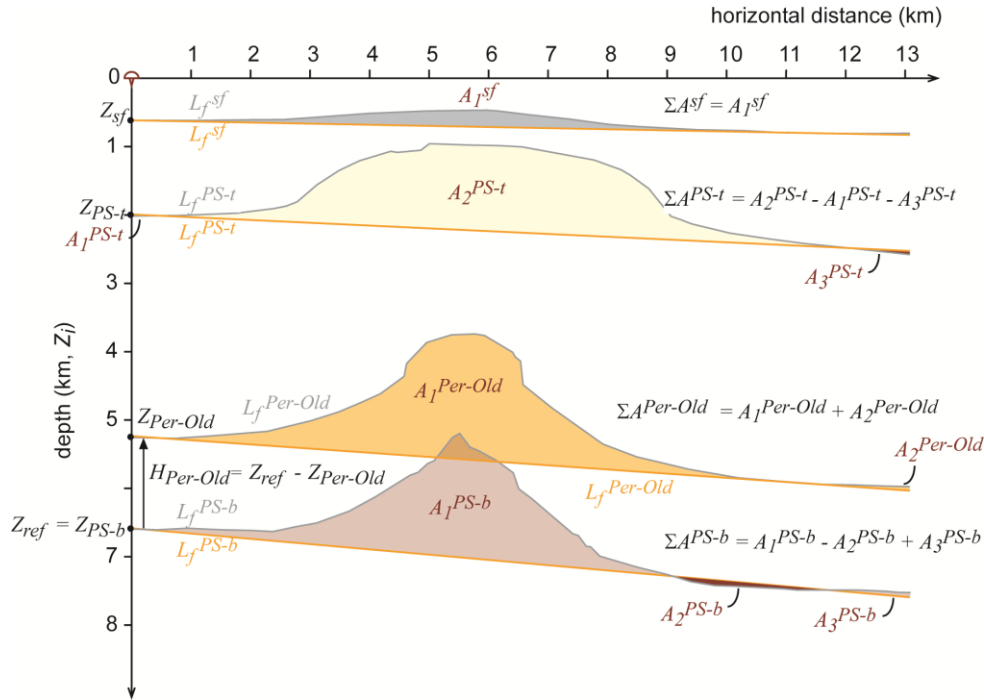


Figure 6.11: Areas calculus in the IL 540 using the nonparametric fit of the seafloor (sf), the top and bottom of the Productive Series (PS-t and PS-b, respectively) and the Pereryva-Old surface. Horizontal and vertical axes are equally scaled. Abbreviations are detailed in Table 6.1 and Figures 6.7 and 6.8. Figure modified from Sánchez-Borrego *et al.*, (submitted).

in *Table 6.1*. Our study is exemplified in *Figure 6.11* for four fitted horizons: the PS-bottom, the Pereryva-Old, the PS-top and the seafloor. The regional line for every horizon is also included. Surfaces are pinned in a referential position where $X=0$ and $Y=0$. The reference level is the PS-bottom surface, thus $Z_{ref} = Z_{PS-b}$.

The measurements of the different folded horizons interpreted in the IL 540 with nonparametric methods and bandwidth parameters equal to 0.02 are detailed in *Table 6.3*. For every surface in *Figure 6.7* we have calculated magnitudes mentioned in *Table 6.1*: estimated depth of regional lines measured from the seafloor (Z_i), their respective height to the reference PS-bottom surface (H_i), initial (L_i) and final (L_f) length of horizons, the Pearson correlation coefficient of the linear regression (r^2), regional (α) and fold dips (β_1 and β_2). *Table 6.3* also includes the mean values of S_C and S_A . The age of formation tops are regionally established and used as reference for additional horizons analysed in this study (e.g., Jones and Simmons; 1997; Abreu and Nummedal, 2007; Forte *et al.*, 2010). Extrapolated ages are contained in brackets in *Table 6.3* (see *section 4.3.1.* and *Table 4.4*).

S.Seq.	Age (Ma)	Hor.	Z_i (km)	H_i (km)	L_i (km)	L_f (km)	r^2	α (°)	β_1 (°)	β_2 (°)	S_C (km)	S_A (km)
Post-PS	0	sf	0.617	5,956	13,126	13,110	0.940	0.9	3.4	6.1	0.016	0.114
	[0.7]	Ap1	0.958	5,614	13,162	13,109	0.999	0.9	10.4	6.2	0.053	0.249
	0.8	Ap2	1,148	5,423	13,213	13,112	0.999	1.4	16.0	7.5	0.101	0.341
	[1.6]	Ak1	1,398	5,174	13,360	13,113	0.997	1.6	14.9	14.2	0.247	0.478
	1.7	Ak2	1,687	4,885	13,465	13,112	0.998	1.5	28.3	8.4	0.352	0.678
Upper-PS	3.1	PS-t	1,994	4,578	13,692	13,119	0.991	2.3	30.4	6.1	0.573	0.913
	[3.2]	Sk 2	2,198	4,374	13,723	13,118	0.991	2.2	30.4	13.6	0.605	0.979
	[3.4]	Sk 6	2,847	3,725	13,838	13,124	0.991	2.8	32.6	23.3	0.714	1,096
	[3.5]	Sk 9	3,296	3,276	13,940	13,125	0.990	2.9	31.2	22.7	0.815	1,158
	[3.6]	Sk 12	3,749	2,823	14,025	13,126	0.992	3.0	13.3	41.4	0.899	1,243
	3.7	Sab	3,983	2,589	14,075	13,126	0.993	3.1	15.6	29.1	0.949	1,277
	4.0	Bk-Upper	4,472	2,100	14,151	13,129	0.993	3.2	30.2	41.6	1,023	1,356
	[4.2]	Bk-Lower	4,794	1,778	14,225	13,131	0.993	3.4	22.6	45.4	1,094	1,381
	[4.5]	Per-Old	5,237	1,335	14,301	13,133	0.995	3.5	18.3	33.3	1,168	1,428
4.9	Per-New	5,673	0.899	14,253	13,135	0.993	3.7	16.5	34.3	1,118	1,530	
Lower-PS	5.2	NKG	5,986	0.586	14,366	13,136	0.993	3.8	21.2	34.5	1,229	1,713
	5.9	PS-b	6,572	0.0	14,241	13,149	0.994	4.5	22.8	34.4	1,092	1,626

Table 6.3: Values of the different magnitudes estimated through nonparametric methods in the IL 540 fold section. *S.Seq.* expresses the sedimentary sequences of the PS (Lower and Upper) and Post-PS, and *Hor.* abbreviates horizons. Planimetric shortening (S_A) is obtained through a polynomial fit. Further details and abbreviations are described in *Tables 6.1* and *4.4*, and in the text. Taken from Sánchez-Borrego *et al.*, (submitted).

Curvilinear shortening

Curvilinear, linear or bed-length shortening (S_C) results detailed in *Table 6.3* are

obtained according to the equation [6-2] and satisfied by $h = 0.02$. Maximum shortening computed in the IL 540 is up to 1.2 km (*Table 6.3*). The half part of complete deformation is registered nearby the top of the PS (S_C ranges between 0.61 and 0.57 km), and the Post-PS rocks absorbed the other part, as this sequence is shortened over 557 m. Nowadays, shortening still occurs, as the seafloor registers over 16 m.

The incorrect selection of the bandwidth parameter may promote up to 60 m of error in shortening magnitudes (S_C) for the bottom of the Productive Series (PS-b), as it is evident in *Table 6.4*. Error magnitudes are > 1 km if the PS-bottom or other deep horizons are fitted by the best parametric function (\hat{m}_{np}) (*Table 6.5*).

Estimator	h	sf	PS-b
		S_C	S_C
\hat{m}_{np}	0.02	16.11	1,092.06
	0.10	12.83	1,055.47
	0.15	10.51	1,052.47
	0.20	8.34	1,045.35
	0.25	6.63	1,039.81
	0.30	5.47	1,033.56
\hat{m}_{par}		1.35	33.06

Table 6.4: Effect of the bandwidth parameter (h) on the curvilinear shortening value (S_C) of nonparametric (\hat{m}_{np}) and parametric (\hat{m}_{par}) estimators and for the surfaces deformed in the anticline shown in *Figure 6.7* (Sánchez-Borrego *et al.*, submitted).

Horizon	\hat{m}_{np}	\hat{m}_{par}	Handwriting
sf	16.11	1.35	25
Ap1	53.13	1.72	0
Ap2	101.25	4.05	
Ak1	247.01	5.62	275
Ak2	352.27	6.72	
PS-t	573.23	9.77	525
Sk 2	605.43	11.15	525
Sk 6	714.32	18.19	725
Sk 9	815.33	21.09	750
Sk 12	899.34	23.14	925
Sab	948.94	25.72	925
Bk-Upper	1,022.87	26.16	1,025
Bk-Lower	1,093.79	30.86	900
Per-Old	1,168.16	32.50	1,100
Per-New	1,117.55	31.93	1,275
NKG	1,229.31	30.48	1,150
PS-b	1,092.06	33.23	1,125

Table 6.5: Curvilinear shortening value (S_C) of nonparametric (\hat{m}_{np}) and parametric (\hat{m}_{par}) estimators, and handwriting measurements for the surfaces deformed in the anticline shown in *Figure 6.7*. Units are in meters. Abbreviations as in *Figure 6.7*. Table taken from Sánchez-Borrego *et al.* (submitted).

Accuracy of handwriting estimations is also very low with evident incongruent values that depart from general tendency (*Table 6.5*); for example, the Apsheron 1 subunit has not apparently shortened, and the Balakhany Lower has contracted with less intensity than surrounding units. Marked divergences may assume areal variations during shortening, only distinguished with the application of nonparametric methods.

Planimetric shortening

Our estimations of planimetric or areal shortening (S_A) described in *Table 6.3* are graphically shown in *Figure 6.12*, calculated with the equations [6-3] and [6-4]. To obtain the planimetric shortening we have plotted the total folded area of each horizon (A_{sr}) against the height of each regional surface above the detachment (H_{det}) (e.g., Epard and Groshong, 1993; Gonzalez-Mieres and Suppe, 2011).

The $A_i:H_i$ distribution is fitted by polynomial and linear functions (*Fig. 6.12*). Consistently to Gonzalez-Mieres and Suppe (2006), within the pre-kinematic sequence, area versus height relationship is better reproduced by a polynomial curve (black line in *Figure 6.12*) because it improves estimates of shortening ($r^2=0.94$), against the less accuracy of the linear fit (blue line and $r^2=0.90$). The maximum of the polynomial function will reveal the boundary between the pre- and syn-growth sequences (*Fig. 6.12*; e.g., Gonzalez-Mieres and Suppe, 2006, 2011).

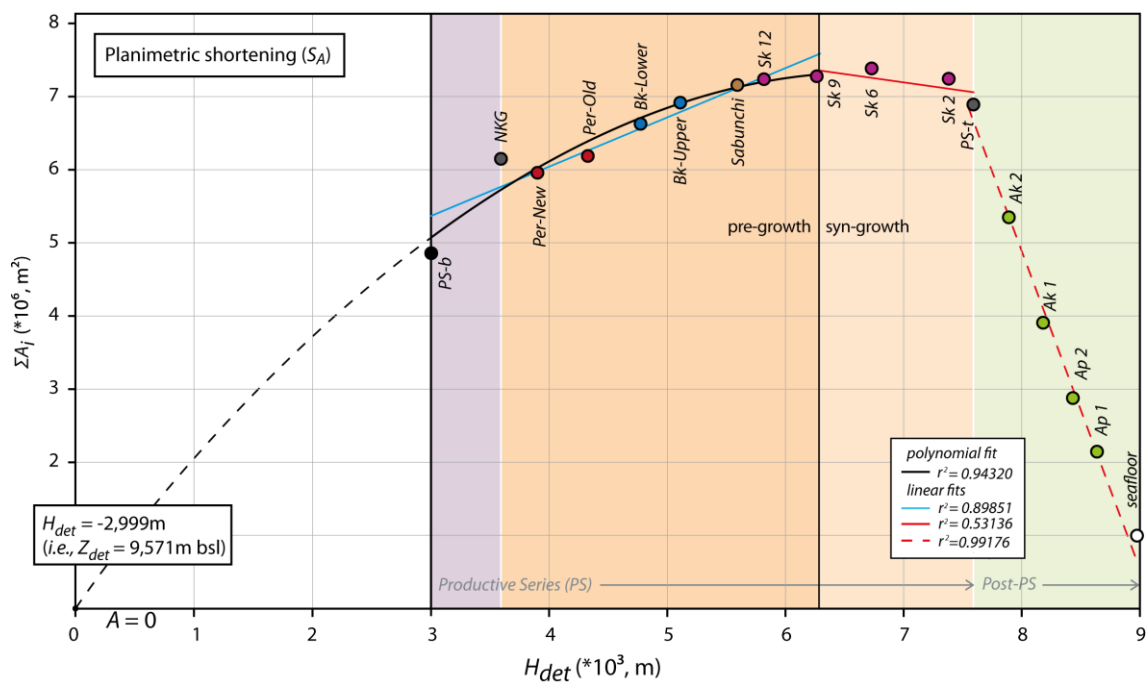


Figure 6.12: Plot of the $A_i:H_i$ relationship for each horizon according to different fits for the studied sequences. The polynomial fitting of the pre-growth distribution, coloured in black, is used to calculate the depth to the detachment in the intersection of the X axis when $A_i = 0$ ($Z_{det} = 9.571$ km bsl) (Epard and Groshong, 1993; Gonzalez-Mieres and Suppe, 2006, 2011). The linear fit is of the pre-kinematic sequence is blue-coloured. PS and Post-PS syn-growth sediments are fitted by linear approaches coloured in red, as continuous and dashed-lines, respectively. H_i is the height to the reference level that corresponds to the PS-bottom (PS-b) and A_i is the structural area for each surface. Horizons abbreviations are as in *Figure 6.7*. Figure inspired in Sánchez-Borrego *et al.* (submitted).

Plot in *Figure 6.12* shows $A_i:H_i$ distribution is clearly divided into two domains,

corresponding to the PS and the Post-PS sequences (Fig. 6.12). The PS show an increasing trend towards the uppermost stratigraphic sequences, as it occurs in the pre-kinematic sequences (Epard and Groshong, 1993). This tendency changes completely within the Post-PS units, where an abrupt and linear drop off is observed, and it reaches values over 1 km² of structural areas in the seafloor surface. A subtle decrease in the folded area is also detected within the uppermost PS from the Surakhany 9 Unit (3.6-3.5 Ma), that represents a maximum $A_i:H_i$ pair (Epard and Groshong, 1993; Gonzalez-Mieres and Suppe, 2006).

Diminishment in structural areas against increasing heights is only possible with simultaneous folding and sedimentation. Thus, the Surakhany 9 horizon should correspond to the top of the pre-growth section composed by the majority of the PS sequences (Fig. 6.12). Within the overlying sequences, the relationships between the folded area and elevation ($A_i:H_i$ crossplot) have demonstrated the occurrence of two growth episodes. The uppermost Surakhany subunits (3.5-3.1 Ma) are the first syn-kinematic deposit in the KAD, that is, the interval between the Surakhany 6 to the PS-top. A second slope break is distinguished after the PS-top due to a dramatic decrease in the $A_i:H_i$ that would explain the Post-PS as a second syn-growth package that continues until nowadays and deforms the seafloor.

The shortening magnitudes registered in the IL 540 by the pre-growth section (equation [6-3]) corresponds to the total deformation at the beginning of fold growth; *i.e.*, where dA_i/dH_i equals to zero (Gonzalez-Mieres and Suppe 2011). Using the polynomial regression the S_A measured in the top of the pre-growth section results to be 1.16 km (Table 6.3).

The intersection of the polynomial fit with the abscise axis when area is 0 shows the position of the detachment level. The root surface is inferred at ~9.6 km depth, below the maximum depth illuminated by the studied section (Figs. 6.7 and 6.12).

Curvimeric vs. planimetric shortening

Both curvimeric (S_C) and planimetric (S_A) shortening patterns in the IL 540 are conjointly illustrated for comparison in the graph of Figure 6.13 as a function of the age of units (*cf.* Table 6.3). They have been built by using polynomial and linear fits and correspond to mean estimations of shortening magnitudes.

The inspection of Figure 6.13 evidences two similar patterns for S_C and S_A curves (Santos Betancor *et al.*, 2013b). Both trends depict a convex-to-linear shape with two great sectors largely coincident with the intervals of the PS and the Post-PS. The comparison between the shortening magnitudes S_C and S_A in Figure 6.13 gives some additional and interesting details to the folding history of this structure. In this case, the curvimeric shortening (S_C) is always significantly lower than the shortening estimated through the $A_i:H_i$ relationships (S_A ; Fig. 6.12). This difference tends to diminish upwards within the pre- and syn-growth sequences, varying monotonically from 0.5 km in the lower portion of the PS to 0.4-0.1 km in the Apsheron and the seafloor. The difference in the pre-growth package is roughly satisfied by $S_A \approx S_C + 0.3$ km (*cf.* Table 6.3).

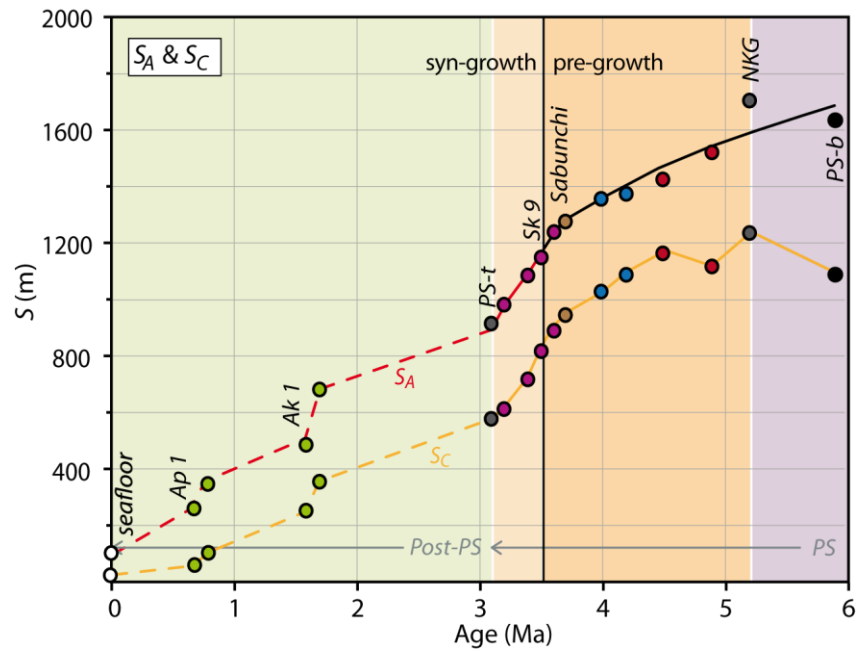


Figure 6.13: Comparative diagrams for both planimetric (S_A) and curvilinear (S_C) shortening in the IL 540 against time during the deposition of the PS and Post-PS. S_A curve is fitted by the best polynomial and linear regressions. S_C minimizes the deformation magnitude computed through the S_A ($S_A \approx S_C + 0.3$ km). Horizons are represented similarly to Figure 6.12. Productive Series are abbreviated as PS. Figure modified from Sánchez-Borrego *et al.*, (submitted).

Regional surfaces

The geometrical variation of the folded surfaces in the studied section is discussed using the relationships between the dip of the regional (α_{reg}) and the age of units. Figure 6.14 shows the dip of regional surfaces for the different horizons in the IL 540.

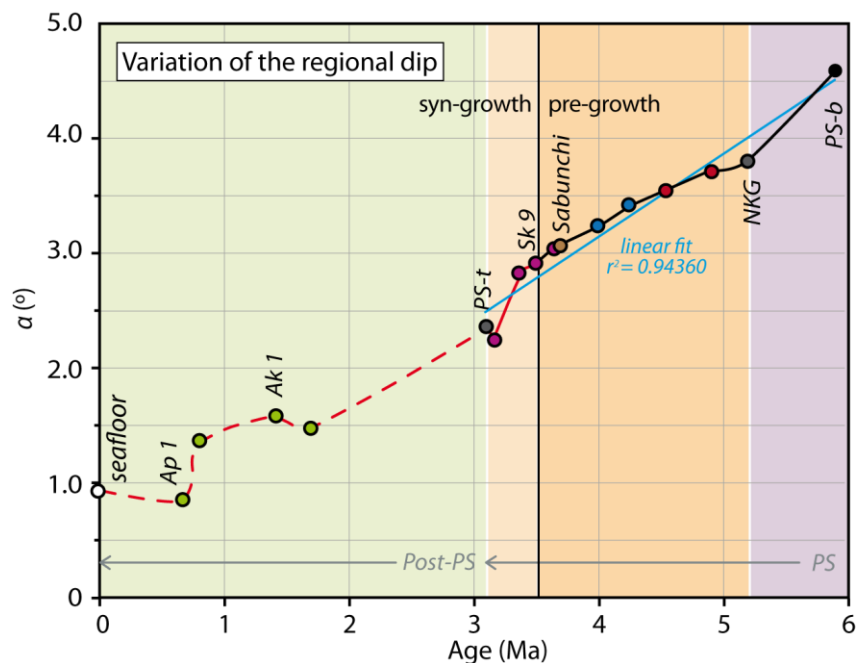


Figure 6.14: Graph that shows the dip of the regional level measured along the different surfaces in the IL 540, as a function of age (Ma). Abbreviations as in Figures 6.12 and 6.13.

The dip of the regional line depicts a linear and majorly decreasing trend. The best parametric fit for the PS distribution corresponds to a linear regression function ($r^2 = 0.94$), with a mean rate of $0.79^\circ \cdot \text{Ma}^{-1}$ and up to $1.50^\circ \cdot \text{Ma}^{-1}$ for the uppermost PS measured from the top of the Surakhany 9 Unit (Fig. 6.14). Conversely, the dip angle for the Post-PS sequence shows a rather fluctuating distribution although it has a mean rate of approximately $0.45^\circ \cdot \text{Ma}^{-1}$.

Fold flanks geometry

The dip of fold limbs (β_1 and β_2) measured along the different surfaces in the IL 540 is plotted against age in Figure 6.15. The difference between both flanks is also included in this diagram for comparison.

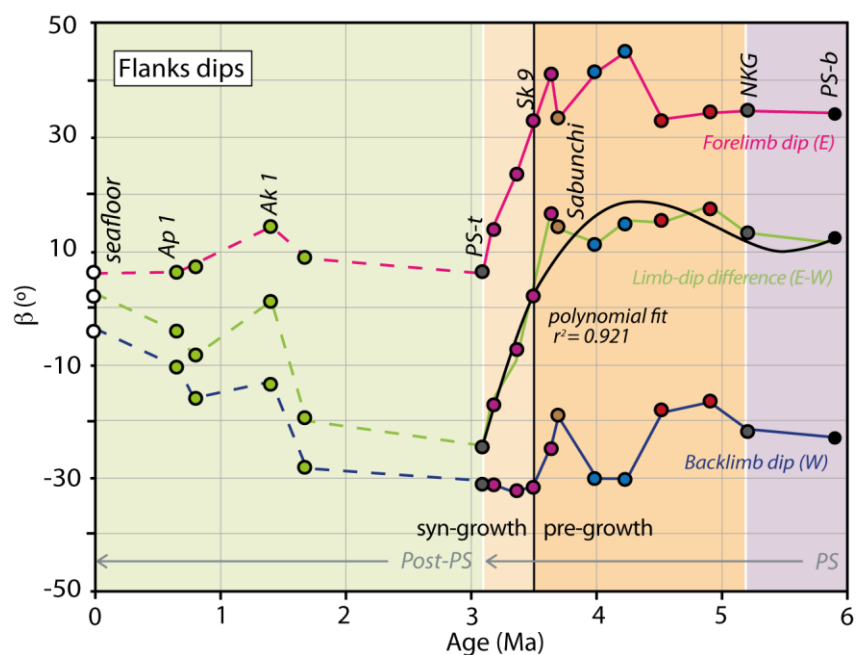


Figure 6.15: Representation of the variation of the flanks dips in the inflexion point in the eastern (pink-coloured line) and in the western (blue-coloured line) limbs of the KAD anticline against time. The difference (green line) between both angles is fitted by a polynomial function. Abbreviations as in Figures 6.12 and 6.13.

With respect to the vertical variation of fold dips in the eastern and western flanks (lines pink and blue, respectively in Figure 6.15), it is inferred the occurrence of some distinctive features. For example, it is observed that the two flanks maintained the same attitude for the lower part of the PS sequence (from the PS-b to Sabunchi reflections), with a slight eastwards asymmetry or vergence, because the eastern limb dips approximately 10° more than the western one. The situation reverses in the Surakhany to PS-top reflections; the eastern limb diminishes progressively its dip, whereas the western limb remains with a constant attitude. During the Post-PS sequence, the observations depict a slightly different scenario. The eastern flank has then a rather constant dip ($\sim 7\text{-}10^\circ$), whereas the western limb tends clearly to smooth upwards (from 30° to $4\text{-}5^\circ$).

Folding evolution

Shortening results give us a crucial idea about folding history and evolution (*Table 6.3* and *Figs. 6.12* and *6.13*). Diagram of $A_i:H_i$ in *Figure 6.12* demonstrates that the folding history is marked by two main episodes. Most of the PS are a clear candidate to represent the pre-growth section. Curve maximum inflection at the end of the Surakhany 9 Unit (3.6-3.5 Ma) may be interpreted as the start of folding growth in the KAD anticline (*Fig. 6.12*). Thus, in this fold section the PS package comprised between the PS-bottom and the Surakhany 9 Unit (5.9-3.5 Ma) represents the pre-kinematic sequence, and the interval delimited by the Surakhany 6 and the PS-top (3.5-3.1 Ma) is the first syn-kinematic strata (Santos Betancor *et al.*, 2013b; Santos Betancor and Soto, 2015; Sánchez-Borrego *et al.*, submitted). Post-PS trajectory evidences second deformation episode started in 3.1 Ma and gradually extends henceforth to Present-day and deforms the seafloor. We infer that the Post-PS were deposited in a different syn-tectonic framework than the PS as pattern totally departs (*cf. Figs. 6.12* and *6.13*). Abundant mobilized sediments also reinforce Post-PS folding (Santos Betancor *et al.*, 2013a).

The analysed relationship of areas against heights above the PS-bottom shows a recognizable indicator of detachment folding (*e.g.*, Epard and Groshong, 1993; Santos Betancor *et al.*, 2013b). The different fits applied to the PS and Post-PS match with the occurrence of a single detachment level that remains below the studied sequence (Gonzalez-Mieres and Suppe, 2006). The estimated depth to the detachment level is sited around 9.6 km (Sánchez-Borrego *et al.*, submitted) and coincides with regional studies (*Figs. 6.7* and *6.12*). This décollement surface in the SCB is presumably located within the 2 km-thick shale-rich Maykop Unit; this is a well-known package with overpressured muds and consistently, a weak layer to root any decoupled surfaces during folding (*e.g.*, Morley *et al.*, 2011; Baganz *et al.*, 2012).

Average rates of shortening (dS_A/dt) are obtained from dS_A/dH_i ratios and estimated sedimentation rates dH_i/dt (Gonzalez-Mieres and Suppe, 2011; Sánchez-Borrego *et al.*, submitted). The initial growth period, corresponding to the Surakhany 6 to the PS-top interval, has a resulting average rate of dS_A/dH_i equal to 0.19. The Post-PS sequence has an associated trend with a linear slope of 0.58. We have computed individual dS_A/dH_i values for the different Post-PS units, resulting average values of 0.73 for the Akchagyl Unit (3.1-1.6 Ma), 0.52 for the Apsheron Unit (1.6-0.7 Ma), and lowering up to 0.40 for the most recent sediments (<0.7 Ma).

By using the position of studied horizons in *Table 6.3*, we have obtained average sedimentation rates in the western syncline of $dH_i/dt = 3.26 \text{ mm}\cdot\text{yr}^{-1}$ for the interval between the top of the Surakhany 9 and the PS-top, and over $0.45 \text{ mm}\cdot\text{yr}^{-1}$ for the Post-PS period. For the latter epoch, it is inferred values of $0.40 \text{ mm}\cdot\text{yr}^{-1}$ in the Akchagyl Unit, and $0.49 \text{ mm}\cdot\text{yr}^{-1}$ for the Apsheron and Recent units.

Combining dS_A/dH_i estimates with the corresponding dH_i/dt values, it is inferred a punctuated history of deformation with diverse shortening rates (dS_A/dt), although they tend to decrease through the growth period (Sánchez-Borrego *et al.*, submitted). The first growth period, from the Surakhany 6 to the PS-top (*i.e.*, during 0.4 my), occurred under a shortening rate of $0.62 \text{ mm}\cdot\text{yr}^{-1}$. The average rate during the Post-PS epoch (*i.e.*, in the last 3.1 my) was of about $0.26 \text{ mm}\cdot\text{yr}^{-1}$ and occurred under variable circumstances. During the first period, with a total duration of 1.5 my and coinciding with the deposition of the Akchagyl Unit (3.1-1.6 Ma), the resulting shortening rate was $0.29 \text{ mm}\cdot\text{yr}^{-1}$. Shortening rates gradually diminished during deposition of the Apsheron Unit ($0.25 \text{ mm}\cdot\text{yr}^{-1}$; 1.6-0.7 Ma) and extended to the most recent sediments that show shortening velocities of $0.20 \text{ mm}\cdot\text{yr}^{-1}$.

These values explain the contrasting geometries identified within the growth sediments (Fig. 6.7). Thus, the imperceptible thinning of the uppermost PS (from the Surakhany 6 Unit) towards the anticline crest during folding may be explained by very high sedimentation rates (up to five times $dH_i/dt > dS_A/dt$), whereas the noticeable diminishment in the dS_A/dt & dH_i/dt differences reinforce the marked onlap geometry identified in the Post-PS (Santos Betancor and Soto, 2015). Onlapping and wedge geometries are especially evident in the Akchagyl Unit where maximum shortening occurs against minimum sedimentation rates, followed by smoother drapping relationships from the Apsheron to the most recent sediments (Santos Betancor and Soto, 2015). All these estimates indicate that a fold pulse was produced during the Akchagyl epoch.

Differences between both S_C and S_A in the overall sequences suggest that the planimetric estimations measure areal variations during folding that bed-length methodology does not support (Table 6.3 and Fig. 6.13). Similar differences have also been found in other folds of this type (Gonzalez-Mieres and Suppe, 2006). We can rule out the occurrence of a volume increase during shortening due to the convex trend for the pre-growth sequence in the $A_i:H_i$ diagram (Fig. 6.12) reinforced by the relationship $S_A \approx S_C + 0.3$ km (Fig. 6.13; Santos Betancor *et al.*, 2013b, Sánchez-Borrego *et al.*, submitted). They might be a result of subcompaction of the pre-growth sequence during burial and/or by lateral flow of the fluid- and shale-rich sediments. In any case, the abundance of mud-escape structures in the fold culminations manifests that mud flows in the subsurface during deformation.

Overpressured sediments in the KAD fold may correspond to the mobile Maykop Unit that promotes an inflation of the fold core during shortening (*e.g.*, Gürgey, 2003; Stewart and Davies, 2006; Roberts *et al.*, 2010; Santos Betancor and Soto, 2015). These processes are relatively common in salt-cored anticlines (*e.g.*, Rowan, 1997; Rowan *et al.*, 2000).

The convex shape in the $A_i:H_i$ plot (Fig. 6.12) also evidences the occurrence of a significant layer-parallel shear during shortening in detachment folding (Groshong and Epard, 1994; Gonzalez-Mieres and Suppe, 2006, 2011). The difference between shortening results based on area of relief (S_A) and bed-length shortening (S_C) observed in plot Figure 6.13 is used to directly evaluate the role of layer-parallel pure shear shortening (Gonzalez-Mieres and Suppe, 2006); *i.e.*, $S_A \gg S_C$ in the KAD anticline may be approximated by the pure shear model of detachment folding with minimum layer-parallel stretching (Groshong and Epard, 1994). Thus, deflection on the overburden due to flexural components acts in a second place and we have to consider carefully our interpretation from S_C results and interpret them as the possible component of apparent shortening instead of tectonic shortening consumed in the horizontal component, such in layer compaction. In folds examples with low fold wavelength as the KAD anticline, simple-shear is negligible (Gonzalez-Mieres and Suppe, 2006).

Regional tilting framework of the SCB crust may explain oscillations of regional dip and higher dips and thickness in the eastern flank of the KAD anticline (Figs. 6.14 and 6.15) (Santos Betancor and Soto, 2015). This process was subtle and continuous in this margin of the SCB and promoted the basin subsidence towards the East, where the depression is presumably floored by a heavy oceanic crust (Berberian, 1983; Mangino and Priestley, 1998; Allen *et al.*, 2002). Syn-sedimentary tilting was majorly constant during the PS period, experienced an acceleration simultaneously to the deposit of the Surakhany 6 and 2 subunits and slightly decreased in the last 3.1 my.

Our geometrical observations in *Figure 6.15* also evidence detachment folding may contribute to the dissymmetry in the KAD fold (Santos Betancor and Soto, 2015). Increasing dips in the western limb from the Surakhany Unit to the PS-top manifest folding burst in that epoch, with major rates than sedimentation ($F>S$). Coetaneous and sharp decreasing trend in the eastern flank is an indicator of its role as the motor flank; *i.e.*, the onset of deformation according to the direction of movement in the detachment fold (Poblet, 2004). This leading flank corresponds to the forelimb, and the dragged flank represents the backlimb, that is, the western limb. Deformation continued during the Post-PS period, and detailed analyses reflect flanks might suffer rotation, especially within the Akchagyl Unit as they follow a different eastern and western pattern (*Fig. 6.15*). Wedge geometries and onlapping features (*Fig. 6.7*) manifest folding rates surpassed sedimentation, with more evidences in the eastern limb, that have decreased from Apsheron times to Present ($F<S$).

6.3.2. ILs 720, 1140, and 1640

Lines 720, 1140 and 1640 (*Fig. 6.9*) are located successively northwards of the IL 540 (*Fig. 6.7*). The IL 720 is sited 3.3 km far, separated 7.8 km from the IL 1140. The northernmost IL 1640 is located >20 km towards the North of the IL 540. Fold section in the IL 720 depicts a kink-band fold, similarly to the southern areas, the IL 1140 crosscuts the Southern Culmination in the KAD structure, and the IL 1640 is selected because it represents the saddle domain between both culmination zones. The strategic position and images of these profiles let us to clarify our interpretation made from the IL 540 and, hereby, to reconstruct the complete history of growth and fold evolution.

Our outcome of shortening results (S_A and S_C) for these sections are presented and compared with the IL 540 results in *Table 6.6*. The absolute depth to the décollement surface from the sealevel in all lines is also included.

Horizons	IL 540		IL 720		IL 1140		IL 1640	
	$Z_{det}=9.571$ km		$Z_{det}=17.847$ km		$Z_{det}=8.962$ km		$Z_{det}=10.999$ km	
	S_C (km)	S_A (km)	S_C (km)	S_A (km)	S_C (km)	S_A (km)	S_C (km)	S_A (km)
sf	0.016	0.111	0.024	0.074	0.066	0.161	0.010	0.112
Ap1	0.053	0.249	0.150	0.138	0.292	0.355	0.042	0.175
Ap2	0.101	0.341			0.227	0.474		
Ak1	0.247	0.478	0.368	0.261	0.245	0.699	0.130	0.333
Ak2	0.352	0.678			0.310	0.936		
PS-t	0.573	0.913	0.685	0.540	0.623	1.384	0.446	0.851
Sk 2	0.605	0.979	0.813	0.576	0.730	1.606	0.473	0.938
Sk 6	0.714	1.095	0.904	0.641	1.018	1.987	0.483	1.116
Sk 9	0.815	1.158	0.960	0.671	1.154	2.170	0.607	1.228
Sk 12	0.899	1.243	0.997	0.679	1.368	2.400	0.614	1.309
Sab	0.949	1.277	1.036	0.698	1.317	2.518	0.557	1.359
Bk-Upper	1.023	1.356	1.264	0.699	1.595	2.832	0.590	1.465
Bk-Lower	1.094	1.381	1.133	0.694	1.709	3.004	0.531	1.479
Per-Old	1.168	1.428	1.328	0.702	2.639	3.379	0.455	1.565
Per-New	1.118	1.530	1.112	0.666	2.734	3.657	0.979	1.560
NKG	1.229	1.714	1.291	0.682	2.868	4.125	0.994	1.626
PS-b	1.092	1.626	1.438	0.722	1.295	3.995	0.850	1.736

Table 6.6: Curvilinear shortening (S_C) and planimetric shortening (S_A) values of for the different seismic sections studied in this thesis. S_A is obtained through a polynomial fit. The absolute depth to the detachment surface Z_{det} is estimated in each fold profile. Horizons abbreviations as in *Table 6.3*.

Curvilinear shortening

Bed-length shortening (S_C) for all lines analysed in this study are obtained according to the equation [6-2] and represented in *Figure 6.16*. Measurements are satisfied by $h = 0.02$. Maximum curvilinear shortening (S_C) occurs in the IL 1140 and it is 2.87 km. These estimations considerably contrast with the less shortened IL 1640, with <1 km. The southern sectors have evolved similarly, with S_C values of 1.23 km (IL 540) and 1.29 km (IL 720). In all lines Present-day deformation is observed, especially noticeable in the IL 1140 where the seafloor is shortened up to 66 m (*cf. Table 6.6*).

Marked spatial differences are described in detail between the PS and the Post-PS. In the South, shortened magnitudes in the PS range over 0.60 km (IL 720) and 0.67 m (IL 540) (*cf. Tables 6.3 and 6.6*). Major shortened areas are registered in central positions (IL 1140), with up to 2.25 km, whereas the IL 1640 presents the lowest magnitudes with 0.45 km of shortening. The evolution of the S_C in the Post-PS epoch substantially changes; Post-PS units were equally shortened in the IL 540 and in the IL 1140, with values of 0.56 km. Maximum shortening was produced in the IL 720, with up to 0.66 km in 3.1 my. By contrast, the IL 1640 was the minorly deformed, with 0.44 km of curvilinear shortening.

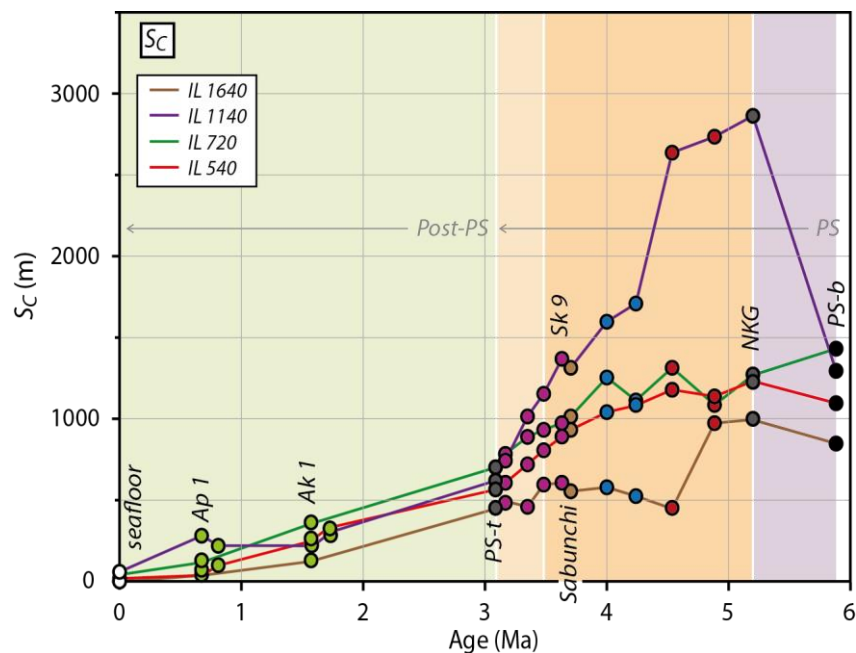


Figure 6.16: Comparative graph of S_C values against time in the studied sections: 540 (*cf., Fig. 6.13*), 720, 1140 and 1640. Abbreviations as in *Figures 6.12 and 6.13*.

Planimetric shortening

In *Figure 6.17* we have represented $A_i:H_i$ curves for all fold sections, including the IL 540, constructed with the equations [6-3] and [6-4] (*cf. Fig. 6.12*). In the graph, polynomial functions join scatter distributions in the pre-growth packages through black lines, and linear approaches are used for syn-growth sequences, separated by a maximum $A_i:H_i$ pair.

An overall inspection evidences similar trend for all profiles as previously described for the IL 540 (*Fig. 6.12*): increasing areas occur as we go upwards in the stratigraphic

sequence as an indicator of the pre-growth sequence, whereas both, a subtle and marked downward linear patterns, are representative of the syn-growth sediments. Maximum structural areas are computed in the PS package of the IL 1140, with values of $\sim 13.8 \text{ km}^2$. The present-day seafloor registers values of up to 1.75 km^2 , observed towards the North in the IL 1640.

Limit between polynomial and linear fits in the PS is located in *Figure 6.17* in the top of the Surakhany 9 Unit (3.5 Ma), as it was established for the IL 540 (*Fig. 6.12*). Congruently with our previous analysis, the Surakhany 6 (3.5-3.4 Ma) represents the first syn-growth sequence in the southern IL 720. Towards the North, the situation substantially changes, and the end of the pre-growth sequence may be represented by an older horizon. Accordingly to the increasing curves within the PS, the maximum $A_i:H_i$ pair, and therefore, the boundary with the linear approach might be positioned in the top of the Surakhany 12 Unit (3.6 Ma) in the IL 1640 or even after the deposit of the Sabunchi Unit (3.7 Ma) in the IL 1140. These observations evidence the Surakhany Unit (3.7-3.1 Ma) might represent the first syn-growth sequence in the KAD fold.

The evolution of the overlying Post-PS sequences reflects a common trend of a sharp decay in all lines, separated from the underlying Surakhany Unit in the PS-top (*Fig. 6.17*). Nevertheless, the Surakhany 2 might mark a pattern change between syn-growth packages in the IL 1140, as it separates a smooth descending trajectory in the PS and an abrupt linear pattern that extends to the Post-PS period.

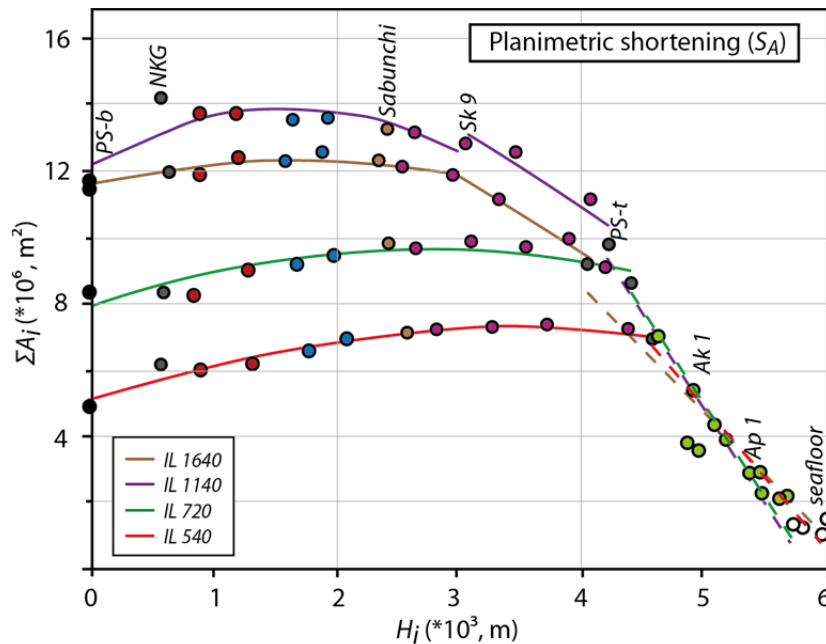


Figure 6.17: Comparison plot of the $A_i:H_i$ relationship for each horizon in the studied inlines: 540 (*Fig. 6.12*), 720, 1140 and 1640. Polynomial fitting is applied to the pre-growth distribution to calculate the depth to the detachment in the intersection of the X axis when $A_i = 0$ (Epard and Groshong, 1993; Gonzalez-Mieres and Suppe, 2006, 2011). Syn-growth units are fitted by linear approaches, as continuous and dashed-lines, respectively. H_i is the height to the reference level that corresponds to the PS-bottom (PS-b) and A_i is the structural area for each surface. Horizons abbreviations are as in *Figure 6.7*.

The shortening magnitudes registered at the top of the Surakhany 9 Unit varies along fold strike, from maximum estimations in the IL 1140 (2.17 km) to minimum of 0.67 km in the IL 720. Intermediate values are equally registered in the IL 540 (1.16

km) and the northernmost line (IL 1640, 1.23 km). These values correspond to the total deformation at the beginning of fold growth in the South, and at the initial stages in the North, where have presumably started at the Surakhany 12 times.

Detachment depths obtained when $A_i = 0$ for all studied transects are detailed in *Table 6.6*, according to our findings presented in *Figure 6.17*. The detachment surface oscillates between 9 and 18 km. Minimum depths coincide with the position of the ILs 1140 and 540, and deeper locations occur in the ILs 1640 and 720.

The graph of *Figure 6.18* reproduces the evolution in time of planimetric shortening (S_A) magnitudes in the selected fold sections. Maximum values are quantified in the IL 1140, that has been shortened >4 km (*cf. Table 6.6*). Minimum deformation occurs in the IL 720, that slightly surpasses 0.7 km. Progression of lines 540 and 1640 are majorly parallel with similar intermediate values (*Fig. 6.18*).

Slope breaks in *Figure 6.18* are consistent with those observed in the $A_i:H_i$ graph, that reinforce proposed folding dates (*Fig. 6.17*). Therefore, the limit pre- and syn-kinematics is located within the Surakhany Unit, established in the top of the Surakhany 9 in the southern regions, and in the base (IL 1140) and top (IL 1640) of the Surakhany 12 subunit towards the North.

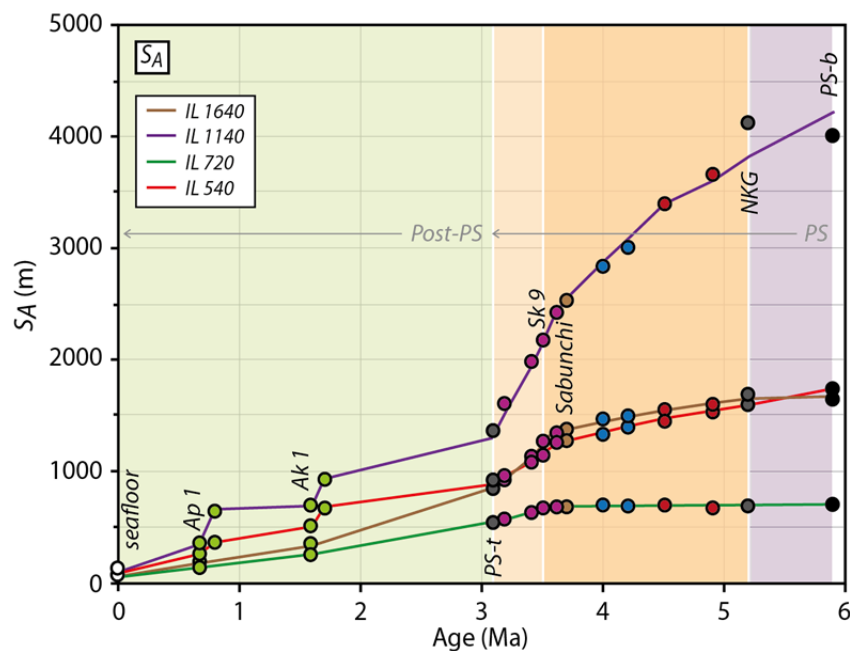


Figure 6.18: Graph that ensembles the S_A values fitted by polynomial functions for lines 720, 1140 and 1640. The curve of the IL 540 represented in *Figure 6.13* is also included for comparison. Abbreviations as in *Figures 6.12* and *6.13*.

Curvilinear vs. planimetric shortening

Comparison between *Figures 6.16* and *6.18* sheds light on the evolution in time of curvilinear (S_C) and planimetric (S_A) magnitudes along the KAD fold that complement our observations of IL 540 (*Fig. 6.13*). Results show that influence of area is crucial because of the equation $S_A > S_C$ obtained in all sections, with some discrepancies in the position of the IL 720 (*cf. Table 6.6*). Major magnitudes of both shortening parameters are registered in the IL 1140, where mean S_A rises up to 1 km higher than bed-length

shortening.

Regional surfaces

Figure 6.19 illustrates a comparison between the dip of the regional stratigraphic gradient of each horizon (α_{reg}) for the 4 analysed sections in time. Dip trend is mostly similar for all profiles, with a clear slope break along the dip curve sited in the PS-top. Mean rates for dip variation within the PS oscillate between $0.79^{\circ}\cdot\text{Ma}^{-1}$ to $1.43^{\circ}\cdot\text{Ma}^{-1}$, with an increasing tendency towards the North, whereas it reverses for the Post-PS, from $0.45^{\circ}\cdot\text{Ma}^{-1}$ in the IL 540 to $0.03^{\circ}\cdot\text{Ma}^{-1}$ in the IL 1640. Mean variations of regional dips in the uppermost Surakhany interval range is $<1.70^{\circ}\cdot\text{Ma}^{-1}$ in the southern lines, and range between 2.60 and $3.0^{\circ}\cdot\text{Ma}^{-1}$ respectively northwards.

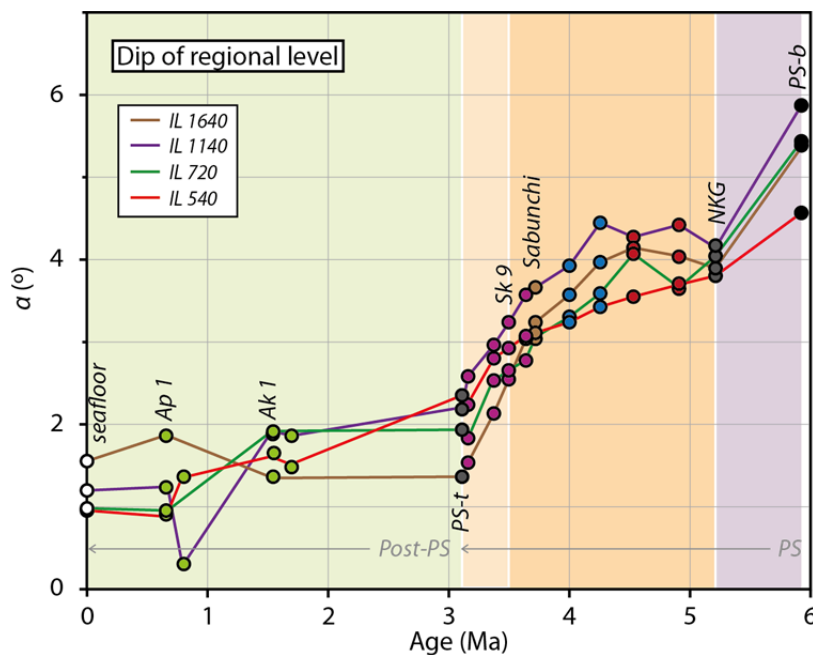


Figure 6.19: Comparative graph for the variation of the regional dip along the different studied sections. Dip evolution in IL 540 is also illustrated in Figure 6.14. Abbreviations as in Figures 6.12 and 6.13.

Fold flanks geometry

Fold flanks geometry in the studied sections is interpreted through the dip analysis of the eastern and western limbs (*cf.* Figs. 6.15 and 6.20). In all cases, major dips are usually measured in the eastern fold limb (Fig. 6.20), with differences that even surpass 10° . Maximum estimations are computed in the IL 720, and locally in the western IL 1140. Less dipping flanks usually correspond to the fold profile of the IL 1640.

Inspection through the PS units shows a rather constant limb dip of 10° in the West of the IL 1640, and 35° in the IL 720, followed by a continues decay of dip trend after the PS-top. Tendency is similar in the eastern limb in both sections. Flanks dip evolution in the remainder lines is characterized by a marked drop in dip in the Surakhany times, and a convulse Post-PS period with local variations of flanks dip. Dip evolution in the IL 1640 depict a relatively quiet setting in the last 5.9 my, only disturbed by a dip variation close to the PS-top.

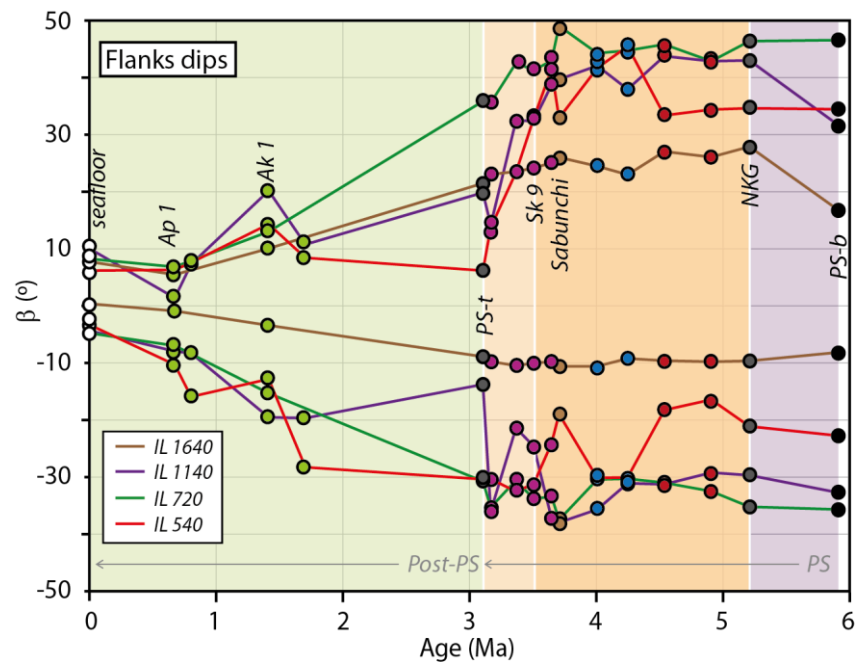


Figure 6.20: Graph of the flanks dip evolution in time in the studied ILs: 540 (cf. Fig. 6.15), 720, 1140 and 1640. Bright colours are used for the eastern flank, and light colours, for the western limb. Abbreviations as in Figures 6.12 and 6.13.

Folding evolution

According to our interpretation of the selected sections we can establish two tectonic events with temporal variations along the KAD anticline, especially evident in the first episode (cf. Figs. 6.16 to 6.20). We also identify spatial discrepancies in the shortening values along fold strike (Table 6.6). Our inspection suggests the evolution of the KAD fold might be separated among the northern and the southern domains.

The KAD fold has presumably burst simultaneously to the syn-kinematic deposit of the Surakhany Unit. We propose an early nucleation in northern areas during the deposit of the Surakhany 12 subunit (3.7-3.6 Ma), and southward propagation after the deposit of the Surakhany 9 (3.6-3.5 Ma). First episode was continued by a second event that took place roughly homogeneous along the KAD anticline in the Post-PS epoch (<3.1 Ma).

Deformation responds to a detachment-folding type that is produced above a single décollement surface majorly constrained between 9 and 11 km of depth within a thick Maykop Unit (Fig. 6.17 and Table 6.6) (Gonzalez-Mieres and Suppe, 2011). Higher depths in our estimations may reflect anomalous values. We infer depth variations may be a result of the deformation of the root surface and local rise, as it occurs in the IL 1140 presumably due to mud ascend due to diapirism.

Accordingly to our previous analysis, shortening rates (dS_A/dt) are obtained from the combination of dS_A/dH_i and dH_i/dt (e.g., Gonzalez-Mieres and Suppe, 2011). Computed ratios are resumed in Table 6.7. Major results of dS_A/dH_i in both syn-growth packages are registered in the IL 1140, with values of 0.65 and 0.81, respectively in the uppermost Surakhany and in the Post-PS. Minimum ratios are variably detected in the southern sectors, that correspond to 0.19 in the interval Surakhany 6-to-PS-top (3.5-3.1 Ma) (IL 540), and 0.34 in the Post-PS in the IL 720. Detailed results evidence major values observed in the Akchagyl Unit (3.1-1.6 Ma) for all sections, with up to 1.0 in the

IL 1140. Ratios decrease progressively to Present (*Table 6.7*).

Sedimentation rates estimated in the first syn-growth stage are very high and range between $2.9 \text{ mm}\cdot\text{yr}^{-1}$ (IL 1640) and $3.3 \text{ mm}\cdot\text{yr}^{-1}$ (IL 540). In the Post-PS package, velocities are rather constant, with values of $0.45\text{-}0.49 \text{ mm}\cdot\text{yr}^{-1}$, except in the vicinities of the IL 1640 that increase to $0.63 \text{ mm}\cdot\text{yr}^{-1}$, with a maximum of $0.89 \text{ mm}\cdot\text{yr}^{-1}$ quantified in the Apsheron Unit (1.6-0.7 Ma).

Combined results reflect shortening rates (dS_A/dt) in the Surakhany times are exceptionally high, that oscillate between $0.62 \text{ mm}\cdot\text{yr}^{-1}$ (IL 540) and $1.95 \text{ mm}\cdot\text{yr}^{-1}$ (IL 1140). In the Post-PS period, mean major values do not surpass $0.40 \text{ mm}\cdot\text{yr}^{-1}$ (IL 1140). The Akchagyl Unit registered in that fold section $0.46 \text{ mm}\cdot\text{yr}^{-1}$, that diminished to $<0.1 \text{ mm}\cdot\text{yr}^{-1}$ in the IL 1640 nowadays.

Intervals	IL 540			IL 720			IL 1140			IL 1640		
	dS_A/dH_i	dH_i/dt	dS_A/dt									
Post-PS	0.58	0.45	0.26	0.34	0.45	0.15	0.81	0.49	0.40	0.38	0.63	0.24
Gelasian	0.40	0.49	0.20	0.20	0.52	0.09	0.53	0.52	0.28	0.18	0.50	0.09
Apsheron	0.52	0.49	0.25	0.31	0.44	0.14	0.75	0.51	0.38	0.20	0.89	0.18
Akchagyl	0.73	0.40	0.29	0.42	0.44	0.19	1.0	0.46	0.46	0.65	0.49	0.34
PS-top to Sk9-top	0.19	3.26	0.62	0.33	3.23	1.06						
PS-top to Sk12-top										0.32	2.90	0.90
PS-top							0.65	3.05	1.95			
Sab-top												

Table 6.7: Summary table with sedimentation (dH_i/dt) and shortening rates (dS_A/dt) obtained for the studied fold in the syn-growth packages recognized through the analysis of ILs 540, 720, 1140 and 1640. Calculus of dS_A/dH_i is also included for all sections. The Surakhany Unit is abbreviated as Sk. Units of shortening and sedimentation rates are $\text{mm}\cdot\text{yr}^{-1}$.

Therefore, the KAD fold has uplifted since or during the deposit of the Surakhany 12 Unit (3.7-3.6 Ma) in the northern areas, and folding propagated southwards after the deposit of the Surakhany 9 (3.6-3.5 Ma). Geometrical discrepancies between both syn-kinematic packages are a response of relative differences between folding and sedimentation rates. High dH_i/dt and dS_A/dt ratios in the uppermost PS are expressed as very subtle thinning of sequences along the buried growing KAD fold. Shortening occurs homogeneously in the last 3.1 my along the complete structure, following $dS_A/dt > dH_i/dt$, responsible for marked wedge shapes in the Post-PS sequences, more noticeably in the Akchagyl Unit (3.1-1.6 Ma) due to a peak of deformation. Shortening rates have decreased progressively to nowadays.

Our results in *Figures 6.16* and *6.18* evidence folding varied along strike. Major shortened areas are detected in the IL 1140 and we infer its structural position may be a response of exceptionally high shortening rates. This interpretation might be extrapolated to the Northern Culmination intersected by the IL 2000 (see *Fig. 5.5*).

Variations and differences among S_C and S_A may be a result of areal changes at depth, due to mud migration and withdrawal along the KAD fold (*Figs. 6.16* to *6.18*). Considering the subtle decay of the A_i/H_i curve in the older syn-growth sequence we assume folding was coetaneous to deep mud migration (*Fig. 6.17*). A large mobilization of mud occurred simultaneously to the second and accentuated fold growth, according to the dramatic fall observed in *Figure 6.17*. Thus, we propose mud diapirism may have

started during the deposit of the Akchagyl in the KAD fold, or locally after the deposit of the Surakhany 2 (3.2-3.1 Ma) in the major deformed area intersected by the IL 1140. Anomaly high shortening rates may have squeezed overpressured muds from the Maykop to locally pierce the IL 1140, and, presumably the IL 2000 as the most deformed sections in both culmination domains in the KAD fold.

Folding and mud diapirism in the KAD are a result of regional shortening in a continuously tilting margin, consistently to dip oscillation of regional surfaces and flanks (*Figs. 6.19 and 6.20*). A punctual episode of tilting may have occurred simultaneously to shortening during the deposit of the uppermost Surakhany after the Surakhany 9 Unit; major subsidence took place in the southernmost sectors. Detachment folding was led by the eastern flank or forelimb that moved towards the East where the oceanic crust floors the SCB. We propose hinge migration as the main mechanism in the PS buckle folding, and responsible for the subtle thinning above the fold crest. The Post-PS period should be mainly characterized by flanks rotation that produced marked thinning and onlapping geometries. Noticeable wedges in the Akchagyl reinforce fold pulse in that epoch, whereas burial of KAD fold is produced towards the North from Apsheron times (1.6-0.7 Ma).

7.DEFORMATION HISTORY AND FOLD EVOLUTION

In this thesis we have compiled numerous data and observations that explain the evolution of the sedimentary basin and the role played by folding and mud diapirism in the western SCB. Results obtained along the different folded sections of the studied anticline have been correlated through the complete volume to analyse the deformation history of the KAD structure. In this chapter, we have shed light on the regional geodynamics in the last 5.9 Ma.

7.1. Basin Sedimentary Evolution

7.1.1. *Isopach Maps*

The SCB is a super-deep basin containing around 20 km of sediments deposited since Jurassic times. Late Miocene to Recent rocks correspond to the fluvio-lacustrine sand-shale sequence of the Productive Series (PS; Late Miocene-Late Pliocene, 5.9 Ma to ~3.4-3.1 Ma; Inan *et al.*, 1997; Jones and Simmons, 1997; Abreu and Nummedal, 2007; Forte *et al.*, 2010) that present thickness of ~6 km (*e.g.*, Zonenshain and Le Pichon, 1986; Brunet *et al.*, 2003). The overlying clastic units are here grouped as the Post-PS (Late Pliocene-Present, <3.4-3.1 Ma) package, and represents over 3 km of the sedimentary sequence.

To unravel folding history and for a better understanding of flanks differences in the KAD structure, we have computed isopach maps. Maps have been created based on techniques of True Stratigraphic Thickness (TST) instead of True Vertical Thickness (TVT), that is, thickness is always measured perpendicular to the top surface of each unit (*Fig. 7.1*). We have used smoothed surfaces of the key folded PS and Post-PS horizons, to avoid local errors in the seismic signal (*Fig. 7.2*) (Santos Betancor and Soto, 2015). Within the PS package, we have selected two intervals separated by the top of the Surakhany 12 Unit (Early-to-Late Pliocene, 3.7-3.6 Ma) as a key level during folding. Thickness displays include structural interpretation of the different upper-bounding surfaces. Our approach assumes sediments are compacted and, in consequence, these maps represent minimum thickness values (Allen and Allen, 2005).

In the interval comprised by the PS-bottom (Late Miocene, 5.9 Ma) and the top of the Surakhany 12 Formation dated as 3.6 Ma, we have identified two major thickness

domains separated approximately by the actual position of the fold hinge (*Fig. 7.2a*) (Jones and Simmons, 1997; Abreu and Nummedal, 2007; Forte *et al.*, 2010). The western fold limb is characterized by a thinner platform of 2.2-2.5 km that thickens to the South up to 3.1 km, following a NW-SE direction. Thickness in the eastern domain remains almost constant with 3.1-3.2 km of sediments, whereas it reaches a maximum thickness of 3.5 km in the SE syncline. In detail, the transition zone between fold limbs take place in a narrow and elongated zone with a maximum thickness of 3.5 km. Southern depocentres are locally separated by tight thinned areas parallel to the NW-SE kink-band structures.

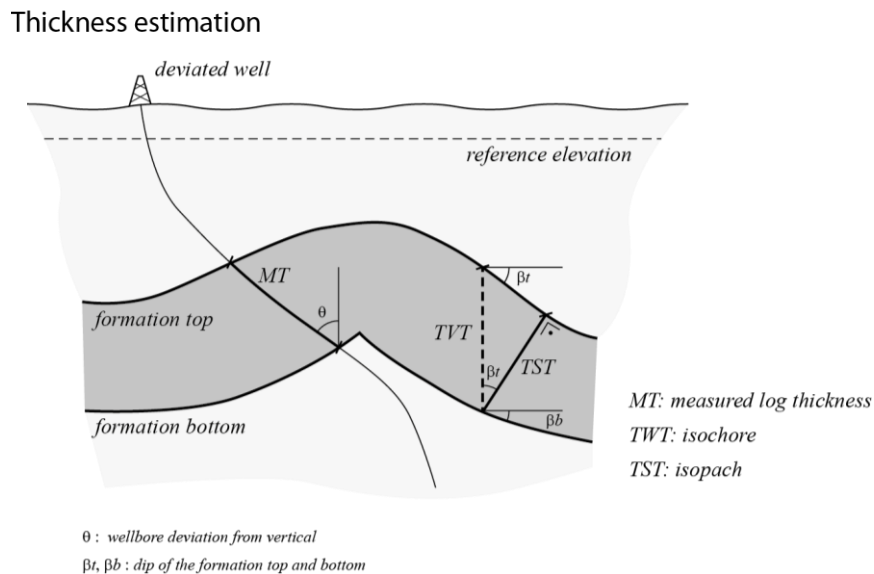


Figure 7.1: Schematic diagram to explain calculations of True Stratigraphic Thickness (TST) and True Vertical Thickness (TVT). Expanded formulas are described in Bateman and Konen (1979).

Map in *Figure 7.2a* evidences the existence of a linear structure along fold trace in the topography that promoted a major sinking of the PS sequences up to the Surakhany 12 Unit (Santos Betancor and Soto, 2015). Differences of up to 1-1.5 km are consistent with the existence of a buried and normal fault dipping to the East. The syn-sedimentary faulting of the PS created a tri-shear domain with a horizontal width and geometry that depends on the dip, depth, and slip of the buried normal fault (*e.g.*, Hardy and McClay, 1999). According to the general pattern of TST in the KAD structure, deep fault should be a high-angle structure, although we cannot rule out the contribution of some right-lateral displacement to the general eastward-downthrown of the master fault, but we interpreted that this strike-slip component of the fault, which has been postulated in the region, exists (*e.g.*, Khain *et al.*, 1966).

The resulting pattern of the uppermost interval, constituted by the Surakhany 9 Unit (Late Pliocene, 3.6-3.5 Ma) and the PS-top (3.1 Ma) (*Fig. 7.2b*), slightly departs from the deeper interval (*Fig. 7.2a*), suggesting a change in the folding history (Jones and Simmons, 1997; Abreu and Nummedal, 2007; Forte *et al.*, 2010). Both anticline culminations and flanks are separated by a narrow (0.8 km-wide) and slightly curved domain (*Fig. 7.2b*). The thickness difference between fold flanks is less evident, although it is recognisable in the central and northern domains of the KAD fold because the mean value of the western limb is about 1.5-1.7 km and the eastern has a constant value over 2.0 km.

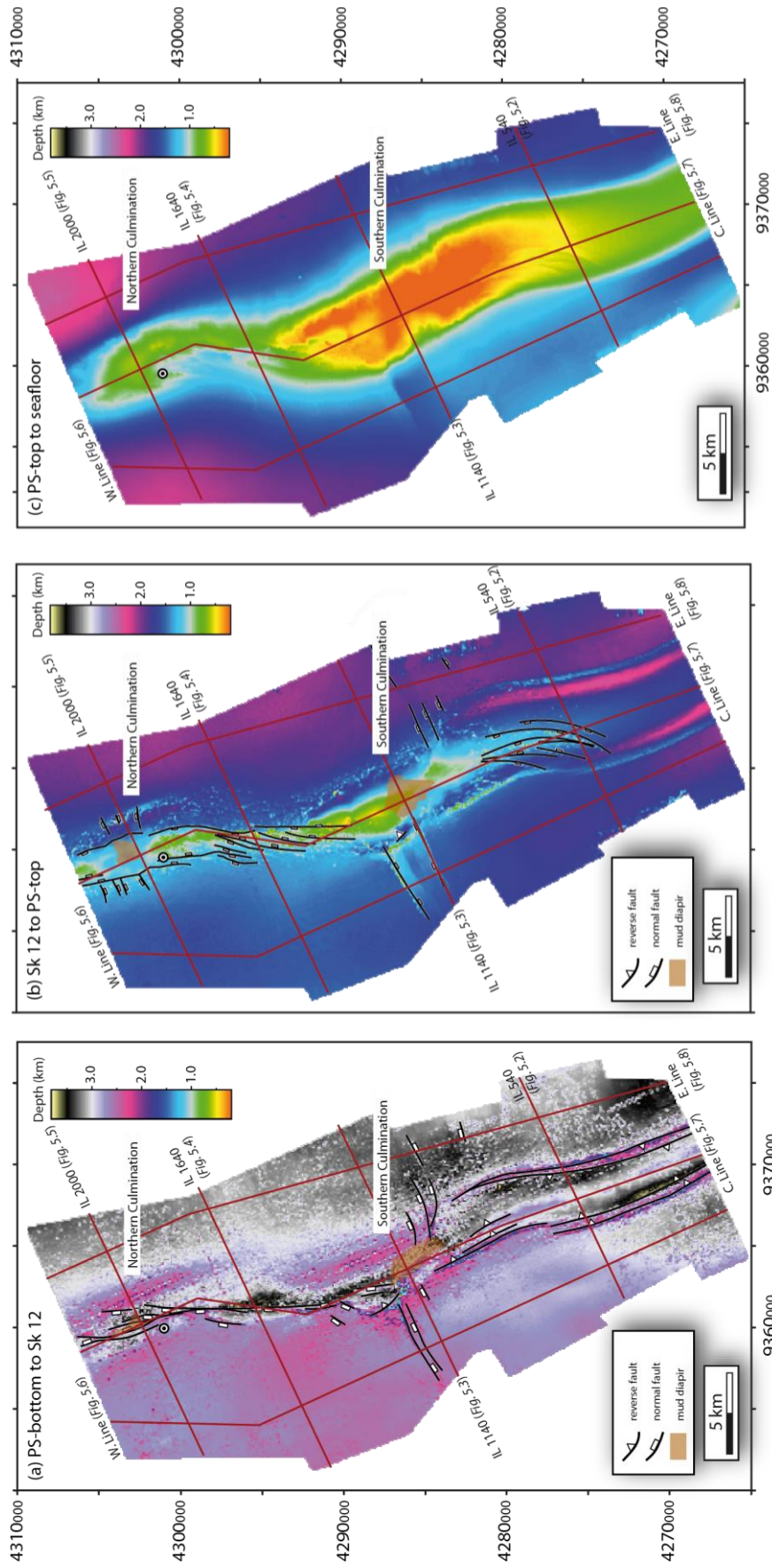


Figure 7.2: True stratigraphic thickness (TST) maps of the intervals between the (a) PS-bottom to the Surakhany 12 Unit (Sk 12), (b) the top of the Sk 12 to the PS-top and (c) the complete package of the Post-PS (Santos Betancor and Soto, 2015). Structural interpretation corresponds to faults and diapirs traces in the top of the Sk 12 (a) and the PS-top (b). Faulting and diapirism in the seafloor is not described (c) the Northern Culmination and in the saddle domain. Two great depocentres are registered in the northernmost sectors (2.25 and 2 km-thick in the NE and NW, respectively), whereas they are thinner in the South (~1.5 km). Eastern limb is generally thicker than the western flank, with differences of about 0.5 km.

We interpret that during the deposition of the uppermost Surakhany package, the region above the deep fault becomes a growing and narrow bulge that joined the Southern and Northern culminations (Santos Betancor and Soto, 2015). The main difference with thickness evolution of the remainder PS sequences is seen in the southernmost sectors, because the two rim synclines appears as subsiding and narrow domains bounding an incipient anticline with a broad and elongated crest (*cf.*, *Figs. 7.2a* and *7.2b*). Therefore, these observations reinforce the studied fold started to uplift at least in the last 3.6 my and the Surakhany 9 subunit should be considered as a syn-growth sequence.

The Post-PS thickness map describes a completely different scenario in the last 3.1 my (Jones and Simmons, 1997; Abreu and Nummedal, 2007; Forte *et al.*, 2010). *Figure 7.2c* clearly reflects a growing anticline bounded by two sinking rim-synclines. Thin packages drape crestal region, especially in the Southern Culmination (<0.25 km-thick), and similar values of ~0.75 km-thick are described in the Northern Culmination and in the saddle domain. Two great depocentres are registered in the northernmost sectors (2.25 and 2 km-thick in the NE and NW, respectively), whereas they are thinner in the South (~1.5 km). Eastern limb is generally thicker than the western flank, with differences of about 0.5 km.

TST estimations in *Figure 7.2c* are consistent to our seismic interpretation; *i.e.*, the Post-PS units clearly represent a syn-growth epoch. We infer that most of the Post-PS sediments prograded southwards, consistently to the overall thickness distribution and our observations conducted in strike seismic lines (*Figs. 5.6* to *5.8*). In the KAD area, sediment progradation interacted with the growing anticline, accumulating preferentially the sediments in the sinking, rim synclines, that acted as ponds, whereas thinner sediments covered the uplifting anticline crest. During the Post-PS epoch the basin margin experienced a subtle tilting towards the East, because the western syncline is slightly thinner than the paired, eastern one.

7.1.2. Sedimentary Sequence: Rates and Burial

Deposition of thick PS and Post-PS units took place under singular sedimentary conditions in the SCB. Late Messinian eustatic sea-level drop (*i.e.*, Pontian salinity crisis; *Fig. 2.20*), active tectonics and subsidence since Pliocene times, promoted the ensuing establishment of large sedimentary bodies in the basin, also controlled by high-frequency climatic cycles on short time scales (Azizbekov, 1972; Priestley *et al.*, 1994; Allen *et al.*, 2002; Morton *et al.*, 2003; Abreu and Nummedal, 2007). This scenario imposed the flexure of the depression and triggered the rapid burial of a 10 km-thick sedimentary load with great burial rates since the Late Miocene to Quaternary (Nadirov *et al.*, 1997; Axen *et al.*, 2001; Allen *et al.*, 2002; Morton *et al.*, 2003).

In the western margin of the SCB, deltaic input comes from several systems (*Figs. 2.17* and *2.20*) (Reynolds *et al.*, 1998; Abreu and Nummedal, 2007; Krijgsman *et al.*, 2010); the Kura River has generated the main delta that drains directly in offshore Azerbaijan from the Lesser Caucasus, and the Volga River has contributed through a large system of submarine channels from the Greater Caucasus, Russian Platform and Urals (Brunet *et al.*, 2003; Morton *et al.*, 2003). According to regional studies, the PS formations were deposited from Pliocene times with an average sedimentation rate of 2 mm·yr⁻¹ (Nadirov *et al.*, 1997; Hinds *et al.*, 2004; Yusifov, 2004; Smith-Rouch, 2006; Stewart and Davies, 2006), and <1 mm·yr⁻¹ for the Post-PS strata in the last 3.1 my (Inan *et al.*, 1997; Allen *et al.*, 2002).

In this thesis, and to unravel sedimentation history in the KAD anticline, we have built several maps that illustrate sedimentary rates in selected intervals of the PS and Post-PS sequences (*Fig. 7.3*). Key packages correspond to: the Lower PS (Late Miocene-Early Pliocene, 5.9 Ma to \sim 5.33-5.2 Ma), the Surakhany (Early-to-Late Pliocene, 3.7 Ma to \sim 3.4-3.1 Ma), the Akchagyl (Late Pliocene-Early Pleistocene, \sim 3.4-3.1 Ma to \sim 1.7-1.6 Ma) and the Apsheron (Early Pleistocene, \sim 1.7-1.6 Ma to \sim 0.8-0.7 Ma) sequences. Velocities of sedimentation are computed based on estimations of thickness in each package (*Figs. 7.1* and *7.2*), and by using regional ages (Jones and Simmons, 1997; Abreu and Nummedal, 2007; and Forte *et al.*, 2010). Maps of sedimentary rates complement our preliminary results presented in *Table 6.7*.

The map of the Lower PS sequence (5.9-5.2 Ma) shows two large domains separated by a linear trend coincident with the actual fold trace (*Fig. 7.3a*). The Present-day eastern fold limb registers major sedimentation rates, with values of $1.5 \text{ mm}\cdot\text{yr}^{-1}$, whereas the western flank contains lower rates that oscillate between \sim 0.75 and $1 \text{ mm}\cdot\text{yr}^{-1}$, that increase to \sim 1.25 $\text{mm}\cdot\text{yr}^{-1}$ locally in the North. These relative low sedimentation values and stratigraphy are consistent with a sea-level lowstand with short-lived lacustrine transgressions in a continuous coastal onlap setting (Morton *et al.*, 2003; Abreu and Nummedal, 2007; Abdullayev *et al.*, 2012).

Dissymmetric sedimentation rates in the Lower PS map reinforce the occurrence of a linear and previously described fault structure that may occur at depth along the fold axis (*Fig. 7.3a*). We postulate that deep faulting, with a normal regime and East-dipping, was the responsible for the relative elevation of the western flank and the sink of the eastern limb, as respective footwall and hanging-wall blocks (Santos Betancor and Soto, 2015). This situation promoted an extra sedimentary contribution towards the East, where major accommodation space and major velocities of accumulation occurred.

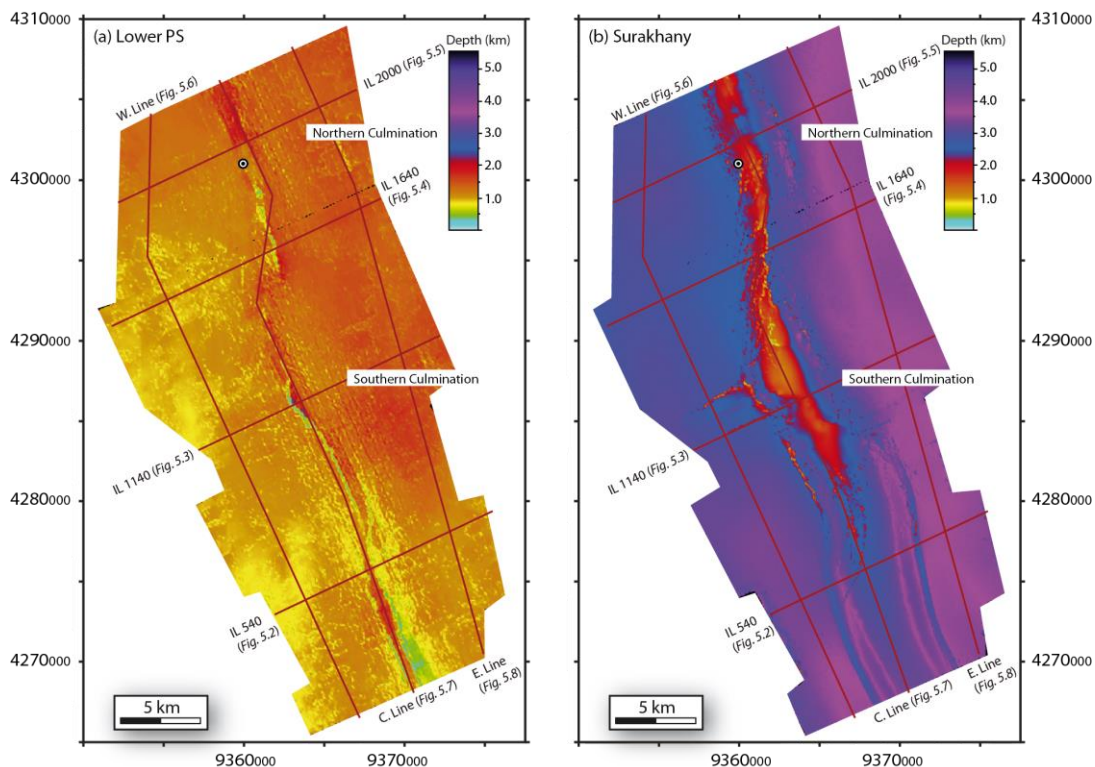


Figure 7.3: Sedimentation rates measured in the Kurdashi Permit in the (a) Lower Productive Series (PS), (b) Surakhany, (c) Akchagyl, and (d) Apsheron units. Continuation in the next page.

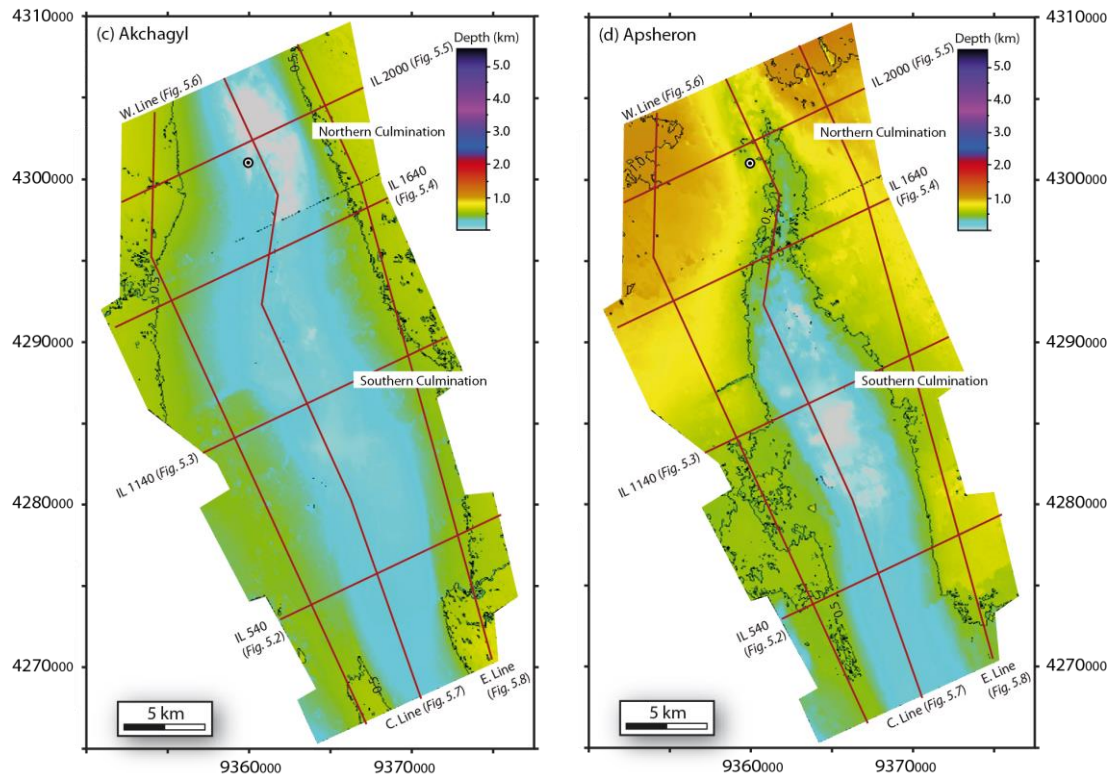


Figure 7.3: Continuation.

Deposit of the Surakhany Unit (3.7-3.1 Ma) slightly departs from the older PS, as a result of a change in sedimentation history (Fig. 7.3b). Noticeable differences are observed between flanks with velocities that oscillate between values of $2.5\text{-}4.0\text{ mm}\cdot\text{yr}^{-1}$, separated by an elongated and thin domain ($< 2.0\text{ mm}\cdot\text{yr}^{-1}$) over the underlying linear region. Highest sedimentation rates are locally identified in an elongated sector in the SW ($3.5\text{-}4.0\text{ mm}\cdot\text{yr}^{-1}$), close to the area of kink-band folding and consistent to estimated rates of $\sim 3.3\text{ mm}\cdot\text{yr}^{-1}$ for the uppermost Surakhany interval in the IL 540 (cf., Table 6.7).

Rapid sedimentation reflects intense fluvial activity that may be correlated with the uplift and exhumation of the Caucasus Mountains westwards. The interplay of Paleo-Volga and Paleo-Kura rivers progradation in this epoch contributed with coarsening-upward facies described in the Surakhany Unit (Abreu and Nummedal, 2007).

Congruently to estimated sedimentary rates and supported by our interpretation of isopach maps, we suggest regional deformation developed fold burst of the KAD anticline during the Surakhany times (Priestley *et al.*, 1994; Allen *et al.*, 2002). We infer folding uplift presumably occurred through the weak plane of the deep fault (Fig. 7.3b). Folding generated concomitant growing synclines flanked by southern kink-band structures.

Map in Figure 7.3c shows a significantly different panorama in the Akchagyl Unit (3.1-1.6 Ma). This interval illustrates a growing anticline with a sigmoidal trace that separate regions with similar sedimentation rates. Mean magnitudes correspond to values of $\sim 0.40\text{ mm}\cdot\text{yr}^{-1}$, although major velocities are $0.75\text{ mm}\cdot\text{yr}^{-1}$ and coincide with fold flanks (cf., Table 6.7). Fold crest registers minimum and nearly null values in both culminated areas.

The Akchagyl deposition represents a widespread transgression in the SCB that

promoted regional flooding over the basin (Jones and Simmons, 1997; Abreu and Nummedal, 2007; Abdullayev *et al.*, 2012). Akchagyl sedimentation overlies the important erosive transition established at the top of the PS sequences, which is recorded diachronously in the SCB margins (*e.g.*, Abdullayev, 2000).

Distribution of sedimentation rates is congruent with the folding event described during the deposit of the syn-growth Post-PS sequences (*Fig. 7.3c*). Anticline uplift was presumably produced simultaneously to strike-slip faulting responsible for curve axial trend. Low sedimentation rates detected along the culminated domains evidence truncation and local erosion of the fold crest due to superior folding rates than sedimentation velocities.

Sedimentation rates in the Apsheron times (1.6-0.7 Ma) (*Fig. 7.3d*) slightly increases with respect to the Akchagyl period (*Fig. 7.3c*). Velocities of deposition rise in the overall KAD area ($\sim 0.5 \text{ mm}\cdot\text{yr}^{-1}$, *Table 6.7*), and especially, in the northern sectors up to $1.0 \text{ mm}\cdot\text{yr}^{-1}$, where the Northern Culmination is partially draped.

Progressive burial in the northern sectors is presumably due to the proximities of the deltaic systems or the shoreline. Direction of sediments provenance is inferred as N-NW, which might represent a combined contribution of the regressive Paleo-Kura and transgressive Paleo-Volga deltas (Morton *et al.*, 2003; Abreu and Nummedal, 2007; Abdullayev *et al.*, 2012). Progradation and retrogradation coexist with climate cooling that extends to Recent (Morton *et al.*, 2003).

In the Apsheron period, the Northern Culmination switched to a submarine platform, due to lower folding rates than sedimentation, which faces against the growing and elevated Southern Culmination. Diminishment in deformation rates might also produce structural collapse of the northern area.

7.1.3. Subsidence and Basin Tilting

An enormous subsidence of the oceanic floor is described in the SCB from the Jurassic epoch, influenced by the Tethys closure (*e.g.*, Brunet *et al.*, 2003). Subsidence was encouraged by later compression of the Arabia-Eurasia collision and surrounding fold-belts uplift (Allen *et al.*, 2003; Artyushkov, 2007). In the Kura depression the West Caspian Fault is supposed to produce an abrupt step in the basement surface that accentuates basin tilting (*Fig. 2.11*) (Khain *et al.*, 1966; Nadirov, 1985; Lerche *et al.*, 1997).

This scenario has triggered a constant basin tilting of the SCB towards the East that extends to Present (Berberian, 1983; Zonenshain and Le Pichon, 1986; Allen *et al.*, 2002; Green *et al.*, 2009; Baganz *et al.*, 2012). Basin tilting in the KAD fold is evidenced through steep dips and geometry of flanks of the PS and the Post-PS sequences (*e.g.*, *Figs. 6.19* and *6.20*), which are also described in sedimentary bodies of the western SCB (*Fig. 2.21*) (*e.g.*, Nadirov *et al.*, 1997; Devlin *et al.*, 1999; Abreu and Nummedal, 2007).

The deep fault that is inferred in the core of the KAD fold may have contributed extra subsidence along the eastern fold limb. Congruently to previous observations and, especially, thickness heterogeneity, we suggest this structure responded to regional tilting to the inner SCB, which should reinforce the normal regime and East-dipping plane of the pre-existent fault (*e.g.*, *Fig. 2.14*) (Santos Betancor and Soto, 2015).

7.2. Folding Style

7.2.1. Fold Geometry

We illustrate in *Figure 7.4* the 3D geometry of the KAD anticline through the folded tops of the Sabunchi (Early Pliocene, 4.0-3.7 Ma) and PS (3.1 Ma) surfaces (*Figs. 5.11c* and *5.11d*) (Jones and Simmons, 1997; Abreu and Nummedal, 2007; Forte *et al.*, 2010). Both surfaces evidence a complex anticline composed by two culmination domains, here called as the Northern Culmination (Araz Deniz Culmination) and the Southern Culmination (Kirgan Deniz Culmination). The 3D view of selected horizons depicts a domal fold with en echelon geometries. Fold plunges southwards and northwards with four periclinal closures (Abrams and Narimanov, 1997; Guest *et al.*, 2007). Anticline trace is sigmoidal and trends NW-SE, consistently with structures in onshore and offshore Azerbaijan (*Fig. 2.11*) (Devlin *et al.*, 1999; Brunet *et al.*, 2003). Axial plane is sub-vertical in central domains, and dips 70-85°W in southern and northern sectors.

Fold shape in both surfaces sketches an open to gentle anticline in the South with a symmetric box-like section where accentuated synclines flank the structure (*Figs. 7.4* and *7.5a*). Kink-fold contains two convergent axial traces that merge forming a deep, single and sub-vertical surface. Northwards, asymmetry along strike is predominant and the anticline evolves to a gentle fold with a single, highly dipping axial plane, locally pierced by mud (*Figs. 7.5b, 7.5c* and *7.5d*). Fold crest has a rounded shape with a broad, sub-horizontal crest that becomes relatively angular to the North (*Fig. 7.4*). The different fold profiles studied to build up these surfaces demonstrate that the fold style, attitude of the axial trace, and the fold vergence change along strike and in depth; variable vergence denotes a non-cylindrical fold (*e.g.*, Devlin *et al.*, 1999). The overall geometry corresponds therefore to an upright anticline with a general eastward vergence.

Geometrical observations for both horizons report a shallow western limb that faces against a deeper eastern flank (*cf. Figs. 7.4* and *7.5*). Synclines are also decoupled in both fold limbs. Flank lengths for the Sabunchi and PS-top surfaces are 1.0-1.8 km in the West, and 1.1-1.6 km in the East and dip limbs are 20-45°W and 30-40°E. Gentle dips (<10°) are detected to the North and to the South in the PS units in fold flanks, corresponding to low-dipping sequences (*Figs. 5.6* to *5.8*). According to folded surfaces, the interlimb angle of the KAD fold slightly increases northwards from 105° to 125°, whereas the axial plane dip varies slightly from ~80°W to 90° (*Fig. 7.5*).

Complexity detected in fold shape is presumably linked to the occurrence of the ductile Maykop Unit (Late Eocene-Early Miocene, ~36-16.5 Ma) (Hudson *et al.*, 2008; Afandiyeva *et al.*, 2009). Our suggestion is supported on estimated differences between S_C and S_A magnitudes, which indicate this fold does not conserve bed length due to volume variations during folding (*e.g.*, *Figs. 6.13* and *6.18*). We propose an increasing volume and mobilization of fluid-rich shales that inflated or upwell into the structurally thickened fold core when shortening occurred (*e.g.*, *Figs. 2.13* and *2.14*) (Dahlstrom, 1990; Homza and Wallace, 1995; Poblet *et al.*, 1997). Differential deep thickening triggers asymmetric and unpredictable geometries in the sedimentary overburden, as it is usually developed in salt-cored anticlines (*e.g.* Rowan 1997; Rowan *et al.* 2000).

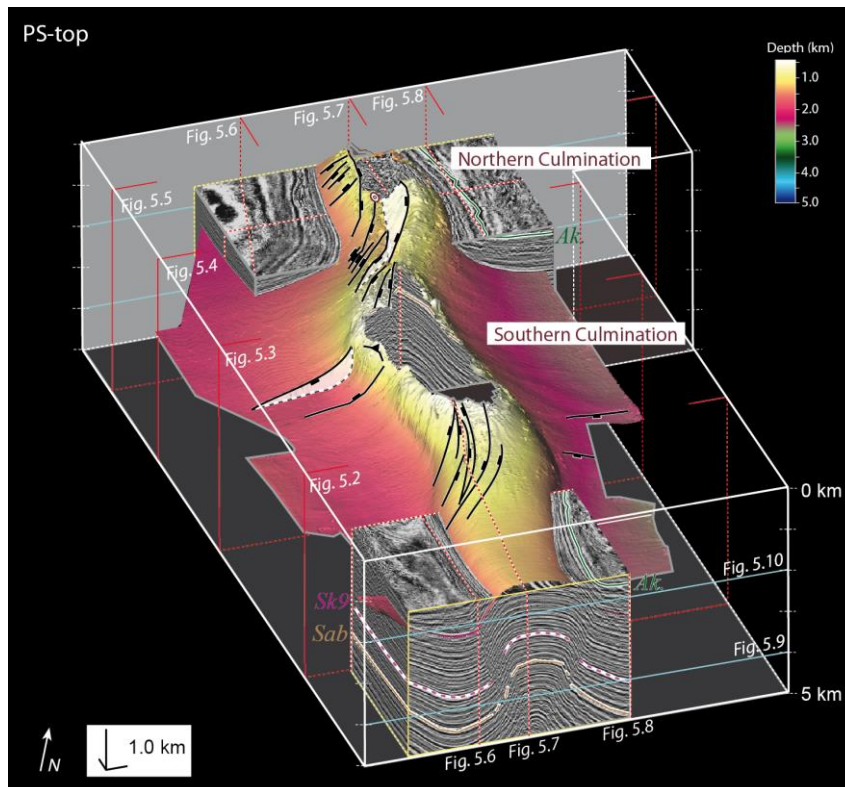
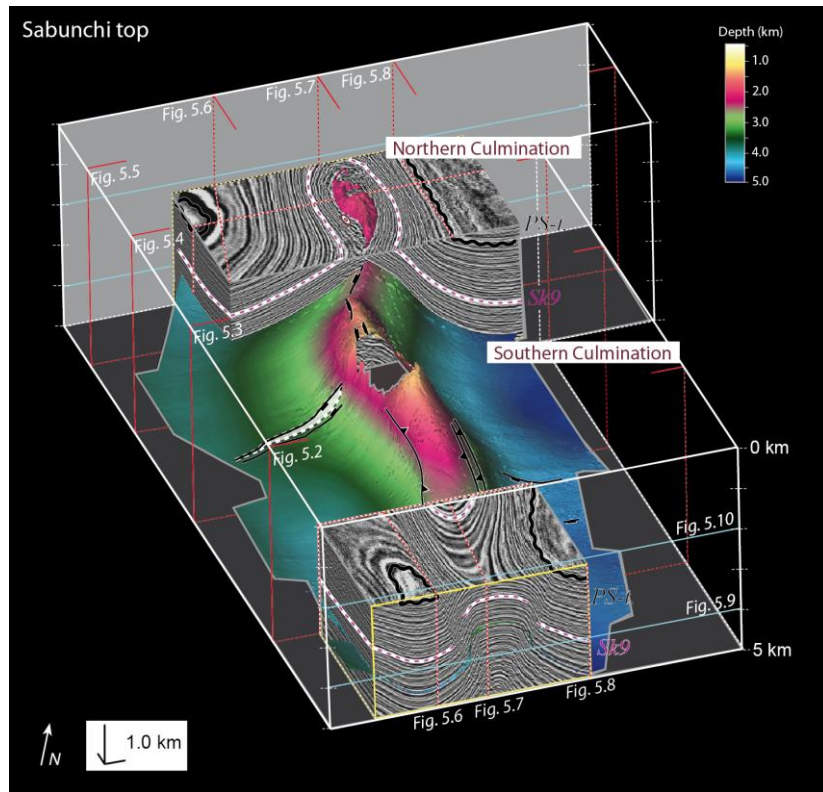


Figure 7.4: Chair-cut seismic volume including the interpreted tops of the (a) Sabunchi Unit and the (b) PS sequences. The Surakhany 9 top is also delineated for reference. Seismic cube is bounded at 5.5 km depth, and upper limits correspond to (a) 2.2 km, and (b) 1.5 km. Vertical margins are the same for both displays (Santos Betancor and Soto, 2015).

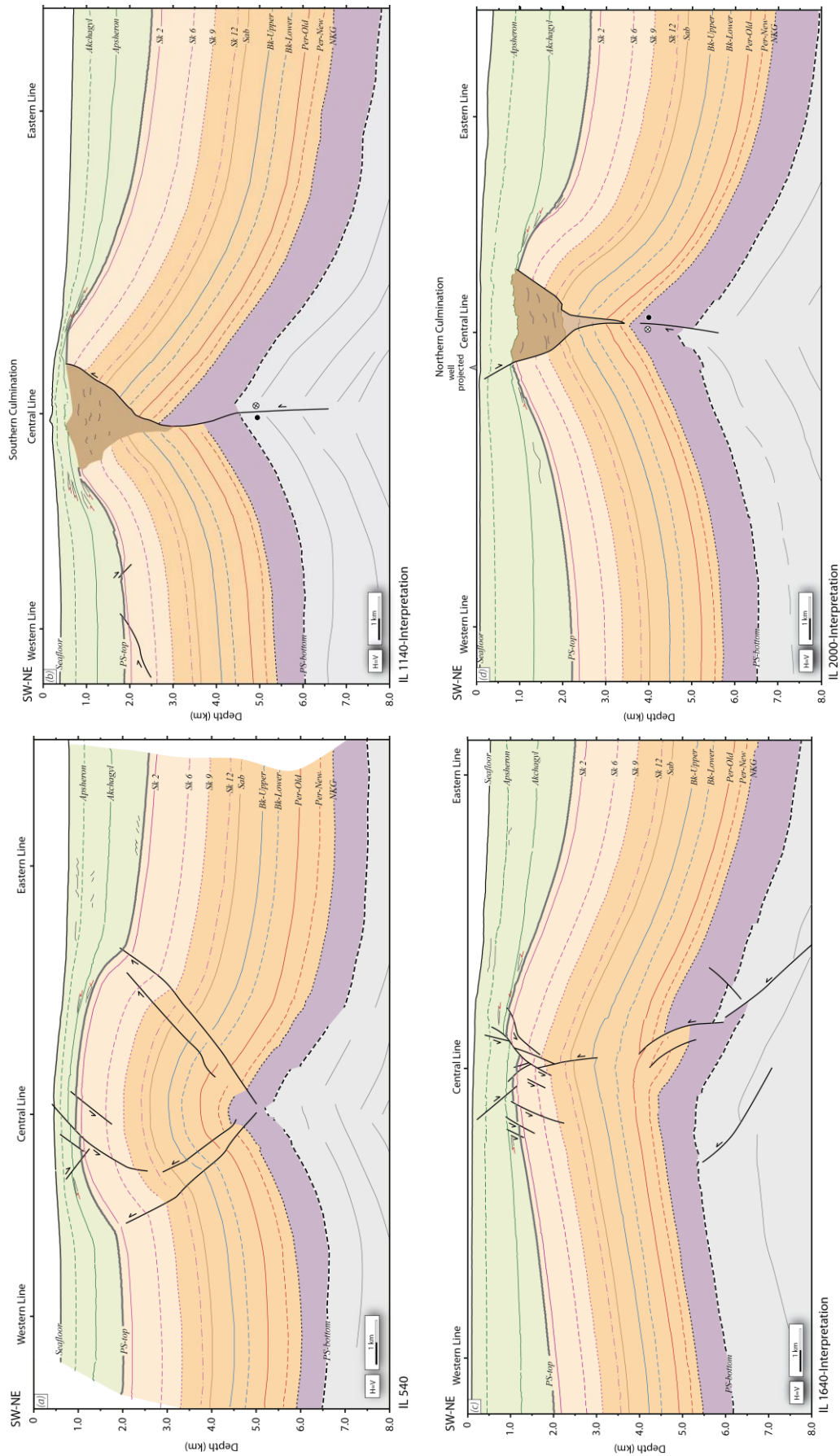


Figure 7.5: Interpreted seismic sections presented in Figures 5.2 to 5.5, respectively (a) to (d). Intersections with Figures 5.6 to 5.8 are also included. Abbreviated horizons correspond to: Balakhany (Bk), Pereryva (Per), Productive Series (PS), Sabunchi (Sab), and Surakhany (Sk).

7.2.2. Folding Type

The Caucasus uplift during Pliocene-to-Present times generated folding in the western SCB. Deformation promoted compression of overpressured shales within the Maykop Formation that triggered the generation of a detachment level (e.g., Devlin *et al.*, 1999; Yusifov and Rabinowitz, 2004; Guest *et al.*, 2007). The decoupled structure above the incompetent Maykop Unit was deformed by buckle folding: the KAD anticline (e.g., Devlin *et al.*, 1999; Brunet *et al.*, 2003). Folding type is conditioned by high competency contrasts between the Maykop and the PS sequences; the lower unit is weak and displays disharmonic folding with significant penetrative deformation deformed by bedding-parallel flexural slip, whereas the upper units exhibit a marked and parallel layering (Mitra, 2003). Thickness of the competent multipackage controls anticline wavelength (Mitra, 2003).

Detachment folding built kink-band structures in the southernmost areas of the KAD anticline (Figs. 7.4 and 7.5a) (Wall and Wiener, 1998), as it occurs in other examples of the SCB, such in the Shah Deniz (Richardson *et al.*, 2011) and in the Apsheron-Balkan uplift (Guzofski *et al.*, 2009). In the central sectors of the studied area, evidences of buckling are inferred through thickening of the uppermost PS units towards the fold crest, as it is distinguished between the Sabunchi and the Surakhany 6 Unit (Figs. 5.6 to 5.8). Significant layer-parallel shear may accompany buckle folding according to the evaluation of the $A_i:H_i$ plot (Fig. 6.17) (Suppe, 1985; Groshong and Epard, 1994; Gonzalez-Mieres and Suppe, 2006, 2011).

Direction of movement in detachment folding is established by the leading flank (e.g., Dahlstrom, 1969; Poblet and McClay, 2004). In the KAD fold, the eastern flank is interpreted as the motor of deformation (forelimb) as it is longer and presents higher dips than the dragged limb or backlimb (Fig. 7.5). Consistently to these results, deformation is transported to the inner SCB, concordant to eastward tilting and offshore sliding of the western marine sediments (Figs. 2.12 to 2.14) (Allen *et al.*, 2002; Jackson *et al.*, 2002).

The detachment level is inferred to be a discrete, low-dipping or sub-horizontal plane rooted within the Maykop Formation (e.g., Epard and Groshong, 1993; Devlin *et al.*, 1999; Yusifov and Rabinowitz, 2004; Gonzalez-Mieres and Suppe, 2011; Guest *et al.*, 2007). According to our numerical reconstruction, the décollement surface may be located between 9 and 11 km depth (Table 6.6), which coincides with the regional assumption of 10-12 km depth in marine settings (e.g., Wall and Weiner, 1998). The detachment level might be East-dipping in offshore Azerbaijan.

7.2.3. Mechanisms of Folding

Geometry of fold and growth strata serves as a kinematic indicator of folding mechanisms (Suppe *et al.*, 1992; Hardy and Poblet, 1995; Poblet *et al.*, 1997). Detachment folds are generated due to hinge migration, limbs rotation or a combination of both mechanisms (see Fig. 6.3). In the KAD anticline, we have recognized evidences of a mixed model (e.g., Poblet, 2004; Mercier *et al.*, 2007; Guzofski *et al.*, 2009).

Shape of the syn-folding sediments differentiate two packages in the studied fold: the uppermost PS (the Surakhany Unit) and the Post-PS. Wedge geometries, clearly observed in the Post-PS sequence, are a result of coeval deposit and fold growth controlled by rotation of flanks, as it was previously suggested through the analysis of

flanks dips in *Figure 6.15*. Migration of folds hinge is the responsible for parallel dips between the pre- and syn-folding strata in the Surakhany Unit (Suppe, 1983).

Kink-band structures, as those observed in the South of the KAD fold (*e.g.*, *Fig. 7.5a*), are typically originated by migration of folds hinge (Suppe, 1983), and preferentially expresses early stages of fold amplification and areas affected by low stress (*e.g.*, Suppe, 1983; Poblet *et al.*, 1996). The displacement of fold hinge is also assumed as the main promotor of syn-sedimentary processes, such as basin floor instabilities (*e.g.*, slides; *Fig. 4.10*), and faulting (*Fig. 7.5*; De Sitter, 1956). Rotation of fold limbs triggers an increment in fold amplitudes and tighter geometries, as it occurs towards northern sectors of the studied fold, reflecting high folding maturity (*e.g.*, Mitra, 2003; Mercier *et al.*, 2007).

These observations support that the KAD fold mainly grew by a non-pinned hinge during the ~0.5 my folding episode, coincident with the Surakhany times. Spinning limbs played a dominant role in the last 3.1 my, simultaneously to the deposit of the Post-PS units. Nevertheless, we postulate both mechanisms acted conjointly through the overall KAD folding, reinforced by the thickening of the forelimb (*e.g.*, *Fig. 6.20*) (*e.g.*, Mitra, 2003).

7.3. Anticline Growth

7.3.1. Growth Sequences

Growth geometry also records the anticline history within the fold crest, through indicators such as layer thinning, onlap features, or the occurrence of gravitational mobilized sediments (Shaw *et al.*, 2005; Poblet, 2012). Flattened sections in *Figure 7.6* represent a powerful tool to illustrate fossilized evidences of fold growth in the PS and Post-PS sequences.

Selected seismic lines correspond to three of the most representative fold sections. Flattening is done in the dip-lines IL 540 (*Fig. 7.5a*) and IL 2000 (*Fig. 7.5d*), which respectively correspond to sections previously interpreted in *Figures 7.6a* and *7.6c*. The unfolded section in *Figure 7.6b* is closely coincident to the IL 1140 (*Fig. 7.5b*). Fold profiles have been flattened with respect to the PS-top surface (Santos Betancor and Soto, 2015).

The Post-PS sequences thin significantly towards the anticline hinge, demonstrating that they clearly correspond to a syn-growth epoch (*Fig. 7.6*). The uppermost PS sequences, particularly the package bounded between the Surakhany 6 Unit and the PS-top, also thin subtly towards the fold crest (*Figs. 7.6b* and *7.6c*) due to a previous syn-folding deposit. In detail, a slight and progressive thinning of sequences can be detected in underlying layers within the Surakhany Unit (*e.g.*, *7.6c*). Thus, the end of the pre-kinematic sequence is located before the conventionally assumed top of the PS (Devlin *et al.*, 1999; Axen *et al.*, 2001). Hypothesis is reinforced based on stratal pinch-outs at the end of the Surakhany sequence in the Apsheron region (Aliiev, 1960; Allen *et al.*, 2002; Guzowski *et al.*, 2009).

An accurate geometrical interpretation of folding history needs to be complemented with other estimations, such as shortening rates (dS_A/dt), computed in this thesis and in Sánchez-Borrego *et al.* (submitted). Evolution of shortening magnitudes in a southern transect of the KAD fold (*i.e.*, IL 540) is shown in *Figure 7.7*. Red-coloured and linear

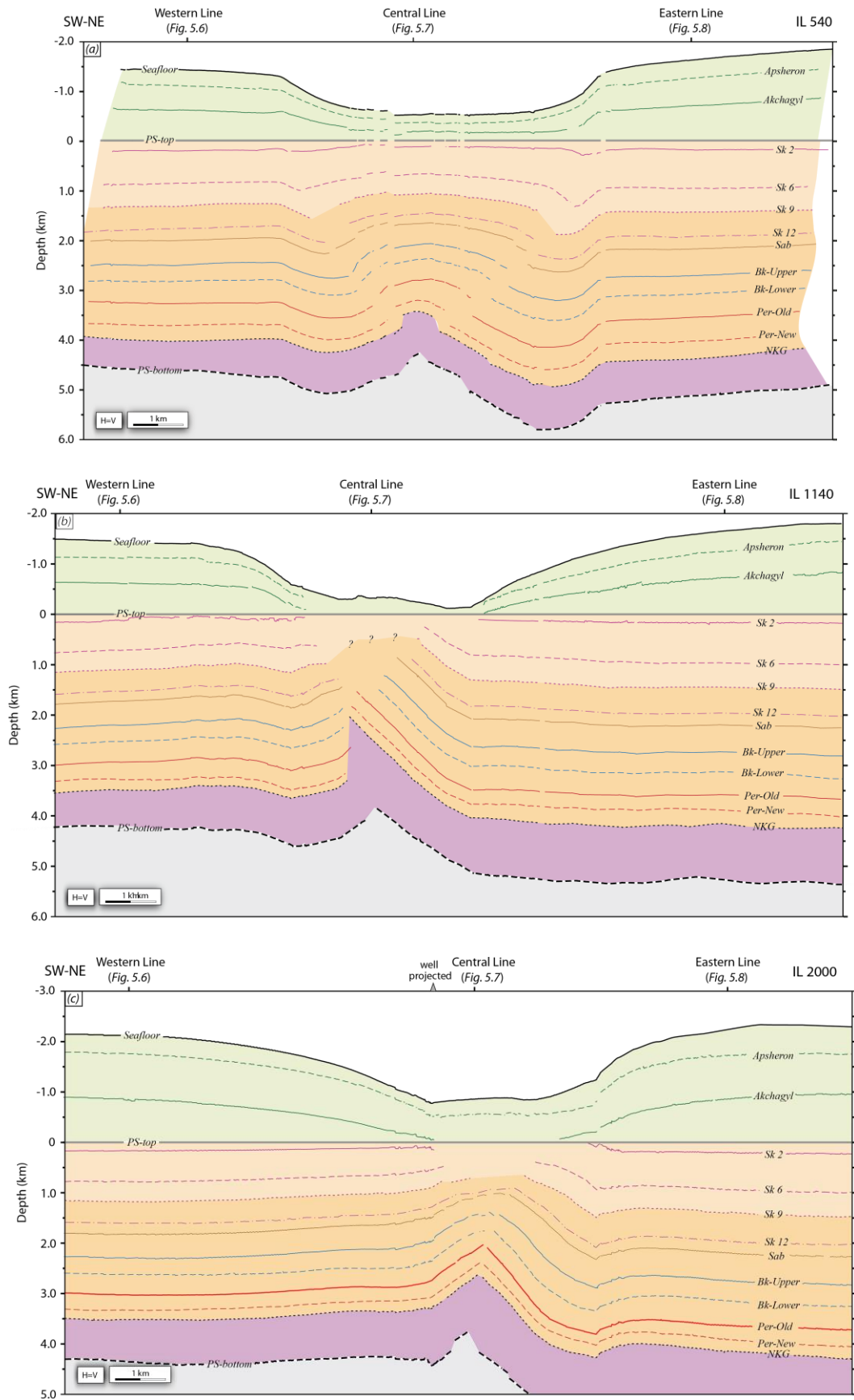


Figure 7.6: Interpreted dip-line sections flattened with respect to the PS-top surface. Unfolded profiles are presented in Figures 7.5a, b and d, respectively from (a) to (c). Intersections with Figures 5.6 to 5.8 are also included. Abbreviations and symbols are summarized in Figure 7.5 (Santos Betancor and Soto, 2015).

fits in *Figure 7.7* document two successive episodes of folding in the KAD anticline. Estimated time for the onset of shortening is 3.5 Ma, synchronously to the deposit of the Surakhany 6 Formation, and established congruently to age extrapolations described in *section 4.3.1*. The PS-top (3.1 Ma) separates a second folding event that took place simultaneously to the deposit of the Post-PS (Jones and Simmons, 1997; Abreu and Nummedal, 2007; Forte *et al.*, 2010).

Analysis extracted from *Figure 7.7* is representative of the southernmost areas of the KAD fold (*i.e.*, IL 540 and IL 720), whereas the domain integrated by the ILs 1140 and 1640 reflect an early folding start towards the North (*e.g.*, *Fig. 6.17*). We propose KAD folding burst after the Sabunchi deposit (<3.7 Ma) in the vicinities of the IL 1140, or during the deposit of the Surakhany 12 Unit (3.7-3.6 Ma), estimated in the IL 1640. PS folding extended southwards 0.1-0.2 my later, and lasted until the PS-top (Jones and Simmons, 1997; Abreu and Nummedal, 2007; Forte *et al.*, 2010). The Post-PS folding coincides along the overall fold, although an early origin might be considered in the Southern Culmination after the deposit of the Surakhany 2 (*i.e.*, IL 1140) (*Fig. 6.17*). Our assumptions of folding in the culminated crest (IL 1140) and saddle domains (IL 1640) should be extrapolated to the IL 2000, in the Northern Culmination.

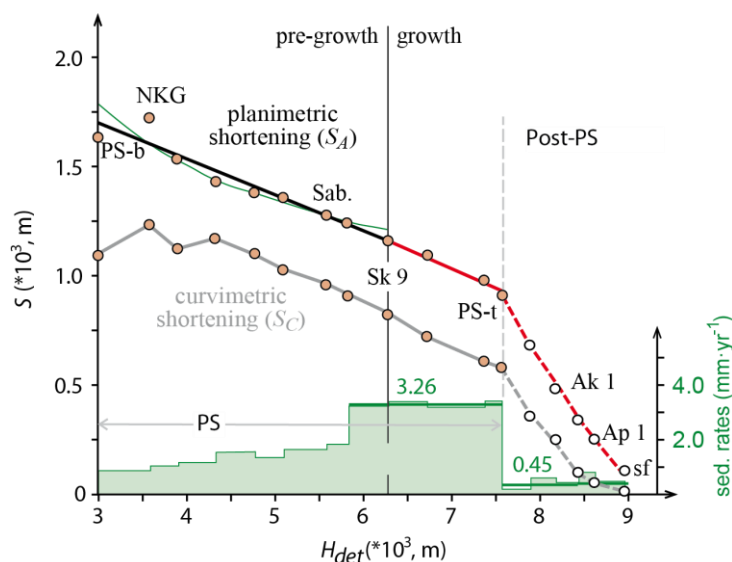


Figure 7.7: Comparative plot that illustrates the variation of the shortening magnitudes (S) with height above the estimated detachment level (H_{det}) in the IL 540, located in the southernmost areas of the KAD fold (*cf.*, *Fig. 6.13* and *Table 6.7*). Sedimentation rates (in $\text{mm}\cdot\text{yr}^{-1}$) calculated in this study are also included and represented by green, horizontal bars (*Table 6.7*). Detailed values of sedimentation velocities are computed with the confidential stratigraphic information provided by REPSOL and shown in the pale green histogram. Shortening estimates are fitted to their appropriate linear and polynomial fits. In the S_A distribution both linear and polynomial trends are depicted for the Productive series (PS) sequences. Horizon labels are according to *Figure 7.5*. Akchagyl and Apsheron tops are respectively abbreviated as Ak. 1 and Ap. 1.

Maximum folding rates of $\sim 2 \text{ mm}\cdot\text{yr}^{-1}$ took place in the first folding interval in the Southern Culmination, with major intensity in the proximities of the IL 1140 (*cf.*, *Table 6.7*). Second folding event occurred with a moderated fold growth ($< 0.50 \text{ mm}\cdot\text{yr}^{-1}$) dated in the Akchagyl times (3.1-1.6 Ma; Jones and Simmons, 1997; Abreu and Nummedal, 2007; Forte *et al.*, 2010). Folding diminished progressively to Recent with minimum values that ranges between $0.10 \text{ mm}\cdot\text{yr}^{-1}$, and $0.30 \text{ mm}\cdot\text{yr}^{-1}$ in the uplifted Southern Culmination (*Table 6.7*). Exceptionally high shortening magnitudes are the

responsible for the marked growth of the Southern Culmination as it constitutes the major shortened area.

Therefore, our statistical findings support a punctuated history of deformation with diverse shortening rates that present temporal variations in folding burst along fold strike. Shortening rates tend to decrease through the growth period. The culmination of the southern bulged area is the major shortened and uplifted domain in the KAD fold.

Maximum shortening and sedimentation rates acted conjointly during the uppermost PS folding (*Fig. 7.7*). Sedimentation values remain majorly similar along the overall fold, with singularities in the area of the IL 1640 (*cf., Table 6.7*). The deposit of the Surakhany Unit is characterized by elevated rates ($3.26 \text{ mm}\cdot\text{yr}^{-1}$; *Fig. 7.7*), that decreased to $0.5\text{-}0.6 \text{ mm}\cdot\text{yr}^{-1}$ in the Post-PS epoch (*Table 6.7*). In detail in the Post-PS, the tendency of sedimentation rates follows a progressive increment to Present.

Rates of folding and sedimentation follows a relationship equivalent to: $dS_A/dt \ll dH_i/dt$, as the sedimentation rates are five times greater than folding uplift (Sánchez-Borrego *et al.*, submitted). Rapid deposition would help to explain that syn-kinematic Surakhany sequences do not show a marked thinning towards the anticline crest and the absence of onlapping features in the first syn-growth episode (Giles and Lawton, 2002; Poblet *et al.*, 1997). Low uplift-sedimentation rates are estimated for the Post-PS period due to a moderated folding growth. According to the geometries observed in the Post-PS sediments, fold uplift rates were nearly equal to sedimentation velocities ($dS_A/dt \sim dH_i/dt$), because the fold crest was tapered by a thin sequence of these sediments, especially in the Akchagyl Unit (Poblet *et al.*, 1997). Folding & sedimentation balance may be the responsible for the erosive features and truncations of the uppermost Surakhany and the PS-top and in the vicinities of the ILs 1140 and 1640 (*Figs. 7.7b* and *7.7c*). Towards Recent, synchronous folding diminishment and increasing sedimentation rates promoted the progressive burial of the Northern Culmination.

7.3.2. Mass-instabilities Processes

Flanks of the KAD anticline are strongly dominated by mass-wasting deposits generated in numerous instability processes in the last 3.1 my. The analysis of the older basin slopes remained out of the scope of this study (*cf. Figs. 4.8* to *4.12*) (Abdullayev, 2000; Abreu and Nummedal, 2007; Santos Betancor *et al.*, 2013a).

Seismic facies, localization, dimensions and flow direction of mass-transport complexes (MTCs) promote a division in three types, which evidence different stages of basin evolution and folding history: A, B and C (see *section 4.3.3*). Internal layering within the mass-transported material of Type A is consistent with primary bedding characteristic from slides with up to 350 m thickness (*e.g., Fig. 4.8*). MTCs of Type B group small slides with not distinguishable headwall scarps in the seismic image (*Fig. 4.10a*). Type C have been interpreted as debris flows composed by incoherent masses of sediments and “cookie-bites” shapes in the headwall (*Fig. 4.11*). In the latter, retrogradation of structures is detected upslope as retreated scars.

To enhance our interpretation of MTCs, we have extracted variance attributes from the seismic dataset. Seismic cube has been sliced at 1.65 and 1 km depth, respectively in *Figure 7.8a* and *7.8b*, to map trace-to-trace similarity between reflections. Variance maps have been proved to be an appropriate tool to study lateral changes and variability in acoustic impedance of MTCs and complement the vertical counterpart computed through RMS displays (*Fig. 4.9*).

Map at 1.65 km shows seismic coherence at stratigraphic levels of the Akchagyl and Apsheron units (*Fig. 7.8a*). Changes observed in the traces signal reflect numerous mobilized sediments along the western fold limb with a variance pattern majorly defined by curved features, and locally flanked by lineated edges. Coefficients of variability in the eastern limb shed light on isolated bodies with convex shapes and linear scarps delineated upslope, close to the culminated Southern crest of the KAD fold.

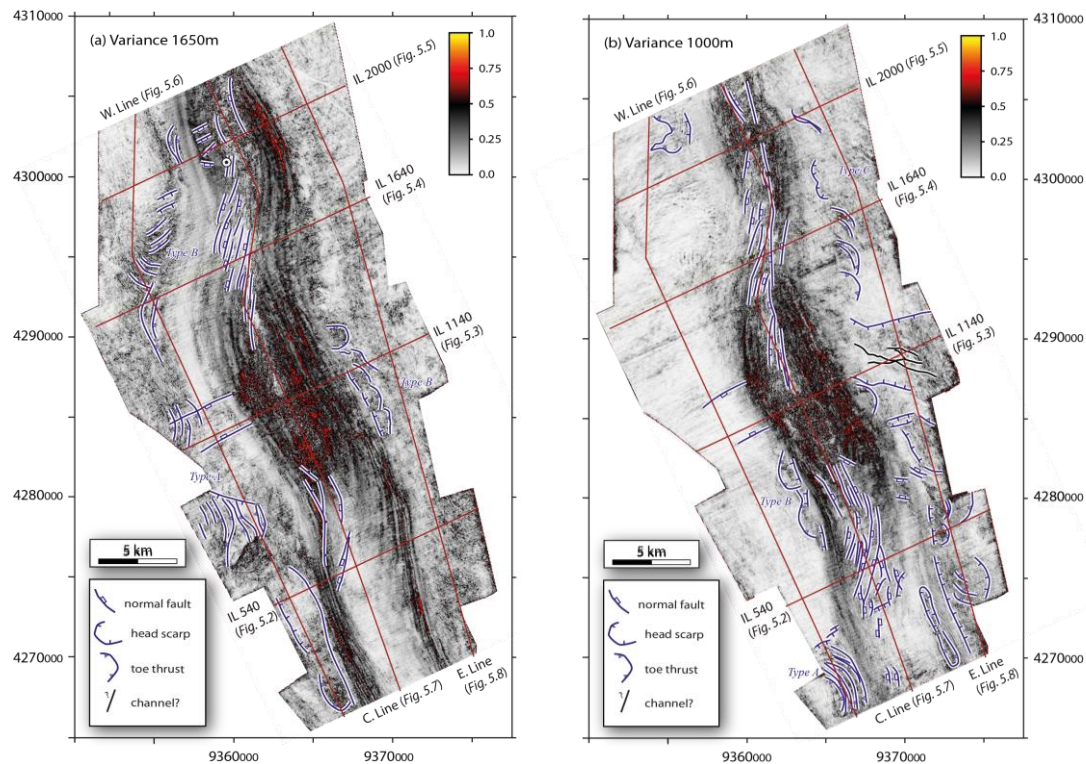


Figure 7.8: Variance maps at (a) 1.65 km depth and (b) 1.0 km depth. Notice the numerous prints of mobilized sediments at those referred depths corresponding to MTCs of types A, B and C. Figure inspired in Santos Betancor *et al.*, (2013a).

Gravitational deposits at these levels are represented by numerous small thrust sheets that preferentially ran in the western domains of the KAD fold in divergent directions (*Fig. 7.8a*). Isolated examples distinguished in the eastern sector flew from the Southern Culmination and accumulated downslope as lobate deposits. Characteristics of described bodies match with abundant slides of Type A, some debris flows of Type C to the NW, and several Type B cases in the East. We infer eastern MTCs originated by KAD folding, whereas growth of a neighbour structure produced the largest western examples. Delta progradation triggered instabilities in the northwestern deposits. Maximum variance coefficients concentrated along the bulged crestal areas may correspond to mud diapirs facies, and highly dipping domains.

Map of traces similarity in *Figure 7.8b* substantially changes in comparison to deeper levels. At 1 km depth, coincident with the intervals of the Apsheron and Gelasian units, widespread gravitational deposits are reported, with a major relevance in the eastern domains. Identified deposits usually appear as small bodies with linear headwalls and convex lobes. In central positions, two well-defined structures delimitate some lineated paths.

Mobilized deposits majorly correspond to debris currents of Type C, which flew to the inner basin, and Type B examples, preferentially westwards-directed (*Fig. 7.8b*). MTCs of Type A appear as local deposits in the southwestern syncline pond, close to older Type A bodies. The combined occurrence and abundance of types B and C indicate they were presumably controlled by fold growth and shelf-edge migration. Flow direction of Type B bodies and their distribution along both fold limbs evidence structural control. Gravitational masses of Type C might be produced by intense deltaic progradation.

Accordingly to the characteristics of the analysed deposits, we infer that basin floor collapses preferentially due Late Pliocene-to-Recent folding, and high sedimentation rates in a tilting SCB (*e.g.*, Richardson *et al.*, 2011; Imbert *et al.*, 2014). Folding reconstruction suggests structural control was maximum during the Akchagyl times (3.1-1.6 Ma; Jones and Simmons, 1997; Abreu and Nummedal, 2007; Forte *et al.*, 2010), when major gravitational deposits were produced (*cf.*, *Figs. 4.8* and *4.9*), coincident with first stages of fold amplification in the Post-PS epoch (*e.g.*, Poblet *et al.*, 2004). Reported examples moved coherently due to slope oversteeping by uplift in the KAD anticline and also in a presumed neighbour structure that was growing in the Southwest. Gravitational flows moved towards the East according to basin tilting. The KAD growth in that epoch also represented an obstacle for lateral flows, as these deposits did not overlap fold crest (*e.g.*, *Fig. 4.8*).

Tectonic activity and sedimentation rates played complementing roles in the transitional Apsheron times (1.6-0-7 Ma) that promoted varied mass-transport processes with examples of three types failed bodies (Jones and Simmons, 1997; Abreu and Nummedal, 2007; Forte *et al.*, 2010). Folding disacceleration in the KAD structure is the responsible for low dimensions of slides of Type B (*e.g.*, *Figs. 4.10* and *7.8*). These small bodies were preferentially developed along the eastern fold flank due to slight failures in the growing culmination, through a continuous rupture of the sedimentary talus. Similar failures are described by Richardson *et al.*, (2011) in the Shah Deniz anticline, termed as “wedge-tip” failures (*Fig. 7.9*). Increasing sedimentation rates due to delta progradation also perturbed basin stability, supported by increasing debris currents that deposited MTCs of Type C. Location of debris flows deposits is consistent with a transport N-NW direction that started to bury the northern domains.

Deltaic progradation represents the main responsible factor of seafloor collapse during the deposit of the Gelasian Unit (0.7 Ma-to-Present), as examples of Type C occur in both western and eastern fold limbs (Jones and Simmons, 1997; Abreu and Nummedal, 2007; Forte *et al.*, 2010). Nevertheless, the active uplift in the Southern Culmination area may have also triggered scarce Type B deposits (*Fig. 7.8*). We can speculate a great development of prograding clinoforms and shelf edge migration in a tilting basin, that started in the Apsheron and completely buried the KAD growing Northern Culmination (Abreu and Nummedal, 2007; Hinds *et al.*, 2004; Morton *et al.*, 2003). Fold geometry and basin tilting conditioned the advance of deltaic systems and contributed to dissymmetrical deposits of failed masses in the popular eastern flank. We assume that the interference between these processes triggered the retrogradation of slopes breaks in the headwalls of debris flows (*Fig. 4.11*).

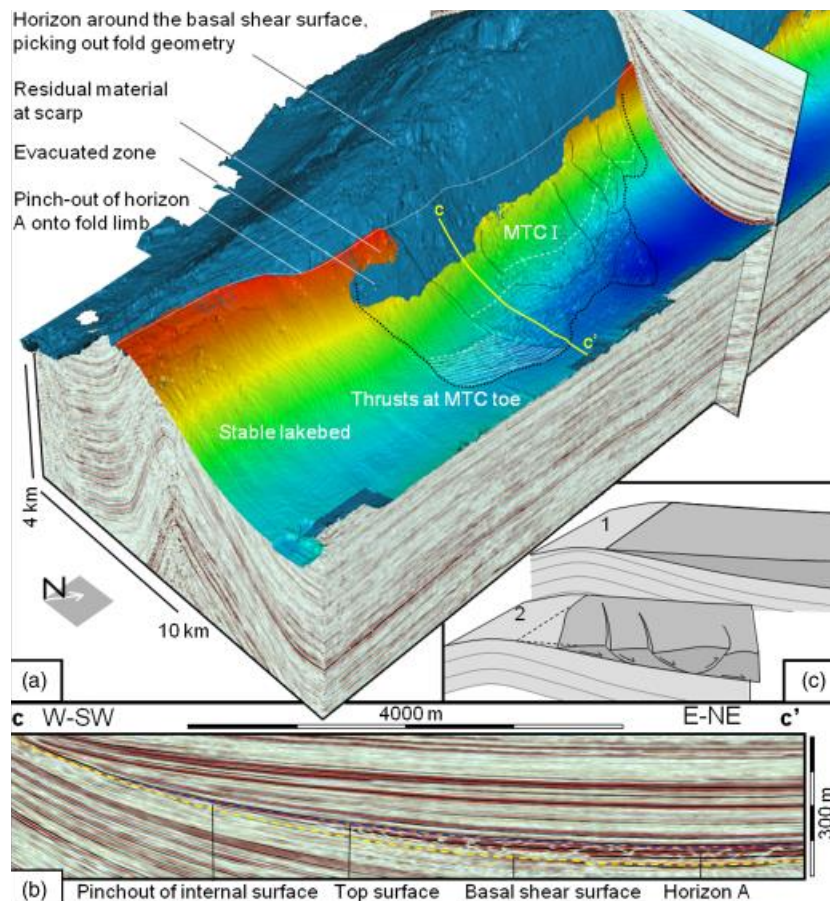


Figure 7.9: Wedge-tip geometries for a mobilized body in the proximities of the Apsheron Ridge. (a) Seismic rendered volume where a depth-coloured Horizon A overlays a basal surface coloured in blue. (b) 2D transect through the deposit illustrating up-dip pinch out of the Horizon A with no recognizable scarp. (c) Interpretative cartoons that show MTC evolution. Image taken from Richardson *et al.* (2011).

7.4. Structural Evolution

7.4.1. Diapirism Episodes

Existence of excessive fluids pressure in the plastic muds of the Maykop Unit (~36-16.5 Ma; Hudson *et al.*, 2008; Afandiyeva *et al.*, 2009) appears to be a key factor for mud diapirism and volcanism in the SCB basin (Lerche *et al.*, 1997; Nadirov *et al.*, 1997; Kopf, 2002; Yusifov, 2004). Pliocene-to-Present compression forced ductile shales to mobilize, pierce the overlying anticlines and release fluids to the surface (Fig. 7.10) (Allen *et al.*, 2002; Fowler *et al.*, 2000; Jackson *et al.*, 2002; Stewart and Davies, 2006).

Mud diapirs are found in the hinge line of the KAD anticline accumulated as shallow structures in culminated domains (Figs. 7.10 and 7.11) (Belopolsky and Talwani, 1999; Smith-Rouch, 2006; Yusifov and Rabinowitz, 2004). Diapirs pierce the PS package and the Post-PS units. Overpressure muds depict teardrop geometries consistent with deep squeezed levels that rose through sub-vertical or vertical paths of fluidized material and spilled upwards (Fig. 7.11). We interpret as welds those depleted and remnant feeder channels that presumably connected with the source rock, although shale pedestals are unidentified at depth (Figs. 7.5b and 7.5d) (e.g., Hudec and Jackson,

2007). Welds structures show reverse to strike-slip motion that can be confused with complex faulting (Fig. 5.17).

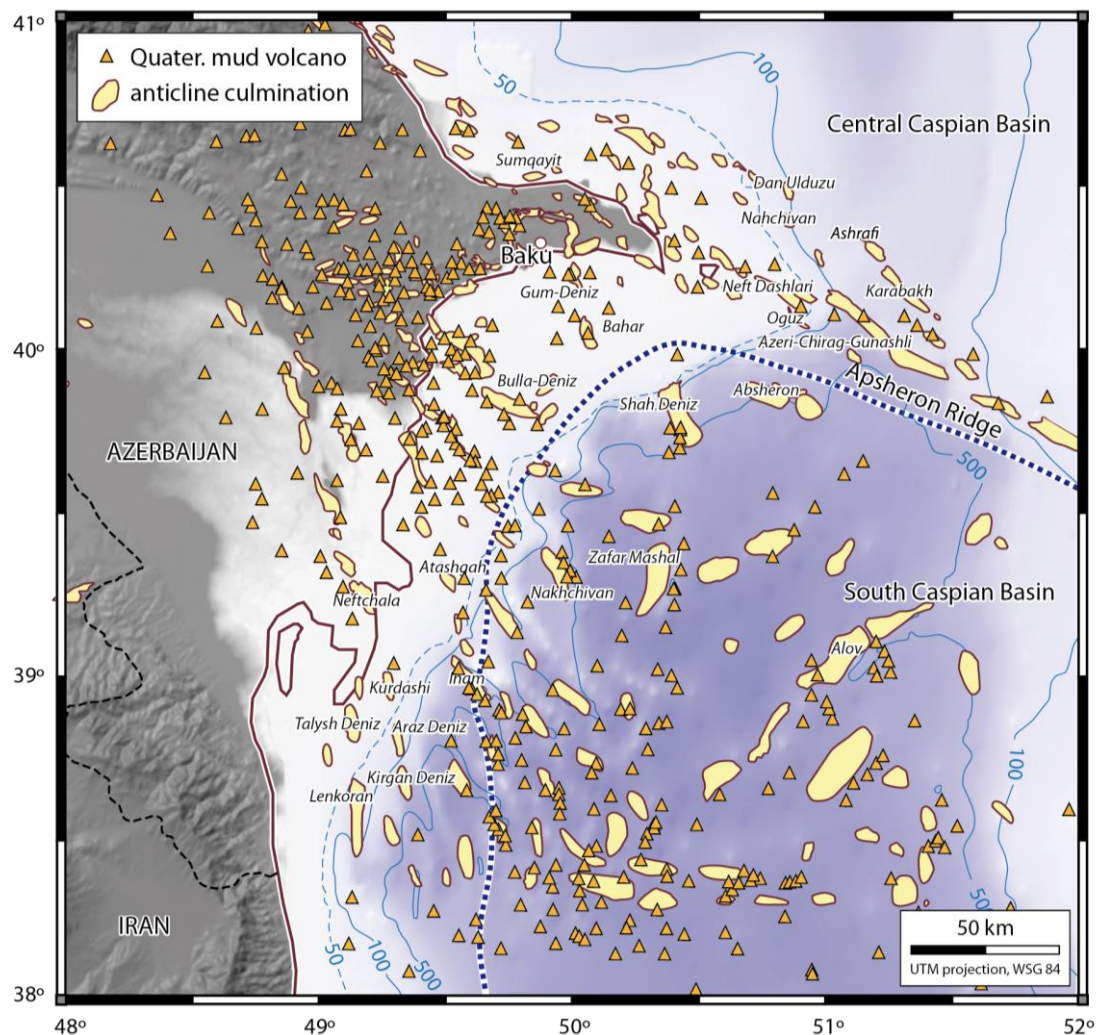


Figure 7.10: Map of the western SCB including the distribution of prospective anticline culminations and active and Quaternary mud volcanoes compiled in Santos Betancor and Soto (2015). Sources for mud volcanoes are: Nadirov *et al.* (1997), Kadirov (2000), Planke *et al.* (2003), Etiopie *et al.* (2004), Guliev and Panahi (2004), Yusifov (2004), Yusifov and Rabinowitz (2004), Mellors *et al.* (2007), Evans *et al.* (2008), and Roberts *et al.* (2010). Anticlines are from Fowler *et al.* (2000), Aliyeva (2005), Baganz *et al.* (2012), Imbert *et al.* (2014), and H. Dobrova (IHS, personal communication). Digital topography is from SRTM30 plus (Becker *et al.*, 2009), with a grid size of 1 km.

Our combined study of geometry and deformation of the KAD fold suggests that diapirism rise occurred simultaneously to folding in the last 3.1 my (Devlin *et al.*, 1999; Abdullayev, 2000; Yusifov, 2004). This hypothesis matches with minimum differences between S_C vs. S_A measurements in the Post-PS epoch (Table 6.6, and Figs. 6.16 and 6.18). Start of diapirs piercing is inferred in the Akchagyl period due to an intense episode (Yusifov, 2004), and cease is established in the Apsheron times (1.6-0.7 Ma) denoted by layers deflection due to mud depletion at fold flanks (Fig. 6.13) (Smale *et al.*, 1997; Abdullayev, 2000). Mobile shales might flow in the subsurface previously to the Post-PS folding, concomitant to shortening and volume variations (Figs. 6.16 to 6.18).

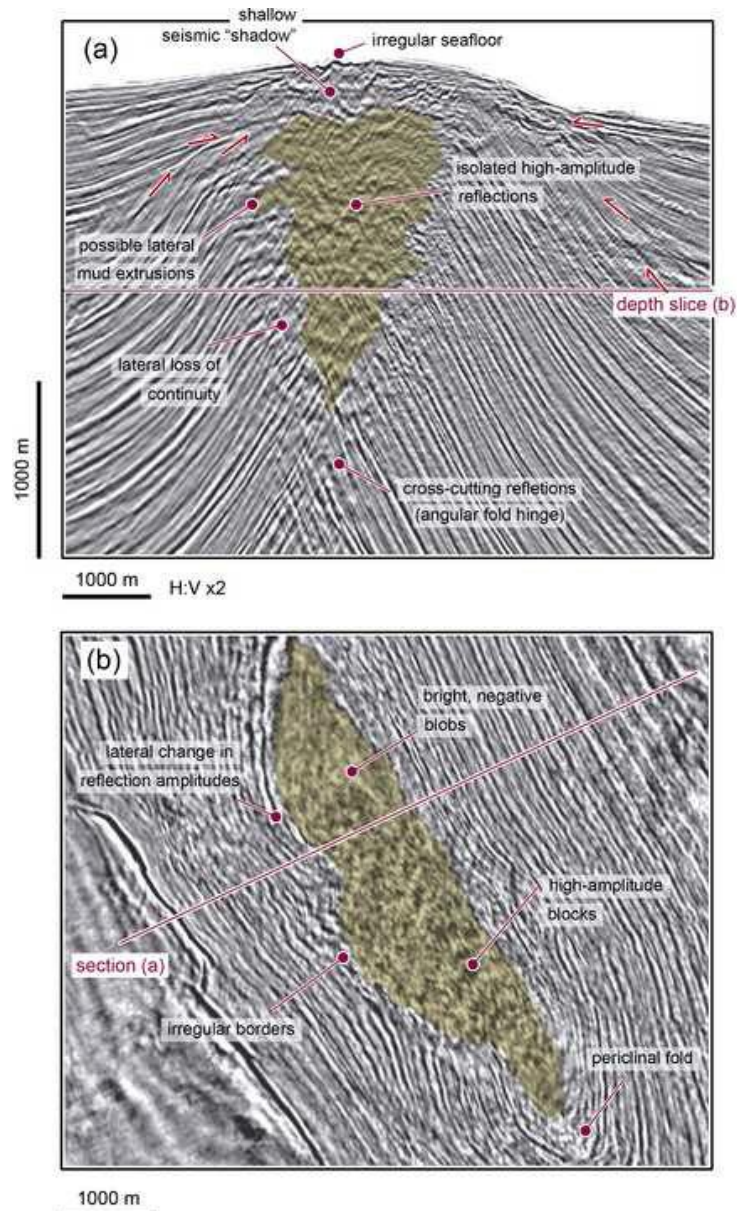


Figure 7.11: Illustration of internal fabric and criteria used to delimitate limits of mud bodies from country sediments. Shown example corresponds to mud diapir that pierces the Southern Culmination through (a) vertical and (b) 1.5km depth seismic sections (Santos Betancor and Soto, 2015).

Diapirism intrusion is controlled by local deformation where both compressional and extensional domains must exist simultaneously at different structural levels (e.g., Hudec and Jackson, 2007). In the KAD anticline mud migrated horizontally and vertically to solve space problems created in extended areas during folding (Figs. 7.5). We interpret saturated shales pierce where maximum shortening rates are registered, as it occurs in the Southern Culmination and, by extrapolation, in the Northern Culmination (e.g., Fig. 7.5b and 7.5d). Decreasing shortening magnitudes presumably triggered structural collapse and diapirism stop in the northern regions, dated in the early Apsheron. Deformation might have continued southwards to the end of the Apsheron deposit as the uplifted Southern Culmination was still shortened and supports late diapirism phenomena. Balance between tectonics and low sedimentation rates may also contribute to Post-PS diapirism, instead of an early origin. Present-day activity is observed through scattered fluids released to the surface in the Southern Culmination in

the vicinities of the IL 1140 (*Fig. 5.3*).

Inverted-triangle shapes, scarce and isolated diapirs, and the existence of welds without shale pedestals evidence mud vertical contribution is relatively low in the studied structure. Subsurface mud mobilization can be reconstructed with a major eastward component of horizontal injection following basin tilting. We infer local vertical ascend through severely thinned sequences over basement faults assuming active stages of diapirism (Dooley *et al.*, 2005). Accentuated shape of synclines in the southernmost sectors also evidences mud evacuation towards the North (Mitra 2003). Out-of-plane withdrawal is also considered.

7.4.2. Faulting Style

The KAD fold is intensely crosscut by fault structures due to the accommodation of variations in strain during the Pliocene-to-Present deformation (*e.g.*, Devlin *et al.*, 1999). Seismic cubes in *Figure 7.12* illustrate how faulting is propagated through the PS and Post-PS packages in the Southern Culmination domain. Complex deformation in the studied anticline may be explained by a wide combination of structures that behave as thrust, normal and strike-slip faults embedded in a detachment folding setting (*Fig. 7.12c*) (Abrams and Narimanov, 1997). Our observations stand out a distinctive stratigraphic and structural position with noticeable variations in fault regimes and timing. Structures are grouped into three systems according to their location: cretal, core and flanks faults.

Populated cretal faulting is formed by normal faults restricted to shallow levels in the anticline culminations, constrained in the Surakhany-to-Apsheron packages (*Figs. 7.5* and *7.12*). Structures converge towards culminated domains as curved fractures with NNE-SSW to N-S directions (*e.g.*, *Fig. 7.12b*). Fractures orientation locally turns to a nearly radial distribution WSW-NNE and NNW-SSE-oriented within the Surakhany Unit (*Fig. 5.10*). Planes of master faults are highly-dipping and preferentially dip to the East, and are responsible for collapse in the culminated regions (*e.g.*, *Fig. 7.5d*). In the Southern Culmination structures describe mutual crosscutting relationships, interpreted as conjugated and keystone-like faults *e.g.*, (*Fig. 7.12c*) (*e.g.*, Ferrill *et al.*, 2000). In the saddle domains (*i.e.*, IL 1640, *Fig. 7.5c*) faults depict planar web-like connections and “horse-tail” shapes towards the Northern Culmination (*Fig. 5.11d* to *5.11f*) (Bertello *et al.*, 2001). In the vicinities of the northern bulged area, faulting diverges into two splay antithetic fractures disconnected from the mud diapir limits (*Fig. 5.10*).

Core faults are abundantly described in the anticline core (*Fig. 7.12c*) coincident with the position of the axial trace, connecting both culmination domains with variable regimes and dip orientation (*Figs. 5.7*, *5.9* and *5.10*). Dip of faults is sub-vertical in deeper levels and occasionally they show low-angle planes. Faults show a reverse behaviour within the PS up to the Balakhany Unit (*Fig. 5.11c*) that usually switches to normal in the Sabunchi Unit (*Fig. 5.11d*) or in the Surakhany Formation and propagates to the top of the PS (*Fig. 5.7*). These normal faults are usually interpreted similarly to cretal structures in the culminated zones of the KAD anticline. Reverse structures are NW-SE-directed and vary from planar to slightly sigmoidal geometries with usually large dimensions.

Reverse and normal core faulting is strategically separated among the inner and outer arc of the studied fold, which respectively represent the compressed and extended domains in buckling folds driven by flexure and collapse (*e.g.*, *Fig. 7.12c*) (Ramsay, 1967; Wall and Wiener, 1998; Devlin *et al.*, 1999; Lisle, 1999). The structural boundary

is established between the Sabunchi and the lowermost Surakhany intervals and describes a layer-parallel neutral surface of deformation (e.g., Bertello *et al.*, 2001). This surface should migrate during shortening due to space unbalance and deep mud migration. In domains where fold is not mud-pierced, as in the southern domains, gap problems are resolved by different structures.

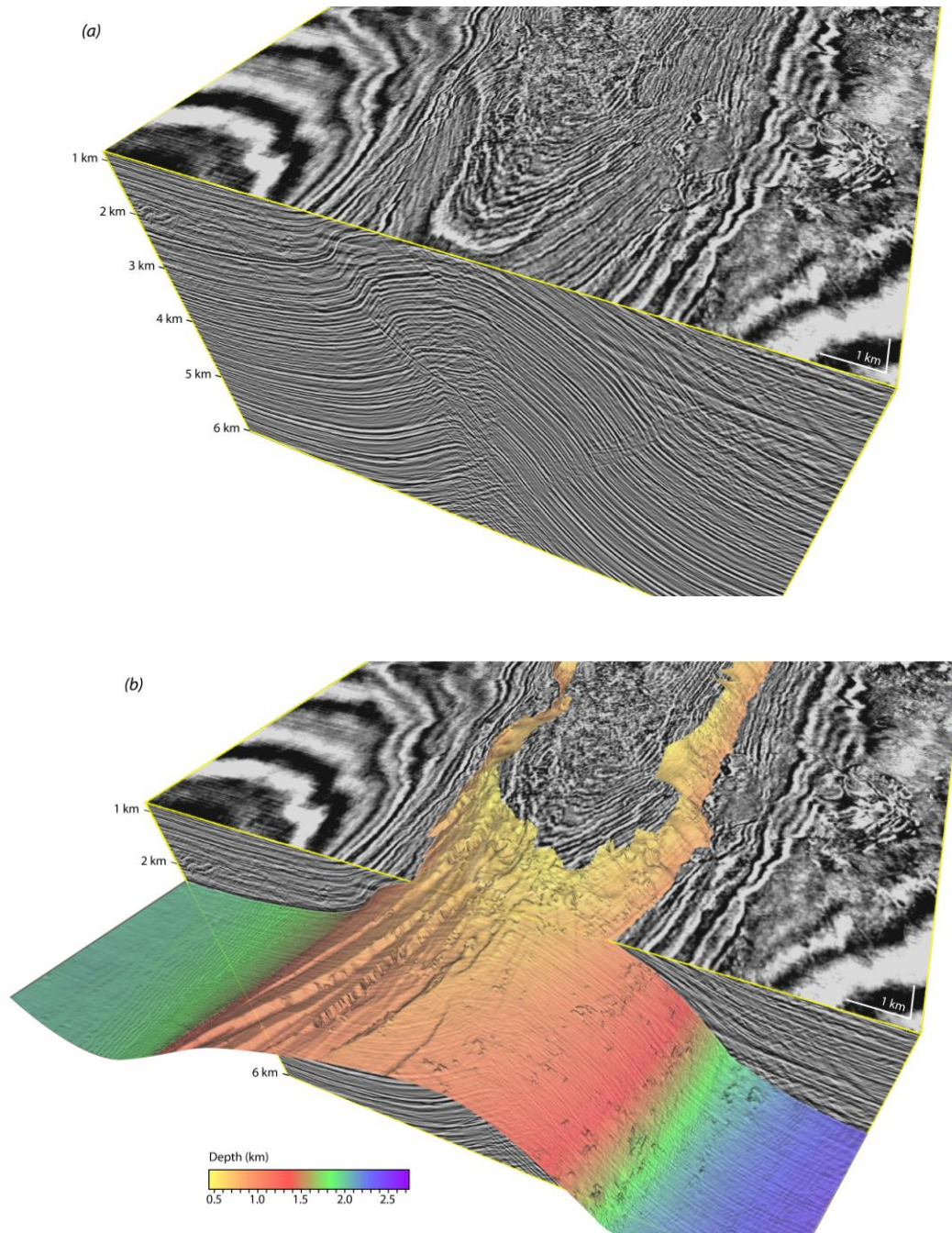


Figure 7.12: a) 3D seismic cube delimited between 860 m and 6 km depth in the Southern Culmination. b) Same volume as in (a) combining the PS-top surface. c) Interpreted volume shown in (a). Reverse and normal faulting occurs in the frontal vertical section at two structural levels separated by the Surakhany Unit (Sk). Normal faults extend along the fold crest towards the culmination. The occurrence of MTCs in the Post-PS package is also highlighted. Horizons and packages are coloured as in previous descriptions (e.g., Fig.7.5). Vertical scale is exaggerated 2.5 times in comparison to horizontal scale. Continuation in the next page.

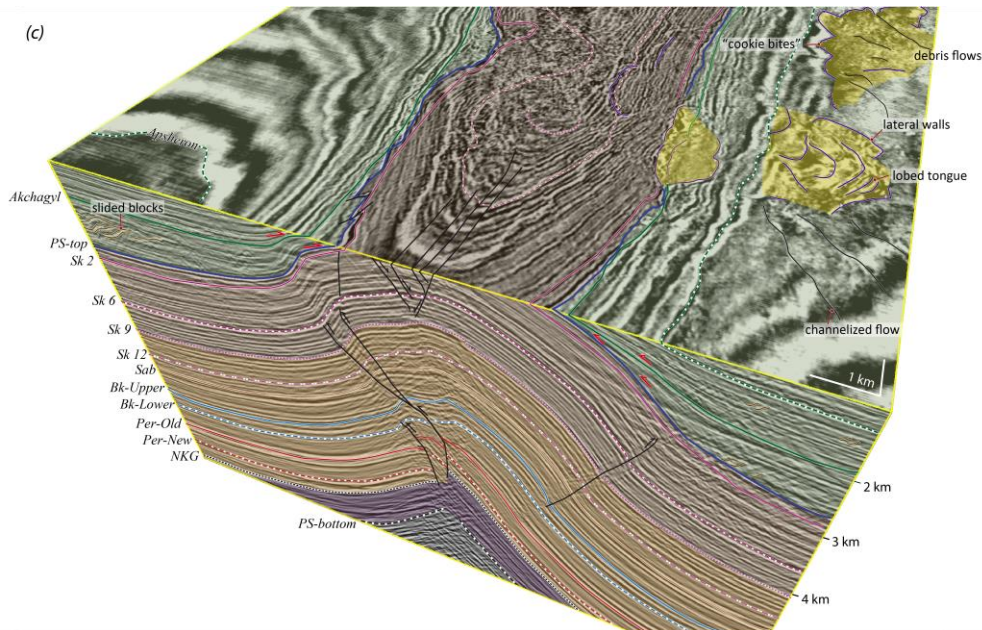


Figure 7.12: Continuation.

Two systems of large structures with perpendicular orientations and opposite regimes characterize flanks faulting (e.g., Fig. 7.4a). Reverse faults accompany the kink-like fold described in the South in the Lower PS units sealed by the PS-top (Fig. 7.12c). They correspond to two pairs of 45° -dipping and planar structures that follow a NW-SE direction parallel to the fold axis. Both pairs act conjugately and bound the fold crest. In central positions, 10-km-long normal faults displace both KAD flanks in successive epochs with a NE-SW orientation. Eastern examples are registered in the PS from the Pereryva Formation (Fig. 5.8), whereas a western pair merges in the Balakhany unit and extend upwards to the Apsheron Formation (Fig. 5.6). Fault surfaces are mostly planar but curve in the proximities of the Southern Culmination where become sub-vertical (Figs. 5.11d to 5.11f). Extensional structures depict synthetic and antithetic conjugated faults.

Faulting in fold flanks may be a result of gap unbalance during shortening in the KAD fold. We suggest rheology of PS units is the conditioning factor to solve space problems by fracturing the folded package in the South through kink-band structures. Northwards, partition of deformation is transferred into folding and mud diapirism. Subsurface mud depletion might be the responsible for collapse structures along fold flanks.

7.4.3. KAD Deformation History

A schematic interpretation of the KAD evolution is illustrated on panels of Figure 7.13. We reconstruct different evolutionary stages of the studied fold since the deposit of the Maykop Unit (Late Eocene-Early Miocene, ~36-16.5 Ma), referred as W in Figure 7.13. The frontal side of the 3D panels are built parallel to fold strike (i.e., NW-SE), and planar views are schematically described in the right-hand side insets.

Accordingly to the numerous descriptions and evidences we interpret that the Maykop Unit behaved ductily and flew during subsequent deformations (e.g., Yusifov and Rabinowitz, 2004; Smith-Rouch, 2006). Due also to its great thickness, the weak unit constitutes a decoupling level during deformation, limiting the connection or

propagation during sedimentation and burial, of the deep structures with the new ones formed above it (Hinds *et al.*, 2004; Smith-Rouch, 2006; Hudson *et al.*, 2008). We believe that these suggestions help to explain some of the singular features identified in the KAD, although our seismic observations have never achieved such deep levels of the structure.

The Maykop Unit was deposited over an underlying sequence and/or basement floor (B; stage 1 in *Figure 7.14*) (Inan *et al.*, 1997; Hudson *et al.*, 2008; Afandiyeva *et al.*, 2009). Shale-rich layer lies above a gentle ramp that dips and tilts eastwards (stage 1 in *Figure 7.13*), where an oceanic crust presumably floors the basin (*Fig. 2.11*). We also consider the occurrence of a weak fault zone composed by two small and disconnected fault strands below the weak layer. Fractures correspond to normal structures with NW-SE direction and eastward dip that defines an incipient normal fault zone in the KAD area (inset in stage 1, *Figure 7.13*).

Fault propagation determines the enlargement of the different fault segments in length and depth, and the possible generation of overlapping and bend zones (stage 2 in *Figure 7.13*). Accompanying fault propagation the weak Maykop Unit spread probably downdip.

Advanced stages of deformation occurred synchronously to the partial deposit of PS sediments, from the Lower PS to the Sabunchi Unit (Late Miocene-Early Pliocene, 5.9-3.7 Ma), represented as #1 in stage 3 in *Figure 7.13* (Jones and Simmons, 1997; Abreu and Nummedal, 2007; Forte *et al.*, 2010). We postulate deep fault segments linked along a high-angle fault zone that described normal faulting, with some component of right-lateral shear.

The occurrence of a pre-existent east-dipping and normal fault is inferred along the NW-SE-directed KAD axis, evidenced by a separated evolution of fold limbs (*cf.* isopach maps in *Figure 7.2*). These suggestions could explain geometrical discrepancies of folded PS sequences: (1) the occurrence of an abrupt increase of sedimentary thickness in the actual position of the KAD anticline hinge; and (2) the thicker domains always occur in the eastern flank. Accordingly to tri-shear models of deformations we propose the thick and highly-dipping eastern limb acted as the hanging-wall, and the western limb represented the footwall.

Faulting promoted the generation of drape folds above the upper-tip of the faults (stage 3, *Fig. 7.13*). We interpret incipient folding as the nucleation of the KAD anticline above the overlapping fault segments and near to the projection of the trace of the buried normal fault (inset in stage 3). The accommodation fold was generated as an extensional and gentle monocline that would have an abrupt bend that mimics the domain with linked strands. Basin evolution was accompanied by subsurface migration of shales in the Maykop Unit towards the inner basin.

Cover shortening controls the deformation in the KAD area in phases 4 and 5 (*Fig. 7.13*), during the deposit of the Surakhany Unit (Early-to-Late Pliocene, 3.7-3.4 Ma) (Jones and Simmons, 1997; Abreu and Nummedal, 2007; Forte *et al.*, 2010). Lowermost subunits 12 (3.7-3.6 Ma) and 9 (3.6-3.5 Ma) are grouped as #2 (stage 4), and the uppermost packages between the Surakhany 6 (3.5-3.4 Ma) to the PS-top are separated as #3 (stage 5). This epoch is characterized by a clear start of KAD folding uplift over the pre-existent fault zone just after the deposit of the Surakhany 9 Unit. An early folding burst would be inferred towards the North coetaneous to the deposit of the Surakhany 12 (3.7-3.6 Ma). Folding congruently deformed the pre-Surakhany sequences, whereas the younger units depict subtle wedge geometries towards the KAD

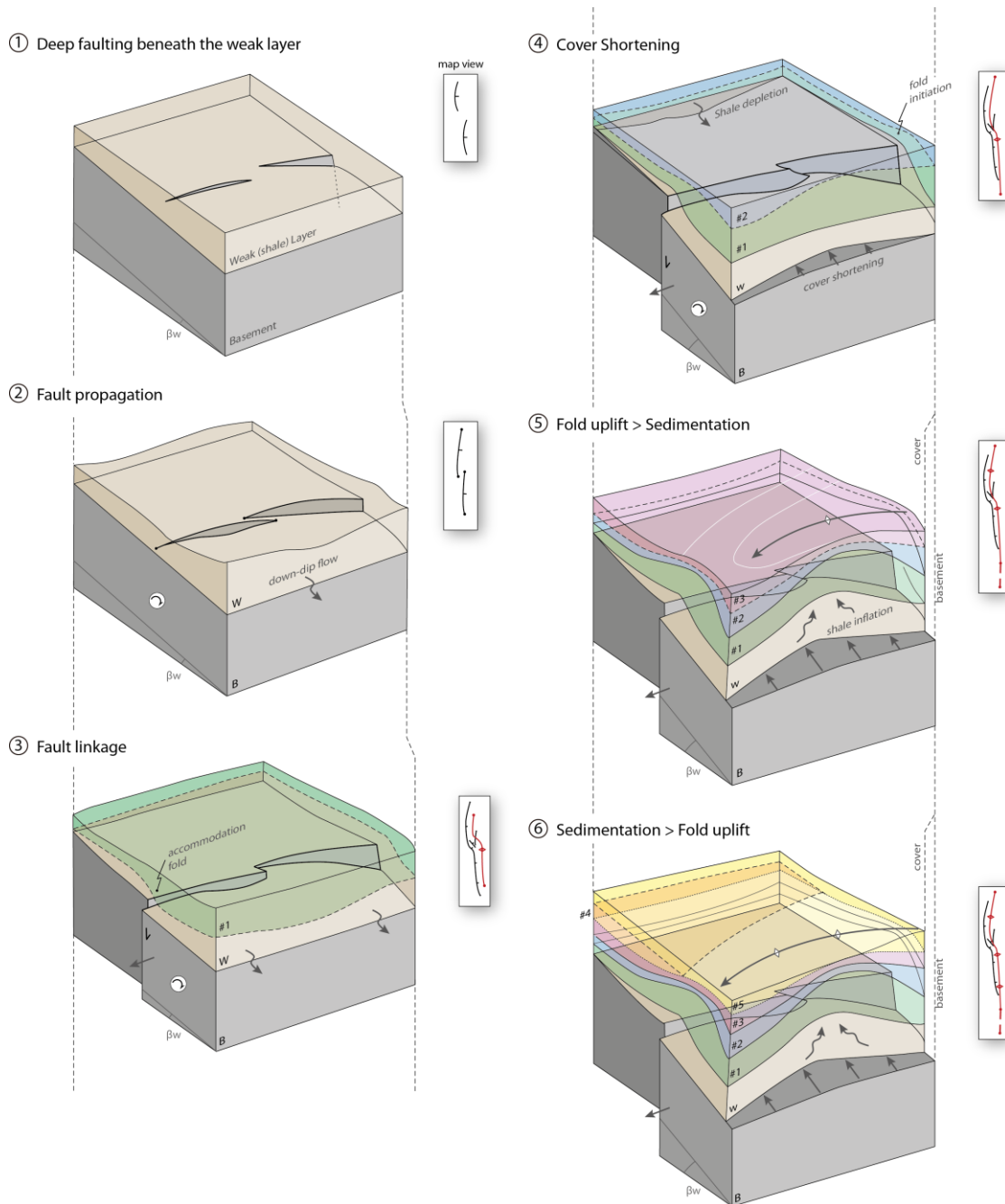


Figure 7.13: 3D schematic panels to show the evolution of the KAD anticline. Reconstruction is done from the deposition of the Maykop Unit to the Present. The frontal side of the blocks is roughly oriented parallel to the fold strike (*i.e.*, NW-SE), whereas the left side represents the perpendicular dip section (*i.e.*, WSW-ENE) (Santos Betancor and Soto, 2015). We highlight the occurrence of: 1) a high-angle normal fault buried at depth that control the deformation of the cover sequences, and 2) detached deformation and variable horizontal extension between the sedimentary overburden and the deeper sediments (including basement), due to the occurrence of a thick, mud-rich layer. This layer represents the Maykop Unit and is labelled as W (weak layer); the pre-Maykop units, including the basement, are labelled collectively as B. PS subunits are represented by numbers #1 (PS-bottom to Sabunchi units), #2 (Surakhany 12 and 9 units) and #3 (Surakhany 6 and 2 units). The Post-PS package is sketched as layers #4 (representing mostly the Akchagyl Unit) and #5 (corresponding to the Apsheron Unit). To better clarify the visualization of 3D panels, shallow faults described in 7.4.2 section and deep fault inversion are not included. β_w shows the dip of the base of the weak shale layer. Inset schemes show in every panel the plan-view of the structures, with faults in black and folds in red colour. Circular arrow expresses active dip-slip faulting.

hinge (stages 4 and 5) (e.g., González-Mieres and Suppe, 2011).

Simultaneously to the deposit of the Surakhany Formation in phases 4 and 5, deep faulting affected the Maykop and the PS units, with both dip-slip and strike-slip components (Fig. 7.13). Dip-slip is dominant reflected by the thicker eastern Surakhany packages over a subsiding flank. Some layer thinning is also observed along the KAD strike and towards the fold culminations related to deep shale migration and downbuilding (e.g., towards the Southern Culmination in Figure 5.7). Mud mobilization is inferred parallel to the fold strike that preferentially accumulated in central domains to inflate fold core (stage 5 in Figure 7.13). Downdip subsurface flow might have depleted the mud layer in the western domains (e.g., stage 4 in Figure 7.13) and promoted flanks collapse (e.g., Fig. 5.6).

The PS-top surface marks a change in the folding history for the deposit of the Post-PS sequences (Late Pliocene-Present, <3.1 Ma) (Jones and Simmons, 1997; Abreu and Nummedal, 2007; Forte *et al.*, 2010). In stage 6 in Figure 7.13 we have labelled the deposit of the Akchagyl Unit as #4 (Late Pliocene-Early Pleistocene, 3.1-1.6 Ma), and the Apsheron (Early Pleistocene, 1.6-0.7 Ma), and Gelasian (Early Pleistocene-Present, 0.7 Ma to Present), sediments are referred as #5. The Post-PS rocks, particularly the Akchagyl Unit, accentuatedly onlaps the KAD crest, which is locally covered only by the overlying Apsheron Unit. This geometry can be seen either in dip sections (e.g., Fig. 7.5) or along strike (e.g., Fig. 5.7). They reflect that the vertical fold growth was nearly equal or surpassed sedimentation rates during the Akchagyl interval (#4 in stage 6 in Figure 7.13). Subsequently, since the onset of the Apsheron sequence and throughout the Gelasian Unit, folding velocities diminished and the sedimentation rate exceeded the fold uplift up to nowadays (both formations are represented by layer #5 in stage 6, Figure 7.13).

These suggestions are concordant with variation of folding and mud diapirism along strike. We postulate that KAD folding was initially nucleated in the Southern Culmination because it represents major shortened area in the studied fold. Later shortening transferred as lateral fold growth. By extrapolation, we also infer that the evolution of the Northern Culmination is similar to the southern case.

Fold culminations may also coincide with domains of preferential upward migration and piercing of the overpressured sediments of the Maykop Unit. The flow of these weak, fluid- and mud-rich sediments probably was east-directed and occurred downdip, following the basement slope and tilting, but also along the KAD strike, to feed and upbuild the fold domains with major horizontal shortening.

Mud piercing started in the Akchagyl times, related to maximum shortening rates. Decreasing shortening magnitudes triggered diapirism halt and structural collapse in the North in the Early Apsheron (Fig. 7.5d). We propose diapirism extended to the Late Apsheron and release of fluids continues at Present in the Southern Culmination, where fold uplift is active (Fig. 7.5b). Nevertheless, shortening rates in the South are estimated insufficient for mud to intrude since Gelasian times. High sedimentation rates are predominant and responsible for KAD burial in the Northern Culmination since the Apsheron deposit, close to coastal contribution (e.g., Fig. 7.3d).

Right-lateral faulting controls the last 3.1 my denoted by sigmoidal trace of the KAD fold and curved pattern for crestal syn-faulting structures with relative offset variation along strike. An early origin might be also suggested (*i.e.*, in the Surakhany Unit). Individual welds of mud diapirs also support our hypothesis, as they reflect combined strike-slip and dip-slip motions. Flank graben WSW-NEE-directed reinforces

mud withdrawal (*e.g.*, Fig. 5.6).

The KAD evolution in the SCB

In summary, the KAD anticline is a Plio-Quaternary compressional structure similarly generated to folds in distal areas of deformed continents underlain by a thick incompetent layer (*e.g.*, Dahlstrom, 1969; Rowan, 2004). Our 3D geometry reconstruction resembles that the studied anticline is a singular detachment fold-type that departs from the classic standard detachment-fold model shaped by parallel layers. We suggest that this is result of punctuated deformation is accompanied by a changing setting: (1) deformation has a probable strike-slip component partitioned along the axial surface, (2) folds present a variable thickness in the pre-growth sequence, (3) a pre-existing NW-SE, normal fault may have generated dissymmetry in the KAD area, and (4) the sedimentary sequences tilt toward the basin progressively.

The apparent absence of syn-faulting geometries and the unfractured sediments in the folded units suggest the deep normal fault is deeply rooted in a pre-PS sequence, and presumably connected with Mesozoic basement faults (Jackson *et al.*, 2002; Allen *et al.*, 2003). The West Caspian Fault could have an important role in the origin the analysed step in the KAD anticline (Fig. 2.11) (Khain *et al.*, 1966; Nadirov, 1985; Lerche *et al.*, 1997). This type of fault commonly occurs in mobile basins that glide from the basin margins (*e.g.*, Morley and Guerin, 1996), and it is interpreted in the regional framework as a result of accentuated basin tilting to the East, where the oceanic basement of the SCB is placed (Berberian, 1983; Zonenshain and Le Pichon, 1986).

We propose this pre-existent structure have been reutilized during the Caucasus deformation due to inversion tectonics (Suppe, 1985; Alsop and Holdsworth, 2002; Jackson *et al.*, 2002; Allen *et al.*, 2003). KAD folding is suggested to be nucleated in this weak plane. Cenozoic reactivation led to a considerable switch of fault mechanisms, as is observed along core faulting planes and expressed by changing regime and offset along strike (*e.g.*, Fig. 5.7) (Abrams and Narimanov, 1997; Bertello *et al.*, 2001). Deformation is transferred into the surface as strike-slip transpressional systems in the last 3.1 my, or even earlier. Right-lateral slip produced and alignment of en-echelon faults and folds, accompanied by strong variations displacement of underlying detachment level along strike (Alsop and Holdsworth, 2002; Allen *et al.*, 2003). In the KAD fold, we suggest the occurrence of parallel fault segments that roughly underlie both culminated domains. Continuous right-lateral movement linked successive fragments on relay by releasing stepover, and developed pull-apart basins. Present-day saddle region matches with a presumable pull-apart basin where structural bend occurs. We postulate the occurrence of fault tip in the southern structure that remained majorly fixed during folding, expressed by low-mature kink-band folding (*e.g.*, Fig. 7.5).

Highest values of stress in the KAD fold are registered in the culminated regions, represented by strategical positions for mud to exhume (Allen *et al.*, 2003). Overpressured muds come from the Maykop Unit at > 9 km depth and pierce the PS through diapiric structures simultaneously to the Akchagyl and Apsheron deposit. We suggest fluids-rich shales used deep fault plane as a migration path, consistently to mud volcanism in the SCB that exhumes along severely thinned areas over basement faults (*e.g.*, Kopf, 2002; Dooley *et al.*, 2005).

We assume the studied structure behaves relatively independent of deep faulting due

to the plastic mud layer acts as a décollement surface (*Fig. 2.6*) (Allen *et al.*, 2002; Jackson *et al.*, 2002; Guest *et al.*, 2007). Singularities of folding and faulting in the KAD fold are interpreted as a result of local accommodation of regional tectonics that make this structure not wide-representative of the basin and only similar to nearby offshore structures. This explains unpredictable structural styles as the location of offshore folding and faults, which do not coincide with the position of the seismicity or in the focal mechanisms (*Fig. 2.6*) (Allen *et al.*, 2002; Alsop and Holdsworth, 2002; Jackson *et al.*, 2002; Guest *et al.*, 2007). Rotation is the responsible for NW-SE trend of the KAD fold that faces against the regional N-S compressional system (*Fig. 2.5*) (Jackson *et al.*, 2002); it would be triggered by differentiated accommodation of the deformation in Talesh and eastern Greater Caucasus systems along the West Caspian Fault (Khain *et al.*, 1966; Priestley *et al.*, 1994; Jackson *et al.*, 2002).

7.5. Implications for the Petroleum System

The SCB is a region of intense commercial interest because of its prodigious hydrocarbon reserves (*Figs. 2.22, 2.25* and *Table 2.1*). The evolution of the petroleum system in the western SCB is schematized in *Figure 7.14*. This diagram shows the burial history of the Maykop Unit, built without any eustatic and decompaction corrections, and assuming that all the sedimentary units are deposited closed to the shoreline; *i.e.*, no paleobathymetry variations. Graph is complemented with important events related to fluids generation, trapping and migration. Timing of main structuration milestones and sedimentation rates are also compiled.

Oil and gas deposits in the western SCB have been discovered in the deltaic Upper-PS reservoirs. The Pereryva Suite (Early Pliocene, ~5.33-5.2 Ma to 4.9 Ma) and the Balakhany Formation (Early Pliocene, 4.9-4.0 Ma) form the most important targets (*Figs. 2.23* and *7.14*) (Abdullayev *et al.*, 2012), whereas secondary hydrocarbon reservoirs are located in the Surakhany Unit (Early-to-Late Pliocene, 3.7 Ma to ~3.4-3.1 Ma) (*e.g.*, Smith-Rouch, 2006). The regional source rock for hydrocarbons is the Maykop Unit (Late Eocene-Early Miocene, ~36-16.5 Ma) (*e.g.*, Abrams and Narimanov, 1997; Devlin *et al.*, 1999; Hudson *et al.*, 2008; Afandiyeva *et al.*, 2009).

Plio-Quaternary anticlines in the sedimentary cover constitute the principal petroleum traps in the region (Devlin *et al.*, 1999; Allen *et al.*, 2002). The KAD anticline was explored in the Kurdashi project, challenged by the NW-SE expected trend alignment from the producing Neftchala field in onshore Azerbaijan (see *Fig. 2.22*). Location of the exploration block is a response of widespread shallow gas, steep dips, and mud volcanoes connected to irregularly shaped mud chambers and associated velocity anomalies (*e.g.*, Corthay and Aliyev, 2000; Stewart and Davies, 2006). Preliminary results and regional studies evidence the KAD anticline satisfies conditions to be a producing structure, although scarce hydrocarbons shows were recovered in the Kurdashi Permit (*Fig. 2.22*).

Our research is focused on the role played by structuration in the petroleum system in the KAD fold, whereas further interpretations are realized based on third parties geochemical and biostratigraphic studies. We speculate the absence of hydrocarbons may lay in the combination of three fundamental factors that differentiate the producing continental areas from the null offshore production in the submarine propagation of the Kura Delta (*cf.*, Lenkoran field in *Figure 2.22*). In the studied area the petroleum system might be incompletely developed due to tectonics, bad-quality facies and low and

immature organic content.

Hydrocarbons generation is dated in the Pliocene (*e.g.*, Abrams and Narimanov, 1997), simultaneously to the Surakhany structuration in the KAD fold (*Fig. 7.14*). This geological framework should have favoured intense fluids migration and trap in growing folds. Nevertheless, the erosive unconformity that crowns the top of the PS may have decapitated the KAD anticline, with the consequent hydrocarbons escape. Faulting and diapirism produced during the second shortening episode may have released new and recharged oil and gas. Gravitational processes might have impacted in hydrocarbons exploration, as MTCs headwalls eroded the uppermost PS and the Post-PS units, representing an additional evacuation area in the fold crest (*Fig. 7.14*).

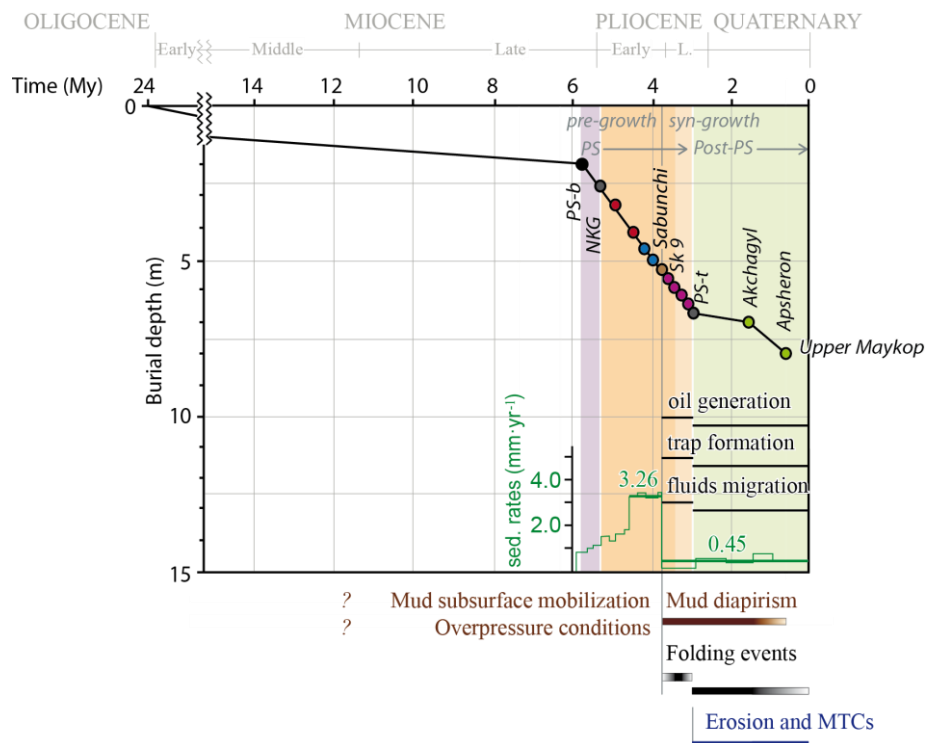


Figure 7.14: Diagram of the evolution of the petroleum system in the KAD fold that illustrates main landmarks in the western margin of the SCB. Burial history of the Maykop Unit (~36-16.5 Ma; Hudson *et al.*, 2008), structuration and sedimentation periods are included, according to results presented in this thesis (ENI, 2002). Hydrocarbons generation and migration history is established by regional authors (Abrams and Narimanov, 1997; Bagirov *et al.*, 1997). Horizons are abbreviated as in *Figure 7.5*. In the time scale, Late Pliocene is referred as L., and the Pleistocene and Holocene epochs are included within the Quaternary.

Folding could also promote the rise of the organic-rich beds, and in consequence, cooling and interruption or stop of hydrocarbons transformation, that would restart when they were reburied. Complex burial and deformation histories in offshore Azerbaijan are evidenced by oil samples that show characteristics consistent with multiple phases of hydrocarbons emplacement (Abrams and Narimanov, 1997; Bagirov *et al.*, 1997). Migration path is supposed to be vertical and eastward-directed favoured by the paleo-orography and gradient of the tilting basin (Inan *et al.*, 1997).

Our seismic and statistical observations (*e.g.*, *Table 6.6*) evidence source layer is located in the oil window (>8 km depth) and shallower than gas window (<12-14 km), coherently to regional studies (Abrams and Narimanov, 1997; Bagirov *et al.*, 1997; Inan

et al., 1997; Devlin *et al.*, 1999; Guliyev *et al.*, 2001). According to burial history of the Maykop Unit in the KAD fold we propose critical depths for organic material transformation were reached in the western SCB simultaneously to the deposit of the Post-PS; *i.e.*, <3.1 Ma (*Fig. 7.14*). Thus, in the KAD structure only oil fields may be developed in contrast to surrounding continental blocks, where gas fields are dominant (*e.g.*, Neftchala in *Figure 2.22*); it might be explained by a shallower source level for gas generation and slower expel of methane fluids than oil after folding event (Kopf, 2002).

Regional studies highlight differentiated evolutions in the continental and marine settings, fundamentally based on the role played by the oceanic floor. Rigidity of the basaltic crust promoted partitioning of deformation and, therefore, differentiation for the petroleum systems. Basement influences and large structures such as the West Caspian Fault (*Fig. 2.11*) may be determinant in depth variations in the Maykop Unit in onshore and offshore scenarios. Thus, different locations of oil and gas windows will be explained and the success in the oil-producing Neftchala field <30 km far onshore Azerbaijan is also justified (*Fig. 2.22*).

The occurrence of low volume of oil and gas accumulation in the KAD area is supported by stratigraphic PS facies and geochemical characteristics of the Maykop Unit (*e.g.*, Abrams and Narimanov, 1997; Guliyev *et al.*, 2001; Hudson *et al.*, 2008). The PS reservoirs contain a low total content of organic carbon (<1.0%; Abrams and Narimanov, 1997), associated to a poor quality of the Paleo-Kura facies, which contain a high proportion of lithic and poor sorted grains, that may result in greater sediment compaction and porosity loss (*e.g.*, Alizade *et al.*, 1985; Morton *et al.*, 2003). These characteristics contrast with very good reservoir properties of the Paleo-Volga sediments. Low to moderate organic maturities of oil in the Maykop shales (VRE=0.75-0.85; Abrams and Narimanov, 1997), and distribution in patches may be an additional impediment for hydrocarbons generation (*e.g.*, Guliyev *et al.*, 2001; Stewart and Davies, 2006). These conditions limit a basin-wide generalization, also dependant on burial rates and thermal models.

Lower maturity than conventional for oil windows could be a result of rapid expulsion from strong hydrodynamic forces. Well logs have shown very low overpressure conditions in the studied area, transcendental for fluids withdrawal, that would also explain scarce fluids released in the KAD anticline. The non-occurrence of mud volcanism and disconnected and scattered mud diapir structures are a strong bastion to consider that in the KAD anticline these structures hardly carry hydrocarbons, in contrast to similar bodies in the Apsheron Ridge where high hydrocarbons proportion may justify abundant subsurface migration (Lerche *et al.*, 1997; Nadirov *et al.*, 1997; Guliev and Panahi, 2004; Yusifov and Rabinowitz, 2004).

8. CONCLUSIONS

- (1) The Kirgan-Araz Deniz (KAD) anticline has been interpreted through the exhaustive interpretation of a 3D seismic dataset, post-stack and migrated in depth that penetrates 9 km in the offshore Azerbaijan. REPSOL has provided us this seismic cube and well-logging information. The analysed fold is composed by two culmination domains and is delineated by a NW-SE sigmoidal axis. Fold attitude changes along strike from a symmetrical to an asymmetrical structure cored by mud, and generally verges eastwards, following the dip of the basement in the western margin of the South Caspian Basin (SCB). The anticline corresponds to a non-cylindrical upright fold that deforms Late Miocene-to-Present sediments locally pierced by overpressured muds. Noticeable differences are recognized between fold flanks along the anticline axis that present different thickness and are characterized by variable limb length and limb dip. Overall fold profiles describe a singular detachment fold type generated by buckling simultaneously to eastward basin tilting towards the oceanic crust of the SCB.
- (2) The sedimentary sequences reflect different delta systems that prograde to the SE during the Pliocene. The majority of the Productive Series (PS; Late Miocene-Late Pliocene, 5.9 Ma to 3.1 Ma) are defined by a constant thickness along the fold anticline, and in consequence they were deposited before folding as pre-growth sequences. Within the PS, the Surakhany Unit (Early Pliocene-Late Pliocene, 3.7 Ma to 3.1 Ma) evidences an early syn-growth, because this unit shows subtle thinning over the crest of the KAD anticline. The sequences that overlie the PS, here referred as Post-PS (Late Pliocene-to-Present, <3.4-3.1 Ma), were deposited over a conspicuous discontinuity, and present marked thinning and onlap geometries in crestral areas because of syn-folding during the most recent episode of folding. An intense event pulse of deformation took place during the deposit of the Akchagyl Unit (Late Pliocene-Early Pleistocene, ~3.4-3.1 Ma to ~1.7-1.6 Ma).
- (3) We have analysed several and parallel NW-SE sections perpendicular to fold trend through nonparametric regression. This method has demonstrated to be a powerful technique that surpasses parametric estimators, as it is able to work with discontinuities in folded horizons and always produces a better fit of the complete shape of the KAD fold. To compute linear (S_C) and areal shortening (S_A) magnitudes we have used a list of variables that are: (1) the total length of the deformed surface; (2) the position of the maximum and minima of the distribution, which coincides with the anticline crest and the syncline troughs, respectively; (3) the location of the inflection points; (4) the dip of the fold flanks in their vicinities; (5) and the length

and dip of the fitted regional line.

- (4) In the KAD structure, folding rates varied in time and along fold strike. Folding initiated after the deposit of the Sabunchi Unit (Early Pliocene, 4.0 Ma to 3.7 Ma), with shortening rates $S_A \sim 2 \text{ mm}\cdot\text{yr}^{-1}$, and extended southwards simultaneously to the deposit of the Surakhany 6 Formation (Late Pliocene, 3.5 Ma to 3.4 Ma). The second syn-folding event was majorly homogeneous along the KAD fold with shortening rates of $0.2\text{-}0.4 \text{ mm}\cdot\text{yr}^{-1}$ that decrease to Present. In both episodes, maximum deformation occurred in the structural high of the Southern Culmination where maximum growth of the KAD is registered. Similar ratios and evolution could also be inferred for the uplift of the Northern Culmination.
- (5) Folding was accompanied by rapid sedimentation ($<3.3 \text{ mm}\cdot\text{yr}^{-1}$) simultaneously to the deposit of the Surakhany Unit (shortening rates \ll sedimentation rates). Sedimentation of the Post-PS sequences descended to $0.5\text{-}0.6 \text{ mm}\cdot\text{yr}^{-1}$ (shortening rates \sim sedimentation rates), with major values registered in the most recent sediments, in the Gelasian Unit (Late Pleistocene to Present, $\sim 0.8\text{-}0.7 \text{ Ma}$). Balance between folding and sedimentation favoured the progressive drape of the KAD anticline in the last 1.7 my in the Northern Culmination.
- (6) Abundant mass-transport complexes (MTCs) are generated due to the basin activity in the KAD anticline in the last 3.1 my. The emersion of the fold crest in an upwarped seafloor promoted the deposit of numerous slides coetaneous to the deposit of the Akchagyl and Apsheron (Early Pleistocene to Late Pleistocene, $\sim 1.7\text{-}1.6 \text{ Ma}$ to $\sim 0.8\text{-}0.7 \text{ Ma}$) strata. Major slides were deposited in the Akchagyl period and seem to be controlled by an accentuated folding event. Prograding deltas over the marine shelf edge are the major responsible for unstable slopes and debris flows in the Gelasian Unit ($<0.8\text{-}0.7 \text{ Ma}$) with retreated headwalls.
- (7) The KAD fold is decoupled from a single and low-dipping surface rooted within a weak and mud-rich layer: the Maykop Unit (Late Eocene to Early Miocene, $\sim 36\text{-}16.5 \text{ Ma}$). Geometrical observations and shortening estimate suggest that the décollement level is East-dipping and buried between 9 and 11 km depth. The eastern limb leads deformation and represents the forelimb, whereas the western flank is dragged, referred as the backlimb. Detachment deformation in the last 3.7 my occurs due to a mix model of folding mechanisms. Hinge migration seems to work as the main factor in the first syn-sedimentary deposit, whereas limb rotation plays a major control in the Post-PS package.
- (8) Significant lower values of S_C than S_A indicate the KAD fold does not conserve bed length and volume varies during deformation due to mud diapirism. Fluid-rich muds pierce the KAD fold shaping structures that broaden upwards and depict teardrop diapirs without extrusion in the seabed. The connection with the source layer or pedestal of mud structures is not identified in the seismic cube, although depleted feeder channels are recognized as vertical and sub-vertical welds. Welding occurred most probably during folding and is seen with some component of dip- and strike-slip (right-lateral) components. The source for overpressured muds is the Maykop Formation. Mobile shales rise as a result of high folding rates in both culmination domains coincident with maximum shortened areas. Piercing starts in the Akchagyl times and vanishes in the early Apsheron in the Northern Culmination, whereas it continued until the end of the Apsheron deposit in the Southern Culmination. We postulate that the ductile Maykop Unit rose according to migration paths perpendicular and parallel disposed to the fold axis; *i.e.*, basinwards and sub-

horizontally, respectively. Subsurface mud mobilization is inferred pre-Pliocene as a response to basin tilting and inflates fold core during the deposit of the PS.

- (9) Faulting in the KAD is separated into two structural levels. Normal structures N-S-directed fracture the fold crest as curve faults, whereas reverse faulting is widespread in the fold core and parallel to the NW-SE axial trace. Two systems of large and planar faults deform fold flanks and depict W-E extended grabens and NW-SE thrusts related to kink-band folding. An oscillating neutral surface situated between the Sabunchi (4.0-3.7 Ma) and the Surakhany Unit (subunit Sk 6) bounds the extensional domains in the outer arc of the anticline and the compressive sectors in the inner arc.
- (10) According to fold evolution and the pattern of layer-thickness variations we propose that folding was nucleated above a buried fault zone. Deep structure was composed by a system of two high-angle faults with eastward dip that linked during the sedimentation of the PS sequence. This fault zone is inferred to have a main, normal displacement, with a limited strike-slip (right-lateral) component, that accompanied margin tilting towards the East. Dextral motion is the responsible for the sigmoidal trace and curved faults in the Post-PS package. Fault zone was used by the ductile Maykop Unit to flow laterally and sub-horizontally.
- (11) In the Caspian region, the main source rock for oil and gas is the Maykop Unit. The absence of hydrocarbons in the studied anticline can be interpreted as a combined result of: tectonics, bad-quality facies of the source rock and reservoirs, and low and immature organic content. Hydrocarbons were presumably released due to intense structuration in the KAD fold. The Surakhany folding episode generated numerous crestal faults that acted as migration paths for the firstly emplaced organic-rich material. The PS-top unconformity and erosive headwalls of MTCs truncated and eroded the anticline, triggering secondary fluids withdrawal. Mud diapirism has also contributed to oil and gas escape in the last 3.1 my.

CONCLUSIONES

- (1) El anticlinal Kirgan-Araz Deniz (KAD) ha sido interpretado mediante la interpretación exhaustiva de un paquete sísmico post-stack en 3D, migrado en profundidad y que penetra hasta 9 km en la plataforma marina de Azerbaiyán. Los datos han sido provistos por REPSOL, acompañados de registros e información de pozo. El pliegue analizado está compuesto por dos culminaciones y está delineado por una traza sigmoidal con dirección NO-SE. La apariencia del pliegue cambia a lo largo de la dirección del mismo, y varía desde una estructura simétrica a asimétrica nucleada por barro, que verge generalmente hacia el Este, siguiendo el buzamiento del basamento del Mar Caspio suroccidental (SCB). El anticlinal responde a un pliegue levantado no cilíndrico que deforma un paquete sedimentario de edad Mioceno Superior-Presente, localmente perforados por barro sobrepresurizado. Diferencias notables se aprecian entre ambos flancos a lo largo del eje del pliegue, que presentan diferente espesor y están caracterizados por flancos de longitud y buzamientos variables. La sucesión de perfiles del pliegue describe un pliegue de tipo de despegue singular, generado por “buckling” simultáneamente al basculamiento de la cuenca hacia el Este, donde el basamento oceánico es más pesado.
- (2) Las secuencias sedimentarias reflejan diferentes sistemas deltaicos que se propagan hacia el SE a través de diversas etapas de plegamiento. La sucesión pre-Surakhany de las Series Productivas (PS; Mioceno Superior-Plioceno Superior, 5.9-3.1 Ma) están definidas por un espesor constante a lo largo del anticlinal, y, en consecuencia, fueron depositadas anteriormente al plegamiento como secuencias pre-crecimiento. Dentro de las PS, en la Unidad Surakhany (Plioceno Superior, 3.7-3.1 Ma), se reconocen evidencias de depósito sincrónico con el crecimiento de la estructura, tales como un sutil adelgazamiento de las capas sobre la cresta del pliegue KAD. Las secuencias que yacen sobre las PS, aquí agrupadas como Post-PS (Plioceno Superior-Presente, <3.4-3.1 Ma) fueron depositadas sobre una discontinuidad notoria, y presentan un acusado adelgazamiento y geometrías onlap en las áreas de cresta, lo que denota unas secuencias sin-crecimiento más jóvenes que las anteriores. Un pico en la intensidad de la deformación se produjo durante el depósito de la Unidad Akchagyl (Plioceno Superior-Pleistoceno Inferior, ~3.4-3.1 Ma a ~1.7-1.6 Ma).
- (3) En esta tesis hemos analizado varios perfiles paralelos orientados NO-SE perpendicularmente al buzamiento del pliegue a través de regresión no paramétrica. Este método ha demostrado ser una potente técnica que supera a los estimadores paramétricos, dado que está capacitado para trabajar correctamente con horizontes

discontinuos y, además, genera un mejor ajuste, el cual ha sido utilizado para reconstruir de forma precisa la forma completa del pliegue KAD. Para cuantificar el acortamiento lineal (S_C) y el areal (S_A) hemos establecido una lista de variables que son: (1) la longitud total de la superficie deformada; (2) la posición del máximo y los mínimos de la distribución, que coinciden con la cresta del anticlinal y los valles de los sinclinales, respectivamente; (3) la localización de los puntos de inflexión; (4) el buzamiento de los flancos del pliegue; (5) y la longitud y buzamiento de la línea regional ajustada.

- (4) En la estructura KAD, las tasas de plegamiento varían en el tiempo y a lo largo de la dirección del pliegue. Interpretamos que el plegamiento incipiente se nucleó tras el depósito de la Unidad Sabunchi (Plioceno Inferior, 4.0 Ma a 3.7 Ma), y se propagó al sur simultáneamente al depósito de la Formación Surakhany 6 con tasas de acortamiento de $S_A \sim 2 \text{ mm} \cdot \text{año}^{-1}$. El segundo evento sin-tectónico fue homogéneo a lo largo del pliegue KAD y ha continuado hasta el Presente con magnitudes que oscilan entre $0.2\text{-}0.4 \text{ mm} \cdot \text{año}^{-1}$. En ambos episodios, la deformación se concentró en el alto estructural de la Culminación Sur donde se produjo el máximo levantamiento del KAD. Una evolución con ratios similares se infiere para la Culminación Norte.
- (5) El plegamiento fue acompañado por una rápida sedimentación ($<3.3 \text{ mm} \cdot \text{yr}^{-1}$), simultáneamente al depósito de la Unidad Surakhany (tasas de acortamiento \ll tasas de sedimentación). Las tasas de sedimentación de las secuencias Post-PS descendieron hasta $0.5\text{-}0.6 \text{ mm} \cdot \text{año}^{-1}$ (tasas de acortamiento \sim tasas de sedimentación), con mayores velocidades registradas en los sedimentos más recientes, en la Unidad Gelasian (Pleistoceno Superior-Presente, $<0.8\text{-}0.7 \text{ Ma}$). El balance entre el plegamiento y la sedimentación favoreció el progresivo cubrimiento del pliegue KAD en los últimos 1.7 ma en la Culminación Norte.
- (6) Abundantes complejos de depósito en masa (MTCs) se han generado en el dominio del pliegue KAD debido a la actividad de la cuenca en los últimos 3.1 ma. La emersión de la cresta del pliegue en un fondo del mar deformado promovió el depósito de numerosos deslizamientos coetáneos al depósito de las unidades Akchagyl y Apsheron (Pleistoceno Inferior-Pleistoceno Superior, $\sim 1.7\text{-}1.6 \text{ Ma}$ to $\sim 0.8\text{-}0.7 \text{ Ma}$). Los mayores deslizamientos fueron depositados en el periodo Akchagyl controlados por un episodio acentuado de plegamiento. La progradación deltaica sobre la plataforma marina es el factor responsable de la inestabilidad de pendiente y flujos de derrubio en la Unidad Gelasian ($<0.8\text{-}0.7 \text{ Ma}$), que muestra una continua evacuación de material en cabecera.
- (7) El pliegue KAD está despegado de una superficie simple y de bajo buzamiento enraizada en una unidad débil e incompetente compuesta por arcillas fundamentalmente: la Unidad Maykop (Eoceno Superior-Mioceno Superior, $\sim 36\text{-}16.5 \text{ Ma}$). Las observaciones geométricas y las estimaciones de acortamiento sugieren que dicho nivel de despegue buza al Este y se encuentra enterrado entre 9 y 11 km de profundidad. El flanco oriental es el motor que dirige la deformación y representa el “forelimb”, mientras que el occidental es arrastrado y se denomina “backlimb”. La deformación del tipo despegue se produce en los últimos 3.7 ma debido a un modelo mixto que combina mecanismos de plegamiento diferentes. La migración de charnelas parece ser el mecanismo principal en el primer evento sin-sedimentario, mientras que la rotación de flancos juega un papel dominante en el paquete Post-PS.
- (8) Valores significativamente inferiores de S_C frente a S_A indican que la longitud de las

capas no se conserva, mientras que el volumen sí varía durante la deformación debido al diapirismo de lodo. Arcillas enriquecidas en fluidos perforan el anticlinal KAD como resultado de estructuras que se ensanchan a niveles someros y definen diapiros “teardrops”. La conexión con la capa fuente o el pedestal de barro se mantiene inidentificada en el cubo sísmico, aunque se reconoce los antiguos conductos de barro que alimentaban al diapiro en forma de “welds” verticales y sub-verticales. Estas estructuras “weld” se produjeron probablemente durante el plegamiento y muestran componentes de salto en buzamiento y dirección (dextro). La roca madre de las arcillas sobrepresurizadas es la Unidad Maykop. El barro es móvil y asciende como resultado de elevadas tasas de plegamiento en ambos dominios de culminación, coincidiendo con las zonas que registran valores máximos de deformación. El diapirismo se inicia en la época del Akchagyl, y su detención está datada en los comienzos de la Unidad Apsheron en la Culminación Norte, mientras que continúa hasta el fin del Apsheron en la Culminación Sur. Postulamos que la unidad dúctil de la Maykop migró en varias direcciones, tanto perpendicular como paralelamente al eje del pliegue; es decir, hacia la cuenca y de forma sub-horizontal, respectivamente. La movilización de barro en profundidad se infiere previa al período pre-Plioceno, debido al basculamiento de la cuenca, y pasa a inflar el núcleo del pliegue durante el depósito de las unidades PS.

- (9) El fallamiento en el pliegue KAD está separado en dos niveles estructurales. Estructuras normales con dirección N-S fracturan la cresta del pliegue como fallas curvas, mientras que las estructuras inversas están distribuidas ampliamente a lo largo del núcleo del pliegue y se disponen paralelas a la traza axial del pliegue (NO-SE). Dos sistemas de fallas largas y planares deforman ambos flancos y definen grabens extensionales E-O y cabalgamientos NO-SE relacionados con plegamiento tipo “kink”. Una superficie neutral y cuya posición oscila entre la Unidad Sabunchi y Formación Surakhany (subunidad Sk 6) es la que limita la extensión en el arco externo del pliegue y la compresión en el interno.
- (10) De acuerdo con la evolución del pliegue y el patrón de variación del espesor de las capas, proponemos que el plegamiento está nucleado sobre una zona de falla enterrada. La estructura en profundidad estaba compuesta por un sistema de dos fallas de alto ángulo y que buzaba al Este, los cuales se unieron en un único segmento durante el depósito de las unidades PS. Esta zona de falla presumiblemente tuvo un desplazamiento normal, con una componente limitada de salto en dirección (dextro), y acompañó el basculamiento de la cuenca. El movimiento dextro es el responsable del carácter sigmoide de la traza y de la curvatura de las fallas en las secuencias Post-PS. Esta zona de falla pudo ser utilizada por la Unidad Maykop para fluir tanto lateral como sub-horizontalmente.
- (11) En la región del Mar Caspio, la roca madre del petróleo y gas es la Unidad Maykop. La ausencia de hidrocarburos en la zona de estudio puede ser resultado de tres factores combinados: la tectónica, la mala calidad de la roca madre y de los reservorios, y la baja generación e inmadurez de hidrocarburos. Los hidrocarburos fueron presumiblemente liberados durante la intensa estructuración habida en el pliegue KAD. El episodio que tuvo lugar en la época Surakhany generó numerosas fallas que afectaron la cresta del pliegue, actuando como vías principales de escape de fluidos. La discordancia registrada a techo de las unidades PS y los escarpes erosivos de los depósitos gravitacionales truncaron y erosionaron el anticlinal, promoviendo la liberación de fluidos de origen secundario. El diapirismo también contribuyó con la migración de petróleo y gas al exterior.

9. REFERENCES

- Abdullayev, N.R. (2000). Seismic stratigraphy of the Upper Pliocene and Quaternary deposits in the South Caspian Basin. *Journal of Petroleum Science and Engineering*, 28, 207-226.
- Abdullayev, N.R., G.W. Riley, and A.P. Bowman (2012). Regional controls on lacustrine sandstone reservoirs: the Pliocene of the South Caspian Basin. *In: Lacustrine sandstone reservoirs and hydrocarbon systems*, O.W. Baganz, Y. Bartov, K. Bohacs, and D. Nummedal (eds.). *AAPG Memoir*, 95, Tulsa, U.S.A., American Association of Petroleum Geologists, p. 71-98.
- Abrams, M.A., and A.A. Narimanov (1997). Geochemical evaluation of hydrocarbons and their potential sources in the western South Caspian depression, Republic of Azerbaijan. *Marine and Petroleum Geology*, 14, 451-468.
- Abreu, V., and D. Nummedal (2007). Miocene to Quaternary sequence stratigraphy of the South and Central Caspian Basin. *In: Oil and gas of the Greater Caspian Sea*, P.O. Yilmaz, and G.H. Isaksen (eds.). *AAPG Studies in Geology*, 55, Tulsa, U.S.A., American Association of Petroleum Geologists, p. 65-86.
- Adamia, S.A., M.B. Lordkipanidze, and G.S. Zakariadze (1977). Evolution of an active continental margin as exemplified by the Alpine history of the Caucasus. *Tectonophysics*, 40, 183-199.
- Afandiyeva, M.A., R.G. Babayev, and C.L. Johnson (2009). Stratigraphy of the Maikopian series of Azerbaijan. *In: Seventh Micropalaeontological Workshop MIKRO-2009*, D. Peryt, and M.A. Kaminsky (eds). *Grzybowski Foundation*, Swieta Katarzyna, Poland.
- Aliiev, A.K. (1960). Geology and hydrocarbons of the Kura-Araks region, Baku, Azerbaijan. State Publisher of Hydrocarbon Literature, Azerbaijan, 631 pp.
- Alizade, A.A., G.A. Akhmedov, A.M. Akhmedov, A.K. Aliiev, and M.M. Zeinalov (1966). Geology of the oil and gas fields of Azerbaijan. Nauka, Azerbaijan, 392 pp.
- Aliyeva, E.G.-M. (2005). Reservoirs of the Lower Pliocene Productive Series at the western flank of the South Caspian Basin. *Lithology and Mineral Resources*, 40, 267-278.
- Allen, M.B., J. Jackson, and R. Walker (2004). Late Cenozoic reorganization of the Arabia-Eurasia collision and the comparison of short-term and long-term deformation rates. *Tectonics*, 23, TC2008.
- Allen, M.B., S. Jones, A. Ismail-Zadeh, M. Simmons, and L. Anderson (2002). Onset of subduction as the cause of rapid Pliocene-Quaternary subsidence in the South Caspian Basin. *Geology*, 30, 775-778.
- Allen, M.B., S.J. Vincent, G.I. Alsop, A. Ismail-zadeh, and R. Flecker (2003). Late Cenozoic deformation in the South Caspian region: effects of a rigid basement block within a collision zone. *Tectonophysics*, 366, 223-239.
- Allen, P.A., and J.R.L. Allen (2005). Basin analysis: principles and applications. Blackwell Publishing, Oxford, U.K., 532 pp.

- Alsop, G.I., and R.E. Holdsworth (2002). The geometry and kinematics of flow perturbation folds. *Tectonophysics*, 350, 99-125.
- Artyushkov, E.V. (2007). Formation of the South Caspian Basin as a result of phase transitions in the lower continental crust. *Doklady Earth Sciences*, 417, 1141-1146.
- Asquith, G., D. Krygowski, S. Henderson, and N. Hurley, eds., (2004). Basic well log analysis. *AAPG Methods in Exploration Series*, 16, Tulsa, U.S.A., American Association of Petroleum Geologists, p. 240-244.
- Axen, G.J., P.S. Lam, M. Grove, D.F. Stockli, and J. Hassanzadeh (2001). Exhumation of the west-central Alborz Mountains, Iran, Caspian subsidence, and collision-related tectonics. *Geology*, 29, 559-562.
- Azizbekov, S.A. (1972). Geology of the USSR (Azerbaijan SSR). Nedra, Moscow, Russia, 433 pp.
- Bacon, M., R. Simm, and T. Redshaw, eds., (2007). 3-D Seismic interpretation. Cambridge University Press, Cambridge, U.K., 238 pp.
- Baganz, O.W., Y. Bartov, K. Bohacs, and D. Nummedal (2012). Productive series play of the Paleo-Volga Delta, South Caspian Basin: exploration history, sedimentation and petroleum system. *In: Lacustrine sandstone reservoirs and hydrocarbon systems*, O.W. Baganz, Y. Bartov, K. Bohacs, and D. Nummedal (eds.). *AAPG Memoir*, 95, Tulsa, U.S.A., American Association of Petroleum Geologists, p. 57-70.
- Bagirov, E., R. Nadirov, and I. Lerche (1997). Hydrocarbon evolution for a north-south section of the South Caspian Basin. *Marine and Petroleum Geology*, 14, 773-854.
- Barnes, A., M. Cole, T. Michaels, P. Norlund, and C. Sembroski (2011). Making seismic data come alive. *First Break*, 29, 33-38.
- Bateman, R., and C. Konen (1979). The log analyst and the programmable pocket calculator. *Log analyst*, 18, 3-11.
- Beaubouef, R.T., and V. Abreu (2010). MTCs of the Brazos-Trinity slope system: thoughts on the sequence stratigraphy of MTCs and their possible roles in shaping hydrocarbon traps. *In: Submarine mass movements and their consequences*, D.C. Mosher, C.D.P. Baxter, J.D. Chaytor, H.J. Lee, L. Moscardelli, R.C. Shipp, and R. Urgeles (eds.). *Advances in Natural and Technological Hazards Research*, 28, Dordrecht, The Netherlands, Springer, p. 475-490.
- Becker, J.J., D.T. Sandwell, W.H.F. Smith, J. Braud, B. Binder, J. Depner, D. Fabre, J. Factor, S. Ingalls, S.-H. Kim, R. Ladner, K. Marks, S. Nelson, A. Pharaoh, R. Trimmer, J. Von Rosenberg, G. Wallace, and P. Weatherall (2009). Global bathymetry and elevation data at 30 Arc Seconds Resolution: SRTM30_PLUS. *Marine Geodesy*, 32, 355-371.
- Belopolsky, A.V., and M. Talwani (1999). Petroleum reserves and potential of the greater Caspian region. *In: Association round table conference*. AAPG, Birmingham, England, U.K., p. 1296-1367.
- Berberian, M. (1983). The southern Caspian: a compressional depression floored by a trapped, modified oceanic crust. *Canadian Journal of Earth Sciences*, 20, 163-183.
- Bertello, F., C. Cooper, P. Castellano, and G.P. Ronchitell (2001). Improved characterization of a complex structure in the Azerbaijan offshore revealed by 3D pre-stack depth migration and depth continuity cube applications. *SEG Technical Program Expanded Abstracts*, 20, 617-620.
- Bowman A.W, A. Pope, and B. Ismail (2006). Detecting discontinuities in nonparametric regression curves and surfaces. *Statistics and Computing*, 16, 377-390.
- BP website (2014). British Petroleum (BP) in Azerbaijan. Accessed on February 2014, http://www.bp.com/en_az/caspian/press/businessupdates/businessupdates.html.
- Brown, A.R., ed., (1986). Interpretation of three-dimensional seismic data. *AAPG Memoir*, 42, Tulsa, U.S.A., American Association of Petroleum Geologists, 315 pp.
- Brown, A.R., ed., (2003). Interpretation of three-dimensional seismic data. *AAPG Memoir*, 42, and *SEG Investigations in Geophysics*, 9, Tulsa, U.S.A., American Association of Petroleum Geologists and the Society of Exploration Geophysicists. 541 pp.
- Brown, A.R., and J.D. Robertson (1985). Seismic interpretation for detailed exploration development and production.

- The Leading Edge*, 4, 60-65.
- Brown, K.M. (1990). The nature and hydrogeologic significance of mud diapirs and diatremes for accretionary systems. *Journal of Geophysical Research*, 95, B6, 8969-8982.
- Brown Jr., L.F., and W.L. Fisher, eds., (1979). Principles of seismic stratigraphic interpretation. *Stratigraphic interpretation of seismic data school notes*, 16, Austin, U.S.A., American Association of Petroleum Geologists and the Society of Exploration Geophysicists.
- Brown, K.M., and G.K. Westbrook (1988). Mud diapirism and subcretion in the Barbados Ridge complex. *Tectonics*, 7, 613-640.
- Brunet, M.-F., Andrei V. Ershov, Yury A. Volozh, Maxim V. Korotaev, Mikhail P. Antipov and Jean-Paul Cadet (2007). Precaspian and South Caspian basins: subsidence evolution of two superdeep basins. *American Association of Petroleum Geologists Bulletin*, 55, 151-155.
- Brunet, M.-F., M.V. Korotaev, A.V. Ershov, and A.M. Nikishin (2003). The South Caspian Basin: a review of its evolution from subsidence modelling. *Sedimentary Geology*, 156, 119-148.
- Bulnes, M., and J. Poblet (1999). Estimating the detachment depth in cross sections involving detachment folds. *Geological Magazine*, 136, 395-412.
- Cairn Energy website (2014). Accessed on January 2014, <http://www.cairnenergy.com/>.
- Camerlo, R.H., and E.F. Benson (2006). Geometric and seismic interpretation of the Perdido fold belt: Northwestern deep-water Gulf of Mexico. *American Association of Petroleum Geologists Bulletin*, 90, 363-386.
- Camerlo, R.H., D. Meyer, and R. Meltz (2004). Shale tectonism in the northern Port Isabel Fold Belt. *In: Salt-sediment interactions and hydrocarbon prospectivity: Concepts, applications and case studies for the 21st Century conference*, P.J. Post, D.L. Olson, K.T. Lyons, S.L. Palmes, P.F. Harrison, and N.C. Rosen (eds.). *SEPM*, Gulf Coast section, Houston, U.S.A.
- Cartwright, J. (2007). The impact of 3D seismic data on the understanding of compaction, fluid flow and diagenesis in sedimentary basins. *Geological Society of London*, 164, 881-893.
- Chamberlin, R.T. (1910). The Appalachian folds of central Pennsylvania. *Journal of Geology*, 18, 228-251.
- Chopra, S. (2001). Integrating coherence cube in imaging and seismic inversion. *The Leading Edge*, 20, 354-362.
- Chopra, S., and K.J. Marfurt (2005). Seismic attributes - A historical perspective, *Geophysics*, 70, 3SO-28SO.
- Cooper, C. (2001a). Mud volcanoes of Azerbaijan visualized using 3D seismic depth cubes: The importance of overpressured fluid and gas instead of non-existent diapirs. *In: Subsurface sediment mobilisation conference. EAGE*, Ghent, Belgium, p. 71.
- Cooper, C. (2001b). Mud volcanoes of the South Caspian Basin: Seismic data and implications for hydrocarbon systems. *American Association of Petroleum Geologists Bulletin*, 85, 231-245.
- Cordsen, A., M. Galbraith, and J. Peirce (2000). Planning land 3-D seismic surveys, B.A. Hardage, and S.J. Hill (eds.). *Geophysical Developments*, 9, Tulsa, U.S.A., Society of Exploration Geophysicists, 204 pp.
- Corthay, J.E. and A.A. Aliyev (2000). Delineation of a mud volcano complex, surficial mudflows, slump blocks, and shallow gas reservoirs, offshore Azerbaijan. *In: Offshore technology conference*, Houston, U.S.A.
- Dahlstrom, C.D.A. (1969). The upper detachment in concentric folding. *Bulletin of Canadian Petroleum Geology*, 17, 326-346.
- Dahlstrom, C.D.A. (1990). Geometric constraints derived from the law of conservation of volume and applied to evolutionary models for detachment folding. *American Association of Petroleum Geologists Bulletin*, 74, 336-344.
- Dalley, R.M., E.C.A. Gevers, G.M. Stampfli, D.J. Davies, C.N. Gastaldi, P.A. Ruijtenberg, and G.J.O. Vermeer (1989). Dip and azimuth displays for 3-D seismic interpretation. *First Break*, 7, 86-95.
- Day-Stirrat, R.J., A. McDonnell, and L.J. Wood (2010). Diagenetic and seismic concerns associated with interpretation of deeply buried 'mobile shales'. *In: Shale*

- tectonics, L.J. Wood (ed.). *AAPG Memoir*, 93, Tulsa, U.S.A., American Association of Petroleum Geologists, p. 5-27.
- DeMets, C., R.G. Gordon, D.F. Argus, and S. Stein (1990). Current plate motions. *Geophysical Journal International*, 101, 425-478.
- De Sitter, L.U. (1956). Structural geology. McGraw-Hill, New York, U.S.A. 551 pp.
- Devlin, W.J., J.M. Cogswell, G.M. Gaskins, G.H. Isaksen, D.M. Pitcher, D.P. Puls, K.O. Stanley, and G.R.T. Wall. (1999). South Caspian Basin: young, cool, and full of promise. *Geological Society of America Today*, 9, 1-9.
- Dimitrov, L.I. (2002). Mud volcanoes—the most important pathway for degassing deeply buried sediments. *Earth-Science Reviews*, 59, 49-76.
- Dooley, T., K. McClay, M.R. Hempton, and D. Smit (2005). Salt tectonics above complex basement extensional fault systems: results from analogue modelling. *In: Petroleum geology conference series. Geological Society of London*, p. 1631-1648.
- EIA (2013). Overview of oil and natural gas in the Caspian Sea region. United States Energy Information Administration (EIA), 25 pp.
- EIA website (2013). The Caspian Sea region, by the United States Energy Information Administration (EIA). Accessed on December 2013, <http://www.eia.gov/todayinenergy/detail.cfm?id=12911>.
- Eisley, G.R., and H. Tieman (2010). A comparison of prestack depth and prestack time imaging of the Paktoa complex, Canadian Beaufort Mackenzie basin. *In: Shale tectonics*, L.J. Wood (ed.). *AAPG Memoir*, 93, Tulsa, U.S.A., American Association of Petroleum Geologists, p. 79-90.
- Engdahl, E.R., J.A. Jackson, S.C. Myers, E.A. Bergman, and K. Priestley (2006). Relocation and assessment of seismicity in the Iran region. *Geophysical Journal International*, 167, 761-778.
- ENI (2002). ENI-E&P Division - EDPSA Kur Dashi - Close Out Report. Confidential reports.
- Epard, J.L., and R.H.Jr. Groshong (1993). Excess area and depth to detachment. *American Association of Petroleum Geologists Bulletin*, 77, 1291-1302.
- Epard, J.L., and R.H.Jr. Groshong (1995). Kinematic model of detachment folding including limb rotation, fixed hinges and layer-parallel strain. *Tectonophysics*, 247, 85-103.
- Etiopie, G., A. Feyzullayev, C.L. Baciu, and A.V. Milkov (2004). Methane emission from mud volcanoes in eastern Azerbaijan. *Geology*, 32, 465-468.
- Evans, R.J., S.A. Stewart, and R.J. Davies (2008). The structure and formation of mud volcano summit calderas. *Geological Society of London*, 165, 769-780.
- Fan, J., and I. Gijbels (1996). Local polynomial modelling and its applications. Chapman and Hall, London, U.K., 360 pp.
- Ferrill, D.A., A.P. Morris, J.A. Stamatakos, and D.W. Sims (2000). Crossing conjugate normal faults. *American Association of Petroleum Geologists Bulletin*, 84, 1543-1559.
- Fisher, M.P., and N.B. Woodward (1992). The geometric evolution of foreland thrust systems. *In: Thrust tectonics*, K. McClay (ed.). Chapman and Hall, London, U.K., p. 181-189.
- Fleuty, M.J. (1964). The description of folds. *Proceedings of the Geologists' Association*, 75, 461-492.
- Forte, A.M., E. Cowgill, T. Bernardin, O. Kreylos, and B. Hamann (2010). Late Cenozoic deformation of the Kura fold-thrust belt, southern Greater Caucasus. *Geological Society of America Bulletin*, 122, 465-486.
- Forte, A.M., Sumner, D.Y., Cowgill, E., Stoica, M., Murtuzayev, I., Kangarli, T., Elashvili, M., Godoladze, T. and Z. Javakhishvili (2015). Late Miocene to Pliocene stratigraphy of the Kura Basin, a subbasin of the South Caspian Basin: implications for the diachroneity of boundaries. *Basin Research*, 27, 247-271.
- Fowler, S.R., J. Mildenhall, S. Zalova, G. Riley, G. Elsley, A. Desplanques, and F. Guliyev (2000). Mud volcanoes and structural development on Shah Deniz. *Journal of Petroleum Science and Engineering*, 28, 189-206.
- Frey-Martínez, J., J. Cartwright, and D. James (2006). Frontally confined versus frontally emergent submarine landslides: A 3D seismic characterisation. *Marine and*

- Petroleum Geology*, 23, 585-604.
- Gee, M.J.R., H.S. Uy, J. Warren, C.K. Morley, and J.J. Lambiase (2007). The Brunei slide: A giant submarine landslide on the North West Borneo Margin revealed by 3D seismic data. *Marine Geology*, 246, 9-23.
- Giles, K.A., and T.F. Lawton (2002). Halokinetic sequence stratigraphy adjacent to the El Papalote diapir, Northeastern Mexico. *American Association of Petroleum Geologists Bulletin*, 86, 823-840.
- Glumov, I.F. (2004). Regional geology and petroleum potential of the Caspian Sea. Nedra, Moscow, Russia, 344 pp.
- Gonzalez-Mieres, R., and J. Suppe (2006). Relief and shortening in detachment folds. *Journal of Structural Geology*, 28, 1785-1807.
- Gonzalez-Mieres R, and Suppe J (2011). Shortening histories in active detachment folds based on area-of-relief methods. In: Thrust fault-related folding, K. McClay, J. Shaw, and J. Suppe (eds.). *AAPG Memoir*, 94, Tulsa, U.S.A., American Association of Petroleum Geologists, p. 39-67.
- Grad, M., T. Tiira, M. Behm, A.A. Belinsky, D.C. Booth, E. Brückl, R. Cassinis, R.A. Chadwick, W. Czuba, A.V. Egorkin, R.W. England, Y.M. Erinchek, G.R. Fougler, E. Gaczyński, A. Gosar, A. Guterch, E. Hegedüs, P. Hrubcová, T. Janik, W. Jokat, E.E. Karagianni, G.R. Keller, A. Kelly, K. Komminaho, T. Korja, J. Kortström, S.L. Kostyuchenko, E. Kozlovskaya, G. Laske, L. Lenkey, U. Luosto, P.K.H. Maguire, M. Majdański, M. Malinowski, F. Marone, J. Mechie, E.D. Milshtein, G. Motuza, S. Nikolova, S. Olsson, M. Pasyanos, O.V. Petrov, V.E. Rakitov, R. Raykova, O. Ritzmann, R. Roberts, M. Sachpazi, I.A. Sanina, M.C. Schmidt-Aursch, I. Serrano, A. Špičák, P. Šroda, F. Šumanovac, B. Taylor, A.G. Vedrentsev, J. Vozár, Z. Weber, M. Wilde-Piórko, T.P. Yegorova, J. Yliniemi, B. Zelt, and E.E. Zolotov (2009). The Moho depth map of the European Plate. *Geophysical Journal International*, 176, 279-292.
- Gradstein, F.M., J.G. Ogg, M. Schmitz, and G. Ogg, eds., (2012). The geologic time scale 2012. Elsevier, Boston, U.S.A., 1144 pp.
- Granath, J.W., K.A. Soofi, O.W. Baganz, and E. Bagirov (2000). Gravity modelling and its implications to the tectonics of the South Caspian Basin. In: AAPG's inaugural regional international conference. AAPG, Istanbul, Turkey.
- Graue, K. (2000). Mud volcanoes in deepwater Nigeria. *Marine and Petroleum Geology*, 17, 954-974.
- Green, T., N. Abdullayev, J. Hossack, G. Riley, and A.M. Roberts (2009). Sedimentation and subsidence in the South Caspian Basin, Azerbaijan. In: South Caspian to Central Iran basins, M.-F. Brunet, M. Wilmsen, J.W. Granath (eds). *Geological Society of London*, 312, p. 241-260.
- Groshong, J.R.H., and J.L. Epard, J.L. (1994). The role of strain in area-constant detachment folding. *Journal of Structural Geology*, 16, 613-618.
- Guest, B., A. Guest, and G. Axen (2007). Late Tertiary tectonic evolution of northern Iran: a case for simple crustal folding. *Global and Planetary Change*, 58, 435-453.
- Guliev, I., and B. Panahi (2004). Geodynamics of the deep sedimentary basin of the Caspian Sea region: paragenetic correlation of seismicity and mud volcanism. *Geo-Marine Letters*, 29, 169-176.
- Guliyev, I.S., M.F. Tagiyev, and A.A. Feyzullayev (2001). Geochemical characteristics of organic matter from maikop rocks of eastern Azerbaijan. *Lithology and Mineral Resources*, 36, 280-285.
- Gürgey, K. (2003). Correlation, alteration, and origin of hydrocarbons in the GCA, Bahar, and Gum Adasi fields, western South Caspian Basin: geochemical and multivariate statistical assessments. *Marine and Petroleum Geology*, 20, 1119-1139.
- Guzofski, C.A., J.P. Mueller, J.H. Shaw, P. Muron, D.A. Medwedeff, F. Bilotti, and C. Rivero (2009). Insights into the mechanisms of fault-related folding provided by volumetric structural restorations using spatially varying mechanical constraints. *American Association of Petroleum Geologists Bulletin*, 93, 479-502.
- Harders, R., C.R. Ranero, W. Weinrebe, and J.H. Behrmann (2011). Submarine slope

- failures along the convergent continental margin of the Middle America Trench. *Geochemistry, Geophysics, Geosystems*, 12, Q05S32.
- Hardy, S., and K. McClay (1999). Kinematic modelling of extensional fault-propagation folding. *Journal of Structural Geology*, 21, 695-702.
- Hardy, S., and J. Poblet (1994). Geometric and numerical model of progressive limb rotation in detachment folds. *Geology*, 22, 371-374.
- Hardy, S., and J. Poblet (1995). The velocity description of deformation. paper 2: sediment geometries associated with fault-bend and fault-propagation folds. *Marine and Petroleum Geology*, 12, 165-176.
- Hardy, S., J. Poblet, K. McClay, and D. Waltham (1996). Mathematical modelling of growth strata associated with fault-related fold structures. *Geological Society of London*, 99, 265-282.
- Hart, B.S. (2008). Stratigraphically significant attributes, *The Leading Edge*, 320-324.
- Herron, D.A., ed., (2011). First steps in Seismic Interpretation. *Geophysical Monograph Series*, 16, SugarLand, U.S.A., Society of Exploration Geophysicists, 203 pp.
- Hinds, D.J., E. Aliyeva, M.B. Allen, C.E. Davies, S.B. Kroonenberg, M.D. Simmons, and S.J. Vincent (2004). Sedimentation in a discharge dominated fluvial-lacustrine system: the Neogene Productive Series of the South Caspian Basin, Azerbaijan. *Marine and Petroleum Geology*, 21, 613-638.
- Hollingsworth, J., M. Fattahi, R. Walker, M. Talebian, A. Bahroudi, M.J. Bolourchi, J. Jackson, and A. Copley (2010). Oroclinal bending, distributed thrust and strike-slip faulting, and the accommodation of Arabia-Eurasia convergence in NE Iran since the Oligocene. *Geophysical Journal International*, 181, 1214-1246.
- Hollingsworth, J., J. Jackson, R. Walker, and H. Nazari (2008). Extrusion tectonics and subduction in the eastern South Caspian region since 10 Ma. *Geology*, 36, 763-766.
- Hölt, T., J. Beyer, F. Gschwantner, P. Muigg, H. Doleish, G. Heinemann, and M. Hadwiger (2011). Interactive seismic interpretation with piecewise global energy minimization.
- Homza, T.X., and W.K. Wallace (1995). Geometric and kinematic models for detachment folds with fixed and variable detachment depths. *Journal of Structural Geology*, 17, 575-588.
- Homza, T.X., and W.K. Wallace (1997). Detachment folds with fixed hinges and variable detachment depth, northeastern Brooks Range, Alaska. *Journal of Structural Geology*, 19, 337-354.
- Hovland, M., A. Hill, and D. Stokes (1997). The structure and geomorphology of the Dashgil mud volcano, Azerbaijan. *Geomorphology*, 21, 1-15.
- Hubert-Ferrari, A., J. Suppe, R. Gonzalez-Mieres, and X. Wang (2007). Mechanisms of active folding of the landscape (southern Tian Shan, China). *Journal of Geophysical Research*, 112, B3.
- Hudec, M.R., and M.P.A. Jackson (2007). Terra infirma: Understanding salt tectonics. *Earth-Science Reviews*, 82, 1-28.
- Hudson, S.M., C.L. Johnson, M.A. Efendiyeva, H.D. Rowe, A.A. Feyzullayev, and C.S. Aliyev (2008). Stratigraphy and geochemical characterization of the Oligocene-Miocene Maikop series: Implications for the paleogeography of Eastern Azerbaijan. *Tectonophysics*, 451, 40-55.
- Huseynov, D.A., and I.S. Guliyev (2004). Mud volcanic natural phenomena in the South Caspian Basin: geology, fluid dynamics and environmental impact. *Environmental Geology*, 46, 1012-1023.
- Imbert, P., Geiss, B., and N. Fatjó de Martín (2014). How to evacuate 10 km³ of mud: saturate with gas and decrease the pressure! *Geomarine Letters*, 34, 199-213.
- Inan, S., M.N. Yalçın, I.S. Guliev, K. Kuliev, and A.A. Feizullayev (1997). Deep petroleum occurrences in the Lower Kura Depression, South Caspian Basin, Azerbaijan: an organic geochemical and basin modeling study. *Marine and Petroleum Geology*, 14, 731-762.
- Jackson, J., K. Priestley, M.B. Allen, and M. Berberian (2002). Active tectonics of the South Caspian Basin. *Geophysical Journal International*, 148, 214-245.
- Jackson, M.P.A., and C.J. Talbot (1991). A glossary of salt tectonics. Bureau of Economic Geology, University of Texas, U.S.A., 44 pp.
- Jamison, W.R. (1987). Geometric analysis of

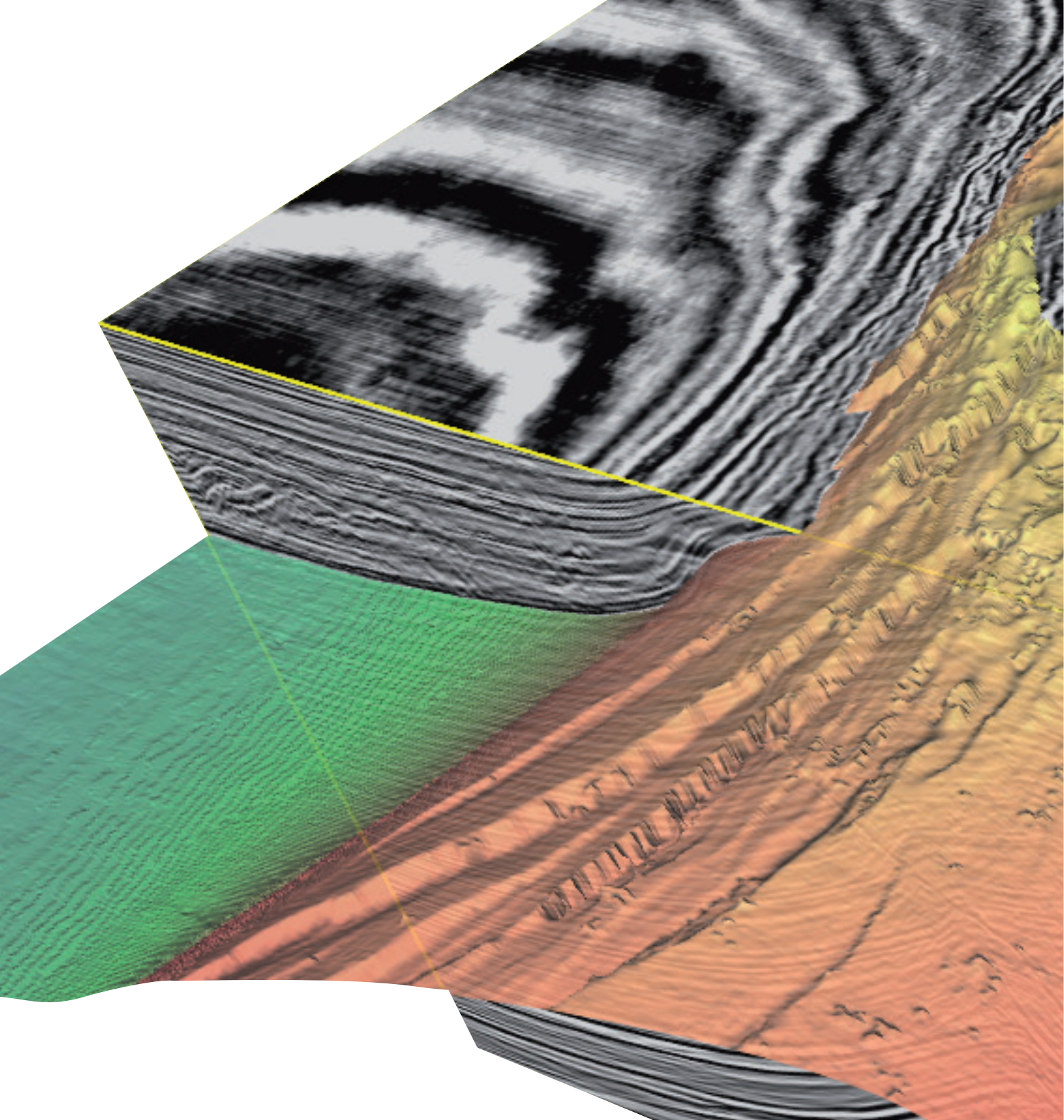
- fold development in overthrust terranes. *Journal of Structural Geology*, 9, 207-219.
- Jones, R.W., and M.D. Simmons (1997). A review of the stratigraphy of Eastern Paratethys (Oligocene-Holocene), with particular emphasis on the Black Sea. In: Regional and petroleum geology of the Black Sea and surrounding region, A.G. Robinson (ed.), *AAPG Memoir*, 68, Tulsa, U.S.A., American Association of Petroleum Geologists, p. 39-52.
- Kadirov, F.A. (2000). Application of the Hartley transform for interpretation of gravity anomalies in the Shamakhy-Gobustan and Absheron oil- and gas-bearing regions, Azerbaijan. *Journal of Applied Geophysics*, 45, 49-61.
- Khain, V.E., A.N. Gadjiev, and T.N. Kengerli (2007). Tectonic origin of the Apsheron Threshold in the Caspian Sea. *Doklady Earth Sciences*, 414, 552-556.
- Khain, V.Y., B.V. Grigoriants, and B.M. Isayev (1966). West Caspian fault and some factors controlling the transverse faults in geosynclinal folded regions. *Bulleten' Moskovskogo Obshchestva Ispytatelei Prirody*, 41, 115-124.
- Knapp, C.C., J.H. Knapp, and J.A. Connor (2004). Crustal-scale structure of the South Caspian Basin revealed by deep seismic reflection profiling. *Marine and Petroleum Geology*, 21, 1073-1081.
- Kopf, A. (2002). Significance of mud volcanism. *Reviews of Geophysics*, 40, 2-52.
- Kopf, A., S. Stegmann, G. Delisle, B. Panahi, C.S. Aliyev, and I. Guliyev (2009). In situ cone penetration tests at the active Dashgil mud volcano, Azerbaijan: Evidence for excess fluid pressure, updoming, and possible future violent eruption. *Marine and Petroleum Geology*, 26, 1716-1723.
- Kovachev, S.A., V.G. Kaz'min, I.P. Kuzin, and L.I. Lobkovsky (2006). New data on seismicity of the Middle Caspian Basin and their possible tectonic interpretation. *Geotectonics*, 40, 367-376.
- Krijgsman, W., M. Stoica, I. Vasiliev, and V.V. Popov (2010). Rise and fall of the Paratethys Sea during the Messinian Salinity crisis. *Earth and Planetary Science Letters*, 290, 183-191.
- Laubscher, H.P. (1961). Die Fernschubhypothese der Jurafaltung. *Eclogae Geologicae Helveticae*, 54, 221-282.
- Lavrushin, V.U., B.G. Polyak, R.M. Prasolov, and I.L. Kamenskii (1996). Sources of material in mud volcano products (based on isotropic, hydrochemical and geological data). *Lithology and Mineral Resources*, 31, 557-578.
- Lebedev, L.I. (1987). *Kaspiyskoe More-Geologiya I Neftegazonosnost'*. Nedra, Moscow, Russia, 302 pp.
- Lerche, I., E. Bagirov, R.S. Nadirov, M. Tagiyev, and I. Guliyev (1997). Evolution of the South Caspian Basin: geologic risks and probable hazards. Azerbaijan Academy of Sciences, Baku, Azerbaijan, 675 pp.
- Lisle, R.J. (1999). Predicting patterns of strain from three-dimensional fold geometries: neutral surface folds and forced folds. *Geological Society of London*, 169, 213-221.
- Loader, C. (1999). Change point estimation using nonparametric regression. *The Annals of Statistics*, 27, 1667-1678.
- Lyberis, N., and G. Manby (1999). Oblique to orthogonal convergence across the Turan block in the Post-Miocene. *American Association of Petroleum Geologists Bulletin*, 83, 1135-1160.
- Malovitsky, Ya.P. (1970). New data on geological structure of CIS-Caucasian shelf of Black Sea. *Doklady Akademii Nauk SSSR*, 195, 174.
- Mamedov, P.Z. (1992). Seismostratigraphical investigations of geological structure of sedimentary cover of South Caspian superdepression and perspectives of oil – gas productivity. Ph. D. thesis, University of Baku, Azerbaijan, 40 pp.
- Mangino, S., and K. Priestley (1998). The crustal structure of the southern Caspian region. *Geophysical Journal International*, 133, 630-648.
- Mellors, R., D. Kilb, A. Aliyev, A. Gasanov, and G. Yetirmishli (2007). Correlations between earthquakes and large mud volcano eruptions. *Journal of Geophysical Research*, 112, B04304.
- Mercier, E., S. Rafini, and R. Ahmadi (2007). Fold kinematics in "fold-and-thrusts belts" the "hinge migration" question, a review. In: Thrust bends and foreland basins, O. Lacombe, F. Roure, J. Lavé, and J. Vergés (eds.). Springer, p. 135-147.
- Miller, K.G., M.A. Kominsz, J.V. Browning,

- J.D. Wright, G.S. Mountain, M.E. Katz, P.J. Sugarman, B.S. Cramer, N. Christie-Blick, and S.F. Pekar (2005). The Phanerozoic record of global sea-level change. *Science*, 310, 1293-1298.
- Mitra, S. (1990). Fault-propagation folds: geometry, kinematics, and hydrocarbon traps. *American Association of Petroleum Geologists Bulletin*, 74, 921-945.
- Mitra, S. (2003). A unified kinematic model for the evolution of detachment folds. *Journal of Structural Geology*, 25, 1659-1673.
- Mitra, S., and J. Namson (1989). Equal-area balancing. *American Journal of Science*, 289, 563-599.
- Mondol, N.H., K. Bjorlykke, and J. Jahren (2008). Experimental compaction of clays; relationship between permeability and petrophysical properties in mudstones. *Petroleum Geoscience*, 14, 319-337.
- Morley, C.K., and G. Guerin (1996). Comparison of gravity-driven deformation styles and behavior associated with mobile shales and salt. *Tectonics*, 15, 1154-1170.
- Morley, C.K., R. King, R. Hillis, M. Tingay, and G. Backe (2011). Deepwater fold and thrust belt classification, tectonics, structure and hydrocarbon prospectivity: a review. *Earth-Science Reviews*, 104, 41-91.
- Morton, A., M. Allen, M. Simmons, F. Spathopoulos, J. Still, D. Hinds, A.I. Zadeh, and S. Kroonenberg (2003). Provenance patterns in a neotectonic basin: Pliocene and Quaternary sediment supply to the South Caspian. *Basin Research*, 15, 321-337.
- Morton, R.A. (1993). Attributes and origins of ancient submarine slides and filled embayments: examples from the Gulf Coast Basin. *American Association of Petroleum Geologists Bulletin*, 77, 1064-1081.
- Murton, B.J., and J. Biggs (2003). Numerical modelling of mud volcanoes and their flows using constraints from the Gulf of Cadiz. *Marine Geology*, 195, 223-236.
- Nadirov, R.S. (1985). The geological structure and oil and gas presence of the Talysh-Vandam gravitational maximum area. M.S. thesis, University of Baku, Azerbaijan, 30 pp.
- Nadirov, R.S., E. Bagirov, M. Tagiyev, and I. Lerche (1997). Flexural plate subsidence, sedimentation rates, and structural development of the super-deep South Caspian Basin. *Marine and Petroleum Geology*, 14, 383-400.
- Nissen, S.E., N.L. Haskell, C.T. Steiner, and K.L. Coterill (1999). Debris flow outrunner blocks, glide tracks, and pressure ridges identified on the Nigerian continental slope using 3-D seismic coherency. *The Leading Edge*, 18, 595-599.
- Philip, H., A. Cisternas, A. Gvishiani, and A. Gorshkov (1989). The Caucasus: an actual example of the initial stages of continental collision. *Tectonophysics*, 161, 1-21.
- Planke, S., H. Svensen, M. Hovland, D.A. Banks, and B. Jamtveit (2003). Mud and fluid migration in active mud volcanoes in Azerbaijan. *Geo-Marine Letters*, 23, 258-268.
- Poblet, J. (2004). Geometría y cinemática de pliegues relacionados con cabalgamientos. *Trabajos de Geología*, 24, 127-146.
- Poblet, J. (2012). 2D kinematic models of growth fault-related folds in contractional settings. In: *Tectonics of sedimentary basins: recent advances*, C. Busby, and A. Azor (eds.). Blackwell Publishing Ltd., Chichester, U.K., p. 538-564.
- Poblet, J., M. Bulnes, K. McClay, and S. Hardy (2004). Plots of crestal structural relief and fold area versus shortening: a graphical technique to unravel the kinematics of thrust-related folds. In: *Thrust tectonics and hydrocarbon systems*, K. McClay (ed.). AAPG Memoir, 82, Tulsa, U.S.A., American Association of Petroleum Geologists, p. 372-399.
- Poblet, J., and K. McClay (1996). Geometry and kinematics of single-layer detachment folds. *American Association of Petroleum Geologists Bulletin*, 80, 1085-1109.
- Poblet, J., K. McClay, F. Storti, and J.A. Muñoz (1997). Geometries of syntectonic sediments associated with single-layer detachment folds. *Journal of Structural Geology*, 19, 369-381.
- Posamentier, H.W., R.J. Davies, J.A. Cartwright, and L.J. Wood (2007). Seismic geomorphology - An overview. In: *Seismic geomorphology: applications to hydrocarbon exploration and production*, R.J. Davies, H.W. Posamentier, L.J. Wood, and J.A. Cartwright (eds.). *Geological Society of*

- London, 277, p. 1-14.
- Posamentier, H.W., and O.J. Martinsen (2011). The character and genesis of submarine mass-transport deposits: insights from outcrop and 3D seismic data. *In: Mass-transport deposits in deepwater settings*, R.C. Shipp, P. Weimer, and H.W. Posamentier (eds.). *SEPM 96*, Tulsa, U.S.A., Society for Sedimentary Geology, p. 7-38.
- Priestley, K., C. Baker, and J. Jackson (1994). Implications of earthquake focal mechanism data for the active tectonics of the South Caspian Basin and surrounding regions. *Geophysical Journal International*, 118, 111-141.
- Ramsay, J.G., and M.I. Huber, eds., (1987). The techniques of modern structural geology: Folds and fractures (volume 2). Academic Press, London, U.K., 406 pp.
- Reilinger, R., S. McClusky, P. Vernant, S. Lawrence, S. Ergintav, R. Cakmak, H. Ozener, F. Kadirov, I. Guliev, R. Stepanyan, M. Nadariya, G. Hahubia, S. Mahmoud, K. Sakr, A. ArRajehi, D. Paradissis, A. Al-Aydrus, M. Prilepin, T. Guseva, E. Evren, A. Dmitrova, S.V. Filikov, F. Gomez, R. Al-Ghazzi, and G. Karam (2006). GPS constraints on continental deformation in the Africa-Arabia-Eurasia continental collision zone and implications for the dynamics of plate interactions. *Journal of Geophysical Research*, 111, B05411.
- Reynolds, A.D., M.D. Simmons, M.B.J. Bowman, J. Henton, A.C. Brayshaw, A.A. Alizade, I.S. Guliyev, S.F. Suleymanova, E.Z. Ateava, D.N. Mamedova, and R.O. Koshkarly (1998). Implications of outcrop geology for reservoirs in the Neogene Productive Series: Apsheron Peninsula, Azerbaijan. *American Association of Petroleum Geologists Bulletin*, 82, 25-49.
- Rich, J.L. (1934). Mechanics of low-angle overthrust faulting as illustrated by Cumberland Thrust block, Virginia, Kentucky, and Tennessee. *American Association of Petroleum Geologists Bulletin*, 18, 1584-1596.
- Richardson, S.E.J., R.J. Davies, M.B. Allen, and S.F. Grant (2011). Structure and evolution of mass transport deposits in the South Caspian Basin, Azerbaijan. *Basin Research*, 23, 702-719.
- Robein, E. (2010). Seismic imaging: a review of the techniques, their principles, merits and limitations. *Education tour series*, 4, The Netherlands, EAGE, 244 pp.
- Roberts K.S., R.J. Davies, and S.A. Stewart (2010). Structure of exhumed mud volcano feeder complexes, Azerbaijan. *Basin Research*, 22, 439-451.
- Rowan, M.G. (1997). Three-dimensional geometry and evolution of a segmented detachment fold, Mississippi Fan foldbelt, Gulf of Mexico. *Journal of Structural Geology*, 19, 463-480.
- Rowan, M.G., F.J. Peel, and B.C. Vendeville (2004). Gravity-driven fold belts on passive margins. *In: Thrust tectonics and hydrocarbon systems*, K. McClay (ed.). *AAPG Memoir*, 82, Tulsa, U.S.A., American Association of Petroleum Geologists, p. 157-182.
- Rowan M.G., B.D. Trudgill, and J.C. Fiduk (2000). Deep-water, salt-cored foldbelts: lessons from the Mississippi Fan and Perdido Fold belts, Northern Gulf of Mexico. *In: Atlantic Rifs and Continental Margins*, Mohriak W, and Talwani M. (eds.). *Geophysical monograph*, 115, American Geophysical Union, p. 173-191.
- Ruppert, D., and M.P. Wand (1994). Multivariate locally weighted least squares regression. *Annals of Statistics*, 22, 1346-1370.
- Sánchez-Borrego, I.R., M.D. Martínez-Miranda, and A. González-Carmona (2006). Local linear kernel estimation of the discontinuous regression function. *Computational statistics*, 21, 557-569.
- Sánchez-Borrego, I.R., J.I. Soto, M. Rueda, and I. Santos Betancor (2015). Nonparametric estimation to reconstruct the deformation history of an active fold in the Caspian Basin. *Submitted to Mathematical Geosciences* (ms. MATG-D-15-00050R1).
- Santos Betancor, I. and J.I. Soto (2015). 3D geometry of a shale-cored anticline in the western South Caspian Basin (offshore Azerbaijan). *Marine and Petroleum Geology*, 67, 829-851.
- Santos Betancor, I., J.I. Soto, L. Lonergan, and C. Macellari (2013a). Gravity-instabilities processes and mass-transport complexes during folding: the case of a shale-cored anticline in the western South Caspian Basin. *In: Proceedings of the 15th annual conference of the international*

- association for Mathematical Geosciences, E. Pardo-Igúzquiza, C. Guardiola-Albert, J. Heredia, L. Moreno-Merino, J.J. Durán, J.A. Vargas-Guzmán (eds.). *IAMG*, Madrid, Spain, p. 775-779.
- Santos Betancor, I., J.I. Soto, L. Lonergan, I. Sánchez-Borrego, and C. Macellari (2013b). 3D Geometry of an active shale-cored anticline in the western South Caspian Basin. *In: Proceedings of the 15th annual conference of the international association for Mathematical Geosciences*, E. Pardo-Igúzquiza, C. Guardiola-Albert, J. Heredia, L. Moreno-Merino, J.J. Durán, J.A. Vargas-Guzmán (eds.). *IAMG*, Madrid, Spain, p. 771-775.
- Schlumberger, Limited website (2014). The oilfield glossary: where the oil field meets the dictionary. Accessed on January 2014, <http://www.glossary.oilfield.slb.com>.
- Shaw, J.H., C.D. Connors, and J. Suppe, eds., (2005). Seismic interpretation of contractional fault-related folds. *In: An AAPG seismic atlas, AAPG Studies in Geology*, 53, Tulsa, U.S.A., American Association of Petroleum Geologists, 156 pp.
- Sheriff, R.E., ed., (1992). Reservoir Geophysics. *Investigations in Geophysics*, 7, U.S.A. Society of Exploration Geophysicists, 400 pp.
- Shikalibeily, E.S., and B.V. Grigoriants (1980). Principal features of the crustal structure of the South-Caspian basin and the conditions of its formation. *Tectonophysics*, 69, 113-121.
- Smale, J.L., Sihkhaliyev Y., and T.I. Beylin (1997). Faulting and associated mud diapirism in the South Caspian Basin: Implication for hydrocarbon trap development. *In: Basin and formation tectonics conference. EAGE*.
- Smith-Rouch, L.S. (2006). Oligocene–Miocene Maykop/Diatom total petroleum system of the South Caspian Basin Province, Azerbaijan, Iran, and Turkmenistan. *United States Geological Survey Bulletin 2201-I*, 1-27.
- Sonneland, L., O. Barkved, M. Olsen, and G. Snyder (1989). Application of seismic wave-field attributes in reservoir characterization. *In: Annual international meeting. SEG*, Dallas, U.S.A.,
- Soto, J.I., F. Fernández-Ibáñez, A.R. Talukder, and P. Martínez-García (2010). Miocene shale tectonics in the northern Alboran Sea (Western Mediterranean). *In: Shale tectonics*, L.J. Wood (ed.). *AAPG Memoir*, 93, Tulsa, U.S.A., American Association of Petroleum Geologists, p. 119-144.
- Stewart, S.A., and R.J. Davies (2006). Structure and emplacement of mud volcano systems in the South Caspian Basin. *American Association of Petroleum Geologists Bulletin*, 90, 771-786.
- Sultan, N., P. Cochonat, M. Canals, A. Cattaneo, B. Dennielou, H. Haflidason, J.S. Laberg, D. Long, J. Mienert, F. Trincardi, R. Urgeles, T.O. Vorrene, and C. Wilson (2004). Triggering mechanisms of slope instability processes and sediments failures on continental margins: a geotechnical approach. *Marine Geology*, 213, 291-321.
- Suppe, J. (1983). Geometry and kinematics of fault-bend folding. *American Journal of Science*, 283, 684-721.
- Suppe, J. (1985). Principles of structural geology: Englewood Cliffs, Prentice-Hall, New Jersey, U.S.A., 560 pp.
- Suppe, J., G.T. Chou, and S.C. Hook (1992). Rates of folding and faulting determined from growth strata. *In: Thrust tectonics*, K. McClay (ed.). Chapman and Hall, London, U.K., p. 105-121.
- Tagiyev, M.F., R.S. Nadirov, E.B. Bagirov, and I. Lerche (1997). Geohistory, thermal history and hydrocarbon generation history of the north-west South Caspian Basin. *Marine and Petroleum Geology*, 14, 362-382.
- Talebian, M., and J. Jackson (2002). Offset on the Main Recent Fault of NW Iran and implications for the late Cenozoic tectonics of the Arabia-Eurasia collision zone. *Geophysical Journal International*, 150, 422-439.
- Thadani, S.G., F. Aldabert, and A.G. Journel (1987). An integrated geostatistical/pattern recognition technique for characterization of reservoir spatial variability. *In: Annual international meeting. SEG*, New Orleans, U.S.A.
- Van Rensbergen, P., C.K. Morley, D.W. Ang, T.Q. Hoan, and N.T. Lam (1999). Structural evolution of shale diapirs from reactive rise to mud volcanism: 3D seismic data the Baram delta, offshore Brunei Darussalam. *Geological Society of*

- London, 156, 633-650.*
- Vernant, P., F. Nilforoushan, D. Hatzfeld, M.R. Abbassi, C. Vigny, F. Masson, H. Nankali, J. Martinod, A. Ashtiani, R. Bayer, F. Tavakoli, and J. Chéry (2004). Present-day crustal deformation and plate kinematics in the Middle East constrained by GPS measurements in Iran and northern Oman. *Geophysical Journal International, 157, 381-398.*
- Wall, G.R.T.W., and R.W. Wiener (1998). Structural reconstruction in the South Caspian Basin: Application to the Nakhchivan Prospect. *Geophysics News in Azerbaijan, 4, 11-13.*
- Wiltschko D.V., and R.H.Jr. Groshong (2012). The Chamberlin 1910 balanced section: Context, contribution, and critical reassessment. *Journal of Structural Geology, 41, 7-23.*
- Wu, S., and A.W. Bally (2000). Slope tectonics-comparisons and contrasts of structural styles of salt and shale tectonics of the Northern Gula of Mexico with shale tectonics of offshore Nigeria in Gula of Guinea. *In: Atlantic Rifs and Continental Margins, Mohriak W, and Talwani M. (eds.). Geophysical monograph, 115, American Geophysical Union, p. 151-172.*
- Wu J, and C. Chu (1993). Nonparametric function estimation and bandwidth selection for discontinuous regression functions. *Statistica Sinica, 3, 557-576.*
- Yakubov, A.A., A.A. Alizade, and M.M. Zeinalov (1971). Mud volcanoes of Azerbaijan SSR. Academy of Sciences, Baku, Azerbaijan, 258 pp.
- Yusifov, M., 2004. Seismic interpretation and classification of mud volcanoes of the South Caspian basin, offshore Azerbaijan. M.S. thesis University of Texas, U.S.A, 94 pp.
- Yusifov, M., and P.D. Rabinowitz (2004). Classification of mud volcanoes in the South Caspian Basin, offshore Azerbaijan. *Marine and Petroleum Geology, 21, 965-975.*
- Zonenshain, L.P., and X. Le Pichon (1986). Deep basins of the Black Sea and Caspian Sea as remnants of Mesozoic back-arc basins. *Tectonophysics, 123, 181-211.*



Universidad de Granada



CSIC

CONSEJO SUPERIOR DE INVESTIGACIONES CIENTÍFICAS



REPSOL

Departamento de Geodinámica (UGR)
Instituto Andaluz de Ciencias de la Tierra (CSIC-UGR)